Synthesis of S-doped Graphitic Carbon Nitride (g-C_3N_4)/CuO/ZrO_2Based Semiconducting Nanostructures for Sensor and Catalytic Degradation of Pollutant Dyes

By

Nigussie Alebachew Ayalew

A Ph.D. Dissertation Submitted to the Department of Applied Chemistry School of Applied Natural Sciences

Presented in Partial Fulfilment of the Requirement for The Degree of Doctor of Philosophy in Applied Chemistry (Material Chemistry)

Office of Graduate Studies
Adama Science and Technology University

February, 2024
Adama, Ethiopia

Synthesis of S-doped Graphitic Carbon Nitride (g-C_3N_4)/CuO/ZrO_2 Based Semiconducting Nanostructures for Sensor and Catalytic Degradation of Pollutant Dyes

By

Nigussie Alebachew Ayalew

Supervisors:

Prof. H C Ananda Murthy (Main Supervisor)

Dr. Bedasa Abdisa Gonfa (Co-Supervisor)

Prof. Taye Beyene Demissie (Co-Supervisor)

Presented in Fulfillment of the Requirement for the Degree of Doctor of Philosophy in Applied Chemistry (Specialization in Material Chemistry)

Office of Graduate Studies

Adama Science and Technology University

February, 2024

Adama, Ethiopia

Declaration

I hereby declare that this Dissertation entitled "**Synthesis of S-doped Graphitic Carbon Nitride (g-C_3N_4)/CuO/ZrO_2 Based Semiconducting Nanostructures for Sensor and Catalytic Degradation of Pollutant Dyes**" is my original work. It has not been submitted for the award of any academic degree, diploma or certificate in any other university. All sources of materials used for this thesis have been duly acknowledged through appropriate citations.

Nigussie Alebachew Ayalew	_____	_____
Name of student	**Signature**	**Date**

Recommendation

We, the supervisors of this dissertation, hereby certify that we have read and revised the dissertation entitled **"Synthesis of S-doped Graphitic Carbon Nitride (g-C_3N_4)/CuO/ZrO_2 Based Semiconducting Nanostructures for Sensor and Catalytic Degradation of Pollutant Dyes"** prepared under our guidance by Nigussie Alebachew Ayalew and submitted in partial fulfilment of the requirements for the degree of Doctor of Philosophy in Material Chemistry. Therefore, we recommend the submission of the dissertation to the department for further review and open defense.

Prof. H C Ananda Murthy **Main Supervisor**	**Signature**	**Date**
Dr. Bedasa Abdisa **Co-supervisor**	**Signature**	**Date**
Prof. Taye Beyene Demissie **Co-supervisor**	**Signature**	**Date**

Approval Page of Ph.D. Dissertation

We hereby certify that the recommendations and suggestions made by the board of examiners are appropriately incorporated into the final version of the dissertation entitled **"Synthesis of S-doped Graphitic Carbon Nitride (g-C_3N_4)/CuO/ZrO_2 Based Semiconducting Nanostructures for Sensor and Catalytic Degradation of Pollutant Dyes"** by Nigussie Alebachew Ayalew.

Prof. H C Ananda Murthy **Main Supervisor**	**Signature**	**Date**
Dr. Bedasa Abdisa **Co-supervisor**	**Signature**	**Date**
Prof. Taye Beyene Demissie **Co-supervisor**	**Signature**	**Date**

We, the undersigned, members of the Board of Examiners of the dissertation open defense by Nigussie Alebachew Ayalew have read and evaluated the dissertation entitled **"Synthesis of S-doped Graphitic Carbon Nitride (g-C_3N_4)/CuO/ZrO_2 Based Semiconducting Nanostructures for Sensor and Catalytic Degradation of Pollutant Dyes"** and examined the candidate during open defense. This is, therefore, to certify that the dissertation is accepted for partial fulfilment of the requirements of the degree of Doctor of Philosophy in Material Chemistry.

Chairperson	**Signature**	**Date**
Internal Examiner 1	**Signature**	**Date**
Internal Examiner 2	**Signature**	**Date**
Prof. Delele Worku **External Examiner 1**	**Signature**	**Date**
Dr. Girum Ayalneh **External Examiner 2**	**Signature**	**Date**

Finally, approval and acceptance of the dissertation is contingent upon submission of its final copy to the Office of Postgraduate Studies (OPGS) through the candidate's Department Graduate Council (DGC) and School Graduate Committee (SGC).

Department Head	**Signature**	**Date**
School Dean	**Signature**	**Date**
Office of Postgraduate Studies, Dean	**Signature**	**Date**

ACKNOWLEDGEMENT

First and foremost, I want to thank the All-Powerful GOD for giving me the stamina and endurance to complete every task of this work. My deepest gratitude goes to my supervisors, Prof. H C Ananda Murthy**,** Dr. Bedasa Abdisa and Prof. Taye Beyene Demissie for their all-rounded and unhindered guidance as well as mentorship from the beginning to the end of the work. I would like to acknowledge the Ethiopian Ministry of Education (MoE), for providing research funds and Wolkite University for sponsoring my Ph.D. study. I would like to thank the Adama Science and Technology University (ASTU) Department of Applied Chemistry for lab facilities during the sensor study and the Department of Material Science and Engineering for the TGA/DSC, XRD measurement and photoreactor access. My thanks go to the Wolkite University, Department of Construction and Management Technology for the furnace instrument access and Food Science and Engineering for providing unreserved lab space during synthesizing my samples. Additionally, I want to express my gratitude to Dr. Taye Beyene for unreserved support in computational study and also facilitating collaboration with Dr. Ernst H. G. Langner, Prof. Karel G. von Eschwege, Department of Chemistry and Prof. E. Coetsee, Department of Physics, University of the Free State, South Africa, as well as their laboratory staff for characterizing my samples using HRSEM/EDS, BET, UV-vis/DRS, and XPS. I appreciate your support. Thank you for your help.

I'm appreciative to Dr. Lemma Teshome Tufa for helping me during my sensor study by supplying a potentiostat instrument. In addition to this, my appreciation goes to Dr. Bedasa Abdisa and Dr. Fedlu Kedir for providing FTO support and other lab-related amenities. I am so thankful to Dr. H C Ananda Murthy for providing the TEM characterization in India. Besides, I appreciate all academic and research assistance of the Department of Applied Chemistry, School of Natural Science, Adama Science and Technology University for their continued and friendly assistance throughout my work.

Last but not least, I'd like to sincerely thank my family for their financial and moral support. I am grateful to my wife, Tiliksew Bezabih, for her unwavering love, tenacity, and support. I want to express my gratitude to my daughters Sosina, Mahilet, and Eden (Mama) for their unwavering support and tolerance during my studies. My father Alebachew Ayalew, my mother Serkalem Birihau, and my brother (Tadele) and sisters (Birhane and Memar) have supported me in all of my endeavors.

Contents Pages

LIST OF TABLES

LIST OF FIGURES

LIST OF ACRONYMS AND ABBREVIATIONS

Abbreviation	Full name
AO II	Acid Orange II
AO7	Acid Orange 7
AP	Ammonium Perchlorate
CV	Cyclic Voltammetry
DFT	Density Functional Theory
DPV	Differential Pulse Voltammetry
DTA	Differential Thermal Analysis
2,4-DCP	2,4-dichlorophenol
EIS	Electrochemical Impedance Spectroscopy
EAS	Electrode Active Surface
FTOE	Fluorine Tin-Oxide Electrode
FESEM	Field Emission Scanning Electron Microscopy
HRSEM	High-Resolution Scanning Electron Microscopy
HRTEM	High-Resolution Transmission Electron Microscopy
MB	Methylene Blue
MO	Metal Oxide
M-S	Moot-Schottky
MO	Methyl Orange
NPs	Nanoparticles
NCs	Nanocomposites
PEC	Photo electrocatalysis
PL	Photoluminescence
RhB	Rhodamine B
SAED	Selected Area Electron Diffraction
SED	Secondary Electrons Diffraction
TC	Tetra Cyclin
TGA	Thermogravimetric Analysis
UV-Vis /DRS	Ultraviolet-Visible Diffuse Reflectance Spectrum

ABSTRACT

Due to the presence of basic surface sites, g-C_3N_4 is utilized for many applications, including catalysis, biosensors, and hydrogen production. However, because of some limitations such as less ability to utilize the visible spectrum of light and low conductivity, g-C_3N_4 suffers from a low efficiency in many applications. The objective of this study was to synthesize S-doped g-C_3N_4/ CuO/ZrO_2-based semiconducting NCs for sensor and catalytic degradation of pollutant dyes using the chemical precipitation method, as well as to elucidate the position of S in S-doped g-C_3N_4 applying computational studies. A facile gas-templating method was developed to realize the synchronous S-doped g-C_3N_4 in one step at 550 ^oC. The XRD results indicate the average crystallite sizes of S-doped g-C_3N_4, binary CuO@S-doped g-C_3N_4(30%), ZrO_2@S-doped g-C_3N_4 (20%) and ternary CuO/ZrO_2@S-doped g-C_3N_4 (30%) to be 13.23,6.50, 6.99 and 3.36 nm respectively. The band gap energy of synthesized samples was determined by UV-vis/DRS studies respectively. The specific surface area of the samples was determined via BET analysis. The position of S in S-doped g-C_3N_4 was visualized with DFT using optimized structures. The presence of N, C, and S elements, monoclinic shape CuO and ZrO_2 in the NCs was confirmed by HRSEM/EDS and XPS study analysis. The morphology and presence of flower-shaped S-doped g-C_3N_4 in the binary and ternary NCs were investigated through HRSEM/EDS/TEM. The electrochemical property for mono, binary and ternary samples was verified by using CV, EIS, and M-S analysis. The ternary NC showed outstanding performance (99.56%) in the reduction study of 4-NP to 4-AP within 300s at the optimized load of 0.01g with pseudo-first-order kinetics. The electrochemical reaction taking place at the modified electrodes was a diffusion-controlled process The sensitivity of the binder-free electrodes for CuO@S-doped g-C_3N_4 (30%)/FTOE, ZrO_2@S-doped g-C_3N_4 (20%)/FTOE, and CuO/ZrO_2@S-doped g-C_3N_4 (30%)/FTOE for 4-NP was determined to be 0.017, 0.007 and 0.004 $\mu A \mu M^{-1} cm^{-2}$ respectively. In the study of BPA sensing, surprisingly the ZrO_2@S-doped g-C_3N_4 (20%)/CPE present the highest LOD (3.21nM) than the CuO@S-doped g-C_3N_4 (30%)/CPE and CuO/ZrO_2@S-doped g-C_3N_4 (30%)/CPE. The higher photocatalytic (99.454%) degradation of MB was recorded by CuO/ZrO_2@ S-doped g-C_3N_4(30%). Generally, this study supports the notion that the synthesized binary and ternary NCs have good promise for multifunctional uses as catalysts, sensors, and photocatalysts.

Keywords: S-doped g-C_3N_4, Nanocomposite, Reduction, Sensor, Photocatalysis, Semiconductor, Doping

CHAPTER 1. INTRODUCTION

1.1 Background of the study

In recent decades, due to rapid industrialization growth, a major cause of water pollution has been organic compounds from different industrial sources. These persistent organic pollutants, introduced into natural water resources or wastewaters, are highly toxic and hazardous to living organisms. Food and beverage industries are among the most polluting industries in terms of the volume and the complexity of treatment of their effluent discharge.

The presence of pharmaceutical waste in water bodies is significantly influenced by hospitals and the pharmaceutical industries. Additionally, it has been claimed that household waste contains pharmaceuticals as a result of improperly discarding outdated or expired medications and excreting unmetabolized drugs. Due to its expanding use in the production of pharmaceuticals, fungicides, paracetamol, herbicide/insecticide industries, and dyes, 4-NP (p-nitrophenol or 4-hydroxy nitrobenzene) has gained environmental significance (G. Chang et al., 2012). Because of this, these industries are producing 4-NP-contaminated effluent, which leads to water pollution, and creates several negative effects such as the cognitive, nervous, and ocular systems in all living things, including the central nervous system, liver, kidneys, and blood of animals and humans (Bogireddy et al., 2020; Carneiro et al., 2010). Due to its toxicity, high stability, solubility in water, and extent and severity of environmental pollution, 4-NP has been listed as a “priority pollutant” by the U.S. Environmental Protection Agency (EPA) (C. Wang et al., 2017). Because of this health problem, the maximum allowable level in drinking water is 60 μg/L (~0.43 μM) (Carneiro et al., 2010; Yin et al., 2010; H. Yuan et al., 2016). This is why one of the research topics that has received a lot of attention recently is monitoring of 4-NP from contaminated wastewater by developing various mechanisms. Many strategies, including solvent extraction, photocatalytic degradation, chemical oxidation, adsorption, chemical precipitation and biodegradation, have recently been developed to remove 4-NP (Sahiner et al., 2010; Sonavane et al., 2007). In this regard, according to (Idris et al., 2020), despite the g-C_3N_4's outstanding performance for quantifying medicines in water, there aren't many studies available on its use for sensing pharmaceuticals in water.

Bisphenol A (BPA) is a chemical produced in large quantities for use primarily in the production of polycarbonate plastics, epoxy resins and paper products (thermal papers). It is also found in

various products including shatterproof windows, eyewear, and water bottles, bottle tops, and water supply pipes (Xing et al., 2022). Literature shows that phenols and parabens are a group of chemicals commonly found in personal care products and household items. Exposure to these chemicals has been associated with gestational length, and several growth parameters at birth, including birth weight and birth length. Previously reported associations with bisphenols show that BPA is associated with changes in birth size, depending on the timing of exposure (Aker et al., 2020). BPA can leach into food from the protective internal epoxy resin coatings of canned foods and consumer products such as polycarbonate tableware, food storage containers, water bottles, and baby bottles. Moreover, disturbances in thyroid hormones during development have been implicated in some neurodevelopmental and cognitive disorders (Zheng & Andou, 2022). Considering the large number of chemicals in the environment that can affect the thyroid system, it is important to consider that a proportion of these public health trends are related to chemical exposures acting on the thyroid system. Although this area of research is relatively not new and not limited, evidence supports the notion of an increased risk of adverse effects with exposure to high concentrations of environmental chemicals BPA and modifying the methods of monitoring the detecting levels of BPA is still at its early stage.

Methylene blue (MB), is a very poisonous and carcinogenic derivative of the phenothiazine used to dye textiles (Imran Din et al., 2023). Although decolorizing textile effluents has been accomplished using coagulation, flocculation, adsorption, and membrane filtration, these processes have drawbacks, including sludge production, adsorbent regeneration, and membrane fouling. For the treatment of wastewater including pesticides, phenols, chlorophenols, dyes, and other substances, advanced oxidation processes (AOPs), which include UV light, Fenton reagents, ozone, etc., have been investigated alone as well as in combination, in the presence and absence of catalysts (Babu et al., 2019). Thus, the treatment of MB wastewater containing such dyes is a vital environmental problem.

Even though the aforementioned techniques can identify and degrade a variety of contaminants, however, the majority of them require time-consuming sample preparation and pre-treatment, expensive equipment, energy, and trained operators (Zheng & Andou, 2022). Recently researchers have developed several instrumental techniques and strategies to maintain a secure environment. However, efficiency and costs are still big challenges. In this context, semiconductors are recommended as prospective candidates for the detection, reduction, and photodegradation of

harmful organic pollutants due to their low cost, lack of toxicity, ease of sample preparation, energy efficiency, and environmental safety (Chegeni et al., 2019; Vasiljevic et al., 2020; Zheng & Andou, 2022).

Graphitic carbon nitride (g-C_3N_4) is considered an intrinsically nitrogen-rich system with a lamellar structure. The polymeric structure of g-C_3N_4 arises from the repetition of tri-s-triazine (symmetry. 1,3,5 triazine) units and the 2D lamellar structure arises from the weak van der Waals interaction between the layers. The lone pair of electrons on nitrogen could provide surface polarity on the electrode material and that could offer several binding sites for the electrolyte ions to interact with the electrode surface. The g-C_3N_4 has exceptional properties such as high mechanical strength, good chemical stability, high level of oxygen-ion conductivity, and corrosion resistance. Due to these exceptional properties, g-C_3N_4 has been a promising candidate for a wide range of applications such as electrochemical biosensors (Kessler et al., 2017; Kimmel et al., 2012) gas sensors (H. Xu et al., 2019), hydrogen evolution (Yu et al., 2017) carbon dioxide storage (Y. Wang et al., 2021), solar cells (X. Yang et al., 2021), and photocatalysis (X. Wang et al., 2012) etc.

However, because of some limitations such less the ability to utilize the visible spectrum of light, low conductivity, and small surface area, g-C_3N_4 suffers from low efficiency in many applications (Kavil et al., 2019). The ideal g-C_3N_4 consists uniquely of an assembly of C−N bonds without electron localization in the π state (this material is a π-conjugated polymer). However, the potential value of this material was not fully recognized until recent decades, most likely because of its chemical inertness, insolubility in acidic, neutral or basic solvents, and its unrevealed structure (Ke et al., 2014; X. Wang et al., 2012).

To improve these limitations scholars have been devoted to altering surfaces by a variety of methods, such as calcination at various temperatures (Dong et al., 2013), doping with nonmetals (Q. Guo et al., 2016; Stolbov & Zuluaga, 2013a) and the effects of metal and metal oxides (Chafi et al., 2018) on different precursors (Tian et al., 2019). However, detailed investigations on the local structure, optical characteristics and composition of fabricated g-C_3N_4-based NC materials are not properly discussed in many related studies and thus uncertainty prevails in many aspects (Ke et al., 2014; Mohammad, Ehtisham, et al., 2020; Tan et al., 2015).

This is why creating low-cost, multifunctional NCs with high catalytic activity has gained popularity as a research area in recent years. Because of its simple, inexpensive, environmentally

friendly manufacturing methods, promising stability, and outstanding physicochemical properties for usage in a variety of the degradation of organic pollutants, g-C_3N_4 is an essential substance in chemistry, physics, and engineering (You et al., 2017; J. Zhu et al., 2014). There are several advantages to employing g-C_3N_4-based NCs for multiple applications over other semiconductors. For instance, ease of synthesis using a variety of techniques, low cost, favorable electrical structural morphologies, and good heat stability up to 600^{o}C. Size reduction, doping, or sensitizers can change the electrical and optical characteristics. Moreover, a technique that facilitates multi-electron transfer is non-toxic and recyclable without significantly affecting the desired activities (Babu et al., 2019; Ong et al., 2016; P. P. Singh & Srivastava, 2022).

By using diverse fabrication procedures, several strategies have been used to enhance the catalytic performance of g-C_3N_4-based materials. Doping with nonmetal elements, such as through nitrogen, (D. Zhu & Zhou, 2021), phosphorus (Matějka et al., 2022) and sulfur (You et al., 2017) exhibited great opportunity to boost the visible light absorption of g-C_3N_4, since the electronic structure and band gap changed dramatically shows much higher activity than the optical prism g-C_3N_4. We consider that two rules should be followed for anion dopant: one is that the electronegativity of the anion dopant must be lower than that of the substituted lattice atom; the other is that the dopant anion should have a radius comparable to that of the substituted lattice atom. In this work, to demonstrate the above considerations, Smaller electronegativity and larger radius (2.58 vs 3.04) than nitrogen (1.09 vs 0.75 Å) was chosen as a dopant into g-C_3N_4 (Lu et al., 2017). However, studies have shown that when two or more semiconductors are combined, the combined semiconductors' properties are improved over those of the individual semiconductors (Chegeni et al., 2019). For instance, the loading of some transition metal oxides such as Ag_3VO_4 (Zhao et al., 2019), ZrO_2 (Sudhaik et al., 2018), SnO_2 (Y. Zhang et al., 2020),and ZnO (S. Zhang et al., 2019) significantly boosted the potential degradation rate of g-C_3N_4. Additionally, numerous studies have been carried out where the addition of transition metal oxides loading CuO (L. Li et al., 2016), TiO_2 (Lachheb et al., 2002) and Fe_2O_5 (Jia et al., 2016) on the g-C_3N_4 was investigated and proven to be effective for the successful detection and degradation of harmful organic contaminants.

CuO, a transition metal oxide with P-type conduction, has drawn a lot of attention because of its adjustable electrical structure, narrow bandgap, affordable price, and eco-friendly composition. However, pristine CuO has some drawbacks like rapid recombination of photogenerated electron-hole pairs and a low rate of light absorption, which significantly lowers the material's

photocatalytic performance (Harish et al., 2017; J. Li et al., 2011). ZrO_2 has also been extensively employed due to its chemical and physical qualities, which include outstanding mechanical strength, high ionic conductivity, low thermal conductivity at high temperatures, and good thermal stability. It also has great refractoriness and chemical resistance. ZrO_2 is also utilized in a wide range of applications, such as solid-state electrolytes, thermal barrier coatings, electro-optical materials, catalyst or catalyst support (Ke et al., 2014; Y. Li et al., 2001) and sensor technology (R. Zhang et al., 2010). ZrO_2 is a promising potential candidate for several applications due to its distinctive features, such as its high surface area and the presence of numerous oxygen vacancies. However, due to its wide band gap energy (>3.5 eV), ZrO_2 is limited in using in photocatalysis, particularly for applications in the UV-Vis range (Najibi-Ilkhechi et al., 2015). As a result, to advance the aforementioned environmental issues as well as the used materials and processes, novel multifunctional semiconducting g-C_3N_4-based binary and ternary NCs must be developed.

Two types of synthetic methods have been mainly employed for the synthesis of g-C_3N_4-based composites. The first one is mixing the substance with a carbon nitride precursor followed by the thermal condensation at the desired temperature; the second one is the post-treatment of the substance with as-formed g-C_3N_4 by deposition or simply mixing (Sudhaik et al., 2018). The g-C_3N_4 is abundant and can easily be prepared via a one-step polymerization of cheap feedstocks such as melamine (G. Liu et al., 2017) cyanamide, (X. Wang et al., 2009), dicyanamide (X. Bai et al., 2014) urea, (Ong et al., 2015; Paquin et al., 2013) and thiourea (G. Zhang et al., 2012). Some researchers preferably synthesized MOs incorporated g-C_3N_4 NCs via the hydrothermal method (J. Cao et al., 2017) and microwave irradiation (Hosseini et al., 2020). However, due to the limitations related to yield and energy consumption, other researchers prefer the familiar and simple pyrolysis method. Notably, because of its feasibility in the economy, ease of use and high yield, nowadays direct pyrolysis of precursor followed by ultrasonication and chemical precipitation technique is the best synthesizing technique of g-C_3N_4-based NCs (L. Bai et al., 2022). Therefore, the synthesis procedure that reduces the stated disadvantages, and that avoids complex preparation procedures should be developed.

Even though there are significant ongoing efforts to improve the functionality of g-C_3N_4, there is a need for accurate and trustworthy data on the entire structural characterization, pore sizes, morphology, crystallinity, photoluminescence, formation energy, charge analysis, band gap energy, etc. There are various ways to synthesize non-metal doped g-C_3N_4 NCs. For instance, S-doped g-

C_3N_4 was created by calcining a precursor made of thiourea, a molecule that contains carbon, nitrogen, and sulfur. Despite the impressive results of such materials, there is disagreement regarding the precise structure of the resulting S-enrichment of g-C_3N_4. Furthermore, there are very few opportunities for such synthesis to be directed in a way that favors a specific type of S-enrichment (it is still unclear precisely which type of S-enrichment is advantageous for a given application). The second approach involves the combined pyrolysis or co-polymerization of a mixture of precursors that are known to contain C and N (urea, cyanuric acid, melamine, or dicyandiamide) and sulphur-containing precursors (trithiocyanuric acid) which is believed to be a sort of S-doped g-C_3N_4. On the other hand, this approach has the same drawbacks as the thiourea pyrolysis. With this information, investigating a novel strategy to gain S-doped g-C_3N_4-based binary and ternary NCs is one of the findings of the current study.

It is evident from the discussion above that MOs, such as ZnO, CuO, and ZrO_2, as well as non-metal elements, such as S, P, and N, are potential candidates to address the drawbacks of g-C_3N_4 semiconductors and have attracted a lot of interest. With this regard, CuO and ZrO_2 NPs have adhered to the surface of the S-doped g-C_3N_4 NCs that served as support in the current study. The reduction of 4-NP, sensing of 4-NP, and BPA were among the applications used to evaluate the electrocatalytic performance. Additionally, the photodegradation of MB was used to gauge the effectiveness of synthesized ternary photocatalysis. Using a variety of advanced experimental characterization techniques, the required foundation for the future synthesis, clarification, and prospective applications of such ternary semiconducting NCs was provided. With this regards, HRSEM/EDS/SED, BET, and TEM methods were used to corroborate the morphology and porous nature of the NCs. In addition to the binary NCs, the presence of S, CuO, and ZrO_2 in the ternary NCs as well as their predicted composition were assessed using HRSEM/EDX/SED, TEM, and XPS analyses. Analytical methods including CV, EIS, and M-S were used to assess the electroconductivity of the synthesized NCs. The DFT calculations were applied to shed more light on the exact substitution positions of S and correlate the experimental and calculated band gaps. The potential sensing procedure was evaluated using the CV, DPV, EIS, and M-S approaches. In addition, the performance of the NCs as electrocatalysts was assessed using the potential pollutant molecule 4-NP. The reduction reaction and adsorption-diffusion process were studied using the pseudo-first-order (PFO), kinetic model. There have been suggestions for potential electrocatalytic

sensing, reduction, and photocatalysis mechanisms of processes. Generally, the aforementioned operations were summed up in the upcoming objectives.

1.2 Statement of the problem

Various human activities related to agriculture and industry in modern societies are releasing a variety of wastes and toxic pollutants into the environment. For a variety of uses, the pharmaceutical, plastics, textile, cosmetics, food processing, and dye manufacturing industries use dyes like 4-NP, BPA, and MB, and they discharge their waste directly into the environment.

In Ethiopia, several industries are producing plastic containers for bottled mineral water production and sales to manufacture drugs, fungicides, insecticides, dyes and tannery processing. BPA is a priority environmental pollutant listed by the United States Environmental Protection Agency (USEPA) and in many other countries (Name et al., 2013). 4-NP is also listed by The Agency for Toxic Substances and Disease Registry (ATSDR) of the United States (Nishimura, 1992). Due to the inconsistency between industrial water consumption, requirements and water pollution, familiarizing novel wastewater treatment and detecting and recycling technologies is essential. Despite the progress, there is a need to bridge the knowledge gap in accessing g-C_3N_4-based NCs capability in pollutant dyes remediation approaches, especially in the electrocatalytic, electrochemical sensor and photocatalysis processes. Hence, compressive theoretical investigations and experimental mechanisms of non-metal doped g-C_3N_4 incorporating MOs for multifunctional applications should be designed and developed. This approach is crucial for designing future structural features, predicting, and comprehending the entire reaction mechanism at the molecular level for the planned applications.

To the best of the researcher's reading and knowledge, there is no information on ternary NCs that are heterostructured composites made of CuO, ZrO_2 and S-doped g-C_3N_4. Therefore, in this study, mono, binary, and ternary semiconductors using S-doped g-C_3N_4, CuO and ZrO_2 for the sensor and catalytic degradation of pollutant dyes applications are reported. The novelty of this study is to enhance conductivity activity and realize the active-site structures of S-doped g-C_3N_4-based nanostructures containing readily available and non-toxic CuO and ZrO_2 NPs for electrocatalyst and sensor active material by experimental and computational modelling studies.

1.3. Objectives

1.3.1. General objective

The general objective of this study is to synthesize S-doped g-C_3N_4 CuO/ZrO_2-based semiconducting nanostructures for sensor and catalytic degradation of pollutant dyes.

1.3.2 Specific objectives

The specific objectives are:

☛ To synthesize intrinsic g-C_3N_4, S-doped g-C_3N_4, CuO and ZrO_2 NPs, binary CuO@S-doped g-C_3N_4 (CuO=5,10,20 and 30%) and ZrO_2@S-doped g-C_3N_4 (ZrO_2=5,10,20, and 30%) NCs and ternary CuO/ZrO_2 @S-doped g-C_3N_4 (CuO/ZrO_2=5,10,20, and30%) NCs by chemical precipitation method.

☛ To characterize the as-synthesized materials by TGA/DTA, XRD, FTIR, UV-Visible /DRS, PL, HRSEM/EDS/SED, TEM, BET, XPS, CV and EIS, M-S techniques.

☛ To optimize some experimental parameters (catalyst dose, pH, concentration of analyte) for the evaluation of the performance of catalytic reduction of 4-NP, photocatalytic degradation of MB, and sensor study of 4-NP and BPA.

☛ To evaluate performance, catalytic reduction of 4-NP, photocatalytic degradation of MB sensing of 4-NP and BPA.

☛ To utilize DFT simulations in optimizing structural and electrical (electronic) properties of S-doped g-C_3N_4 and predicted the position of S in the s-triazine rings.

1.4 Significance of the study

Utilization of semiconductor-based NCs from carbon-rich resources effectively and efficiently is generally regarded as one of the many potential options. To improve the drawbacks of g-C_3N_4, one of the many strategies employed was doping g-C_3N_4 semiconductors with non-metal elements as the hottest study topics in contemporary material science. Copper (II) and zirconia are promising materials due to their excellent conductivity, low hazardous characteristics, chemical and thermal stability and environmentally friendly features.

This study established S as the sought-after chemical that served as the dopant. Because of the potential for mixed metal-sulphur-doped materials, all metallic salts were avoided. Ammonium

sulphate ($(NH_4)_2\ SO_4$) was selected in light of these requirements and it is an N and S-containing compound that isn't frequently thought of as a sulphur dopant for such materials. Thus, the findings of the preliminary studies on S-doped g-C_3N_4 produced in a single step utilizing $(NH4)_2\ SO_4$ as a pre-pyrolysis agent and sulphur source were presented. These days, some researchers employ organic solvents, more precisely those that fall within the worldwide harmonized system's category of "hazard and precautionary" and "severe human health risk phrases." Particularly these organic solvents, which have high vapor pressures and low boiling temperatures, can also result in potentially fatal explosions. With this regard, this work simply uses water as a solvent.

It is also important to mention that the benefits of this study in preparing intrinsic S-doped g-C_3N_4, binary CuO@S-doped g-C_3N_4, ZrO_2@S-doped g-C_3N_4 and CuO/ZrO_2@S-doped g-C_3N_4 materials with ease of construction, enhanced surface area, improved conductivity, chemical stability, non-toxicity, catalytic and electrochemical activities. Generally, through the current work, the groundwork for upcoming experimentally-based syntheses, clarifications, and prospective uses of such semiconducting NCs is established.

CHAPTER 2. LITERATURE REVIEW

2.1 Historical background of graphite carbon nitride (g-C_3N_4)

In 1989, Cohen and Liu published an article based on the crystal structure calculation of β -Si_3N_4 in Science, predicting a carbon-nitrogen compound β-C_3N_4 with an elastic modulus comparable to that of the diamond. They calculated that the elastic modulus of the compound is similar to that of a natural diamond, and it is assumed that its hardness may be close to that of the diamond (A.~Y.~Liu & M.~L.~Cohen, 1989). In 1996, Teter and Hemley recalculated C_3N_4 using the minimum energy pseudopotential method and proposed five various phases of several allotropic forms of carbon nitride, possible structures of C_3N_4. They are α phase, β phase, cubic phase, quasi-cubic phase and graphite-like phase (Teter & Hemley, 1996). Numerous researchers have contributed to the creation of the current state of carbon nitride, as demonstrated in Figure 1's history of the material's historical background (Siddiquee et al., 2020).

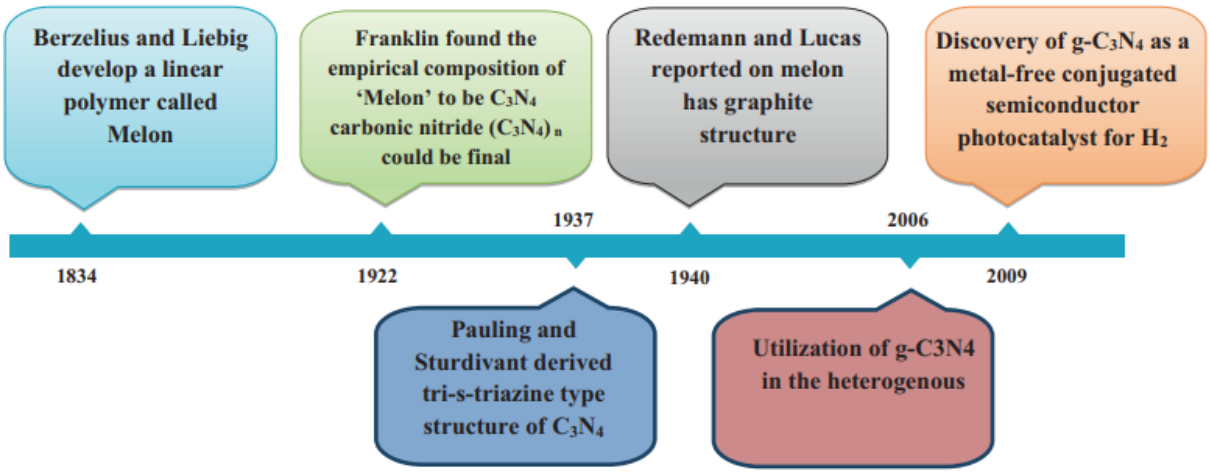

Figure 1.The historical background of g-C_3N_4

With a moderate energy bandgap of 2.7 eV, the covalent connection between the carbon and nitrogen atoms in C_3N_4 has been robust and largely persistent. As a result, after the carbon-nitrogen compound in the β-C_3N_4 covalent crystal was proposed. More elucidation on the type of bond that exists in g-C_3N_4 shows the presence of the bond by sp^2 hybridization between the carbon and hydrogen atoms in g-C_3N_4. The C-N bond connects each of these triazine rings, which together form the structure known as a triazine ring. The tri-s-triazine ring (C_6N_7) and the g-C_3N_4 with a

triazine ring (C_3N_3) are the two chemical structures of graphitic carbon that are generally accepted to exist (Figure 2).

One of the two allotropes of g-C_3N_4 is formed by joining triazines together, whilst the other is created by joining together tri-s-triazines units. However, due to the different sizes of the nitrogen in the structure, the two g-C_3N_4 allotropes lead to different electron environments for the nitrogen atoms, as a result of the different stability of the two g-C_3N_4 species. Importantly, a thorough investigation through DFT calculations revealed that the tri-s-triazine-based g-C_3N_4 is more stable. As a result, catalysis research has recently focused on the tri-s-triazine structural unit g-C_3N_4 (Kroke et al., 2002). g-C_3N_4, is also a polymeric material consisting of C, N, and some impurity H, connected via tri-s-triazine-based patterns (Figure-2b). Compared with the majority of carbon materials, it has electron-rich properties, basic surface functionalities and H-bonding motifs due to the presence of N and H atoms. It is thus regarded as a potential candidate to complement carbon in material applications (Alaghmandfard & Ghandi, 2022).

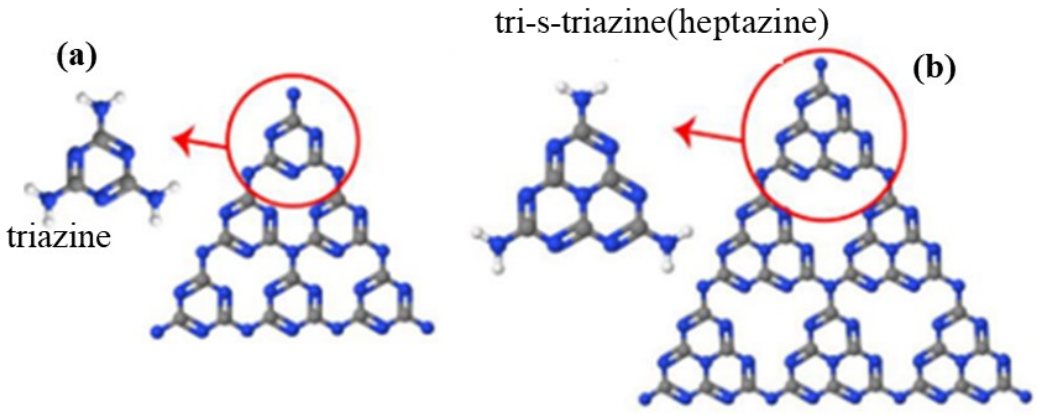

Figure 2.The proposed chemical structure for g-C_3N_4 of (a) s-triazine and (b) tri-s-triazine

2.2 Properties of graphitic carbon nitride

The ideal g-C_3N_4 (a π-conjugated polymer) consists uniquely of an assembly of C–N bonds without electron localization in the π state. The carbon and hydrogen atoms in g-C_3N_4 are bonded together by sp^2 hybridization. Both the carbon and nitrogen atoms in the g-C_3N_4 are sp^2 hybridized and are joined by σ bonds to form a hexagonal structure. The small units, the C–N bond connect each of these rings to form the structure, a triazine ring (Idris et al., 2020). As can be seen in Figure 3, real materials, such as those made by polycondensing cyanamide, contain a small amount of

hydrogen in the form of primary and/or secondary amine groups on the terminal ends. Hence, the presence of hydrogen shows that the real g-C_3N_4 is partly condensed and that several surface defects exist, which can be useful in for example to promote electron relocalization on the surface, which indicates the Lewis-base character toward metal-free coordination chemistry and catalysis (Figure 3). Moreover, due to the presence of hydrogen and the fact that nitrogen has one more electron than carbon, g-C_3N_4 has rich surface properties that are important features, such as basic surface functionalities, electron-rich properties, H-bonding motifs, etc. Among the advantages of g-C_3N_4 properties, the most important one is stability. Hence, in a variety of conventional solvents, such as water, alcohols, dimethylformamide, tetrahydrofuran, diethyl ether, and toluene, g-C_3N_4 exhibits good chemical stability, making it an excellent material for both liquid-phase reactions and gas-phase reactions carried out at high temperatures. TGA studies reveal that g-C_3N_4 can withstand temperatures of up to 600 ^oC and that its profiles are comparable in atmospheres of inert gas or oxygen, indicating that it has a high degree of thermal stability and is inert to oxygen (J. Zhu et al., 2014). Its capacity to operate in liquid or gaseous settings and at high temperatures, together with its excellent thermal stability (up to 600 ^oC in air) enhance its variety of uses in heterogeneous catalysis (J. Liu et al., 2011; Mo et al., 2015). This shows that g-C_3N_4 can withstand high temperatures, even in an oxidizing environment, and that the weight loss at temperatures above 600 ^oC is caused by g-C_3N_4's thermal breakdown rather than the material's oxidation by oxygen (to create oxides like CO or CO_2). In contrast to conventional inorganic materials that are reactive to molecular oxygen, it is anticipated that g-C_3N_4 can demonstrate interesting outcomes in catalysis (J. Zhu et al., 2010).

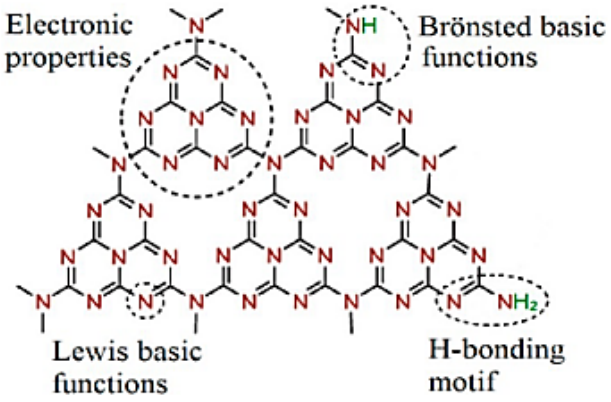

Figure 3. Multiple surface functionalities found on g-C_3N_4 (Thomas et al., 2008)

In addition to its role as a metal-free catalyst, g-C_3N_4 also has an essential role in catalysis. For example, g-C_3N_4 can be used as a functional material to graft metal NPs in catalyst preparation, and as a reference material to manufacture catalysts to distinguish the oxygen activation sites. Based on the improved thoughtful of the intrinsic characteristics which can restrict its application, such as small specific surface area and rapid recombination of the photogenerated electron–hole pair, several types of research have been attempted which will certainly widen its applications and lead to magnificent results (J. Zhu et al., 2014).

According to the reported investigations, the UV-Vis absorption qualitatively confirm that the calcination temperatures affect the unique electrical characteristics and catalytic activity of g-C_3N_4. The g-C_3N_4 exhibits the typical characteristic absorption pattern of a semiconductor with a noticeable band gap at about 420 nm which gives the material slightly yellow. However, the calcination temperature also affects the g-C_3N_4 bandgap. Hence, when calcined at 550ºC, the bandgap is narrower than when calcined at 450 and 650 ºC. Surprisingly, for g-C_3N_4 synthesized at the calcination temperature of 450, 550 and 650 ºC respectively, the BET-specific surface areas were found to be 37.8, 73.7 and 65.6 $m^2 \cdot g^{-1}$ respectively. In general, this shows that at higher temperatures, the degree of g-C_3N_4 polymerization, the larger the π-plane conjugation degree of heptazine rings via N_2 atoms (Alaghmandfard & Ghandi, 2022).

Further evidence for the complete synthesis of g-C_3N_4 can be obtained by the two typical diffraction peaks seen in the XRD spectra of g-C_3N_4. The diffraction peak at 27.54° typically represents the interlayer stacking of conjugated aromatic structures indexed for graphitic materials as the (002) peak, and the diffraction peak at 13.38° is attributed to in-plane (100) ordering of tri-s-triazine units indicating the successful synthesis of g-C_3N_4. The FTIR measurement is helpful to examine the chemical bonding of the sample. The out-of-plane bending vibration typical of heptazine rings and the characteristic mode of the triazine units of g-C_3N_4 are responsible for the sharp peak at 810 cm^{-1} originates from the characteristic breathing mode of s-triazine (T. Wang et al., 2020). The weak peak at 2137 cm^{-1} is assigned to the C=N double bonds. Due to incomplete condensation, there are more or less undeleted amino groups in g-C_3N_4 prepared by thermal condensation polymerization. The absorption peaks between 1650 and 890 cm^{-1} correspond to the usual stretching vibration modes of repeated units and connected units of C−N(−C)−C (full condensation) or C−NH−C (partial condensation) (Kavil et al., 2019; J. Zhu et al., 2014). The

broad band in the range of 3500–3000 cm^{-1} is attributed to the stretching mode of the O−H bond and the vibration mode of the N−H bond (J. Zhu et al., 2010).

Elemental analysis results reveal the molar ratios of C to N of the g-C_3N_4 is around 0.60 (theoretical value of g-C_3N_4 = 0.75), implying incomplete crystallization. A recent study shows that the PL emission spectra of g-C_3N_4 samples that used urea as a precursor were recorded at a lower PL intensity. This suggests a lower recombination rate of the electron–hole pairs under light irradiation (K. Li et al., 2023). A similar study reveals that the optical bandgaps were moved towards higher energies (from 472 nm to 420 nm emission maxima) due to the result of better layer packing and electrical coupling. This shows that the PL sensitively depends on the degree of condensation and the packing between the layers. While the uncondensed melem still shows a PL peak maximum at around λ_{max} = 366 nm, this peak shifts for melon-like materials (condensed for 4 h at 550 °C) to around λ_{max}=472 nm, in agreement with lowering the optical band gap by condensation of single molecules to an extended solid material (Thomas et al., 2008).

The survey (Figure 4a) and high-resolution XPS spectra measurement have been used to investigate the binding energy of carbon (Figure 4 b) and nitrogen elements (Figure 4 c) in g-C_3N_4. Thus, the sp^2 -bonded carbon in C–C (284.6 eV) and N–C=N (288.1 eV), the sp^2-bonded N in C–N=C (398.7 eV), the nitrogen in tertiary N–$(C)_3$ groups (400.3 eV), and the presence of amino groups (C–N–H, 401.4 eV) caused by imperfect polymerization (K. Li et al., 2023).

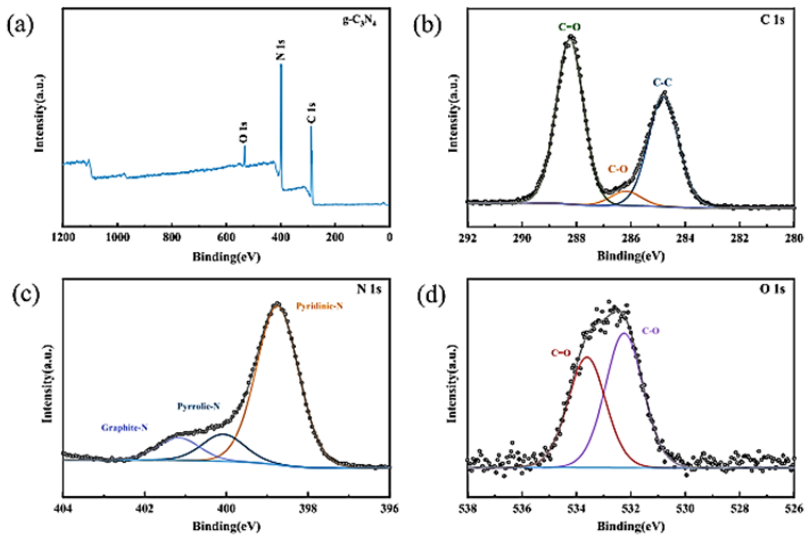

Figure 4. XPS spectra of g-C_3N_4: (a) full spectrum, (b) C1s, (c) N1s and (d) O1s (G. Zhang et al., 2012).

2.3 Synthetic techniques of graphitic carbon nitride

Graphitic carbon nitride (g-C_3N_4) can be prepared by one-step thermal polymerization of oxygen-free and nitrogen-rich compound precursors having bonded core structures (triazine and heptazine derivatives) such as melamine (G. Liu et al., 2017) cyanamide,(X. Wang et al., 2009) dicyanamide, (X. Bai et al., 2014; G. Liu et al., 2010), melamine, (G. Liu et al., 2017) urea, (Dong et al., 2011; Fang et al., 2016; Ong et al., 2015; Paquin et al., 2015; Y.-P. Yuan et al., 2013; X.-X. Zou et al., 2011) and thiourea (G. Zhang et al., 2012). To create the polymeric g-C_3N_4 network, these C and N precursors have straightforward and effective condensation routes. Solvothermal, plasma sputtering and chemical vapor deposition (CVD) are methods for making g-C_3N_4. To synthesize high-quality composites, CVD does not require high vacuum and can deposit a wide variety of materials and does not require a high vacuum. On the other hand, physical vapor deposition (PVD) involves a high vacuum atmosphere. The disadvantage of CVD is that some CVD precursors are costly, highly toxic, explosive, or corrosive, such as Ni $(CO)_4$, B_2H_6, and $SiCl_4$, respectively. The by-product of this method, such as CO, or HF, can also be hazardous. Additionally, since the substrates must withstand high temperatures, the substrates are limited (Alaghmandfard & Ghandi, 2022).

Several studies reported that g-C_3N_4 can be synthesized utilizing a template technique or an adequate precursor (such as urea), which can result in the synthesis of g-C_3N_4 with better photocatalytic H_2 generation (Y.-P. Yuan et al., 2013). A straightforward thermal condensation process and inexpensive precursor (melamine) were used to create the g-C_3N_4 that was prepared at various temperatures (450 ^oC, 500 ^oC, 550 ^oC, 600 ^oC, and 650 ^0C), Figure 5. As the calcination temperature rises, the photocatalytic activity of the g-C_3N_4 improves, and the maximum photocatalytic activity was seen in g-C_3N_4 synthesized at 650 ^0C (Mo et al., 2015). According to (H.-Y. Y. Xu et al., 2015), pyrolytic synthesis of g-C_3N_4 conducted by heating dicyandiamide and melamine has shown slight differences in crystal and morphology. Generally speaking, the crystallite size of the g-C_3N_4 sample made from dicyandiamide was lower than that made from melamine at the same pyrolysis temperature. Literature shows that the precursor type and synthesis process can strongly affect physical and chemical properties and the C/N ratio in g-C_3N_4. As an example, Figure 5 illustrates how nitrogen-rich precursors can be polycondensed or pyrolyzed to produce g-C_3N_4. In this regard, the bandgap of the g-C_3N_4 synthesized from such precursors ranges from 2.58 to 2.89 eV. The majority of these precursors are unstable, challenging to obtain, and/or

extremely explosive. Due to their low thermodynamic stability, single-phase sp^3-hybridized carbon nitrides are difficult to synthesize (Thomas et al., 2008). It appears that the imperfect materials are significantly more useful than the ideal ones, especially for catalysis, which necessitates surface defects. Therefore, when the substance is going to be used in catalysis, the synthesis of g-C_3N_4 with defects is an interesting topic.

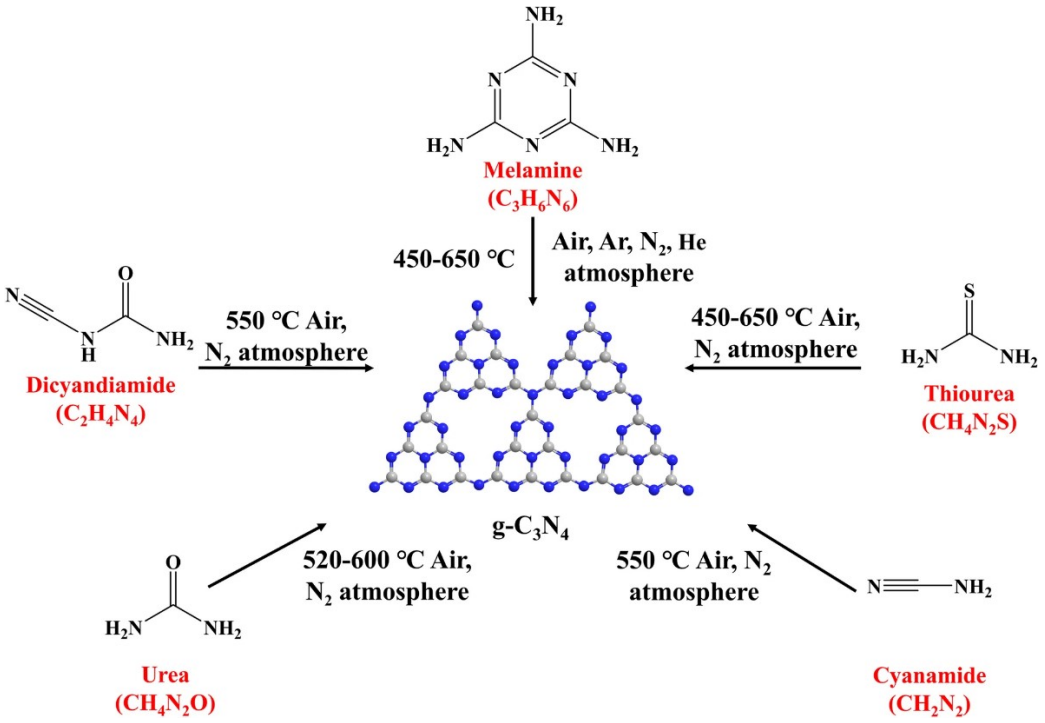

Figure 5. Preparation of g-C_3N_4 using different precursors (Luo et al., 2023)

2. 4 Cupric oxide

Transition metal oxides (TMOs) are widely investigated materials, which have been widely used due to many advantages as co-catalysts or co-photocatalysts in g-C_3N_4 heterojunction systems. By adjusting the ratio of precursors and synthesis conditions, different crystal structures with distinct energy band structures can be obtained, which provide great flexibility in the design of Type I/II, Z-scheme, p-n and Schottky junctions. TMOs show different d-orbital electronic activities and their electronic structures can be adjusted to enhance the conductivity of the TMOs as co-catalysts and to improve the carrier transfer efficiency of heterojunctions (L. Bai et al., 2022). Most MO semiconductors such as ZrO_2 (band gap of 3.75 eV) are unable to absorb visible light because of their wide band gap. While small band gaps containing semiconductors like CuO exhibit a fast recombination phenomenon, photo-generated holes and electrons are unable to act efficiently for

photocatalytic conversion. A co-catalyst can be used to trap photo-generated electrons or holes, delay the recombination time by monitoring the defect density in the semiconductor lattice, or dope heteroatoms and functionalize photocatalysts (Henderson, 2011; Kamat, 2012; Szczepankiewicz et al., 2000).

The study of CuO NPs conducted earlier made a significant contribution to its future outlook of semiconductor photocatalysis. The prospect of potential applications of CuO nanostructures has led to substantial research and development efforts to have various types of nanostructures. Studies on CuO show that it is a p-type semiconductor with a band gap of 1.2 eV, large surface area, and a very intriguing reactive morphology. It has also high catalytic reusability, minimum cost, superior chemical and thermal stability, low toxicity, and ease of handling. compared to organic and microbial agents, CuO NPs are stable, robust and have a longer shelf life. CuO NPs can be produced by using various synthesizing techniques typically the wet chemical synthesis technique, which involves the nucleation and development of liquid substances, is the main type of bottom-up synthesizing technique. This method has the advantage of consistent particle size and shape with fewer chances of surface defects and impurities (Behari, 2010; L. Li et al., 2016).

2.5 Zirconia

Zirconium oxide known as zirconia (ZrO_2) is a polymorphic metal oxide with a white crystal. It has different types of polymorphs including cubic, tetragonal and monoclinic (Figure 6). It is a potential catalyst and catalyst support, with superior mechanical strength, high ionic conductivity, and low thermal conductivity at high temperatures. ZrO_2 is used for a variety of applications including electro-optical materials catalyst or catalyst support (Y. Li et al., 2001; B.-Q. Xu et al., 2003; R. Zhang et al., 2010). Literature shows that ZrO_2 exists in three distinct crystal phases: monoclinic, tetragonal, and cubic (Figure 6). ZrO_2 can be prepared using a variety of methods, including precipitation, hydro-thermal, microwave heating, etc. It is well known that ZrO_2, wide band gap (>3.5 eV) TMO nanostructures can be used to make materials that are electro-optic, dielectric, and nanocomposites. Mesoporous materials have opened up several new possibilities because of the enormous surface area of ZrO_2, tunable pore size, and simple functionalization (Dourandish et al., 2011; Sathyaseelan et al., 2017).

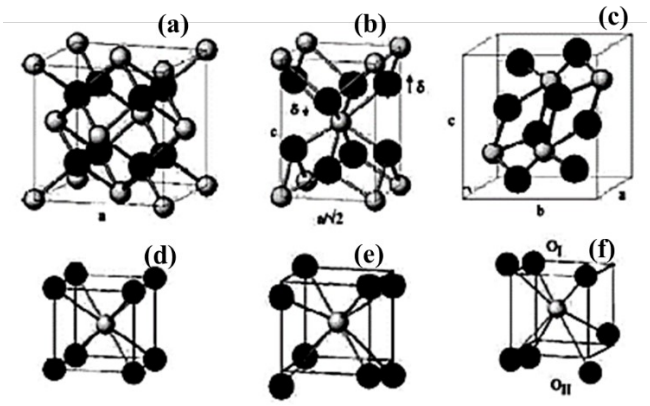

Figure 6. Atomic structure (a-c) and Zr to O coordination units (d-f) for the three low-pressure polymorphs of ZrO_2: cubic (a and d), tetragonal (b and e), and monoclinic (c and f). Large dark circles denote O atoms, and small light circles, Zr (Dourandish et al., 2008).

The most stable phase at ambient temperature and normal air pressure is monoclinic zirconia (m-ZrO_2). On the other hand, the pH at which the precursor gels precipitate is what determines whether the material would form the monoclinic or tetragonal phase after being calcined at 400–600 °C. As a result, the monoclinic phase could be produced in the medium pH (8-11) range whereas the tetragonal phase can be produced at a high pH (13-14) (Srinivasan et al., 1988, 1992). Accordioning to (Srinivasan et al., 1991),the crystal structure formation, polymorphic transition, and crystalline development are strongly influenced by the solution chemistry of zirconia precursor materials. Because of the similarity of their lattice parameters (a_0 = 0.5124 nm for the cubic, and a_0 = 0.5094 nm and c_0 = 0.5177 nm for the tetragonal structures), the assignment of the tetragonal and cubic structures can be accurate. The tetragonal and cubic phases can be distinguished from one another by the presence of the distinctive splitting of the tetragonal phase reflections, (002), (200), (113), (311), (004), (400), and (006), whereas the cubic phase only displays single reflections at all of these positions.

According to the researchers, zirconia began to form almost devoid of organics, nitrates, and hydroxides at about 450 ºC and no additional weight loss was observed up to 1200 ºC. Tetragonal zirconia was visible in the x-ray diffraction pattern at 500 ºC after drying an amorphous material at 100 ºC. Pure amorphous zirconia made from gels or hydroxides crystallizes first as a metastable tetragonal phase, which transforms into a stable monoclinic form at temperatures below 1000 º

(Sathyaseelan et al., 2017; Srinivasan et al., 1991).

2. 6 Modification techniques of graphitic carbon nitride (g-C_3N_4)

Despite the significant achievements over the years, there are still several obstacles in the way of the use of g-C_3N_4 particularly related to modification techniques. As depicted in Figure 7, there are several methods to modify the physical and chemical behaviors of g-C_3N_4-based materials. First, changes need to be made to g-C_3N_4's surface area and structural stability. It is known that g-C_3N_4 prepared via condensation technique typically suffers from incomplete poly-condensation, leading to various structures/composites from batch to batch. The surface area of such obtained g-C_3N_4 material is low, which reduces its catalytic activity. Although a template approach can produce g-C_3N_4 with an increased surface area, the surface morphology and characteristics may suffer as a result of the extreme conditions employed during the template etching process. Thus, the search for better, milder, and more reversible procedures to synthesize g-C_3N_4 with enhanced surface area is of crucial importance. Second, the physicochemical properties of g-C_3N_4 need to be further explored. Although g-C_3N_4 has been demonstrated to be an effective catalyst for some processes, its actual role is not clear. To better understand the reaction and improve the material, it is therefore necessary to relate the knowledge of g-C_3N_4's physicochemical characteristics and their impact on the catalytic activity. As depicted in Figure 7, the most important is to improve the catalytic efficiency of g-C_3N_4 in the reactions either by functionalization (doping) with nonmetal, alkali metals, transitional metal elements and rare earth metals. Since g-C_3N_4 is a covalent molecule, it contributes to reactions by donating of electrons to the substrate, which necessitates the splitting of the complex and subsequent establishment of the covalent bond. Because dissolving a covalent bond requires a lot of energy, this procedure slows down the electron donation process and lowers reaction rates. Therefore, to speed up the rate of electron donation, g-C_3N_4's surface energy and/or surface basicity must rise. In conclusion, two types of synthetic methods have been mainly employed for the synthesis of g-C_3N_4-based composites. The first one is mixing the substance with a carbon nitride precursor followed by the thermal condensation at the desired temperature; the second one is the post-treatment of the substance with as-formed g-C_3N_4 by deposition or simply mixing (Sudhaik et al., 2018).

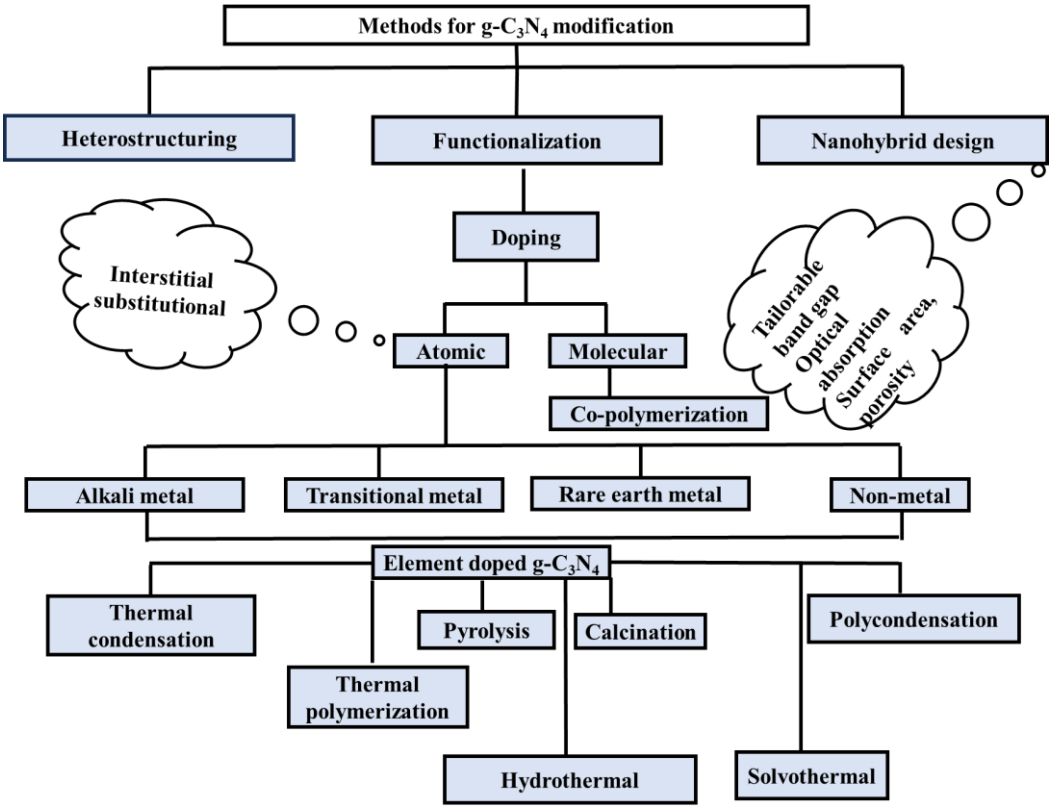

Figure 7. Flow chart showing modification methods for g-C_3N_4 and various doping strategies.

2.6.1 Template-assisted methods

Templating **(**Hard and soft templating methods**))** approaches offer a promising strategy to modify the structural and physical properties of semiconductor materials by varying the overall morphology and introducing porosity. Thus, larger guest-accessible surface areas, more active sites and more efficient charge separation can be achieved; all thought to benefit overall photocatalytic activity. Hard-templating is a multi-step process that involves filling a rigid template with a precursor, treatment of that precursor to generate the target material, and the removal of the template to yield a replica. In this approach, organic/inorganic molecules are used as templates to synthesize porous g-C_3N_4-based semiconductors. For example, the mesoporous carbon nitride photocatalyst was prepared by the replication of silica nanoparticles with a size of (12 nm) with melon obtained through the thermal condensation process of cyanamide precursors. The mesoporous g-C_3N_4 varied surface area from 8 to 373 m^2/g (X. Wang et al., 2009). Similarly, soft-templating offers an alternative, potentially greener method for the manufacturing of carbon nitride nanostructures. Soft structure-directing agents such as surfactants, amphiphilic block polymers, and ionic liquids were used to introduce porosity into a carbon nitride framework. 1-butyl-3-

methylimidazolium tetra-fluoroborate ([Bmim][BF_4]) and 1-butyl-3-methylimidazolium hexafluorophosphate ([Bmim][PF_6]) ionic liquid-butyl- 3-methylimidazolium tetrafluoroborate ($BmimBF_4$) has been used as soft template for the preparation of B and F doped mesoporous g-C_3N_4 with a high surface area of 444 m^2/g with active sites for catalytic reactions (Kessler et al., 2017).

2.6.2. Non-metal doped graphitic carbon nitride

Doping is a useful technique for increasing the efficiency of NCs in many applications, because it helps semiconductor materials' optical response ranges to become more flexible. Doping foreign elements onto the matrix structure is likely to modify the semiconductor's chemical makeup, atomic arrangement, electronic properties, and band position, leading to variations in its capacity to absorb photons and separate electron-hole pairs (J. Zhu et al., 2014). The lattice disorders caused by ion modification are known to have a significant impact on the electronic structure and surface characteristics by creating dopant-related states or mid-gap states, which may reform the conduction band (CB) and valence band (VB), and as a result, act as the active centers for electron-hole excitation and tune the optical response of semiconductors. Non-metal ion doping of g-C_3N_4 is thought to be one of the most effective alterations that might reduce the bandgap and increase the visible light absorption of g-C_3N_4, causing a red shift of the absorption edge and its luminescence. Non-metallic elements having accessible d-orbitals, such as sulphur and phosphorus are known to tailor electronic (Shylo et al., 2019).

Additionally, the electro-negativity and ionization energies of non-metals are always high as a result, non-metals often pick up electrons during reactions to create covalent connections with other substances. As shown in Table 1, to date, there are some studies on the non-metal ions employed for doping on g-C_3N_4 matrix such as nitrogen (D. Zhu & Zhou, 2021), phosphorus (S. Liu et al., 2018), boron (S. Zhang et al., 2017) oxygen (J. Zhang et al., 2022) and sulfur (You et al., 2017) exhibiting great opportunity to boost the visible light photocatalysis of g-C_3N_4 (Pollutant & Visible, 2017). Non-metal doped g-C_3N_4 NCs are discussed in more detail in the following sections.

Nitrogen-doped graphite carbon nitride

An exceptionally narrow band gap nitrogen-doped g-C_3N_4 (NCN) was produced and used for the photodegradation of phenols. Similar in thought, experimental tests and DFT research revealed

that N-doping was introduced in the g-C_3N_4 matrix by swapping out C atoms. By using DFT, PL spectra, optical property, and photoelectrochemical (PEC) analysis, it was reported that N-doped g-C_3N_4 has an incredibly narrow band gap, effective photogenerated carrier separation, efficient charge transfer, improved absorption of visible light (D. Zhu & Zhou, 2021).

Sulphur-doped graphite carbon nitride

The preparation of porous S-doped g-C_3N_4 can be employed from different precursors and synthesizing methods (Table 1). The first set of methods in the pyrolysis of compounds containing sulphur, carbon and nitrogen in one molecule (thiourea) is a common example of such precursors. With this regard, the pyrolysis of known C and N-rich precursors like urea, cyanuric acid, melamine or dicyandiamides and sulphur-containing compounds or sulphur precursors is a hot research area. However, as an example, the mixture of melamine and elemental sulphur (S_8) is known not to provide any of S-doped g-C_3N_4 (J. Zhang et al., 2012) only structurally transformed g-C_3N_4 is produced. Melamine and trithiocyanuric acid were co-polymerized to produce an intriguing substance that is thought to be a form of S-doped g-C_3N_4 (Shylo et al., 2019). On the other hand, the above-mentioned method suffers from similar shortcomings as shown with the thiourea pyrolysis (Shylo et al., 2019). However, there are several mechanisms proposed for the enhancement of catalytic activity but no clear research evidence was presented where the band gap and the separation of charge carrier are indicated as responsible factors for such improvements. Additionally, it is assumed that these non-metals replace the C, N, and H constituents in the tri-s-triazine structural unit. Therefore, the separation of photogenerated electrons and holes efficiently occurs when certain elements are substituted, leading to the establishment of a lattice defect in g-C_3N_4 and increased catalytic performance. Despite the remarkable results of such materials, still there is a lack of accordance about the detailed structure of resulting sulfur enrichment of g-C_4N_4, hence, the possibilities of the direction of such synthesis in favour of one particular kind of sulfur enrichment are very limited. Hence, there is still a lack of detailed information on which kind of sulfur enrichment is advantageous to a target application. To circumvent this constraint, recently some research groups have attempted by using DFT to designate the position of non-metal dopants such as S atom, which likely replaces the first N atom, while a P atom preferentially positions the interstitial sites of in-planar of g- C_3N_4 (Ma et al., 2012).

Sulfur-doped g-C_3N_4 by treating g-C_3N_4 powder in a gaseous H_2S atmosphere at 450°C was synthesized for the first time by (G. Liu et al., 2010). The S-doped g-C_3N_4 exhibits a larger VB width along with a higher CB minimum and a slightly lower absorbance. This unusual electronic structure is brought about by the homogeneous replacement of sulfur for lattice nitrogen and a concurrent quantum confinement effect. This results in the S-doped g-C_3N_4 with outstanding photoreduction of H_2 evolution and photo-oxidation of phenol. Researchers in this field hypothesize that the g-C_3N_4 matrix generated by pyrolyzing melamine and thiourea with a relatively low S content (<1wt.%) has both structural and optical characteristics. S-doped g-C_3N_4 had greater surface areas, a wider light adsorption range, and smaller band gaps than bulk g-C_3N_4 as a result of the synergistic effects of sulfur and g-C_3N_4, which led to improved photocatalytic activity (G. Liu et al., 2017).

Among the various ways to synthesize S-doped g-C_3N_4, the first technique involves pyrolyzing precursors like thiourea that contain carbon, nitrogen, and sulfur all in one molecule. Despite the impressive results of such materials, there is disagreement over the precise structure of the resulting g-C_3N_4 S-enrichment. Moreover, there are very few opportunities to steer such a synthesis in favour of a certain type of S-enrichment (there is still a lack of detailed knowledge of which kind of S-enrichment is beneficial to a target application). The second approach involves the combined pyrolysis or co-polymerization of a mixture of precursors that are known to contain C and N (urea, cyanuric acid, melamine, or dicyandiamide) and sulphur-containing precursors (trithiocyanuric acid, ammonium sulphate) Figure 8, which is thought to be a form of S-doped g-C_3N_4 (Guan et al., 2021).

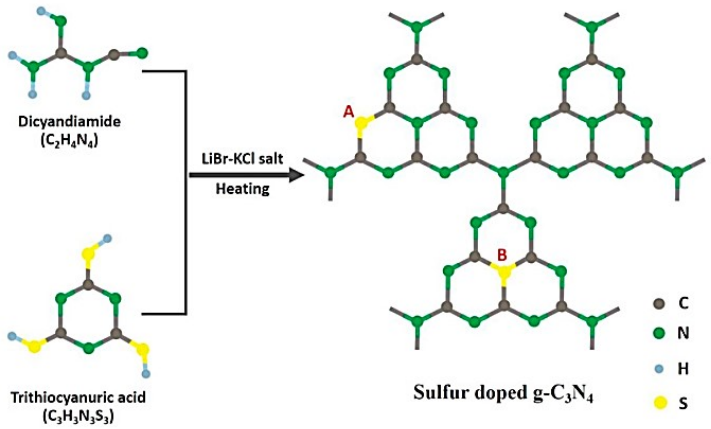

Figure 8. A schematic of the synthesis of S-doped g-C_3N_4 from different precursors.

As shown in Table 1, the properties of an S-doped g-C_3N_4 catalyst depend on the variety of precursors and treatment conditions. The best option is to change the precursors and modify the synthesis parameters such as time and temperature to attain a specific surface area of S-doped g-C_3N_4 and particle size to optimize the electronic structure and reaction sites. Nano-porous S--doped g-C_3N_4 microrods were synthesized by direct thermal condensation of melamine and trithiocyanuric acid supramolecular cocrystal in the N_2 atmosphere. The prepared S-doped g-C_3N_4 semiconductor was having a larger surface area and enhanced visible light absorption afforded an activity about 9.3 times higher than that of pure g-C_3N_4 for H_2 evolution and exhibited satisfactory stability (J. Chen et al., 2015). Recently, S-doped g-C_3N_4 porous rods with enhanced photocatalytic activity for the degradation of RhB in visible light were produced using the same precursor. The enhanced photocatalytic activity was attributed to greater mass and charge transfer in the mesoporous structure as well as stronger and longer light absorption brought on by sulfur doping (Fan et al., 2016). A study show that the substitution of the edge of the N atom in g-C_3N_4 with the S atom was practically advantageous due to the similar electro-negativities of S and N, which was compatible with the DFT studies examined by (Ma et al., 2012).

Figure 9 shows the XPS spectra of survey for g-C_3N_4, S-doped g-C_3N_4 and high-resolution spectra for C, N and S elements. The high-resolution C *1s* XPS spectra of the sample S-doped g-C_3N_4 in comparison to the g-C_3N_4 sample are displayed in Figure 9b. Consequently, the S-doped g-C_3N_4 sample exhibits three peaks at binding energies of 284.2, 284.8, and 287.9 eV. The main peak at 287.9 eV is assigned to the sp^2 - bonded carbon of N=C−N in g-C_3N_4, whereas the peak at 284.2 eV is ascribed to the C−C coordination due to carbon impurities. The characteristic peak centered at 284.8 eV is related to the C−S bond, which reveals that the S atom is indeed covalently bound to the CN framework. The high-resolution N *1s* XPS spectra of the samples were split into three peaks. The highest intensity peak at 398.5 eV is assigned to the sp^2 - bonded nitrogen of the C=N−C group. The peaks at 399.5 and 400.9 eV are attributed to the tertiary nitrogen of N-$(C)_3$ and the amino functional groups with hydrogen (C−N−H), respectively. For the S *2p* XPS spectrum (Figure 9d), the S *2p* peak centered at 164.2 eV can be assigned to the S-C chemical bonds formed in g-C_3N_4 by substituting the lattice N atoms with the S atoms. Accordingly, it can be concluded that a part of nitrogen is substituted with sulfur (An et al., 2019). The S *2p* peak at about 164 eV can further establish the presence of the S-C bond created by substitution lattice nitrogen atoms in the g-C_3N_4 skeleton with sulfur (J. Chen et al., 2015; G. Liu et al., 2017).

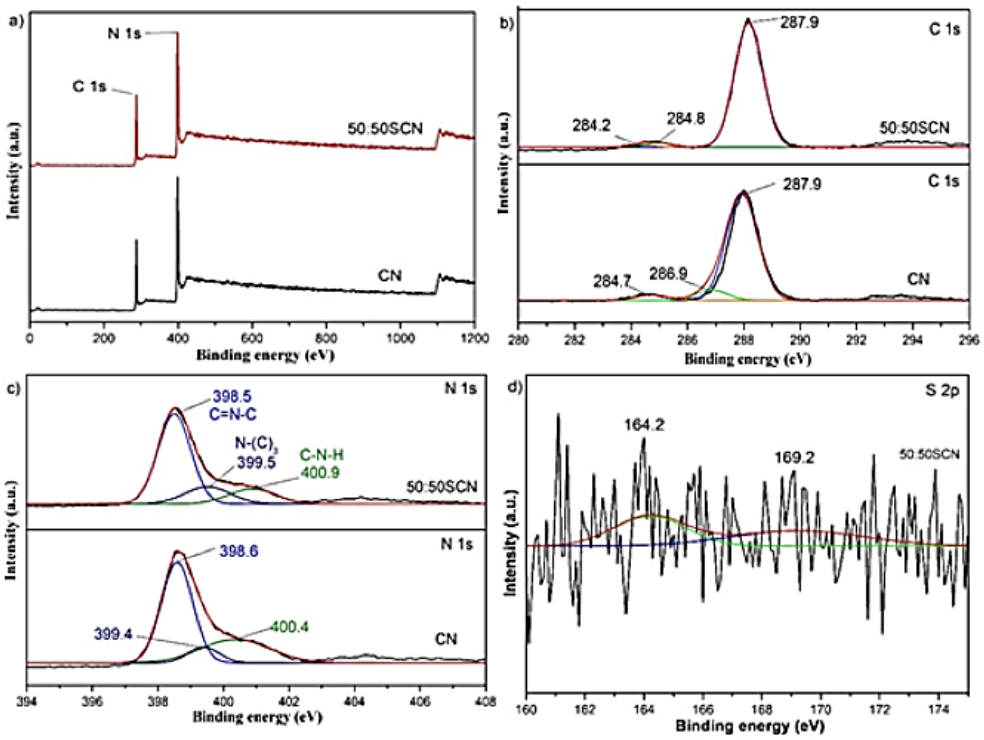

Figure 9. XPS spectra of survey for (a) g-C_3N_4 (CN) and S-doped g-C_3N_4 (SCN) and high-resolution spectra for (b) C*1s*, (c) N *1s* and (d) S *2p* for S-doped g-C_3N_4

In summary, according to the studies on Table 1, one advantage of doping g-C_3N_4 with a non-metal element is that, it lowers the band gap, improves the ability to capture visible light and so enhancing the photocatalytic. It can be realized that even though the optical properties of g-C_3N_4 are enhanced by doping with non-metal elements, however, are not favorable for catalytic reactivity of carbon nitrides due to the generation of further electron-hole recombination sites and due to potential side reactions, that give rise to light-obstructive minority phases (Kessler et al., 2017). However, in some non-metal doped g-C_3N_4 semiconductors, unexpected blue shifts occasionally appeared in the PL spectra and absorption edge of those modified products, which was inconsistent with the usual redshifts in earlier reports, especially for the B-doped samples (Q. Guo et al., 2016). This is because of some factors such as the different local structure, length of interlayer periodicity and defects formed during the modification processes. This leads to the adjustment of the lowest unoccupied molecular orbital (LUMO) and the highest occupied molecular orbital (HOMO).

Table 1. Summary of non-metal doped g-C_3N_4 NCs with applications

Type of material	Precursor		Method	Properties		Application	Pollutant	Ref.
	g-C_3N_4	Dopants		°C:h	E_g (eV)			
P-doped g-C_3N_4	$(NH_2)_2CO$	$C_2H_4N_4$ $CH_5N_3 \cdot HCl$	Pyrolysis	525:2	N/A	Photocatalyst	Rh B	(Matějka et al., 2022)
S-doped g-C_3N_4	$(NH_2)_2CO$	$(NH_2)_2CS$	Calcination	550	N/A	Photocatalyst	Rh B	(An et al., 2019)
S-doped g-C_3N_4	$C_3H_6N_6$	$C_3H_3N_3S_3$	Calcination	550:4	2.50	Photocatalyst	H_2	(J. Chen et al., 2015)
N-doped g-C_3N_4	$(NH_2)_2CO$	$C_6H_8O \cdot H_2O$	Calcination	550:4	N/A	Photocatalyst	Phenol	(D. Zhu & Zhou, 2021)
S-doped g-C_3N_4	$C_3H_6N_6$	$(NH_4)_2S_x$	Calcination	550:4	2.67	Photocatalyst	AO7	(Shylo et al., 2019)
P-doped g-C_3N_4	$C_3H_6N_6$	$C_3H_6N_6$ $C_2H_8NO_3P$	Thermal exfoliation	500;2	2.68	Photocatalyst	H_2	(Ran et al., 2015)
O-doped g-C_3N_4	$(NH_2)_2CO$	$(NH_4)_2C_2O_4$ $C_2H_5NO_2$	Thermal	550:2	2.63	Photocatalyst	BPA	(J. Zhang et al., 2022)
S-g-C_3N_4	$C_2H_4N_4$	$C_3H_3N_3S_3$	Calcination	500:3	N/A	Photocatalyst	MB	(Guan et al., 2021)
P-doped g-C_3N_4	$CH_5N_3 \cdot HCl$	$Cl_6N_3P_3$,	Calcination	550	N/A	Photocatalyst	Rh B	(Y. Zhou et al., 2015)
O-g-C_3N_4	$C_3H_6N_6$,	H_2S_4				Sensor	4-NP	(Mammadova et al., 2022)
S-doped g-C_3N_4	Melamine	Thiourea	Pyrolysis	550:4	N/A	Photocatalyst	RhB	(G. Liu et al., 2017)
		$(NH4)_2SO_4$						(H. Guo et al., 2020)
S-doped g-C_3N_4	Thiourea	CS_2	Pyrolysis	520;2	2.49	Photocatalyst	UO_2^{2+}	(Lu et al., 2017)

°C: h Calcination temperature per hr., D: crystallite size (nm), N/A; not available

2.7 Modification of graphitic carbon nitride by metal oxides

An interesting group of materials such as metal-oxides exhibits several unique properties, like exceptional carrier mobility, increased optical transparency, and mechanical stress endurance. MO NPs readily aggregate and agglomerate with one another due to their huge surface area and high surface energy. The aggregation/agglomeration of metal oxide NPs reduces the generation of the radioactive oxygen species and hydroxyl radicals. This is due to the quenching of holes and electrons with neighboring aggregate electrons and holes, respectively. Unfortunately, g-C_3N_4 has some disadvantages, such as rapid recombination of photogenerated electron-hole pairs, and insufficient visible light absorption (L. Bai et al., 2022; Moeinian & Akhbari, 2015). Thus, there is an urgent need to explore the modification strategy of the g-C_3N_4. Some of the primary strategies include designing heterojunctions (C.-C. Wang et al., 2019), defect engineering (P. Yang et al., 2019; Yu et al., 2017), and doping (Jiang et al., 2017). The synergistic effect of both g-C_3N_4 and MO results in enhanced stability, visible light range, separation and transfer of charges and more effective oxidizing species formation to improve the limitations of g-C_3N_4 (the electro-hole recombination, and promoting the charge carriers' separation, specific surface area, band gap energy) (Siddiquee et al., 2020). The following sections discuss the typical synthesis and characterization methods of CuO/g-C_3N_4 and ZrO_2@S-doped g-C_3N_4 NCs and their potential applications.

2.7.1. Cupric oxide /graphitic carbon nitride binary nanocomposites

The MO/g-C_3N_4-based NCs have been applied in various applications such as sensing pollutants especially, phenol-group molecules (BPA, 4-NP), tetracycline, photocatalytic reduction of toxic organic pollutants, removal of hazardous metal species such as Cr (VI) from water, etc. (Table 2). CuO exists in cubic, tetragonal or monoclinic structures, which is a Mott or charge transfer insulator driven by strong electron correlation with a bandgap of 1.4–1.7 eV (Figure 10a) (Mishra et al., 2016). Among several MOs used to improve g-C_3N_4 properties, researchers used CuO binary composites to increase the applications of these kinds of composites. Accordingly, the synergetic interactions between CuO and the g-C_3N_4, have been evaluated by different characterization methods including XRD, FTIR, UV-Vis/DRS, XPS, SEM, TEM etc. (Huang et al., 2019; L. Li et al., 2016; J. Zou et al., 2018).

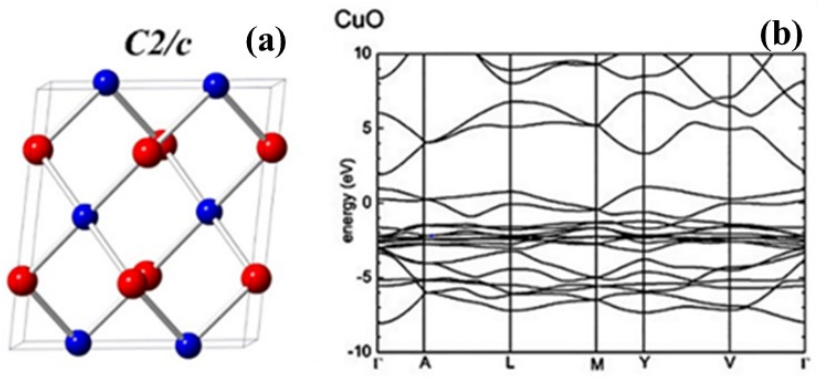

Figure 10.Crystal structure of (a) CuO and (b) its band structure

For instance, (C. Zhou et al., 2020) used the chemical precipitation approach to prepare the CuO/g-C_3N_4 composite. As shown in Figure 11 a, from the XRD pattern of CuO, the main diffraction peaks centred at 32.5º, 35.6º,38. º, 48.8º, 53.6º, 58.2º, 61.6º, 66.2º, 67.8º, 72.4º, 74.8º and 83.0º corresponding to (110), (111), (111), (202), (020), (202) (113), (311), (113), (311), (004), and (222) planes of CuO (Huang et al., 2019). Furthermore, the presence of CuO in the composite is demonstrated by a sequence of additional absorption peaks at the wavelength range of 400–800 cm−1, which correspond to the Cu–O bond as shown in the FT-IR Figure 11 b. These findings further supported the existence of two phases in the composite by correlating with the XRD patterns. The primary diffraction peak at 27.3 º originates from g-C_3N_4's surface (C. Zhou et al., 2020). Moreover, XRD and TEM studies revealed the existence of nanobelt CuO structure, supporting the composite's synergistic impact between CuO and g-C_3N_4. However, due to the strong peak of CuO, the diffraction peak of g-C_3N_4 at 13.1º was not shown in the composite. Only the main diffraction peaks of CuO can also be detected in the composite. The EIS study confirms the electrochemical improvement of g-C_3N_4 by CuO which significantly improved the performance in the capacitance of the composite compared to that of the bulk g-C_3N_4. The nitrogen adsorption–desorption isotherms show that the specific surface of g-C_3N_4 is 86.05 m^2/g while that of CuO is 26.218 m^2/g. Due to the addition of CuO nanobelts, the specific surface of CuO/g-C_3N_4 composites has been significantly improved, reaching 17.856 m^2/g. This larger specific surface can increase the reversible adsorption of the electrolyte ions on the surface of the electrode material, and provide more active sites for the rapid and reversible redox reaction during the charging/discharging process. Finally, the authors recommended that the chemical precipitation

technique is safe and reliable because it does not require a high-temperature-pressure environment and the preparation process is simple and short (C. Zhou et al., 2020).

Figures 12a, b, and c display the UV-vis diffuse reflectance spectra of g-C_3N_4 and CuO, which can be obtained using the Kubelka-Munk (K-M) theory. Equation (1) was used to measure the bandgap g-C_3N_4 and CuO.

$$(hv)^{1/n} = A\,(hv - E_g) \qquad (1)$$

where, *hv* and A are the absorption coefficient, incident light frequency and proportionality constant, respectively. The exponent 'n' gives the nature of the electronic transition of the semiconductor. Among them, 'n' refers to 1/2 for direct transition and 2 for indirect transition. The values of 'n' for CuO and pure g-C_3N_4 are 1/2 and 2, respectively. g-C_3N_4 's bandgap was calculated to be 2.7 eV, whereas CuO's bandgap was 1.7 eV (Sharma et al., 2020).

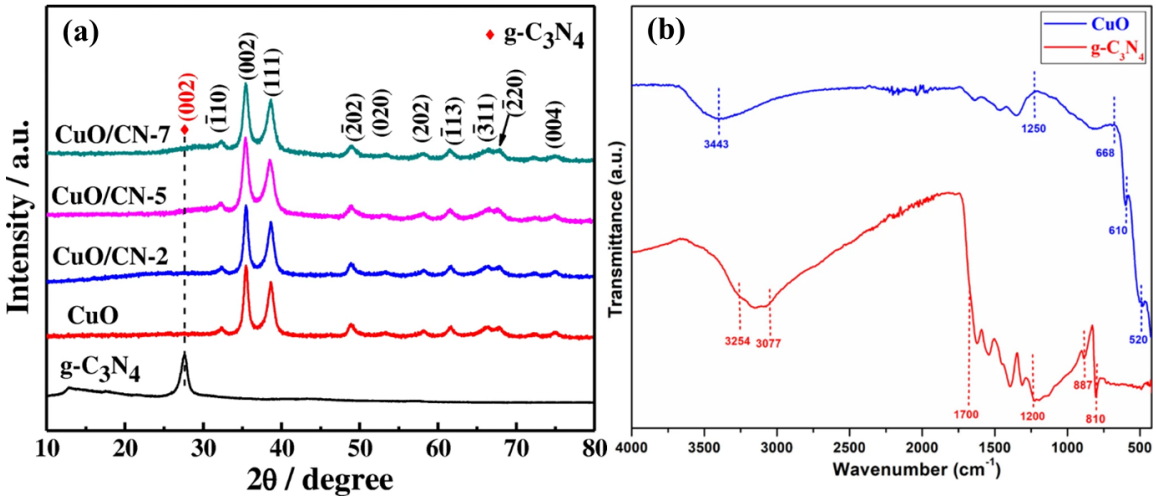

Figure 11. (a) XRD and (b) FTIR patterns of g-C_3N_4, CuO, and CuO/g-C_3 N_4 composite

The efficiency of charge carrier transfer and separation from photo-generated charge sources was further examined using electrochemical EIS and PL spectroscopy. It was found that the g-C_3N_4 photocatalyst's PL emission intensity was more than 4% CuO loaded. The decrease in the intensity of PL emission in 4% CuO-loaded g-C_3N_4 photocatalyst was attributed to the effective increase in migration and separation of photogenerated electron-hole pair at the 4% CuO/g-C_3N_4 interface. The charge transfer resistance of the photocatalysts can be determined from the arc radii of the Nyquist plots. As can be seen in Figure 12d, the 4% CuO/ g-C_3N_4 composite sample had a smaller Nyquist arc radius than the sample made up entirely of g-C_3N_4. It was found that when 4% CuO

was loaded onto g-C_3N_4, the charge carriers separated better and the charge carriers generated more than when g-C_3N_4 was used alone (Sharma et al., 2020).

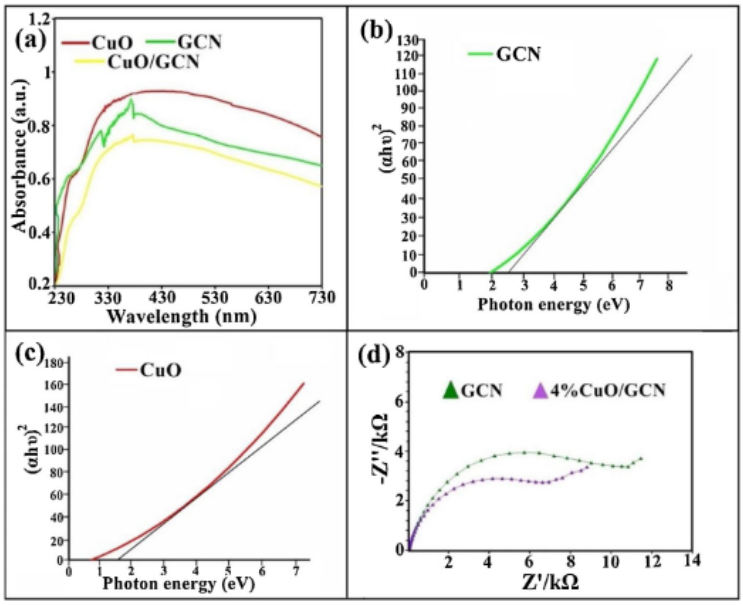

Figure 12. (a) UV analysis of CuO, g-C_3N_4, and CuO/ g-C_3N_4 photocatalyst (b and c) Taut plots of g-C_3N_4 and CuO and (d) EIS Nyquist plots of bare g-C_3N_4 and 4% CuO/ g-C_3N_4.

The survey XPS spectra, as displayed in Figure 13a, provide additional proof that the constructed composite contains the anticipated atoms. The N *1s* emission was deconvoluted revealing the presence of two distinct peaks with core locations at 398.2 and 399.2 eV. These peaks were the result of C-N sp^3 nitrogen groups and C=N sp^2-hybridized nitrogen, respectively, and corresponded to the nitrogen in the structure (Figure 13b). Cu-O-Cu coordination sites in CuO were responsible for the O *1s* peak at 531.67 eV and the two further peaks at 529.92 eV that were seen (Figure 13c). Additionally, the presence of C *1s* emissions at 285.6 eV, which may be associated with C-C in g-C_3N_4, confirmed the existence of one type of carbon (Figure 13d). Similarly, the high-resolution Cu *2p* spectra were deconvolved to reveal four different binding energies: 934.7, 943.4, 954 and 962.1 eV. This allowed for the assignment of significant peaks with centres at 934.7 and 954 eV around the valence states of Cu $2p^{3/2}$ and Cu $2p^{1/2}$, respectively, confirming the presence of Cu in the Cu^{2+} oxidation state (Figure 13e). The Cu^{2+} d^9 structure was also supported by two satellite peaks, located at 943.4 and 962.1 eV, respectively (Karthik et al., 2020; Pei et al., 2018; Sharma et al., 2020).

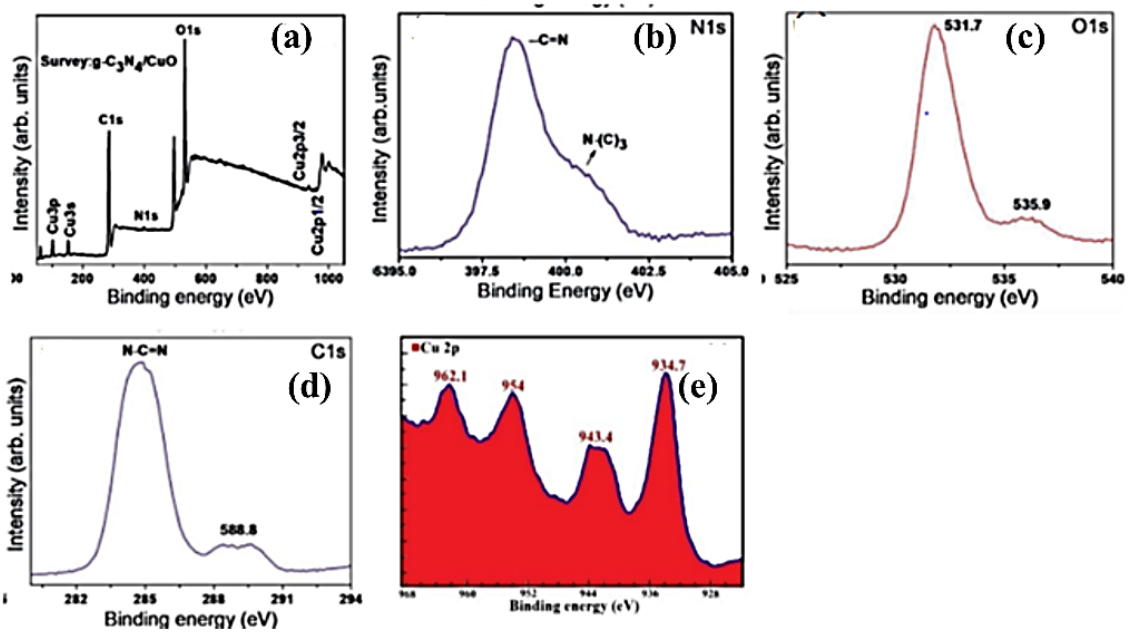

Figure 13.XPS spectra (a) survey for CuO/g-C_3N_4 (b) high resolution for N *1s* (c) O *1s* (d) C *1s* and (e) Cu *2p* (Sharma et al., 2020)

Other scholars have reported CuO/g-C_3N_4 synthesized via calcining synthesis with the aid of ultrasound to serve as a 2-butanone gas sensor. CuO NPs with a high density and homogeneity were equally disseminated on g-C_3N_4 sheets to create a heterogeneous composite based on the results obtained by XRD, XPS, and TEM studies. The prepared sensor demonstrated quick reaction and recovery behaviour, with times of less than 2 and 40 s, respectively. The linear range of the 2-butanone gas sensor was 16.11–161.08 μgmL^{-1} (r = 0.998) and the limit of detection was 11.06 μgmL^{-1} (S/N = 3). Due to the addition of mercaptosuccinic acid which is supported by ultrasonic and calcining the synthesis step, it became evident that there was a new, easy method for creating g-C3N4 sheets that were coated with CuO nanoparticles (CuO/g-C_3N_4). This technique's key is good for the formation of uniformly distributed CuO nanoparticles on the g-C_3N_4 sheets, which not only successfully minimized stacking of the g-C_3N_4 sheets but also avoided CuO NPs' agglomeration. The authors claim that the CuO/g-C_3N_4 composite-based gaseous sensor as designed exhibits exceptional analytical characteristics, including high sensitivity, quick response, and relative stability for the measurement of 2-butanone (L. Li et al., 2016). To solve the problems of low photocatalytic effectiveness caused by electron-hole pairs recombination and restricted photo-response range, a new g-C_3N_4/Cu_2O composite photocatalyst was effectively designed and produced. When exposed to visible light, the g-C_3N_4/Cu_2O composite demonstrated noticeably

higher photocatalytic activity for the breakdown of acid orange-II (AO-II) than did bare Cu_2O and g-C_3N_4 (Peng et al., 2014).

CuO/g-C_3N_4 NCs were prepared in a different work by combining calcination and hydrothermal techniques. Maximizing the g-C_3N_4 (2, 5, 7 weight percent) for the glucose and dopamine sensor was the aim of the investigation. As a result of the characterization, it was discovered that g-C_3N_4 sheets are covered in CuO particles, which retain their structural integrity but have a rougher surface. EDS element mapping shows that the C, N, Cu, and O elements make up 5% wt of the g-C_3N_4 in the CuO/ g-C_3N_4 samples. It offers to prove the coexisting of g-C_3N_4 and CuO. Also, the presence of the ring-like CuO, which was composed of many particles with sizes of several nanometers, was confirmed by the TEM images of CuO and CuO/ g-C_3N_4 (5%) in both samples. By using the CV and DPV techniques, the electrochemical response of a modified glassy carbon sensor toward glucose and DA was assessed. CuO and CuO/CN composites react to 50 M dopamine at 20 mVs^{-1} in phosphate buffer (pH 7.0). Anodic and cathodic peak currents were higher in the modified CuO/ g-C_3N_4 (5%) than in the other materials. The authors claim that the strong electrocatalytic activity of CuO/ g-C_3N_4 5%) can be attributable to its good conductivity and comparatively high adsorption capacity. Moreover, a diffusion-controlled process controls the oxidation of the dopamine molecule on the CuO/ g-C_3N_4 5%) GCE. To measure how the modified CuO/ g-C_3N_4 (5%)/GCE responded to dopamine in phosphate buffer, the standard DPV was carried out (pH 7.0). The results showed that at a working potential of 0.22 V (*vs.* Ag/AgCl), the oxidation peak current increases with increasing dopamine concentration, and that the current is linearly dependent on dopamine concentration with two linear dynamic ranges (Table 3). From 0.2-16.0 μM, the linear regressing equation was Ip^1 (μAcm^{-2}) = 0.834C (μM) + 4.372 (R^2 = 0.992) with a sensitivity value of 0.834 $\mu A \mu M^{-1} cm^{-2}$. Another linear relationship is Ip^2 (μAcm^{-2}) = 0.331C (μM) + 12.276 (R^2 = 0.990) in the range of 16.0-78.7 μM with a sensitivity value of 0.331 $\mu A \mu M^{-1} \cdot cm^{-2}$. In comparison to CuO, the CuO/ g-C_3N_4 (5%) sensor has a wider linear range (0.2-78.7 M) and lower detection limit (0.06 M). The sensing properties can be improved by combining the active CuO with the carbonaceous substance, g-C_3N_4. Due to its high conductivity and the synergistic effect of CuO and g-C_3N_4, the sensor exhibited considerable electrocatalytic activity toward both glucose and dopamine (Huang et al., 2019).

2.7.2 Zirconia/graphite carbon nitride binary nanocomposites

As shown in Table 3, combining g-C_3N_4 with zirconia becomes another study area to amend the limitations of g-C_3N_4. Using calcination and hydrothermal treatment techniques, researchers have created a unique ZrO_2/g-C_3N_4 composite photocatalyst for the first time (Ke et al., 2014). They found significant advantages for the photocatalytic destruction of phenolic compounds when comparing nanomaterials to more conventional oxidation processes, such as biological and physical methods. In addition to this, the NCs of ZrO_2 and g-C_3N_4 were effectively synthesized to quantify 4-chlorophenol (4-CP) photoelectrochemically (PEC) in water. The results show that ZrO_2 NPs and ZrO_2/ g-C_3N_4 NCs have increased the surface area and ability of intrinsic g-C_3N_4 to absorb light (Zarei, 2020b). Recent research has demonstrated the potential of g-C_3N_4-based hybrid NCs to be used as photocatalysts and electrochemical sensors. For example, (Kavil et al., 2019) used g-C_3N_4/ZrO_2 to degrade various organic contaminants, such as RhB, MO, and AO II, when exposed to visible light. Similarly, (Ke et al., 2014) who prepared a ZrO_2 and graphitic carbon nitride (g-C_3N_4) composite photocatalyst by calcination method and hydrothermal treatment for photodegradation of MB, the binary composite showed much greater performance than either pure g-C_3N_4 or ZrO_2 alone. A visible-light-driven PEC detection platform was developed using a ZrO_2/g-C_3N_4 nanocomposite as the transducer and a tetracycline (TET) binding aptamer as the biorecognition molecule. The g-C_3N_4 nanosheets were produced by pyrolyzing melamine, and the ZrO_2/g-C_3N_4 NC was prepared using a simple ultrasonication technique. The combination of high thermal, chemical, and photocatalytic stability, robust photocatalytic activity, and well-visible light absorption g-C_3N_4 nano-sheets with ZrO_2 NPs with outstanding adsorption capacity yield a unique platform for efficient tetracycline detection (Zarei, 2020a).

The FT-IR spectra of ZrO_2 shown in Figure 14a exhibited the broad bands in the region 500–550 cm^{-1} and at 800 cm^{-1} wavelengths attributed to the Zr–O vibration absorptions. Moreover, a broad region 3350 cm^{-1} corresponds to the hydroxyl groups of hydrated oxide. The breathing mode of triazine units is responsible for the acute peaks in g-C_3N_4 that were observed between 1200-1700 cm^{-1} region, and the N-H groups correspond to the broad absorption band that reached a maximum at about 3200-3700 cm^{-1}. The FT-IR spectra of pristine g-C_3N_4 and ZrO_2/ g-C_3N_4 NCs show a significant similarity, however, the differences in the bands of 800 and 3300 cm^{-1} with the variation of ZrO_2 still show the presence of ZrO_2 NPs (Zarei, 2020b). The hybrid structure and behaviour of ZrO_2/g-C_3N_4 were validated by the FT-IR, which exhibited a correlation with XRD results.

Similarly, the PL spectra (Figure 14b) show the effect of the ZrO_2/g-C_3N_4 hetero-junction on the separation efficiency of electron–hole pairs. The strong emission peak (380 nm) in pristine g-C_3N_4 is attributed to the emission of band-gap transition with the energy equal to the bandgap energy of pristine g-C_3N_4. However, fluorescence quenching can be seen in a similar region of the PL spectrum of ZrO_2/g-C_3N_4. Additionally, the charge transfer between g-C_3N_4 and ZrO_2 prevented the electron-holes from recombining. In comparison to the pristine g-C_3N_4, the emission intensities in ZrO_2/g-C_3N_4 NC are much lower, which demonstrates the efficient electrons-holes separation, resulting from incorporating ZrO_2 NPs into the g-C_3N_4 nanosheets. On the other hand, the addition of ZrO_2 NPs increased the surface area of g-C_3N_4 nanosheets, as shown in Table 3, and the modified sensor's samples with 30 weight percent ZrO_2/g-C_3N_4 were 65.3 m^2 g^{-1}. However, due to its shape, the g-C_3N_4 showed a comparatively small surface area of 51.8 m^2 g^{-1}. According to the BET results, the surface area of the g-C_3N_4 nanosheets was enhanced by the addition of ZrO_2 NPs (Zarei, 2020a).

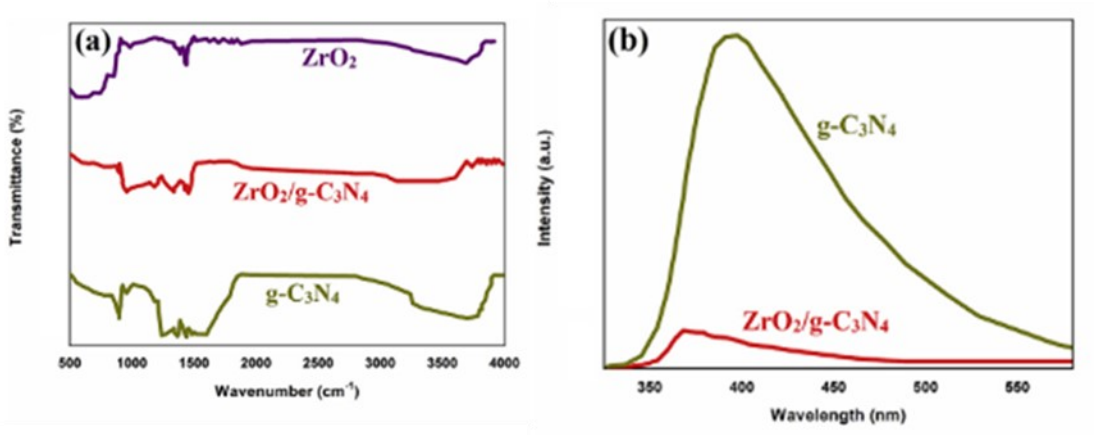

Figure 14.(a) FT-IR spectra of ZrO_2, g-C_3N_4, and ZrO_2/ g-C_3N_4 (b) PL spectra of g-C_3N_4 and ZrO_2/ g-C_3N_4 NCs (Zarei, 2020b).

Recent research on ZrO_2/ g-C_3N_4 NCs synthesized by melamine pyrolysis and then ultrasonication with ZrO_2 may qualify as one technique to modify g-C_3N_4. The interfacial behaviour of the ZrO_2/g-C_3N_4 modified electrode was investigated using electrochemical impedance spectroscopy (EIS) with $[Fe(CN)6]^{3-/4-}$as a redox probe.

Table 2.Summary of CuO/(g-C_3N_4) binary nanocomposites with different applications

Synthesis method	Precursor	Properties					Application	Ref.
	g-C_3N_4/ CuO	°C: h	Size SEM/TEM	LR µgmL^{-1}	LOD µgmL^{-1}	Target pollutant		
Wet impregnation/ calcination	Melamine $Cu(NO_3)_2$	540;5	N/A	N/A	N/A	H_2	Photocatalytic	(Karthik et al., 2020)
Ultrasound-calcining	Melamine $Cu(NO)_2{\cdot}3H_2O$	N/A	0.253 curled	16.11–161.08	11.06	2-butanone	Sensor	(L. Li et al., 2016)
Hydrothermal Calcination	Melamine $Cu(NO_3)_2{\cdot}3H_2O$	550:4	ring-like	0.5 µM - 8.5 mM 0.2-16.0 µM 16.0-78.7	0.150 60 nM	Glucose and Dopamine	Sensor	(Huang et al., 2019)
Microwave	Urea, CuO	N/A	Nano feathers	N/A	N/A	H_2	PEC	(Hosseini et al., 2020)
One-pot	Melamine $Cu(NO_3)_2{\cdot}3H_2O$	350:5	0.23	N/A	N/A	salicylic acid	Photocatalytic	(Duan, 2018)
Calcination	Urea $Cu(NO_3)_2$	N/A	Flakiness	N/A	N/A	2, 4 dimethyl phenol	Photocatalytic	(Sharma et al., 2020)

°C: h Calcination temperature per hr., LR; Linear range, N/A; not available

The Nyquist plot of the EIS demonstrates that the interfacial charge-transfer resistance (Rct) value of the bare FTO electrode is 370. By coating FTO with ZrO_2/ g-C_3N_4 composites, the R_{ct} value is raised to 680 Ω, demonstrating the low conductivity of these nanocomposites and the obstruction of electron transmission between $[Fe\ (CN)_6]^{3-/4-}$ reaction species and electrode. The aptamer immobilization on the ZrO_2/g-C_3N_4/FTO electrode surface was demonstrated by the improved R_{ct} of the aptamer ZrO_2/g-C_3N_4/FTO electrode (Zarei, 2020a).

On g-C_3N_4/ZrO_2, g-C_3N_4, and ZrO_2, UV-vis DRS was used to determine the sample's optical characteristics Figure 15 a and b. To determine the absorption wavelength threshold, the cut line approach was utilized to create the tangent and intersection with the abscissa. ZrO_2 can absorb light with a maximum wavelength of 247 nm. Compared to g-C_3N_4, with a maximum absorption wavelength of 428 nm, the absorption band edge of g-C_3N_4/ZrO_2 is red-shifted hence, its absorption of visible light is significantly increased as investigated by UV-vis DRS (Figure 18a) and PL studies (Figure 18b). The 4: 1 ratio of g-C_3N_4/ZrO_2 composite absorption band reaches 465 nm, which indicates improvement of the visible light absorption performance of g-C_3N_4 due to the incorporation of ZrO_2. Using the Kubelka-Munk equation, the calculated values for ZrO_2 and g-C_3N_4 using the n= 1/2 value were estimated to be 2.68 eV, 2.82 eV, and 4.91 eV, respectively, corresponding to g-C_3N_4 /ZrO_2, g-C_3N_4, and ZrO_2. As a result of the interaction of ZrO_2 with g-C_3N_4, the 4:1 g-C_3N_4 /ZrO_2 composite exhibits greater light absorption capabilities than g-C_3N_4 which was also displayed by the PL study (Figure 18b). It is indicated that g-C_3N_4 exhibits a significant emission peak at about 460 nm, which is a result of band gap transition emission. The fluorescence emission intensity of g-C_3N_4/ZrO_2 composites is much less than that of pure g-C_3N_4. The degree of fluorescence quenching first drops and then increases as the g-C_3N_4/ZrO_2 ratio rises. The 4:1g-C_3N_4/ZrO_2 composite has the lowest electron-hole recombination rate, and it appears that this rate falls initially before rising (Bi et al., 2020).

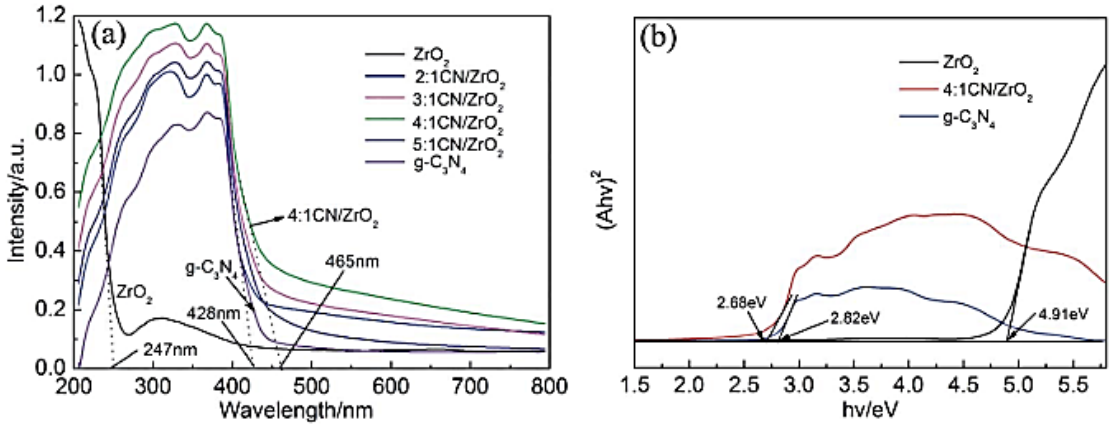

Figure 15.UV-vis spectra of g-C_3N_4/ZrO_2 composites and g-C_3N_4, ZrO_2 (a); the Transformed diffuse reflectance spectra (b).

2.8 Graphitic carbon nitride-based ternary composites

A practical technique to improve the properties of the composite is to build the binary, ternary, quaternary, etc. structure by incorporating additional elements or compounds. The use of g-C_3N_4 in conjunction with inorganic semiconductors is a promising method for separating charge carriers in three dimensions. With binary composites, the issues surrounding charge carriers and their role in the photocatalytic mechanism are still somewhat unclear. To create effective sites for catalytic reactions, ternary composites with the inclusion of a cocatalyst or support were also created and researched (Jo & Selvam, 2017).

An ideal semiconductor NC is typically thought to simultaneously possess the benefits of an appropriate band gap, a wide surface area, and cost-effectiveness. The fabrication of binary g-C_3N_4/MOF and ternary g-C_3N_4/MOF/X (X is one of the semiconductors photocatalysts) heterojunction composites in both macroscale and nanoscale have been proven to be an effective strategy for overcoming the shortcomings of MOFs and g-C_3N_4. The construction of the heterostructures can achieve the following advantages: (i) high surface area which improves reactant/catalyst interactions via increasing adsorption performance toward targeted models; (ii) it can also result in improved separation rates of photoinduced electron-hole activities. Since, the formed junction can speed up charge transfer across the interface and shortens the charge transport distance; (iii) critically, the π-π interactions between the large aromatic ligands of MOs and triazine rings of g-C_3N_4 enable active close contact, heterojunction building, and efficient electron

transmission rings and (iV) broadening the light spectrum to a visible light region (C.-C. Wang et al., 2019).

Table 4 provides a summary of the synthesizing techniques and application of the g-C_3N_4 /MO-based composites. The benefits of the strong visible light absorption of all three materials used, their appropriate band structures, and the high oxidation power of the VB holes in Bi_2O_3 have been reported in a ternary photoactive system composed of Bi_2O_2, g-C_3N_4, and CuO. In this work, CuO has also been used for enhancing the photocatalytic activity of Bi_2O_3 and g-C_3N_4 through the Z-scheme mechanism. When exposed to visible light with a wavelength greater than 420 nm, the suggested ternary system of CuO/g-C_3N_4/Bi_2O_3 was demonstrated to be photoactive for the breakdown of 2,4-dichlorophenol (2,4-DCP). In the crystal structure study, the typical diffraction patterns of CuO and g-C_3N_4 were not observed, according to the authors, this is probably because they are present in low concentrations (Sudrajat & Hartuti, 2018). Similarly, the potential application of TMOs/g-C_3N_4-based ternary NCs fabricated from a variety of precursors has been explored by researchers. As example, g-C_3N_4/TiO_2 (TO)/$PbTiO_3$ (PTO) films were prepared by the sol-gel followed by the CVD to explore PEC water splitting. It was stated that the interface of CN0.10/TO0.4/PTO had a lower interface (RCT) than pure PTO and CN0.10/TO0.4/PTO which made the charge transfer easier and reduced electron-hole recombination (Alaghmandfard & Ghandi, 2022).

Visible light-active g-C_3N_4 (0.94)/CeO_2(0.05)/Fe_3O_4 (0.01) ternary composite nanosheets were made using a straightforward co-precipitation technique. Density functional theory calculations show that the geometry and electrical properties of g-C_3N_4 were altered by the addition of CeO_2 and Fe_3O_4. DRS and PL spectroscopy demonstrated that the energy band gap tailoring ranged from 2.68 eV for bulk g-C_3N_4 and 2.92 eV for CeO_2 to 2.45 eV for the ternary nanocomposite. Due to effective electron/hole pair separation, an increase in redox species, and significant band gap tailoring, the degradation efficiency of g-C_3N_4(0.94)/CeO_2(0.05)/Fe_3O_4(0.01) is high. Superior photocatalytic breakdown of 2-chlorophenol was reported with g-C_3N_4 with CeO_2 loading up to 5wt. The addition of 1% weight percent Fe_3O_4 to the binary composite of g-C_3N_4 and CeO_2 nanocomposites increased visible light catalysis as predicted by DFT studies and also made magnetic recovery possible (Rashid et al., 2019).

Table 3.Summary of ZrO_2 /g-C_3N_4 binary nanocomposites with different applications

Synthesis method	Precursor for g-C_3N_4 and ZrO_2	Properties					
		°C:h	Eg (eV)	LOD	Target pollutant	Application	Ref.
Precipitation	$ZnCl_2$, $CdCl_2 \cdot H_2O$, Urea	550:3		N/A	MR	Photocatalytic	(Berhanu et al., 2022)
Calcination	$ZrOCl_2$.8H2O, Melamine	400:4	2.44	N/A	RhB, MO, II (AO II)	Photocatalytic	(K. Zhang et al., 2020)
Ultrasonication	$C_3H_6N_6$ $ZrOCl_2.8H_2O$	N/A		N/A	TET	Sensor	(Zarei, 2020a)
Hydrothermal treatment.	Melamine $ZrOCl_2.8H_2O$	530:4		N/A	MB	Photocatalytic	(Ke et al., 2014)
Ultrasonication	$C_3H_6N_6$ $ZrOCl_2.8H_2O$	600:2	2.6	50–150	TET	Sensor	(Bi et al., 2020)
Calcination	$C_3H_6N_6$ Cl_2H_2OZr	520:4		N/A	Hydroxyl	Catalyst	(Ghafuri et al., 2018)
Hydrothermal	$C_3H_6N_6$ $ZrO(NO_3)2.H_2O$	600:4	3.46	N/A	MB	Photocatalytic	(Ahilandeswari, 2022)

°C: h Calcination temperature per hr., N/A; not available

As indicated in Table 4, CuO, Bi_2O_3, and g-C_3N_4 were combined to create a novel ternary photocatalyst, CuO/g-C_3N_4/Bi_2O_3.The electron population has been observed to grow significantly when $B_{i2}O_3$ is doubly coupled with CuO and g-C_3N_4. The enhanced electron population has improved photocatalytic activity for the breakdown of 2,4-dichlorophenol under visible light (Sudrajat & Hartuti, 2018). Recently Hanif et al., (2022) reported the synthesis of a ternary ZnO/CuO/ g-C_3N_4 heterostructured NCs to remove contaminants (MB and CR) from wastewater via a photocatalytic process. The results show remarkable photocatalytic performance in MB within 50 minutes, with efficiencies of 75.3%, 39.2%, 15.6%, and 13.0% for ZnO/CuO/g-C_3N_4, g-C_3N_4, and ZnO, respectively. As shown in the Figure 16 (a-c) g-C_3N_4, ZnO-NPs, CuO-NPs, and ternary ZnO/CuO/g-C_3N_4 NC had computed E_g values of 2.33, 2.25, 1.46, and 1.69 eV, respectively. Remarkably, after forming the NC, the E_g value was significantly lower than that of the constituents of the NC, with the exception of CuO-NPs. The composite's lower E_g speeds up the creation of e^-/h^+ pairs and reduces the rate at which they recombine. Due to the photocatalytic efficiency being susceptible to several parameters, including crystalline size, heterojunction formation, and charge recombination effect, pure CuO demonstrated low photocatalytic efficiency. Therefore, the nanocomposite's small crystallite size and modification of surface morphology and form, such as the production of heterojunctions, may account for the ternary composite's higher photocatalytic activity than that of a pristin CuO (Hanif et al., 2022).

By applying the impregnating method, ternary ZnO/Fe_2O_3/g-C_3N_4 NCs' photocatalytic performance was assessed in the H_2 production from water splitting. Figure 17 shows the XRD patterns of samples of ZnO/Fe_2O_3/ g-C_3N_4 and bare g-C_3N_4 (a). Two peaks at 13.5 and 27.4^o were found in the XRD pattern for the pure g-C_3N_4 and were attributed to the (100) and (002) crystal planes, respectively. The XRD patterns of 11-ZnO/Fe_2O_3/g-C_3N_4 and ZnO/Fe_2O_3 exhibit diffraction peaks at 30.4, 35.6, 57.2, and 62.7°, which correspond to (220), (311), (440), and (511) Fe_2O_3 crystal planes, respectively, hence establishing the existence of Fe_2O_3 in the composite material. Both diffractograms' peaks at 22.5°, 34.8°, and 36.8° were indexed as ZnO crystal planes (100), (002), and (101), demonstrating that the composite also comprises the ZnO phase. When the ZnO/Fe_2O_3 proportion increases in the composite samples, the strength of the peaks corresponding to pure g-C_3N_4 decreases.

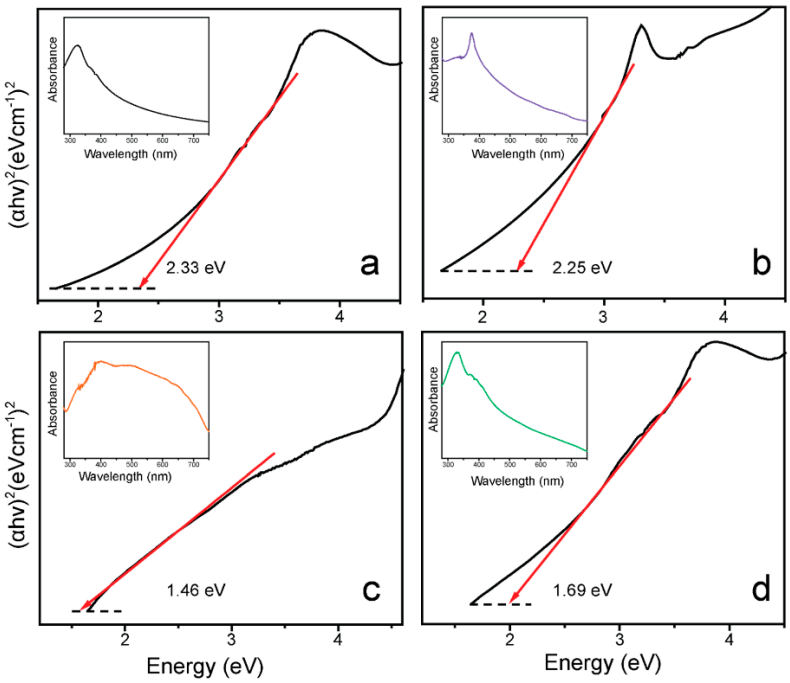

Figure 16. Tauc plots for (a) g-C_3N_4, (b) ZnO NPs, (c) CuO NPs, and (d) ZnO/CuO/ g-C_3N_4 NC. (Hanif et al., 2022).

Because the concentrations of ZnO and Fe_2O_3 were too low, the typical peaks of ZnO and Fe_2O_3 could not be seen in the XRD pattern of the ZnO/Fe_2O_3/g-C_3N_4 samples. The characteristic ZnO/Fe_2O_3 diffraction peaks were recognized in the diffractogram when the ZnO/Fe_2O_3 (2:1) content was higher than 10%. The XRD pattern of 11-ZnO/Fe_2O_3/ g-C_3N_4 did not reveal any more novel crystal phases. It was observed that the pure g-C_3N_4 did not lose its crystal structure as a result of the preparation procedure or the thermal treatment applied to the samples to alter the nitrate precursors in the related oxides. The FT-IR spectra of pristine g-C_3N_4 and ZnO/Fe_2O_3/g-C_3N_4 samples are shown in Figure 17b. The benzene ring's C-N-C vibrations are responsible for the bands at 1620–1500 cm^{-1}, whereas the bands at 3450 and 1390 cm^{-1} are caused by the vibrations and bending stretching of N–H and C–N, respectively. The bands found in the ZnO/Fe_2O_3/ g-C_3N_4 composites' spectra between 1620 and 1500 cm^{-1} are related to the benzene ring's stretching C-N-C vibration modes. The vibrations of C-N and N-H, respectively, are responsible for the bands at 1390 and 3450 cm^{-1}. The bending and stretching vibrations of the Zn-O and Fe-O bonds in the ZnO and Fe_2O_3 networks are attributed to the peaks at 551-652 cm^{-1}. The bands between 551-650 cm^{-1} in the ZnO/Fe_2O_3 spectra correspond to the vibrations of Zn-O and Fe-O. Hence, the infrared

data are comparable to the XRD results in depicting that Fe_2O_3 and ZnO were formed on the surface of g-C_3N_4 (Mao, 2019).

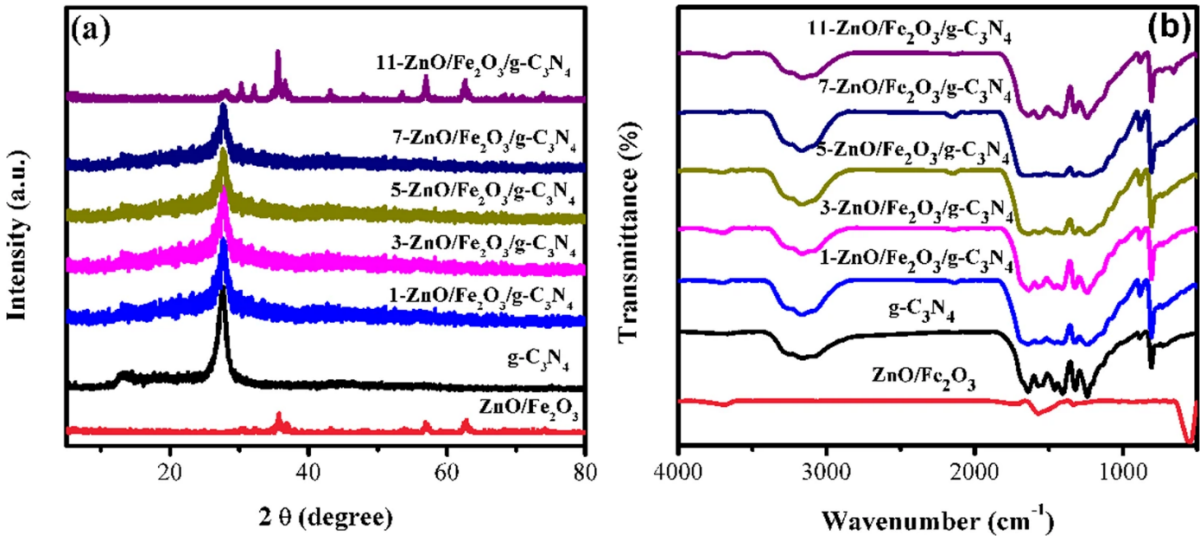

Figure 17. (a) XRD and (b) FT-IR spectra of ternary ZnO/Fe_2O_3/g-C_3N_4 and constituent samples (Mao, 2019).

2. 9 DFT methods

Many researchers have worked hard to find accurate and detailed information about the structure, formation energy, charge density, band structure, the density of states, etc. of g-C_3N_4 and S-doped g-C_3N_4. Most of the research groups suggested using the density functional theory (DFT) to examine the structure and electronic structure of the g-C_3N_4 and S-doped g-C_3N_4. The weak interaction between the g-C_3N_4 layers is also taken into account in estimating the equilibrium structure and the formation energy of S dopant in various non-equivalent locations using a semi-empirical correction to the exchange-correlation functional. The difference in electronic structure between undoped and doped g-C_3N_4 is closely examined, and the connection between the electronic structure variation and the photocatalytic property is emphasized. They concluded that an S atom substitutes the N atom bonded only with the two nearest C atoms in g- C_3N_4 (G. Chen & Gao, 2012) (Figure 18).

Table 4. Summary of g-C_3N_4-based metal oxide ternary NCs and applications

Nanocomposite	Precursor	Synthesis	°C: h	Size	Pollutant	Application	Ref.
ZnO/CuO/g-C_3N_4 $C_3H_6N_6$,	$C_3H_6N_6$, $ZrOCl_2.8H2O$,	Crystallization	530:4		MB, CR	Photocatalytic	(Hanif et al., 2022)
CuO/g-C_3N_4/Bi_2O_3	Bi $(NO_3)_3.5H_2O$	Precipitation	450:2	5 nm	2,4- DCP)	Photocatalytic	(Sudrajat & Hartuti, 2018)
g-C_3N_4@CdO/ZnO	ZnCl2, $CdCl_2{\cdot}H_2O$) $C_{12}H_{28}O_4$, Urea	Precipitation	550:3	N/A	MR	Sensor	(Berhanu et al., 2022)
ZnO/Fe_2O_3/g-C_3N_4	$C_3H_6N_6$,$Zn(NO_3)_2{\cdot}6H_2O$, $Fe(NO_3)_2{\cdot}9H_2O$	Impregnation & hydrothermal	550:4	0.247	Water splitting	Photocatalytic	(Mao, 2019)
Fe_2O_3/$EuVO_4$/g-C_3N_4	$C_3H_6N_6$, $Eu(NO_3)_3{\cdot}6H_2O$, $Fe(NO_3)_3{\cdot}9H_2O$, $FeSO_4{\cdot}7H_2O$	Sonochemical.	550:5	N/A	RhB	Photocatalytic, and electrocatalytic	(Monsef et al., 2021)
g-C_3N_4/ZnO/AgCl	$C_6H_8O_7$ Urea	Hydrothermal	520	N/A	RhB	Photocatalytic	(Akhundi & Habibi-Yangjeh, 2015)
Fe_3O_4/ g-C_3N_4/MoO_3	$C_3H_6N_6$, $FeCl_3$, $FeCl_2$	Doping	N/A	N/A	Tetracycline	Photocatalytic	(He et al., 2020)
GCE/rGO	Graphite	Hummers			4-NP	Sensor	(Wiench et al., 2017)
g-C_3N_4/Fe_3O_4/BiOI	$C_3H_6N_6$, $FeCl_3.6H_2O$, $FeCl_2.4H_2O$, $Bi(NO_3)_3{\cdot}4H_2O$	Magnetically	N/A	N/A	MB, MO, RhB	Sensor	(Mousavi & Habibi-Yangjeh, 2016)
GO/g-C_3N_4 Fe_3O_4	Urea, $FeCl_2$, $FeCl_3$	Hydrothermal	N/A	N/A	TC, Antibiotic and MB	Adsorption	(Sahoo et al., 2020)

°C: h Calcination temperature per hr. N/A; not available

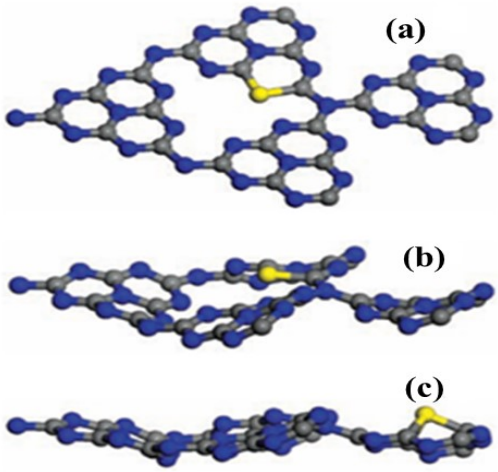

Figure 18.The schematic view of different doping sites of S in the S-doped g-C_3N_4

Similar research indicates that the position of S when doped on g-C_3N_4 affects the catalytic, optical, and electrical performance in the CO_2 reduction reaction. Moreover, the adsorption spectra of S-doped g-C_3N_4 was predicted to redshift in comparison to g-C_3N_4 due to the narrower band gap of S-doped g-C_3N_4 than that of g-C_3N_4. In S-doped g-C_3N_4, the LUMO is primarily located on the S atom while the HOMO is mainly located on N atoms, that are far from the S atom (Y. Wang, Tian, et al., 2018). On the other hand, the unit cells of g-C_3N_4 and S-doped g-C_3N_4 were utilized in the first-principles calculations. A study shows that a single S atom was added by swapping out one bidentate N atom in the supercell to simulate S-doped g-C_3N_4 (Jiang et al., 2017). Generally, the electronic structure of g-C_3N_4 can be modified by doping nonmetal elements to replace the lattice nitrogen, according to both theoretical and experimental research. This results from a narrowed band gap with the tuned CB and VB levels alone, as well as efficient electron-hole separation and carrier mobility (Chu et al., 2020).

2.10 Charge-carrier separation mechanisms of graphitic carbon nitride-based catalysts

Numerous studies have confirmed the hybrid g-C_3N_4-based NCs' charge-carrier separation mechanism. For instance, according to the recent literature, there are five different ways for g-C_3N_4 incorporated metal oxide photocatalysts to separate charge carriers (Alaghmandfard & Ghandi, 2022; L. Bai et al., 2022).

(1) Type I heterojunction, (2) Type II heterojunction, (3) Z-scheme heterojunction, (4) p-n heterojunction, (5) Schottky junction.

The primary heterojunctions of MO/g-C_3N_4-based NCs exhibit type II and Z-scheme processes for charge carrier separation. In type II heterojunctions, two semiconductors are bound to form a stable heterojunction, and the position of the VB of semiconductor A is higher than that of semiconductor B. In this case, because of the difference in voltages, the photoinduced hole migrated from the VB of semiconductor B to that of semiconductor A (Figure 19). On the other side, electrons are transferred from the CB of semiconductor A to that of semiconductor B. The improved hole and electron separation will lengthen the lifespan of the electrons and slow down recombination. It is highly desirable to build type II systems for photocatalysis in a variety of applications. It is important to understand the fundamental principles underlying the three different forms of heterojunctions before introducing the g-C_3N_4-based heterojunction photocatalysts. The smaller band gap semiconductor (semiconductor 2)'s VB and CB potentials are constrained within the larger band gap semiconductor (semiconductor 1), resulting in a straddling band alignment for the Type I band alignment. It transfers and accumulates all charge carriers into a single component within a hybrid structure as a result of the band edge positions occurring upon light irradiation with sufficient energy equivalent to or greater than the band gap of the semiconductors (Alaghmandfard & Ghandi, 2022).

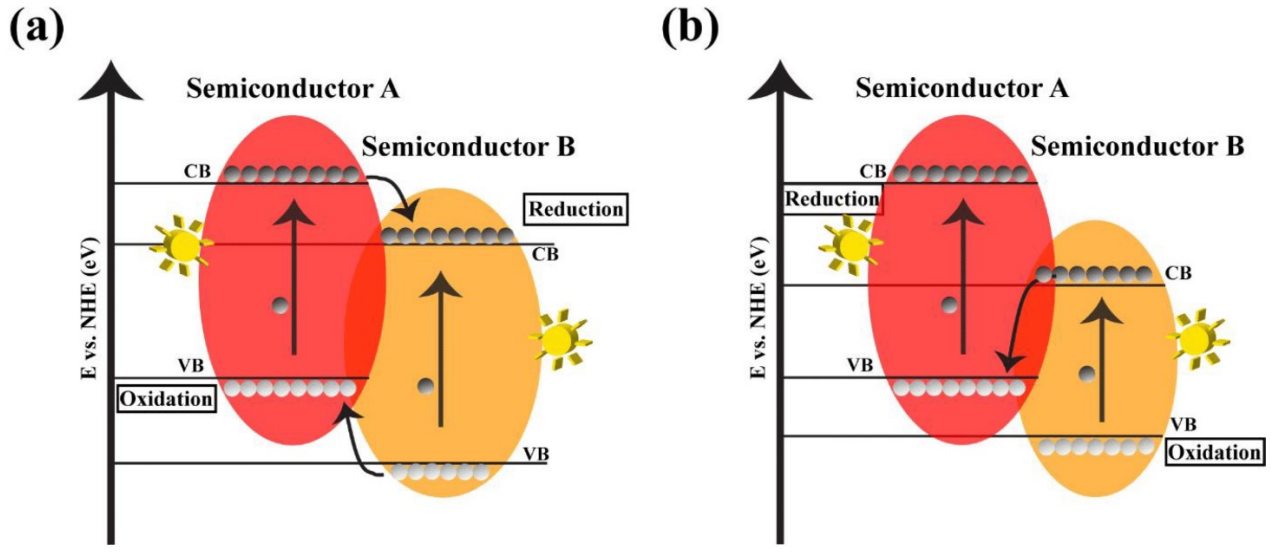

Figure 19. The two most common heterojunction types in g-C_3N_4 –metal oxide photocatalysts: (a) type II heterojunction, (b) Z-scheme heterojunction (white and dark balls are holes and electrons, respectively) (Alaghmandfard & Ghandi, 2022).

Since the charge carriers are accumulated in a semiconductor, there is no evident overall enhancement of charge separation thus commonly impairing the photo-redox efficiency. On the other hand, for the Type II heterojunction, the band edge potentials are staggered between semiconductor 1 and semiconductor 2. As a result of the chemical potential between both semiconductors, upward or downward band bending was formed, leading to the migration of charge carriers in the opposite direction. This significantly enhances the electron−hole spatial separation on various parts of heterojunction to retard the charge recombination to prolong the lifetime of free electrons and holes. The Type II alignment is where the majority of the NC heterojunctions are mentioned as shown in Figure 20. As a result, the oxidation and reduction processes employ two different semiconductors. While this is going on, in a Type III heterojunction, a semiconductor's VB and CB edges (semiconductor 2) are both above the CB potential of semiconductor 1 without crossing. For the three types of heterojunctions, selecting an appropriate semiconductor to couple with g-C_3N_4 in a heterostructured NC is of utmost importance not only to expand the optical light absorption range but also to ameliorate the charge migration and separation *via* a coherent and distinguished interface for the advancement of photochemistry reactions (Fu et al., 2018).

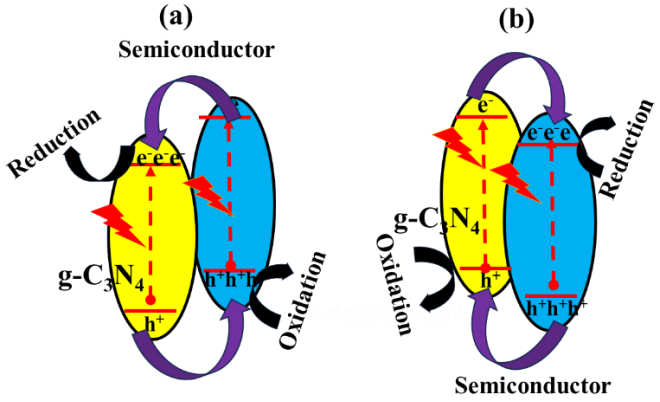

Figure 20. Charge transfer in the conventional type II g-C_3N_4 -based heterojunction systems constructed by coupling g-C_3N_4 to a second semiconductor a) with more negative CB and b) with more positive VB.

2.11 Pollutant dyes

2.11.1 4-Nitrophenol

4-Nitrophenol, (also called p-nitrophenol or 4-hydroxy nitro-benzene) is a phenolic compound that has a nitro group at the opposite position of the hydroxyl group on the benzene ring. The chemical profile of 4-NP shows Chemical Abstracts Service Registry Number: 100-02-7 l with synonyms: 4-Hydroxynitrobenzene, p-hydroxynitrobenzene, NCI-C55992, Niphen, 4-nitrofenol (Dutch), p-nitrofenol, paranitrofenol (Dutch), and paranitrofenolo (Italian). 4-nitrophenol shows two polymorphs in the crystalline state. The alpha form is colorless pillars, unstable at room temperature, and stable toward sunlight. The beta form is yellow pillars, stable at room temperature, and gradually turns red upon irradiation of sunlight. Usually, 4-nitrophenol exists as a mixture of these two forms. 4-nitrophenol is used in the manufacturing of drugs (e.g., acetaminophen), fungicides, methyl and ethyl parathion insecticides, dyes, and to darken leather. However, exposure to the 4-NP substance can be absorbed into the body by inhalation, through the skin, and by ingestion (Abdollahi & Mohammadirad, 2014).

The catalytic reduction of 4-NP to 4-AP was widely applied as an industrial chemical and metabolite of common household analgesics such as paracetamol (Cekic et al., 2005), which was for the first time applied to test the catalytic activity of free and immobilized NPs. Recently, this system has been established as a model reaction to evaluate the catalytic performance of different mono and binary NCs (Esumi et al., 2004; Pradhan et al., 2002).

By carrying out the catalytic reduction of 4-NP, several researchers have already investigated their synthetically produced effective catalytic nanostructured materials presence of reducing agents. Due to the simplicity with which kinetic parameters can be measured by observing the reaction using UV-Visible spectroscopic methods, reductions of 4-NP have come to be regarded as the most widely used model catalytic reaction (Kanti et al., 2022). The common electron transfer mechanism which involves the irreversible catalytic reduction of 4-NP tends to lose four electrons and four protons ($4H^+$, $4e^-$) at first to form 4-hydroxylaminophenol followed by the reversible two electrons and two protons ($2H^+$, 2e-) oxidation-reduction reaction to form 4-nitrosophenol as presented in Figure 21 (Rajkumar et al., 2018).

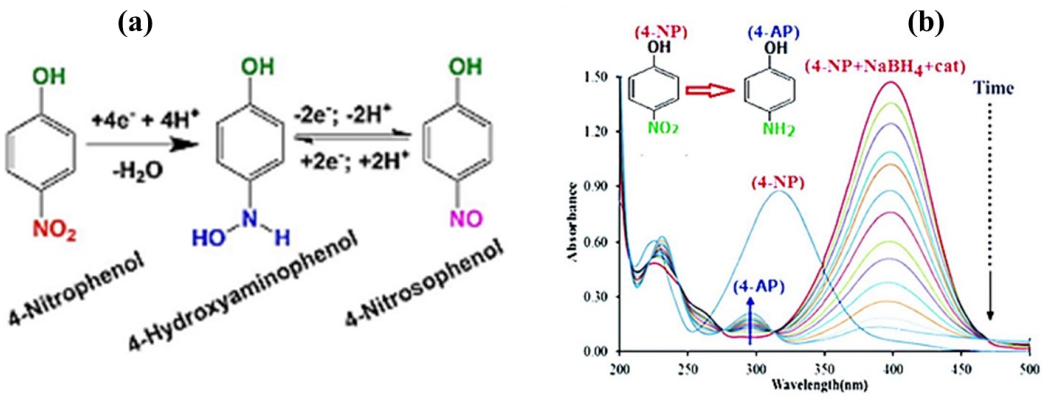

Figure 21. (a)The possible electrooxidation mechanism of 4-NP in the presence of the catalyst and (b) representative time-dependent UV–visible spectra of catalytic reduction of 4-NP.

2.11.2 Bisphenol A

Bisphenol A, BPA (2,2-bis (4-hydroxyphenyl) propane), is a primary ingredient widely employed for the commercial production of macromolecular products viz polycarbonate polymers and epoxy resins Figure 22b. BPA is a monomeric compound used for producing plastics and resins but also has an important environmental disadvantage due to its strong interference with normal working hormones and metabolisms (Shi et al., 2017). BPA which has low vapor pressure, low volatility, and moderate water solubility inevitably drifts into food items and drinking water from packaging material, and subsequently, children, women, men, and even animals regularly ingest this chemical.

However, the presence of BPA in different media including water sources has been substantiated while it is partially treated in the water treatment terrain. Human exposure to BPA that leaches from packaging or storage containers into foods and beverages is a great public health concern, due to the endocrine-disrupting potentials of this compound which imitates the natural estrogens' hormonal system. Concurrently, the toxic chemical further severely impairs the human nervous function, reproductive system, and cardiovascular role apart from being potentially a carcinogen (Kumunda et al., 2021).

Due to its widespread human exposure and toxicity, BPA has drawn considerable attention from monitoring organizations and the general public in recent years. Because of the health problems, in many developed countries restrictions on the use of BPA in certain consumer products have been suggested. For example, the U.S. Food and Drug Administration (FDA) banned the use of

BPA in baby bottles and children's drinking cups in July 2012. BPA also has been prohibited from the manufacture, sale, or distribution of some consumer products, such as reusable food or beverage containers, infant formula containers, and thermal receipt paper, by several states in the United States since 2009. Similarly, the European Commission restricted the use of BPA in plastic infant feeding bottles in January 2011 and also established a migration limit of 600 µg/kg for BPA in food or food simulators from plastic materials and articles intended to come in contact with foodstuffs (Maragou et al., 2008).

2.11.3 Methylene blue dye

Methylene Blue (MB) is a heterocyclic aromatic compound. Methylene blue ($C_{16}H_{18}ClN_3S$) is a cationic dye that is a commonly used substance for dying garments such as cotton, wool, and silk Figure 22c. The IUPAC name of MB is [7-(dimethylamino) phenothiazine-3-43 ylidene]-dimethylammonium; chloride. MB could be dangerous if inhaled or come in contact with skin. It can cause eye burns which may be responsible for permanent injury to the eyes of humans and animals. Inhalation of MB dye can give rise to short periods of rapid or difficult breathing while ingestion through the mouth produces a burning sensation and may cause nausea, vomiting, profuse sweating, mental confusion, and methemoglobinemia. Due to its known strong adsorption onto solids, MB often serves as a model compound for removing dyes and organic contaminants from aqueous solution (Hameed et al., 2007).

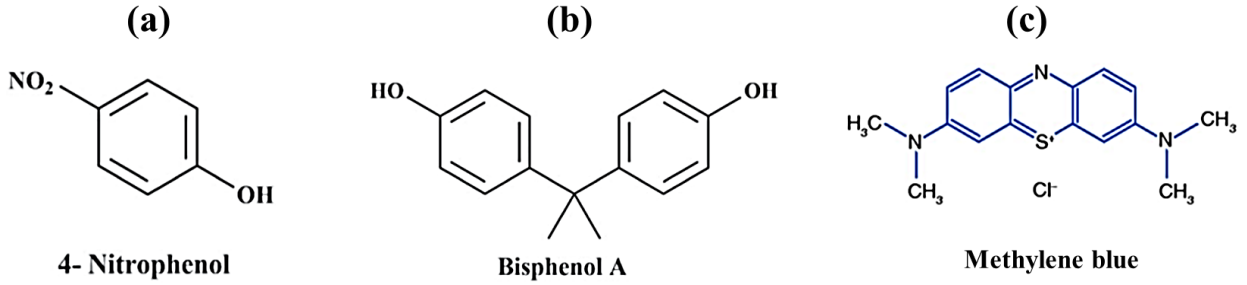

Figure 22.Chemical structures of organic phenolic pollutants found in water and wastewater.

2.12 Operating variables

It is important both from a mechanistic and an application point of view to study the dependence of substrate concentration on the electrochemical, electrocatalytic, and photocatalytic reaction rate. Catalyst amount and concentration of pollutant optimization have similar plot flow properties. As the initial concentration of the analyte increases, the efficacy of analyte adsorption decreases

according to the saturation of adsorption sites on the surface of the adsorbent. At a low concentration of analyte, there will be unoccupied binding sites on the surface of the catalyst and when the initial concentration of analyte increases, there will be insufficient sites for the analyte molecules to adsorb, so decreases the removal efficiency(Hameed et al., 2007; Sharma et al., 2020). Additionally, a rise in substrate concentration may result in the production of intermediates, which may then adsorb on the catalyst's surface. The catalyst's active sites may become inactive by slow diffusion of the produced intermediates from the catalyst surface, which would lower the rate of reduction. According to apparent first-order kinetics, at low concentrations, the number of catalytic sites will not be the limiting factor and the rate of reduction will be proportionate to the substrate concentration (Hanafi & Sapawe, 2020).

The common catalytic reduction of 4-NP in the presence of various reducing agents, such as $NaBH_4$, hydrazine (N_2H_4), etc. is a widely used reaction to study the activity of catalysts in an aqueous environment. However, as shown in (Figure 23), the catalytic reduction of the 4-NP reaction has been affected by various parameters (Kanti et al., 2022). Various studies revealed that with increasing concentration of 4-NP, for instance, the rate constant of the reduction reaction decreases as well as time to complete the reduction process increases. The reaction in the presence of Au NPs with various amounts of 4-NP and they explored that reaction time as well as TOF value was increasing with an increment of 4-NP concentration in the reaction medium (J. Li et al., 2012).

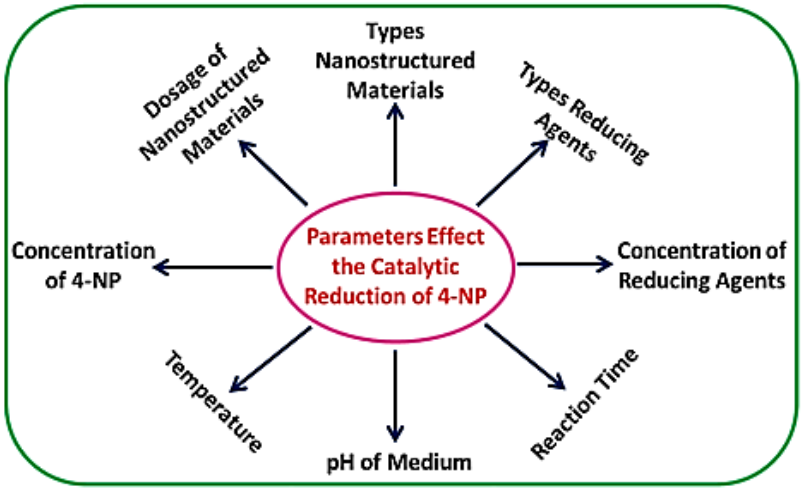

Figure 23. A schematic representation of the effect of parameters on the catalytic reduction of 4-NP

Cyclic voltammetry (CV), which is also used to determine the active surface area of electrodes modified with NC materials, can be utilized to study the kinetics of the analytes' electrocatalytic processes on modified electrodes. The modified electrodes are frequently subjected to CV measurements with redox probes like $[Fe(CN)_6]^{3-/4-}$ at various scan rates. The scan rate or the square root of the scan rate can be used to plot the anodic and cathodic peak currents. However, when the peak currents on the plot exhibit a linear relationship with the square root of the scan rate, a diffusion-controlled mechanism is typically present. When the plot shows a linear relationship between the peak currents and scan rate, a surface-controlled mechanism is usually present. The following Randles-Sevcik equation can be used to determine the active surface area of the electrode for an electrochemically reversible electron transfer process that exhibits typical diffusion-controlled electrochemical behavior (Paixão, 2020).

$$I_{pa} = (2.69 \times 10^5) n^{3/2} D^{1/2} C A v^{1/2} \qquad (2)$$

where I_{pa} refers to the anodic peak current, n is the electron transfer number, A is the surface area of the electrode, D is the diffusion coefficient of the redox species such as $[Fe(CN)_6]^{3-/4-}$, C is the concentration of freely diffusing redox species and v is the scan rate. Usually for 5 mM $[Fe(CN)_6]^{3-/4-}$, it is assumed that n = 1 and D = 7.6×10^{-6} cm s^{-1}; the active surface areas of the nanocomposite-modified electrodes are obtained from the slope of the $I_{pa} - v^{1/2}$ relation.

2.13 Electrochemical activity of graphitic carbon nitride-based NCs

Several articles explained that g-C_3N_4-based materials can be used to detect organic pollutants. For example, barium stannate was blended using g-C_3N_4 by ultrasonic-assisted synthesis to form barium stannate–graphitic carbon nitride NC (BSO–g-C_3N_4), and the resulting NC was utilized for the electrochemical detection of 4-NP via electro-oxidation. To test 4-NP electrochemically using the linear sweep voltammetry (LSV) method, the synthesized BSO- g-C_3N_4 was drop-cast on a pre-treated glassy carbon electrode (Idris et al., 2020). It is critical to stress that the discrepancy in detection limits reported by researchers can be attributed to the following factors: (1) analyte detection methods (2) utilizing nanomaterials to change the conducting substrate (3) conductivity of the g-C_3N_4 matrix's incorporated nanomaterials and (4) substrate conducting.

The oxidation of the g-C_3N_4 helps to attract the analyte on the conducting substrate. The oxidized graphitic carbon nitride (Ox–g-C_3N_4) was reported to possess excellent electrocatalytic activities

towards 4-NP. The sensor was fabricated by drop-casting Ox–g-C_3N_4 on a screen-printed electrode (SPE). The DPV response of the fabricated sensor showed a good linear range from 0.0033 to 0.313 µM, with a detection limit value of 0.075 µM. The g-C_3N_4 was oxidized to incorporate some exciting functional groups, including carboxyl, hydroxyl, and ketone, which helped attract the analyte on the electrode surface. This helps to have a lower detection limit (Idris et al., 2020).

In the application of ternary MO/ g-C_3N_4 NCs-based electrochemical BPA sensors, little is known about the detection of BPA by scholars. However, earlier research suggests the process of electrochemical oxidation of BPA on modified electrochemical sensors as shown in Figure 24 (Kunene et al., 2020; Yan et al., 2015).

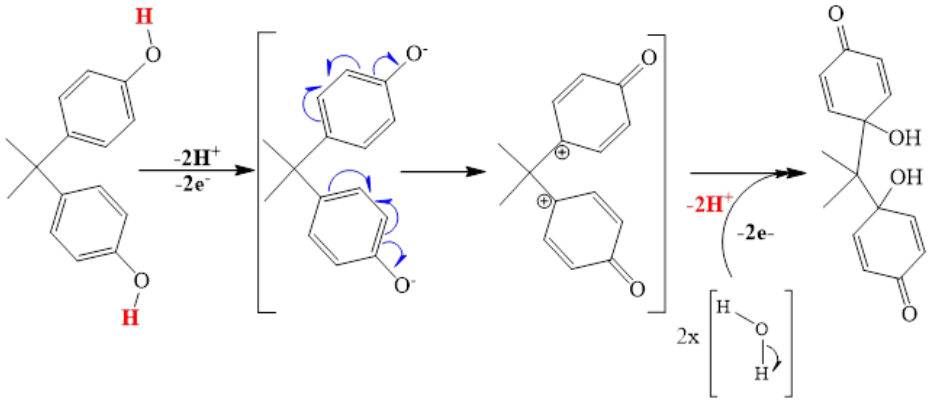

Figure 24. The possible electrooxidation mechanism of BPA at Lac/Ag-ZnO NPs/ MWCNTs/C-SPE (Kunene et al., 2020).

CHAPTER 3. MATERIALS AND METHODS

3.1 Study area

Synthesizing of NCs was done at Wolkite University. The sensor and catalytic reduction experiments were conducted at the Department of Applied Chemistry, the photocatalytic study, TGA/DTA and XRD experiments were conducted at the Department of Material Science, the PL study was done at the Department of Applied Physics, Adama Science and Technology University. The FT-IR study was done at the Department of Chemistry, Addis Ababa University. UV-Vis/DRS, BET, HRSEM/SED/EDS, and XPS studies were conducted at Free State University, South Africa. Characterization of synthesized samples by TEM was done in India.

3.2 Chemicals and reagents

The chemicals and reagents used are urea ($CO(NH_2)_2$), ammonium sulphate ($(NH_4)_2SO_4$), absolute ethanol (CH_3CH_2OH) 97%, sulfuric acid (H_2SO_4), sodium hydroxide (NaOH), ammonia water ($NH_3(OH)$ zirconia oxychloride hydrated ($ZrOCl_2.8H_2O$), copper nitrate hydrated Cu $(NO_3)_2{\cdot}3H_2O$ and hydrochloric (98%) HCl. 4-nitrophenol ($C_6H_5NO_3$), BPA ($C_{15}H_{16}O_{2)}$, Na_2SO_4 $NaBH_4$, Fe $(CN)_6^{3-/4-}$, KCl, and MB obtained from Sigma Aldrich (99.9%). All the reagents and chemicals were of analytical-grade purity and used without further purification 4-NP was selected as the target contaminant and used without purification. Double distilled water was used for all solutions.

3.3 Preparation of sulfur-doped graphitic carbon nitride (S-doped g-C_3N_4) nanocomposite

The S-doped g-C_3N_4 NC was prepared by modifying an upgraded gas templating method (H. Guo et al., 2020). Briefly, measured amounts of ammonium sulphate ($(NH_3)_2SO_4$, 2 g) and urea $(NH_3)_2CO$, 8 g) were used *via* the following process. First, $(NH_3)_2SO_4$ was placed at the bottom of a crucible and distributed uniformly (to be used as a bed), and then urea was laid over ammonium sulphate uniformly distributed on the upper surface. The crucible was then covered with aluminum foil and placed in a muffle furnace at 550 ºC with a heating rate of 15 ºC/min for 4 hrs. in an atmospheric environment. After cooling the furnace, the prepared bulk material was dissolved in 100 mL C_2H_5OH and sonicated (model; Bandelin electronic Heinrichstrabe 2.4, 12207 Berlin, Germany) for 2 hrs. To remove the unexfoliated impurities the obtained sulfur-doped graphitic carbon nitride was centrifuged at 4000 rpm. After filtering, the sample was dried at room

temperature and collected. The exfoliated sample was abbreviated as S-doped g-C_3N_4 sheets. For comparison, g-C_3N_4 was prepared using pyrolysis of urea at the same heating temperature and time except the absence of sulfur.

3.3.1 Synthesis of CuO@ S-doped g-C_3N_4 NCs

The binary CuO@S-doped g-C_3N_4 NCs were prepared by employing a simple chemical precipitation method (Sudrajat & Hartuti, 2018). First, the CuO NPs were synthesized from solid Cu $(NO_3)_2{\cdot}3H_2O$ using the chemical precipitation method. In a typical synthesis, first a mixture of C_2H_5OH and S-doped g-C_3N_4 that was already synthesized in the previous step was sonicated for 2 hrs. and labelled as solution "A". In the meantime, the desired amount of solid Cu $(NO_3)_2{\cdot}3H_2O$ (7.54 g) was stirred by dropwise addition of 0.1 M of NaOH while heating at 70 ^oC (using a hot plate) until a black precipitate formed, this was labeled as solution "B". Then, solution "B" was added to solution "A" and stirred for an extra 4 hrs. with the addition of deionized water until the pH=10. After filtering and washing with distilled water and ethanol repeatedly, the mixture solution was transferred to an oven to dry at 60 ^oC overnight. After grinding, the sample was transferred into a muffle furnace at 500 ^oC, heating at a rate of 5 ^oC/min for 3 hrs. Finally, after allowing the furnace to cool CuO@S-doped g-C_3N_4 (CuO=5%) powder was obtained. Applying similar experimental procedures, different amount of CuO sample was prepared to get CuO@S-doped g-C_3N_4 (10%), CuO@S-doped g-C_3N_4 (20%), and CuO@S-doped g-C_3N_4 (30%) powder samples.

3.3.2 Synthesis of ZrO_2 @ S-doped g-C_3N_4 NCs

Applying a similar method used in section 3.3.1, ZrO_2@S-doped g-C_3N_4 NCs were prepared from ZrO_2 powder and the S-doped g-C_3N_4 NCs following a previously reported method. To synthesis binary NC, first ZrO_2 was synthesized from the precursor $ZrOCl_2.8H_2O$ by chemical precipitation method. Briefly, approximately 6.5 g $ZrOCl_2.8H_2O$ was added to 100 mL deionized water to prepare 0.2 $molL^{-1}$ $ZrOCl_2$ aqueous solution. Slowly ammonia water was added to adjust pH to 10–11 and stirred till a white precipitate was formed. On the other hand, measured S-doped g-C_3N_4 was stirred for 2 hrs. Then, to this, the homogenous white colour solution of zirconia was added. The mixture was stirred for an additional 2 hrs. to make the mixture uniform. After filtering and washing with distilled water and ethanol repeatedly, the sample was transferred to an oven at 60^o C overnight. Finally, the dried sample was transferred to a muffle furnace at 500 ^{o} C for 3 hrs.

with a heating rate of 15 ^{o}C min^{-1}. After cooling down at room temperature, a ZrO_2@ S-doped g-C_3N_4 (ZrO_2=5%**)** powder sample was prepared. Following a similar procedure, different amounts of ZrO_2 were prepared to have ZrO_2@S-dopedg-C_3N_4 (10,20, and 30%) powder samples.

3.3.3 Synthesis of CuO/ZrO_2@ S-doped g-C_3N_4 NCs

The ternary CuO/ZrO_2@S-doped g-C_3N_4 NCs were prepared by employing a simple chemical precipitation method. In a typical synthesis, a mixture of C_2H_5OH and S-doped g-C_3N_4 was sonicated for 2 hrs., labelled as solution "A". Applying the same procedure, CuO solution was prepared from the desired amount of Cu $(NO_3)_2 \cdot 3H_2O$ (3.77 g), labelled as solution "B". In the other experiment, the measured amount of $ZrOCl_2.8(H_2O).3H_2O$ (3.25 g) was prepared as described above and labelled solution "C" " Then to prepare ternary powder sample, both solutions "A" and "B" were added to solution "C" and the mixture was stirred further for 4 hrs. by dropping of deionized water until the pH reached approximately 10. After filtering and washing with deionized water and ethanol (98%) repeatedly, the mixture was transferred to an oven to dry at 180 ^{o}C overnight. After grinding, the sample was placed into a muffle furnace at 500 ^{o}C, heating at a rate of 5 ^{o}C/min for 3 hrs. After allowing the furnace to cool, the resulting sample was named as ternary CuO/ZrO_2@S-doped g-C_3N_4 powder sample, Following the same experimental conditions, the remaining ternary CuO/ZrO_2@S-doped g-C_3N_4(5%), CuO/ZrO_2@S-doped g-C_3N_4 (10%) and CuO/ZrO_2@S-doped g-C_3N_4 (20%) NCs and CuO/ZrO_2@S-doped g-C_3N_4(30%) powder samples were prepared.

3.4 Characterization of synthesized nanocomposites

To observe the effects of combining S, CuO and ZrO_2 NPs in the preparation of binary and ternary NCs, either being supported or as support itself. The synthesized samples were characterized through advanced instrument techniques. The following sections describe the characterization methods used in this study.

3.4.1 Thermal stability

Thermal stability properties of the S-doped g-C_3N_4, CuO@S-doped g-C_3N_4, ZrO_2@S-doped g-C_3N_4, and CuO/ZrO_2@S-doped g-C_3N_4 samples were measured using capillary tubes with a digital melting point apparatus. TGA and DTA were performed under an N_2 atmosphere (20 mL/min) using a DTG-60H Shimadzu thermal analyzer. The rate of heating of the sample was set at 15

°C/min; TGA/DTA techniques were performed with a NETZSCH STA 409 PC/ PG, in which a heating rate of 15 ºC/min was applied between room temperature and 1000 ºC. The weight loss was recorded between 25 – 1000 °C with a heating rate of 15 ºC/min.

3.4.2 Crystal structure, phase, and purity

Since many substances have known crystal structures, powder X-ray diffraction (XRD) can be used as a fingerprint technique. This technique uses powder or polycrystalline materials to create patterns arising from all possible crystalline orientations for each material. A powder diffractometer essentially consists of an X-ray source, a sample holder, a detector, and a data storage device. The phase structure of the synthesized samples was studied by powder XRD with X-ray tube Cu Kα radiation target Cu, a voltage of 40.0 kV, and a current of 30.0 mA at a scanning rate of 3.0 deg/min (Shimadzu Corporation, Japan, Model XRD-7000X-RAY diffractometer). Similarly, the chemical bonding behaviors of the samples were evaluated using Fourier transform infrared (FTIR, Frontier) measured on Spectrum 65 FT-IR (PerkinElmer) in the range 4000-400 cm^{-1}.

3.4.3 Optical properties

UV-visible spectroscopy is a robust characterization technique that can be used for the structure elucidation of organic molecules and also for both qualitative and quantitative analyses.

Optical properties of pristine g-C_3N_4, CuO, ZrO_2, and S-doped g-C_3N_4 based binary and ternary samples were investigated by Ultraviolet–Visible (UV–Vis) diffused reflectance spectra (DRS) using a scanning-type UV–Vis spectrometer (Perkin Elmer, Lambda 950) with a $BaSO_4$-based integrating sphere in the wavelength range of 200 to 800 nm.

Moreover, the effect of CuO and ZrO_2 NPs on S-doped g-C_3N_4 based binary and ternary samples on the separation efficiency of electron-hole pairs was investigated by steady photoluminescence (PL) spectra carried out on a Cary Eclipse Fluorescence Spectrophotometer (Agilent, Malaysia) with excitation wavelength at 324 nm using xenon (Xe) flash lamp as excitation source.

3.4.4 Surface area

The determination and control of the surface areas and porosities of materials are very important in heterogeneous catalysis since they have a strong influence on catalytic activity. The most widely technique for surface area measurement is the Brunauer–Emmett–Teller (BET). Nitrogen

adsorption–desorption isotherms and BET was applied for surface area and porosity measurements (isotherms) of g-C_3N_4, S-doped g-C_3N_4, CuO, ZrO_2, and S-doped g-C_3N_4 based binary and ternary samples were obtained with a Micrometrics ASAP 2020 surface area and porosity analyzer and ASAP 2020 v2.0 software. Data refinement was done with Microactive v1.01 software. Approximately 30 mg of samples were activated under vacuum at 150 ^oC for 16 hrs. Samples were cooled to room temperature and N_2 adsorption-desorption measurements were done at 77 K.

3.4.5 Morphology study

The morphologies of the prepared samples were visually characterized using high-resolution scanning electron microscopy/Energy-dispersive X-ray spectroscopy/Secondary electrons diffraction (HR-SEM/EDS/SED) HR-SEM: JEOL 7800F Field Emission SEM, with an Oxford EDS, EM: Jeol IT200 SEM, with a Jeol EDS.

In addition to the type of morphology, the formation of CuO and ZrO_2 NPs in the S-doped g-C_3N_4-based binary and ternary samples were further characterized by high-resolution transmission electron microscopy (Jeol TEM 2100 HRTEM).

3.4.6 Chemical composition

The chemical or elemental composition determines the purity and performance of the composite. X-ray photoelectron spectroscopic (XPS) analysis (model PHI 5000 Versaprobe) was conducted to study the chemical compositions of the prepared samples. A low-energy Ar^+ ion gun and low-energy neutralizer electron gun were used to minimize charging on the surface. A 100 μm diameter monochromatic Al Kα X-ray beam (hν = 1486.6 eV) generated by a 25 W; 15 kV electron beam was used to analyze the different binding energy peaks. Multipack version 9.8 software was utilized to analyze the spectra to identify the chemical compounds and their electronic states using Gaussian–Lorentz fits.

3.4.7 Electrochemical characterization

To investigate the electrochemical behaviors of g-C_3N_4, S-doped g-C_3N_4, CuO, ZrO_2, and S-doped g-C_3N_4 based binary and ternary samples, cyclic voltammetric studies were conducted using a 0.1 M KCl 5 mM $Fe(CN)_6^{3-/4-}$ redox probe electrolyte solution at a scan rate of 50 mV^{-1} using a conventional three electrodes electrochemical cell with Ag/AgCl (3.0 M KCl aqua electrolyte) as reference electrode, platinum wire as counter electrode and fluorine tin-oxide electrode (FTO)

(area = 1×1 cm^2) coated with the prepared samples as working electrodes, connected to a potentiostat (Auto lab Ivium Technologies B V De Zaale 11 5612 AJ Eindhoven, Netherlands) coupled with a personal computer.

Electrochemical impedance spectroscopy (EIS) measurements were performed by using 5 mM Fe $(CN)^{-3}$/Fe $(CN)^{-4}$, applying an AC potential with an amplitude of 5 mV in the frequency range from 0.1 Hz to 1x10^{-5} Hz and applied potential of 0.22 V. A To evaluate the electrochemical performance of the modified electrodes, the Mott-Schottky curve study was conducted by using a two-electrode configuration test in 0.5 M Na_2SO_4 solution.

3.4.8 Computational studies

In this study, s-triazine rings from heptazine units (C_6N_7) were constructed, it consists of three fused s-triazine rings joined by nitrogen atoms. To mimic the doping of g-C_3N_4 with sulfur, substitutions of N1, N2, and N3 with S, respectively, for the three different sites were investigated. The findings of geometric optimizations of g-C_3N_4 and S-doped g-C_3N_4, models were used as input. The results were visualized using Chemcraft 1.8 software. The ABAB-stacking order of s-triazine rings from heptazine units (C_6N_7) was assumed to ease DFT computations. The DFT method has been used to investigate electrostatic potential (ESP) analyses, such as electronic delocalization between donor and acceptor bonds. DFT simulations employing the Becke 3–Lee–Yang–Parr (B3LYP) hybrid function were used to estimate the electronic characteristics of the optimized geometries, wavefunctions, and energies of all structures(Stephens & Devlin, 1995). For all of the atoms, the B3LYP/6-31+G (d, p) method was employed in *Gaussian* 09. The structural stability of the models was calculated using the energies of the lowest unoccupied molecular orbital (LUMO) and highest occupied molecular orbital (HOMO).

3.5. Catalytic reduction studies

3.5.1 Preparation of 4-nitrophenol solution

To evaluate the catalytic performance of g-C_3N_4, CuO, ZrO_2 and S-doped g-C_3N_4 based binary and ternary NCs in the reduction study of 4-NP into 4-AP, first 0.012M of 4-NP stock solution was prepared using double distilled water. Briefly, about 0.3783 g $NaBH_4$ was dissolved in 100 mL double distilled water in a 250 mL beaker; then 1 mL 4-NP (0.012 M) solution was added, to this solution measured amount of catalyst (g-C_3N_4, S-doped g-C_3N_4, S-doped g-C_3N_4 based binary and

ternary NCs) was added, in the meantime the solution mixture change in colour was observed. The catalytic reduction reactions of 4-NP were performed in a standard 3 mL quartz cuvette with a 1 cm path length. The absorbance of the reaction progresses the mixture of $NaBH_4$ and 4-NP was monitored using UV-Vis spectroscopy in the wavelength range of 250–500 nm after a constant min time interval.

3.6 Preparation of MB for photocatalysis study

Photocatalytic activity of the prepared ternary CuO/ZrO_2@ S-doped g-C_3N_4 (5,10,20 and 30 %) NCs was investigated by degradation of MB under visible-light irradiation at room temperature. In this study, CuO/ZrO_2@ S-doped g-C_3N_4 (5,10,20 and 30 %) photocatalyst (10 mg) was dispersed in 100 mL(10ppm) MB solution with an initial concentration of 10 mg L^{-1} by sonication for 10 min. Then it was kept in the dark for 30 min under stirring to reach saturation adsorption. After that, the photocatalytic decomposition of MB started under visible light irradiation. The experiment was conducted in a 176.6 cm^2 circular glass reactor under 125 W mercury vapour lamp irradiation from the top. In every 5 minutes, 5 mL of the dye solution was taken, and the concentrations at time t were measured by UV-vis spectrophotometer. The photocatalytic degradation efficiency of the ternary samples was computed as a percentage. The pseudo-first-order and second-order kinetic equation (equation 3 and 4) was used to study reaction dynamics (Guan et al., 2021).

$$\ln({}^{A}/_{A_0}) = -kt \qquad (3)$$

$$\frac{1}{A} = \frac{1}{A_0} + kt \qquad (4)$$

Where A_0 and A are the initial and the final concentration of MB at time t (min) respectively and k is the observed rate constant in min^{-1}

3.7 Electrochemical sensor studies

3.7.1 Preparation of binder-free modified sensors for 4-nitrophenol

Before modification, the bare FTOE was polished using 0.05 mm Al_2O_3 polishing powder, followed by thorough washing with ultrapure water and successive ultra-sonication with acetone, absolute ethanol and deionized water, respectively, for 15 min each time. This procedure was done repeatedly for the entire study to ensure that there was no contamination. After drying, the

electrode was sealed with Scotch tape with an exposed geometric area of 1×1 cm^2. To disperse the synthesized samples (g-C_3N_4, S-doped g-C_3N_4, CuO, ZrO_2, S-doped g-C_3N_4 based binary and ternary NCs), 0.5%wt. solution of samples was prepared in DMF solvent by sonicating vigorously for 2 hrs. at room temperature. For deposition, the resulting suspension (25 µL,) with a measured mass loading of modified active electrode was used by drop cast method on FTO (1×1 cm^2) and dried naturally to get g-C_3N_4/FTO, S-doped g-C_3N_4/FTO, CuO/FTO, ZrO_2/FTO, S-doped g-C_3N_4 based binary and ternary (CuO@S-doped g-C_3N_4/FTO, ZrO_2@S-doped g-C_3N_4/FTO, and CuO/ZrO_2@S-doped g-C_3N_4/FTO) modified electrodes. Afterwards, the dried modified electrodes were gently washed with deionized water to remove loosely attached samples on the modified electrodes' surface. Finally, the modified binder-free electrodes were used for the electrochemical measurements. For the detection of 4-NP, the modified binder-free electrodes, the Ag/AgCl saturated KCl electrode, and a platinum wire were used as a working, reference, and counter electrode, respectively. The sensing capability of the modified FTOEs was evaluated using 4-NP as reported by similar studies (Faisal et al., 2022; Khan et al., 2014).

3.7.2 Preparation of 4-NP solution for binder-free sensors

0.5 mM stock solution of 4-NP was prepared by dissolving 70 mg 4-NP in 100 mL distilled water and then filled to 1000 mL in a volumetric flask. A series of 4-NP solutions were freshly prepared from the stock solution by appropriate dilution of the stock solution with 10 mL phosphate buffer solution (PBS, pH = 7.0). All the solutions were prepared with doubly distilled water and all the measurements were carried out at room temperature (25 ± 5 ^oC).

3.7.3 Preparation of carbon paste-modified sensors for BPA

To evaluate the synthesized semiconductors' performance of the g-C_3N_4, S-doped g-C_3N_4, binary CuO@S-doped g-C_3N_4, ZrO_2@S-doped g-C_3N_4 and ternary CuO/ZrO_2@S-doped g-C_3N_4 NCs, in another type of electrode modification system, carbon pates modified by the prepared samples were fabricated to detect BPA in aqueous solution. Briefly, to prepare g-C_3N_4/CPE, S-doped g-C_3N_4/CPE, CuO@S-doped g-C_3N_4/CPE, ZrO_2@S-doped g-C_3N_4/CPE and, CuO/ZrO_2@S-doped g-C_3N_4 /CPE sensors, a mixture of 0.455 g of graphite powder 0.025 g of synthesized NCs, and 0.4 mL of paraffin oil was blended by hand, mixed in a mortar and pestle and then inserted in the bottom of a plastic tube syringe (internal radius: 2 mm and 10 cm long). Electrical contact was performed by pushing a conductive copper wire into the end of the glass tube to stick to the carbon

paste. When it is necessary to have a fresh electrode surface, the new surface is generated by extruding a small plug of the carbon paste with a stainless-steel rod rapidly and smoothing the resulting surface on the white paper.

3.7.4 Preparation of BPA solution

0.5 mM stock solution of BPA was prepared by dissolving 70 mg BPA in 100 mL distilled water and then filled to 1000 mL in a volumetric flask. A series of BPA working solutions were freshly prepared from the stock solution by appropriate dilution of the stock solution with 10 mL phosphate buffer solution (PBS, pH = 7.0). All the solutions were prepared with doubly distilled water and all the measurements were carried out at room temperature (25 ± 5 ^{o}C) (T. Yang et al., 2015).

CHAPTER 4. RESULTS AND DISCUSSIONS

To observe the main reaction parameters during the conversion of ammonium sulphate and urea to S-doped g-C_3N_4 NCs, we examined the retainability behind the releasing impacts of the self-supporting environment formed by pyrolysis and the reaction temperature. It was noticed that a solid with a pale-yellow type was produced on the surface of a closed crucible when a specific quantity of ammonium sulphate and urea was mixed. However, in an open crucible, all of the components were thermally destroyed and no solid precipitate was observed on the surface. According to the literature, on the thermal decomposition of urea, when the gas sources, in this case, ammonium sulphate, are placed on the bottom urea, gases transfer from the bottom to the top of the crucible, resulting in better utilization of decomposed gases and disruption of g-C_3N_4 growth. This method uses the bottom-placed $(NH_4)_2SO_4$ as a bi-functional gas template source and doping agent to transform the up-placed urea into S-doped g-C_3N_4. As a result of the high-temperature self-polymerization of sulfur and graphitic carbon nitride, the yellow-coloured solid phase formed inside the crucible in a one-step (H. Guo et al., 2020).

4.1. Characterization results analysis

4.1.1. Thermal stability studies

It was used to investigate the thermal stability property of the precursors to synthesize the pristine, binary and ternary samples. The thermal stabilities of the g-C_3N_4, S-doped g-C_3N_4, CuO@S-doped g-C_3N_4, ZrO_2@S-doped g-C_3N_4 and CuO/ZrO_2@S-doped g-C_3N_4 samples was investigated from the precursors $CO(NH_2)_2$, $((NH_4)_2SO_4$, Cu $(NO_3)_2{\cdot}3H_2O$ and $ZrOCl_2.8H_2O$ before calcination by TGA/DTA technique under an N_2 atmosphere.

The TGA curve for $CO(NH_2)_2$ and $(NH_4)_2SO_4$, (Figure 25a, blue line) demonstrates a progressive four weight loss steps that include the evaporation of adsorbed water molecules, the breakdown of NO_3 from ammonium sulphate and/or the breakdown of amorphous parts of urea, and finally the decomposition of the crystalline part to produce carbon, nitrogen, sulphur, hydrogen, and ash above 400 ^oC. Afterwards, the remaining portion of urea and ammonium sulphate is decomposed very slowly up to higher temperatures. The DTA curve of (Figure 25b black line) reveals an endothermic transformation at 132.19, 237.51 and 380.91^oC in the formation of S-doped g-C_3N_4. When the weight loss rate reaches its maximum, the breakdown reaction of urea and ammonium sulfate produces gases that could overflow and absorb heat from the system, replacing the

isomerization process. Thus, considering the TG/DTA property of this information, the temperature, 550 ºC was carefully chosen for synthesizing S-doped g-C_3N_4 (H. Guo et al., 2020; K. Li et al., 2023; J. Zou et al., 2019).

Similarly, as seen in the Figure 25b of DTA curve, endothermic transformations were observed at 101.8, 240.71 and 747.03 ºC. The decomposition reaction of the precursors, $CO(NH_2)_2$, $(NH_4)_2SO_4$ and Cu $(NO_3)_2{\cdot}3H_2O$ produces gas that exits and removes heat from the system causing the increase of the weight loss rate during isomerization (J. Zou et al., 2019). In the range of 400–615 °C, the TGA (blue line) plots exhibited behavior that is comparable to that of Figure 25a, with large ongoing weight losses. This demonstrates a new feature of $CO(NH_2)_2$, $(NH_4)_2SO_4$, and Cu $(NO_3)_2$.$3H_2O$'s thermal stability till 747 ºC. But, as mentioned in the literature section, urea is calcined at a temperature between 520 and 550 ºC while g-C_3N_4 is being made. To preserve the fundamental structure of the S-doped g-C_3N_4 during the synthesis of binary CuO@S-doped g-C_3N_4, a calcination temperature of 500 ºC was chosen (Berhanu et al., 2022; Jones & Rollinson, 2013; Kumari et al., 2008).

Figure 25 c displays the ZrO_2@S-doped g-C_3N_4 sample's thermal stability property. The TGA (blue line) displays the thermal stability of the precursors' $CO(NH_2)_2$, $(NH_4)_2SO_4$ and $ZrOCl_2.8H_2O$) throughout a variety of temperatures. Stabilization took place in three steps, beginning at 520 ºC. Very little weight loss was seen at temperatures over 520 ºC, indicating improved thermal stability (blue line). Additionally, the DTA results show that the precursors thermally decomposed at 126.94 and 217.26 ºC as a result of water molecule breakdown, carbon dioxide evaporation, and amino group (NH_3) volatilization. The last stage suggested that a consistent weight loss curve was seen at higher temperatures as a result of the phase shift from the ammonium sulphate/urea to the S-doped g-C_3N_4 structure. Therefore, taking into account this finding and literature references, 500 ºC was chosen for the calcination of binary ZrO_2@S-doped g-C_3N_4 composite (J. Zou et al., 2018).

For the preparation of ternary CuO/ZrO_2@S-doped g-C_3N_4, the thermal properties of Cu $(NO_3)_2.3H_2O$ and $ZrOCl_2.8H_2O).3H_2O$ described above were considered. As shown in Figure 25d, the TGA curve begins to stabilize around 400.62 ºC, which is caused by the mixing up of the precursors Cu $(NO_3)_2.3H_2O$ and $ZrOCl_2.8H_2O$. From the above TGA/DTA results, it can be observed that the total decomposition temperature of the mixture of the precursors($(NH_4)_2SO_4$,

$CO(NH_2)_2$, Cu $(NO_3)_2.3H_2O$ and $ZrOCl_2.8H_2O).3H_2O$ ends around at >520 °C. In order to synthesize ternary samples, the temperature of 500 °C was selected by considering the thermal stability of the precursors and the preservation of Cu (II), which keeps it from converting into Cu (I) at higher temperatures (J. Liu et al., 2011).

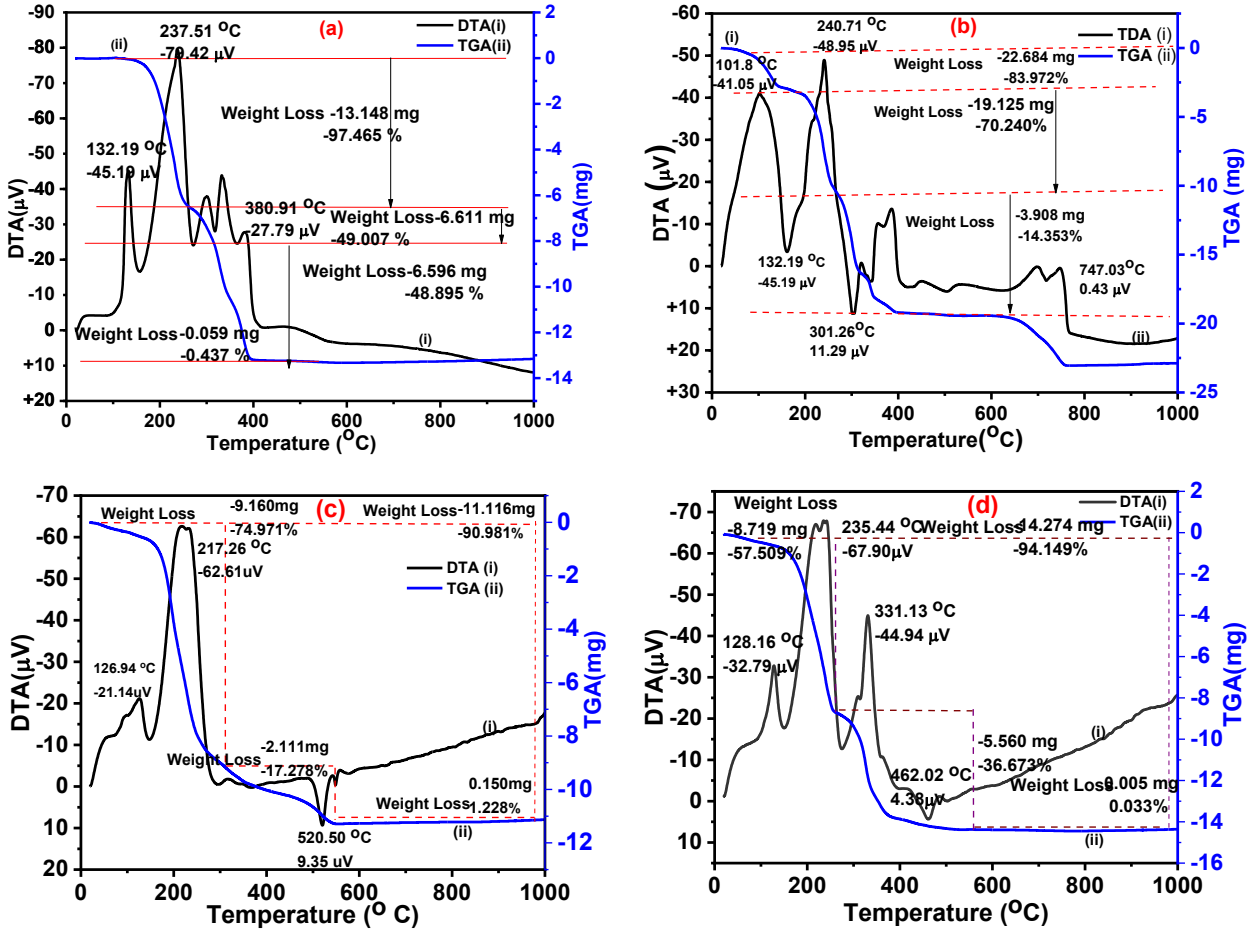

Figure 25.TGA (blue)/DTA (black) thermogram for mixture of precursors (a) $CO(NH_2)_2$, and $(NH_4)_2SO_4$:(b) $CO(NH_2)_2$, $(NH_4)_2SO_4$ and Cu $(NO_3)_2.3H_2O$:(c) $CO(NH_2)_2$, $(NH_4)_2SO_4$ and $ZrOCl_2.8H_2O$: and (d) $CO(NH_2)_2$, $(NH_4)_2SO_4$, Cu $(NO_3)_2.3H_2O$ and $ZrOCl_2.8H_2O$ before calcination.

4.1.2 Crystal structure, phase and purity analysis

XRD analysis

To verify the phase, crystallinity and structural changes occurred during the integration of S, CuO and ZrO_2 into g-C_3N_4, the XRD study for intrinsic CuO, ZrO_2, g-C_3N_4, S-doped g-C_3N_4, binary

CuO@S-doped g-C_3N_4 (5, 10, 20, and 30%), and ZrO_2 @S-doped g-C_3N_4 (5, 10, 20, and 30%) and ternary CuO/ZrO_2@S-doped g-C_3N_4 (5, 10, 20, and 30%) NCs were recorded, as shown in Figure 26-28.

Figure 26 shows the two significant peaks for g-C_3N_4 and S-doped g-C_3N_4. The low-intensity peak at 2θ = 13.4° and strong peak at 26.99° are attributed to (100) and (002) diffraction planes respectively indicating the unique graphitic structure of g-C_3N_4 (K. Wang et al., 2015; D. Zhu & Zhou, 2021). In comparison to g-C_3N_4, the strong peak due to S-doped g-C_3N_4 is sharper and more intense, which indicates its more crystallite nature. Moreover, the value of 2θ and major peak for S-doped g-C_3N_4 was found to have shifted negatively to 2θ = 23.98 ° (Table 5) indicating the presence of impurities, in this case, S. This reveal that there is no obvious change in the basic structure of g-C_3N_4 and S-doped g-C_3N_4 showing S-doped C_3N_4 still retain the molecular structure of g-C_3N_4 which complies with the reported literature (Al-saadi & Hameed, 2015).

The presence of Tenorite phase of monoclinic crystal CuO in the CuO@S-doped g-C_3N_4 NC is CuO (JCPDS card №. (05-0661)) which was assigned to the typical strong peaks at 2θ = 35.728°, 38.940°, 49.031° in the synthesized and standard XRD pattern shown in Figure 26 (Huang et al., 2019; D. Liu et al., 2018). Due to the higher amount of CuO (CuO=30%), the diffraction peak of CuO@S-doped g-C_3N_4 at 2θ =23.98 ° is low (Figure 26 Inset), probably because of the low content of S-doped g-C_3N_4 in CuO@S-doped g-C_3N_4. Thus, the signals were found to rise as the amount of CuO in the NCs increased, indicating the possibility of generating a metal-organic hybrid material or a coordination compound dominated by CuO NPs (Ahilandeswari, 2022; Tahir et al., 2007). The average crystallite size of each catalyst was calculated using Scherrer's formula as given in equation 5.

$$D = \frac{0.9\lambda}{\beta cos\theta} \qquad (5)$$

where θ is the angle between the incident and diffracted beams (degree), β is the full line width at half maximum height (rad.) D is the average particle size of the sample (nm) and λ is the wavelength of the X-ray.

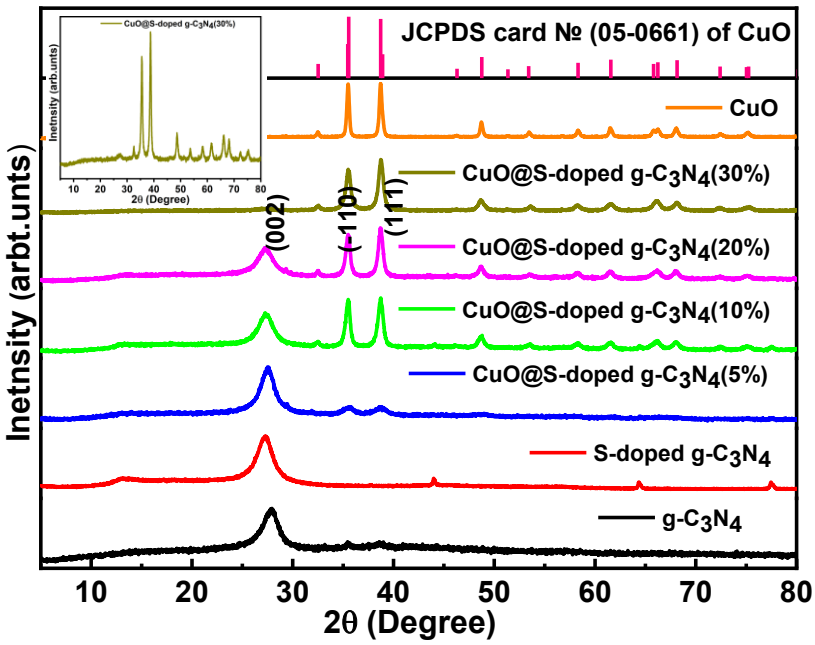

Figure 26.XRD pattern of g-C_3N_4, S doped g-C_3N_4, CuO@S-doped g-C_3N_4 (5,10,20 and 30%) NCs and CuO.

The average grain size of prepared g-C_3N_4, S-doped g-C_3N_4, CuO@S-doped g-C_3N_4 (5, 10, 20 and 30%) NCs and intrinsic CuO NPs were found to be 5.52, 13.23, 9.28, 6.80, 9.32, 6.50 and 30.09 nm respectively, as presented in Table 5. Generally, due to kinetics during processing, particles of CuO@S-doped g-C_3N_4 NCs evolved from agglomeration of small grains than particles of CuO@S-doped g-C_3N_4 (10 and 20%) NC.

The crystal structures of binary ZrO_2@S-doped g-C_3N_4 (5,10, 20, and 30%) NCs and intrinsic ZrO_2 NPs were recorded using XRD. As seen in Figure 27, for comparison, intrinsic g-C_3N_4, S-doped g-C_3N_4, and ZrO_2 was presented. The result shows the presence of a cubic phase ZrO_2 with corresponding characteristic peaks at $2\theta = 30.22°, 35.27°, 50.73°$ and $60.20°$ with fundamental plane orientations at (111), (200), (220), and (331) (Bi et al., 2020) of (JCPDS card № (00.049.1642). The binary ZrO_2@S-doped g-C_3N_4 NCs has three major peaks encompassing ZrO_2 NPs and S-doped g-C_3N_4 NCs, no other phases were found. The peak intensity of ZrO_2 grows with increasing ZrO_2 amount while the peak intensity of S-doped g-C_3N_4 drops. This demonstrates the effective integration of S-doped g-C_3N_4 with ZrO_2. The average crystallite size (D) of each sample was calculated using Equation 5. As shown in Table 5, ZrO_2@S-doped g-C_3N_4 NCs particles

developed from the agglomeration of tiny grains, obtaining different crystal sizes as a result of the processing kinetics (Krishna & Philip, 2022).

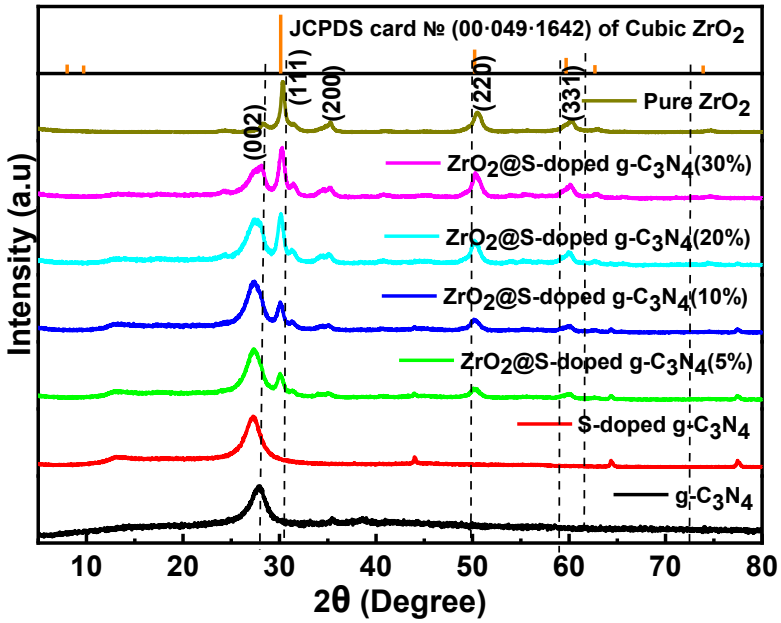

Figure 27. XRD patterns of g-C_3N_4, S doped g-C_3N_4, ZrO_2@S-doped g-C_3N_4 (5,10,20 and 30%,) NCs and ZrO_2

Figure 28 shows the XRD patterns of the intrinsic g-C_3N_4, S-doped g-C_3N_4, NPs and ternary CuO/ZrO_2@S-oped g-C_3N_4 (5,10,20 and 30%) NCs. As shown in Figure 28, no significant diffraction peaks of CuO and ZrO_2 can be perceived in the ternary CuO/ZrO_2@S-doped g-C_3N_4 (5,10,20 and 30%) samples through XRD examination. This may be due to the sample depth for XRD being in micron sizes, hence the CuO and ZrO_2 species may be related to the size of synthesized materials, which is the only plausible explanation for the absence of peaks for CuO and ZrO_2 in the XRD investigation of ternary NCs (L. Bai et al., 2022).

The average crystal size of the prepared CuO/ZrO_2@S-doped g-C_3N_4 (5, 10, 20 and 30%) NCs intrinsic CuO and ZrO_2 NPs were found to be 5.52, 13.23, 13.23, 17.53, 5.80, 3.36, 30.09 and 13.10 nm respectively as presented in Table 5. By considering the presence of the skeleton structure of the ternary NCs, the CuO and ZrO_2 NPs amount optimization was conducted by increasing the total amounts of the two metal oxides (5-30%).

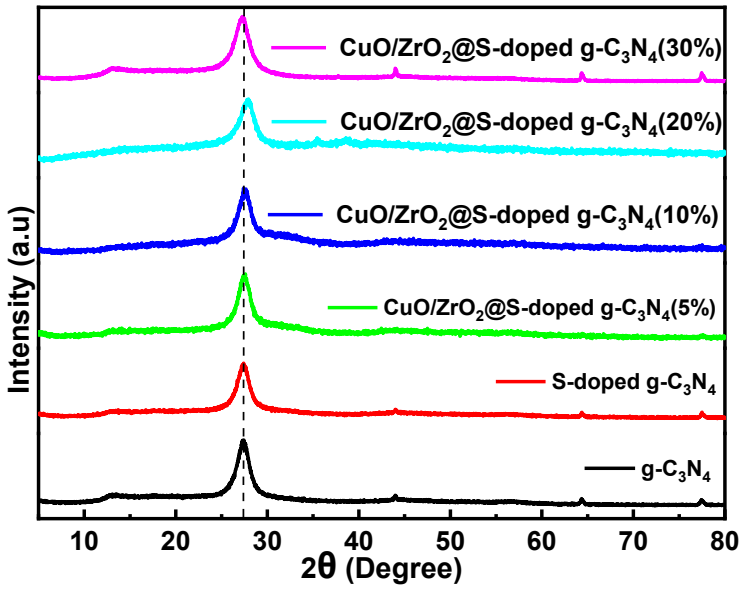

Figure 28.. XRD pattern of (a) g-C3N4, S-doped g-C3N4, CuO and ZrO2 NPs CuO/ZrO2@S-doped g-C_3N_4 (5,10,20 and 30%) NCs (b) CuO/ZrO_2@S-oped g-C_3N_4, CuO and ZrO_2

As depicted in Table 5 the crystal size of CuO/ZrO_2@S-doped g-C_3N_4 NCs is smaller (3.36 nm) than the g-C_3N_4 (5.52 nm), S-doped g-C_3N_4 (13.23 nm), CuO (30.09 nm) and ZrO_2 (13.10 nm). Clearly, this shows that by increasing the amounts of CuO and ZrO_2 NPs, the approximate crystalline size of the ternary NCs decreased from 13.23 nm to 3.36 nm. This shows the synergetic effect of the metallic NPs with the host S-doped g-C_3N_4 which is consistence with similar studies reported earlier (Hanif et al., 2022). When compared with the binary CuO@S-doped g-C_3N_4 and ZrO_2@S-doped g-C_3N_4 NCs, the ternary NCs CuO/ZrO_2@S-doped g-C_3N_4 NCs showed smaller approximate average crystalline size. In addition to this, the full width at half maximum (FWHM) of the ternary NC shows a broader FWHM than the binary NCs which is consistence with the smaller the approximate size of crystalline the broader the FWHM.

FT-IR analysis

The chemical structure of g-C_3N_4, S-doped g-C_3N_4, CuO@S-doped g-C_3N_4 (5, 10, 20 and 30%) NCs and pure CuO NPs catalysts were investigated by FT-IR technique (Figure 29). The intense band observed at 811 cm^{-1} represents a typical bending vibration mode of the s-triazine ring (the out-of-plane bending vibration characteristic of heptazine rings). The fingerprint region of 1200–1700 cm^{-1} is dominated by the C-N and C=N stretching vibrations of tri-s-triazine rings. The

prominent bands in the region of the wide absorption at band 3000–3500 cm^{-1} are attributed to the stretching modes of the terminal -NH groups and C-N of the terminal amino groups by incomplete condensation in g-C_3N_4. The FT-IR curve of CuO-NPs and the most significant peaks are found at 585 and 531 cm^{-1}, corresponding to the stretching vibrational mode of Cu–O bond (Ke et al., 2014).

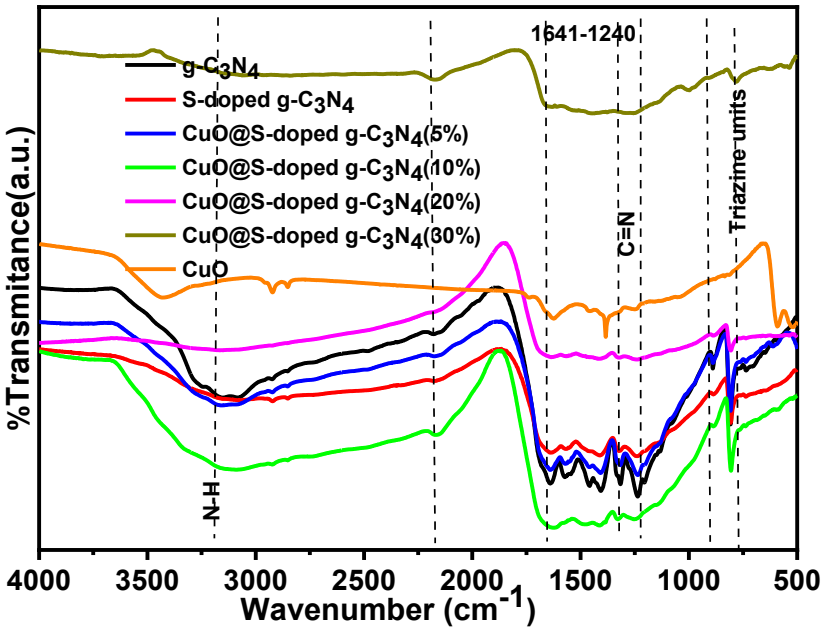

Figure 29.FTIR spectra of g-C_3N_4, S-doped g-C_3N_4, CuO@S-doped g-C_3N_4 NCs. and CuO NPs

The FT-IR spectrum of bulk g-C_3N_4, S-doped g-C_3N_4, ZrO_2@S-doped g-C_3N_4 (5, 10, 20 and 30%) NCs and ZrO_2 NPs is shown in Figure 30. As discussed in Figure 29, the chemical structure of g-C_3N_4 and S-doped g-C_3N_4 display a sharp absorption peak at 808 cm^{-1}, associated with s-triazine ring modes, and a strong absorption peak in the range of 1200–1700 cm^{-1}. The spectrum peak at 1645 cm^{-1} is attributable to C = N stretching vibration modes. Similarly, the peaks at 1241, 1319, and 1404 cm^{-1} are due to aromatic C–N stretching. This is due to the bending vibration of the *tri*-s-triazine C–N bond. The broad peak at 3040 to 3302 cm^{-1} matches a broad absorption caused by an aromatic ring defect (H. Guo et al., 2020; Mohammad, Khan, et al., 2020). The hydroxyl groups on the surface of hydrated oxide together with adsorbed water generate the broad absorption peak at 3373 cm^{-1}. The weak peak around 710 cm^{-1} appeared in the FT-IR spectrum of S-doped g-C_3N_4, demonstrating a successful integration of sulfur into the g-C_3N_4 structure by substituting N with S atoms forming C-S chemical bonds in the structure of g-C_3N_4. These features demonstrate the structural similarities of g-C_3N_4 and S-doped g-C_3N_4, although sulfur doping resulted in a small

change in the band position for the *tri*-substituted *tri-s*-triazine ring. This shows that S-doping does not change the skeleton structure of g-C_3N_4 (Bi et al., 2020).

The stretching vibration of Zr–O causes ZrO_2 to have absorption peaks at approximately 509 cm^{-1} and 750 cm^{-1}, as Figure 30 illustrates. The peak centered at 478 cm^{-1} mainly attributed to Zr-O vibrations (Kavil et al., 2019; S. Zhang et al., 2019). It can be seen that the FT-IR spectrum is consistent with the XRD results, indicating the formation of ZrO_2@S-doped g-C_3N_4 heterostructures.

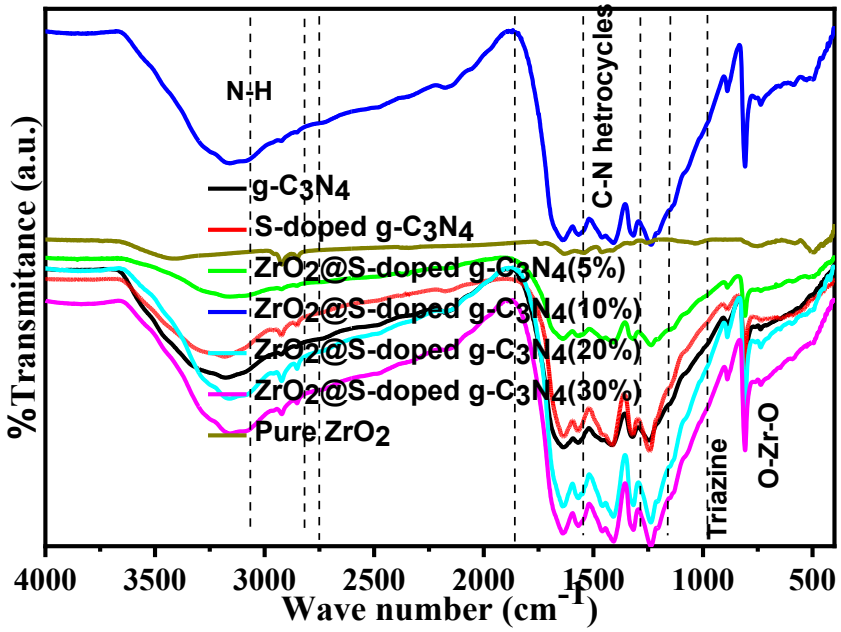

Figure 30.FTIR spectra of g-C_3N_4, S-doped g-C_3N_4, ZrO_2 @S-doped g-C_3N_4 NCs and ZrO_2 NPs

The FT-IR spectra of S-doped g-C_3N_4, CuO, ZrO_2, and CuO/ZrO_2@ S-doped g-C_3N_4 (5,10, 20 and 30 %) NCs are shown in Figure 31. The C=N stretching vibration modes are attributed for the absorption bands at 1572 and 1645 cm^{-1} in the spectra of S-doped g-C_3N_4, whereas the aromatic C–N stretching N stretching frequency of heptazine derivatives is belongs to some peaks at 1241, 1319, and 1404 cm^{-1} and 1649. Similar to the above results, the peak at 805 cm^{-1} is related to the s-triazine ring modes which was associated with the condensed CN heterocycles. The sulfur doping was revealed by the peak at 705 cm^{-1}, which was attributed to the C–S stretching vibration (S. Cao et al., 2015; J. Zhu et al., 2014). The peak at 537 cm^{-1} is the stretching vibrational band of the Cu–O bond in monoclinic CuO crystal (López & Gómez, 2012). For the pure ZrO_2, the absorption peaks at 509 cm^{-1} and 745 cm^{-1} are attributed to the stretching vibrations of Zr–O (Kavil et al.,

2019). It is important to notice that the FT-IR spectra of the pristine g-C_3N_4, S-doped g-C_3N_4 and CuO/ZrO_2@S-doped g-C_3N_4 (5,10,20 and 30%) NCs show a notable degree of similarity however, the shifting of the major peak in S-doped g-C_3N_4 in CuO/ZrO_2@S-doped g-C_3N_4 NCs positively indicating the incorporation of impurities which is in this case the CuO and ZrO_2. Generally, the hybrid structure and behavior in CuO/ZrO_2@S-doped g-C_3N_4 NCs validated by the FT-IR result also showed an agreement with the XRD results (Zarei, 2020a).

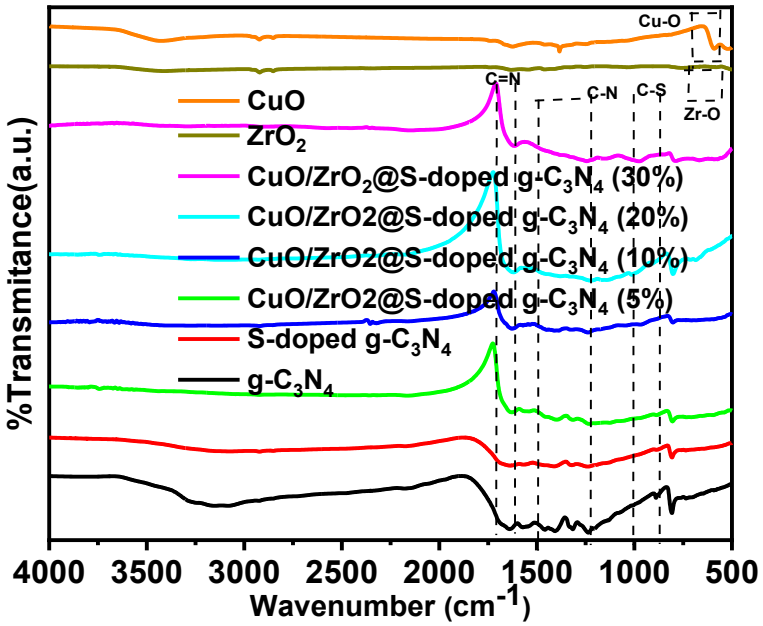

Figure 31.FT-IR spectra of g-C_3N_4, S-doped g-C_3N_4, CuO/ZrO_2@S-doped g-C_3N_4 NCs, CuO and ZrO_2 NPs.

4.1.3 Optical property analysis

UV -Vis/DRS analysis

UV−Visible/DRS spectral studies of the pristine g-C_3N_4, S-doped g-C_3N_4, binary CuO@*S*-doped g-C_3N_4 and ZrO_2@S-dopedg-C_3N_4 and ternary CuO/ZrO_2@S-dopedg-C_3N_4 NCs, CuO and ZrO_2 NPs were conducted at room temperature within the wavelength range 200-800 nm. Using the band-gap energy relationship (E_g =1240/λ_g) (López & Gómez, 2012) and Kubelka–Munk function (Bi et al., 2020; Ke et al., 2014) , the variations of all band gaps are displayed in Figures 32-34. The tangent and horizontal lines parallel to the abscissa are provided by the cut line method to determine the absorption wavelength threshold. The Kubelka-Munk equation was used to calculate

optical band gap energies (E_g) for the prepared samples. This equation (Equation 6) was used to determine diffused reflectance (R) (Mitra et al., 2016; Vu et al., 2018).

$$F(R) = \frac{(1-R)^2}{2R} \quad (6)$$

To determine E_g, the Kubelka-Munk function was used as represented by equation 1.

where λ is the wavelength of the light source, A is a constant that depends on the transition probability related to effective masses associated with the valence band and conduction bands, while n is the power index related to the optical absorption process, depending on transition characteristics in the semiconductor. The n value was chosen to be ½ for directly allowed transitions, h is Planck's constant, v is the frequency of light, E_g stands for the energy gap between the bottom of the conduction band (C_B) and the top of the valence band (V_B).

As shown in Figure 32a, all the synthesized materials exhibited a broad absorption band near 700 nm, showing an obvious red shift from 450 to 700 nm with the addition of S and CuO, as compared to g-C_3N_4. Weak absorption tails were observed due to structural defects in the heterostructured samples, which may improve the visible absorption of materials. This is probably attributed to structural defects formed in the samples treated at a given temperature showing the doping of impurities in g-C_3N_4.

As depicted in Figure 32(b-h), the direct band gap (E_g) values of the samples are between 2.66 eV for the g-C_3N_4 and 1.76 eV for CuO, while the band gap of the binary NCs was found to decrease as the amount of CuO increased (Table 5). This could be attributed to shifting to the visible range by doping-induced modification in the lattices and structure of the S-doped g-C_3N_4 layers shift that are observed for CuO@S-doped g-C_3N_4 (5,10,20 and 30%) NCs.

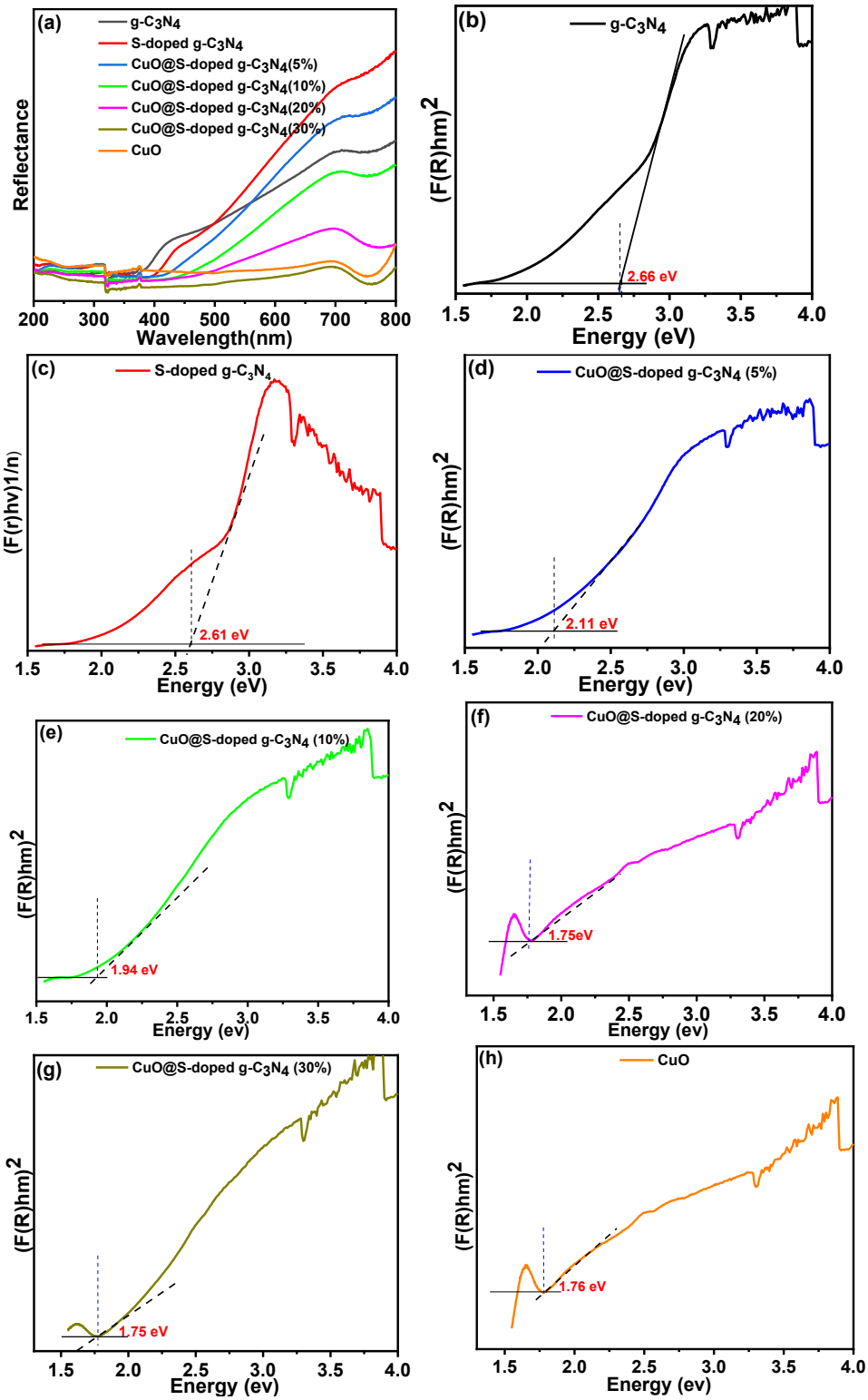

Figure 32. Diffuse reflectance absorption spectra (a) and optical band gap plot transformed by Kubelka–Munk function (b - h) of pristine g-C_3N_4, S-doped g-C_3N_4, CuO@S-doped g-C_3N_4 NCs and CuO.

The values were closer to the known values reported in the literature (Mitra et al., 2016; Vu et al., 2018). It was noticed that ZrO_2@S-doped g-C_3N_4 NC has better light absorption properties than pristine g-C_3N_4, S-doped g-C_3N_4 and ZrO_2. It is due to the synergistic effect between the interactions of ZrO_2 with S-doped g-C_3N_4. Due to the formation of chemical bonds between the S-doped g-C_3N_4 and ZrO_2, the E_g value was dramatically reduced., as depicted in Table 5. This provides more evidence that the ZrO_2 NPs improve the optical characteristics of S-doped g-C_3N_4 NC over a wider range of wavelengths.

For the ternary NCs, it was observed that with the loading of S, CuO and ZrO_2, as compared to bulk g-C_3N_4 there is an obviously a broad absorption band with a red shift in the hybrid NCs from 450 nm to near 700 nm (Figure 34). The photo-absorption edge of CuO/ZrO_2@S-doped g-C_3N_4 (5,10,20 and 30%) NCs shows a slight red-shift from ~450 nm a higher wavelength to ~700 nm. This is likely due to structural defects formed in the NCs treated at a given temperature which demonstrate how easily S, CuO, and ZrO_2 were incorporated into the g-C_3N_4.

From the UV-visible/DRS spectra of the NCs, the corresponding band gap energy (E_g) was determined using the Kubelka–Munk (K-M) equation 1, n = ½) value. From the corresponding K–M plots (Figure 34), the obvious change in E_g was observed with an increasing percentage of CuO and ZrO_2 NPs, resulting in further narrowing of the band gap from 2.66 eV of g-C_3N_4 to 1.85 eV of CuO/ZrO_2@S-doped g-C_3N_4 NCs (30%). This could be attributed to the shifting to the visible range by the doping-induced modification in the lattices and structure of the S-doped g-C_3N_4 layers shift that can be observed for Cu/ZrO_2@S doped g-C_3N_4 NCs (Mohammad, Ehtisham, et al., 2020). This shows that it is possible to suitably tune the band gap with the incorporation of CuO and ZrO_2 NPs in the S-doped g-C_3N_4 host. Compared to the pristine and binary NCs, the ternary NCs showed a slight bandgap tuning (redshift/to the higher wavelength) for the CuO/ZrO_2@S-doped g-C_3N_4 NCs.

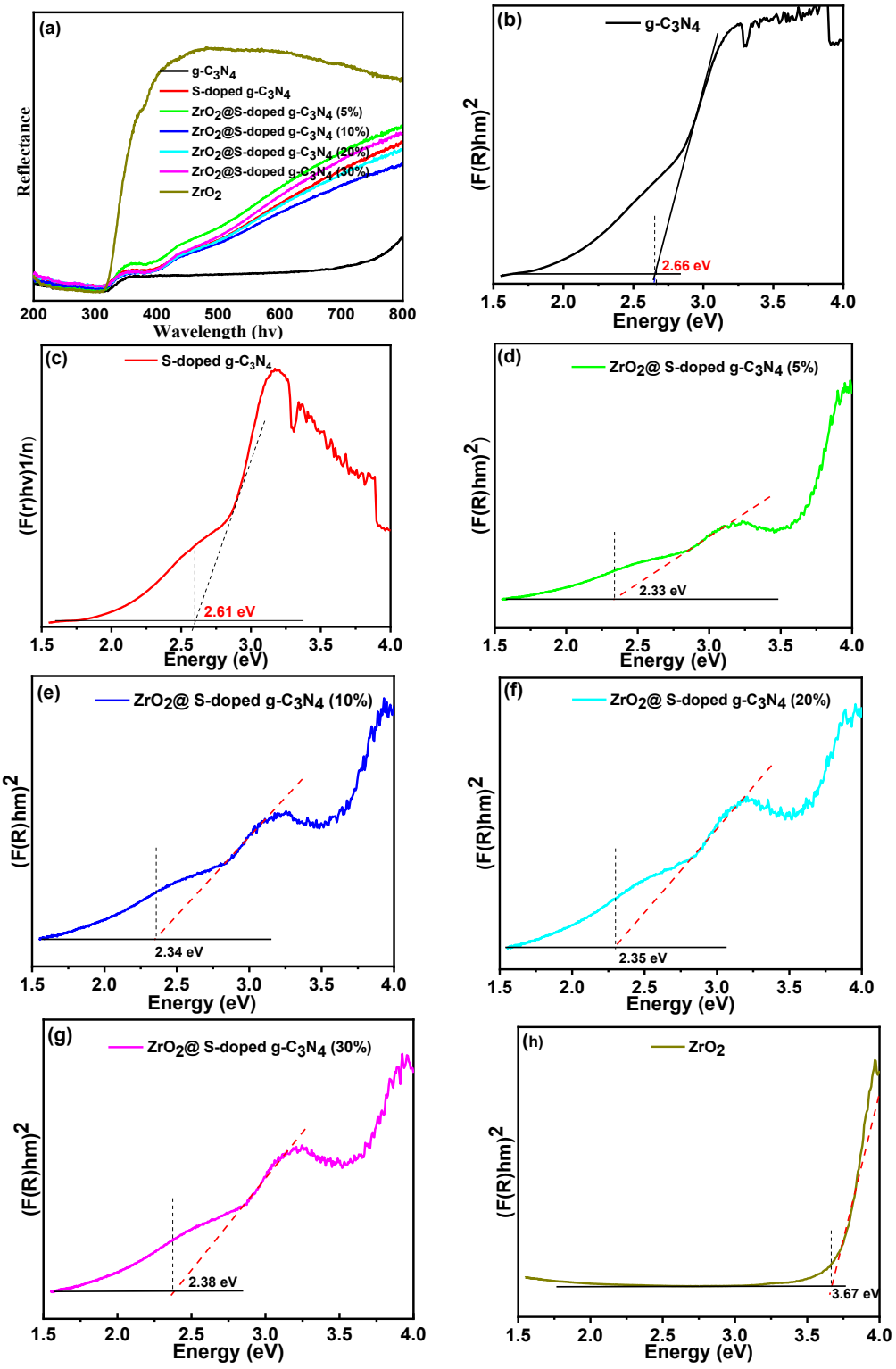

Figure 33. Figure Diffuse reflectance absorption spectra (a) and optical band gap plot transformed by Kubelka–Munk function (b-h) of pristine g-C_3N_4, S-doped g-C_3N_4, ZrO_2@S doped g-C_3N_4 NCs and pure ZrO_2

As shown in Table 5, the calculated E_g values of the pristine g-C_3N_4, S-doped g-C_3N_4, CuO, ZrO_2 NPs, and ternary CuO/ZrO_2@ S-doped g-C_3N_4 (30%) were 2.66, 2.61, 1.76, 3.67 and 1.85eV, respectively. Interestingly, except for CuO NPs, after the construction of the NC, the E_g value was noticeably lower than that of the constituents of binary and ternary NCs. This could be due to several reasons one is the CuO/ZrO_2@ S-doped g-C_3N_4 heterojunctions can be ascribed to the "shading effect" since S-doped g-C_3N_4 were wrapped by both CuO and ZrO_2 NPs as can be seen from HR-SEM and TEM images (Alaghmandfard & Ghandi, 2022; Zarei, 2020a).

In general, compared to the binary, CuO@S-doped g-C_3N_4 NCs (30%) with a band gap, of 1.75 eV and ZrO_2@S-doped g-C_3N_4 (30%), with a band gap of 2.35 eV, the ternary CuO/ZrO_2@S-doped g-C_3N_4 (30%) NC show remarkable band gap change with band gap value of 1.85 eV. Clearly, this shows the synergistic effects of CuO and ZrO_2 with the host S-doped g-C_3N_4 (E_g=2.61 eV) attributed to the quantum confinement effects. CuO and ZrO_2 integration on S-doped g-C_3N_4 results in the absorption edge of the ternary NC CuO/ZrO_2@S-doped g-C_3N_4 redshift, showing the higher visible light harvesting contribution (Alebachew et al., 2022; M. Li et al., 2016). This shows that it is possible to suitably tune the band gap with the incorporation of ex-situ generated CuO and ZrO_2 NPs in the S-doped g-C_3N_4 host.

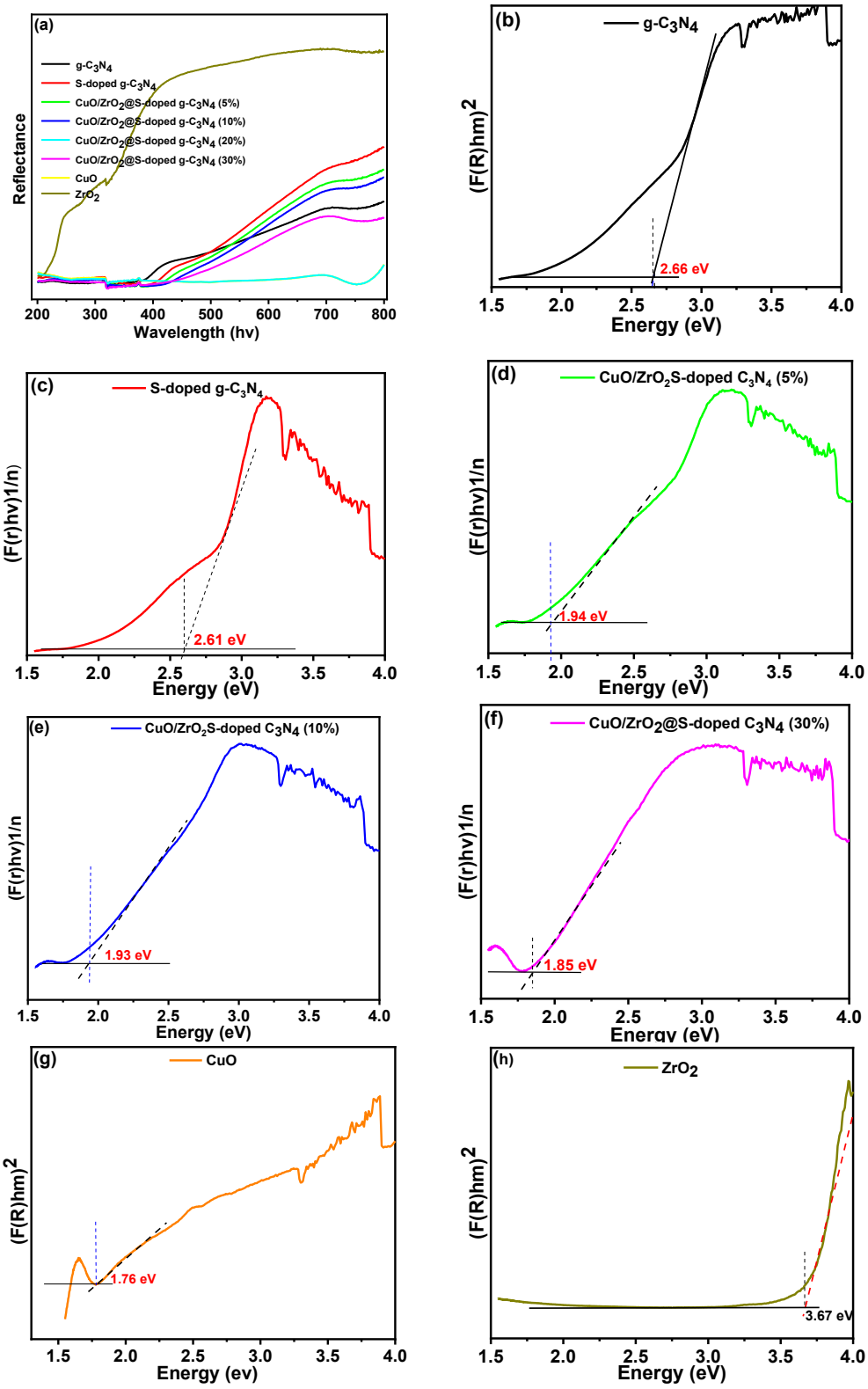

Figure 34. Diffuse reflectance absorption spectra (a) and optical band gap plot transformed by Kubelka–Munk function (b - h) of pristine g-C_3N_4, S-doped g-C_3N_4 CuO/ZrO_2@S doped g-C_3N_4 NCs and CuO and ZrO_2.

PL analysis

By observing the buildup of electrons on the conduction band, PL is an effective technique for figuring out the rate at which photogenerated electrons and holes recombine in catalysts. As a response to light, it can produce fluorescence by combining photogenerated electrons with holes. It is generally accepted that the photogenerated carriers separate more quickly the lower the fluorescence intensity.

To investigate the separation and recombination rate of photogenerated charge carriers, PL spectra of pristine g-C_3N_4, S-doped g-C_3N_4, CuO@ S-doped g-C_3N_4 (5,10,20,30%) NCs and CuO NPs at 380 nm excitation were examined. As depicted in Figure 35, the PL spectrum of the pristine g-C_3N_4 shows a major characteristic peak at 423.67 nm. On the other hand, in the S-doped g-C_3N_4 higher intensity was observed at 406.13. This indicated that it is easy to generate the recombination of electrons/hole pairs over S-doped g-C_3N_4 semiconductor. However, in the binary CuO@S-doped g-C_3N_4 NCs, the PL intensity was decreased. This suggests that CuO inhibits the catalysts' photogenerated carrier recombination rate, which helps to improve the catalysts' optical characteristics. It is noteworthy to note that the binary CuO@S-doped g-C_3N_4 (5%) exhibits a greater PL intensity at 420 nm compared to CuO@S-doped g-C_3N_4 (10.20 and 30%), suggesting that the charge carriers have a short lifespan due to the fast electron/hole recombination rate. The intermediate intensity peak was observed for CuO@S-doped g-C_3N_4 (10, 20 and 30 %) NCs between S-doped g-C_3N_4 and g-C_3N_4 sheets suggesting intermediate electron/hole recombination due to surface modification. This dramatic change in PL intensity magnifies the synergistic effect among g-C_3N_4, S-doped g-C_3N_4 and CuO which results in the influence of the CuO@S-doped g-C_3N_4 hetero-junction on separation efficiency of electron–hole pairs charge transfer at the interfaces of S-doped g-C_3N_4 and CuO. The lower recombination rate of photogenerated electron and hole pairs of CuO@S-doped g-C_3N_4 (10%) which could be caused by structural defects resulted in fluorescence quenching (Zarei, 2020a).

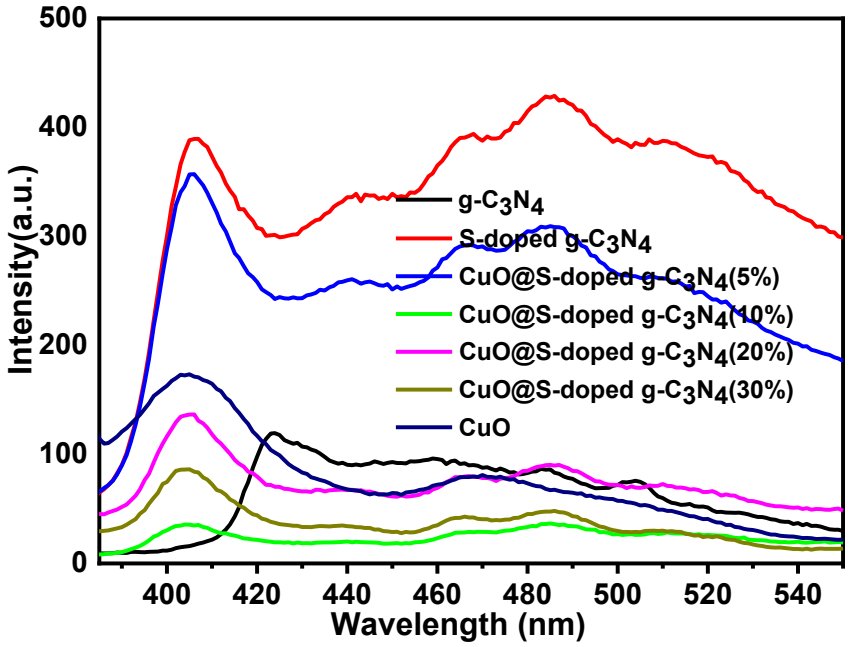

Figure 35.PL of pristine g-C_3N_4, S-doped g-C_3N_4, CuO@S-doped g-C_3N_4 NCs and CuO NPs.

The photoluminescence spectra of pristine g-C_3N_4, S-doped g-C_3N_4, ZrO_2@S-doped g-C_3N_4 (5, 10, 20 and 30%) NCs and ZrO_2 NP is shown in Figure 36. The effect of g-C_3N_4, S-doped g-C_3N_4 and ZrO_2 on ZrO_2@S-doped g-C_3N_4 NCs on the separation efficiency of electron-hole pairs was investigated. As the energy of the light released is roughly equal to the band gap energy, at approximately 405 nm, ZrO_2 exhibits significant emission associated with its band gap transition. When compared to the ZrO_2 NPs, the intensity of fluorescence emission from ZrO_2@S-doped g-C_3N_4 NCs was observed to be dramatically reduced. Thus, when ZrO_2 NPs were added to S-doped g-C_3N_4, the degree of fluorescence quenching showed a significant enhancement. As a result, it was shown that the electron-hole recombination rate increases initially, then declines among the ZrO_2@S-doped g-C_3N_4 (5, 10, 20, 30%) NCs, while the ZrO_2@S-doped g-C_3N_4 (5%) NC recombination rate being the lowest and the ZrO_2@S-doped g-C_3N_4 (30%) NC being the largest. On the other hand, ZrO_2@S-doped g-C_3N_4 (10 and 20%) NCs have a band similar to the quenched PL emission peak at approximately 486 nm. In contrast to g-C_3N_4 and ZrO_2, this reveals a suppressed recombination of the photogenerated charge carriers produced by the doping with S. This implies that the synergistic effect between S-doped g-C_3N_4 and ZrO_2 plays a big role in the optimum electron-hole recombination rate of the binary ZrO_2@S doped g-C_3N_4 NCs. The optimum intensity of ZrO_2@S-doped g-C_3N_4 NCs suggests a successful introduction of an impurity phase (S and ZrO_2) in ZrO_2@S-doped g-C_3N_4 compared to the lower g-C_3N_4 and higher ZrO_2

recombination rate of the photogenerated electrons and hole pairs, respectively(Ke et al., 2014; Y. Li et al., 2018; Zarei, 2020a).

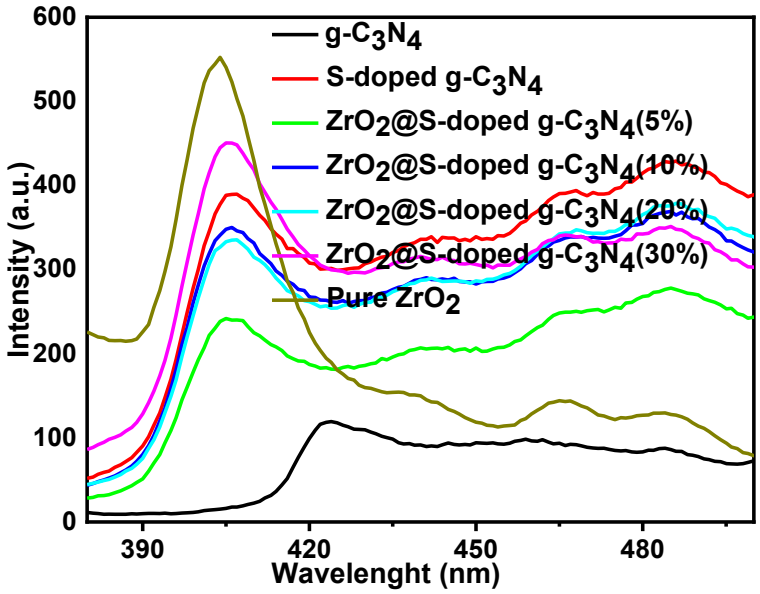

Figure 36..PL of pristine g-C_3N_4, S-doped g-C_3N_4, ZrO_2@S-doped g-C_3N_4 NCs and ZrO_2 NPs

The PL properties of pristine g-C3N4, S-doped g-C_3N_4, CuO, and ZrO_2 are displayed in Figure 37 a, whereas the PL properties of CuO/ZrO_2@S-doped g-C_3N_4 (10, 20 and 30%) NCs are displayed in Figure 37 b. It is clearly shown that the PL intensity of the samples in Figure 37 a is higher than the ternary NCs in Figure 37 b. This shows that there is an optimization of the electron/hole recombination rate for ternary NCs. It is worth to be observed that CuO/ZrO_2@S-doped g-C_3N_4 (5%) shows a higher PL intensity than CuO/ZrO_2@S-doped g-C_3N_4 (10,20and 30%) indicating the short-lived fate of charge carriers owning to the rapid recombination. On the other hand, the PL intensity slows down for CuO/ZrO_2@S-doped g-C_3N_4 (20%) NC, which may be attributed to surface defects and fluorescence quenching (Zarei, 2020a). On the other hand, the enhanced recombination center should be responsible for the intense PL intensity observed in CuO/ZrO_2@S-doped g-C_3N_4 (30% and 20%) NCs when ZrO_2 and CuO percentage increase. Based on the above analysis, it can be concluded that as-synthesized ternary CuO/ZrO_2@S-doped g-C_3N_4 NCs possess both shifting to the higher wavelength and better ability to separate photo-generated carriers than binary CuO@S-doped g-C_3N_4 and ZrO_2@S-doped g-C_3N_4 NCs which is beneficial for the electrolytic and photocatalytic activities. It is commonly understood that the lower the fluorescence intensity, the better the photogenerated carriers' separation (Ke et al., 2014; Y. Li et al., 2018).

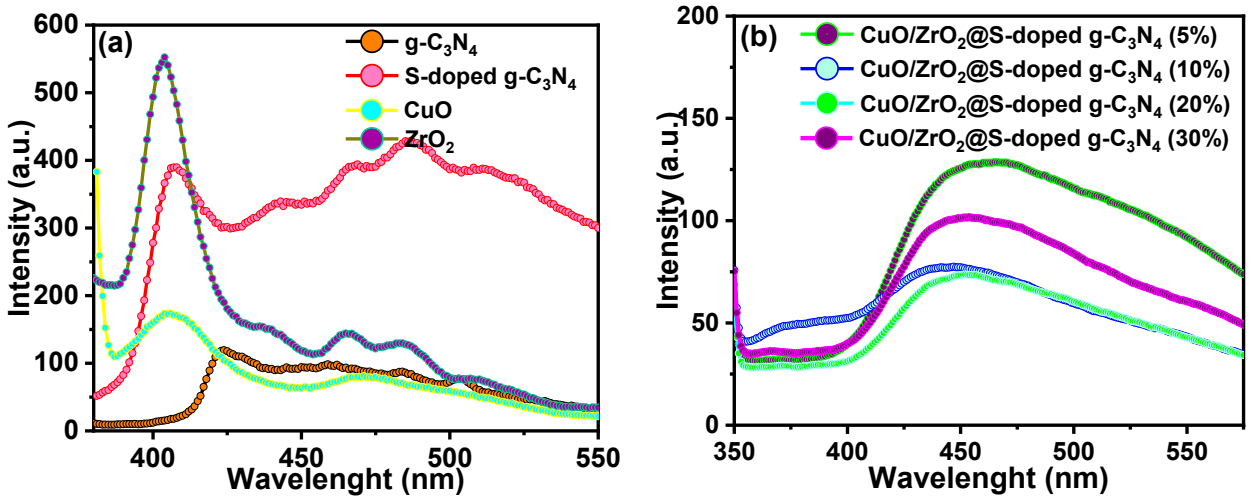

Figure 37. PL of (a) pristine g-C_3N_4, S-doped g-C_3N_4, CuO and ZrO_2. NCs and (b) CuO/ZrO_2@S-doped g-C_3N_4 NCs

4.1.4 Surface area analysis

The surface features of the synthesized samples were evaluated by the BET and Barrett–Joyner–Halenda (BJH) methods, as presented in Figures 38-40 and Table 5. Nitrogen adsorption isotherms of pristine g-C_3N_4, S-doped g-C_3N_4, CuO@S-doped g-C_3N_4, ZrO_2@S-doped g-C_3N_4 and ternary CuO@ZrO_2@S-doped g-C_3N_4, CuO and ZrO_2 samples were measured to gain information about the specific surface area.

The specific surface area and pore features of pristine g-C_3N_4 S-doped g-C_3N_4, binary CuO@S-doped g-C_3N_4 for (5, 10,20, and 30% of CuO) NCs and CuO NPs is presented in Figure 38. The isotherms are typical of Type IV behavior indicating the presence of the mesoporous and some macroporous structures formed by the aggregation of the constituents in the samples. As shown in the Figure 38 a, greater adsorption capacity was obtained in the high-pressure range ($P/P° > 0.2$) for the pristine g-C_3N_4 ($P/P° > 0.2$). This suggests that the isotherms are typical of Type IV formed by the aggregation of constituents in the samples, which consists of some macroporous and mesopores structures. Except for pristine g-C_3N_4, the surface-specific area of the binary NCs was found to be lower than 81.6 m^2g^{-1} but higher than that of the S-doped g-C_3N_4 (24.4 m^2g^{-1}). The enhanced surface area for S-doped g-C_3N_4 is attributed to its special morphology and the disappearance of the small pores in g-C_3N_4 after doping by S. But was gradually boosted by the appearance of additional small pores when CuO was confined within the S-doped g-C_3N_4 (Duan, 2018). This is confirmed by the pore size distribution and textural properties as shown in Table 5

and Figure 38b. Similarly, the BJH pore size and volume of CuO@S-doped g-C_3N_4 NCs were also increased, implying cavities or tunnels developing in CuO@S-doped g-C_3N_4 NCs due to aggregation of CuO NPs (Y. Wang, Zhang, et al., 2018).

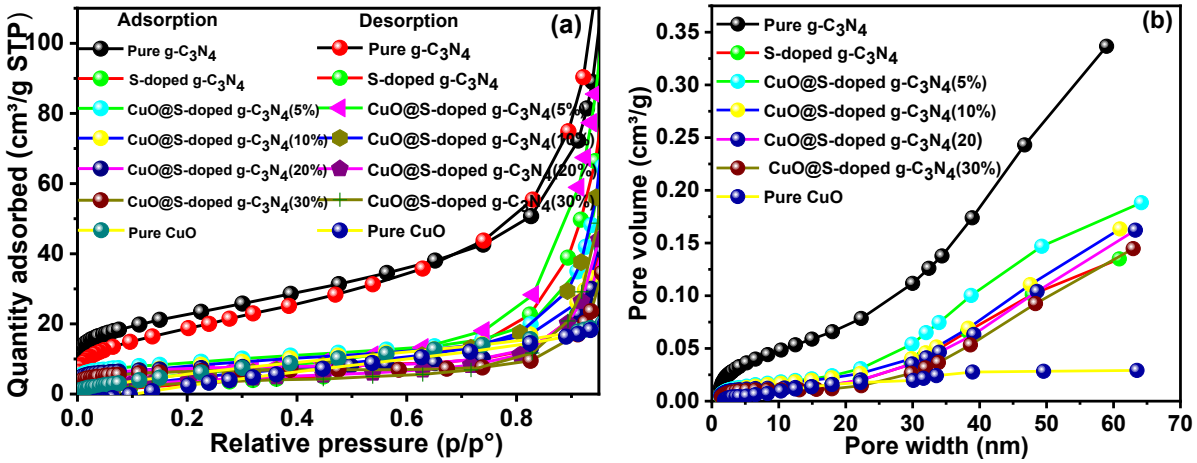

Figure 38. (a) N2 adsorption-desorption BET isotherms and (b) pore size distribution curves of pristine g-C_3N_4, S-doped g-C_3N_4, CuO@S-doped g-C_3N_4 NCs, and CuO NPs, measured at 77 K.

Figure 39a shows the nitrogen adsorption-desorption isotherm of binary ZrO_2@S-doped g-C_3N_4 (5,10,20 and 30%) and ZrO_2 samples. For comparison, the BET isotherms of g-C_3N_4, and S-doped g-C_3N_4 were presented. In this study, in addition to a typical type IV curve most of the N_2 adsorption was found between 0.5 and 0.9, indicating the presence of the mesoporous and macro porous structures formed by the aggregation of the constituents in the ZrO_2@S-doped g-C_3N_4 samples (Kavil et al., 2019). Thus, the S_{BET} of g-C_3N_4 increases from 24.4 to 27 m^2 g^{-1} as the amount of ZrO_2 increases, arising from the high crystallinity of monoclinic ZrO_2 NPs. This is confirmed by the pore size distribution, as shown in Table 5 and Figure 39b. In a similar manner, ZrO_2@S-doped g-C_3N_4 NCs showed increased BJH pore size and volume, suggesting the development of cavities or tunnels inside the material. While the significantly lower pore size of ZrO_2@S-doped g-C_3N_4 (5, 10 and 30%) results from carcass construction, the higher pore size of ZrO_2@S-doped g-C_3N_4 (20%) NC arises from intra-crystalline pores and aggregation of ZrO_2 NPs (Hanif et al., 2022).

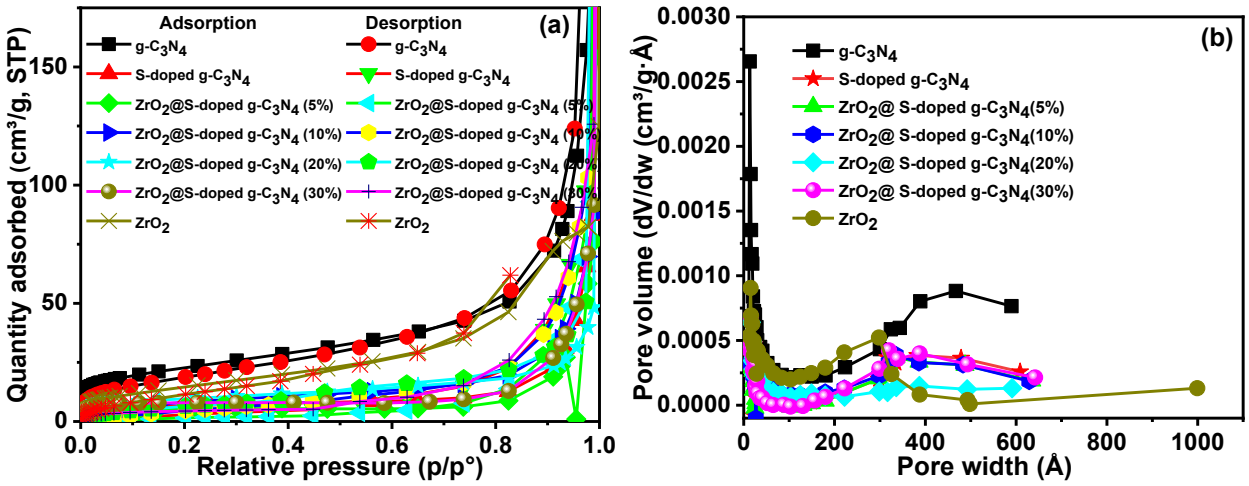

Figure 39. (a) N_2 adsorption-desorption isotherms and (b) pore size distributions of g-C_3N_4, S-doped g-C_3N_4, ZrO_2@S-doped g-C_3N_4 NCs and ZrO_2 NPs.

For ternary NCs, the specific surface area increases when the amount of CuO and ZrO_2 increases (Figure 40 a and b). Ternary samples' sorption isotherms show type IV isotherms with hysteresis loops, which often correlate to the materials' mesoporous and macroporous characteristics. The use of S, CuO and ZrO_2 NPs has resulted increase in the surface area and pore volume with a profound decrease in pore diameter as compared to g-C_3N_4. Thus, when the amount of CuO and ZrO_2 is 30%, the surface area increases to 46.5 m^2g^{-1} as compared to 28.2 m^2 g^{-1} in CuO/ZrO_2@S-doped g-C_3N_4 (5%). As shown in Table 5, the CuO/ZrO_2@S-doped g-C_3N_4 NCs' surface area showed an increase in specific surface area with a decrease in crystallite size and profound change in pore volume (Duan, 2018; Zarei, 2020a).

Generally, the pore size distribution of the binary CuO@S-doped g-C_3N_4 (30%), ZrO_2@S-doped g-C_3N_4 (20%) and ternary CuO/ZrO_2@S-doped g-C_3N_4 (30%) NCs samples shows that most of the pores fall into a size range of 2 to 50 nm with adsorption isotherms of type IV and type H3 hysteresis loops. The increase in surface area facilitates surface adsorption and creates a greater number of active sites.

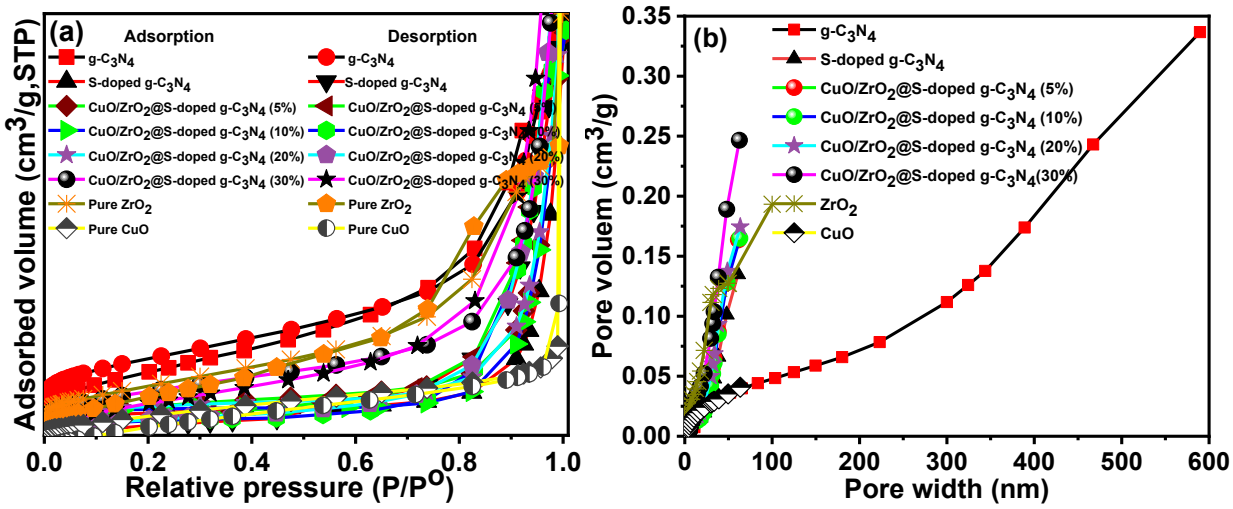

Figure 40.(a)N2 adsorption-desorption isotherms and (b) pore size distributions of pristine g-C_3N_4, S-doped g-C_3N_4, CuO/ZrO_2@S-doped g-C_3N_4 NCs and CuO and ZrO_2 NPs.

4.1.5 Morphology analysis

HR-SEM/EDS analysis

This method involved employing the HR-SEM/EDS methodology of the magnified images to investigate several physical and chemical properties such as size, shape, elemental composition, and crystallography. As shown in Figure 41-45, the HR-SEM/EDS images of pristine g-C_3N_4, S-doped g-C_3N_4, and CuO@S-doped g-C_3N_4 ZrO_2@S-doped g-C_3N_4 and CuO /ZrO_2@S-doped g-C_3N_4 revealed aggregated particles with irregular shapes and varying packing densities. The HR-SEM picture of the pristine g-C_3N_4 at various magnifications displays the highest porosity with a specified surface area value (Table 5), an amorphous form, and desultorily assembled particles, which is consistent with findings in other studies (Miller et al., 2017). The CuO@S-doped g-C_3N_4 NCs exhibits unique features of morphological microspheres (Figure 41), a thin straight bar, i.e. rode-shaped S, flower-shaped microsphere S-doped g-C_3N_4 (Figure 41 c and d), sphere and cubic-shaped CuO NPs. This type of hybrid heterostructured composite will increase the accumulation of electrons on the conduction band to maintain electron flow and lower the rate of electron-hole recombination, which will increase the material's photocatalytic efficiency. These findings support the fact that CuO@S-doped g-C_3N_4 NCs were successfully formed (Tan et al., 2015).

Table 5. Crystallinity, optical and S_{BET} properties of synthesized intrinsic, binary and ternary NCs

Samples	2θ	FWHM (radians)	D (nm)	E_g (eV)	S_{BET} (m^2g^{-1})	Pore Volume ($cm^3\ g^{-1}$) BJH Adsorption	Pore Volume ($cm^3\ g^{-1}$) BJH Desorption	Pore Size (nm) BJH Adsorption	Pore Size (nm) BJH Desorption
Pristine g-C_3N_4	27.25	1.55	5.52	2.66	81.6	0.33	0.75	12.7	35.9
S-doped g-C_3N_4	23.98	0.64	13.23	2.61	24.4	0.13	0.24	15.1	23.5
CuO@S-doped g-C_3N_4 (5%)	33.86	0.94	9.28	2.11	30.7	0.19	0.23	15.9	21.2
CuO@S-doped g-C_3N_4 (10%)	31.91	1.27	6.80	1.94	28.6	0.16	0.22	14.4	27.0
CuO@S-doped g-C_3N_4 (20%)	33.85	0.93	9.32	1.75	26.6	0.16	0.26	16.6	45.5
CuO@S-doped g-C_3N_4 (30%)	26.51	1.55	6.50	1.75	22.9	0.14	0.26	15.9	41.6
ZrO_2@S-doped g-C_3N_4 (5%)	26.53	1.55	5.50	2.33	21.3	0.12	12.8	22.3	22.3
ZrO_2@S-doped g-C_3N_4 (10%)	27.26	1.29	6.59	2.34	28.7	0.13	12.4	17.2	17.2
ZrO_2@S-doped g-C_3N_4 (20%)	35.97	1.25	6.99	2.35	35.6	0.07	5.4	9.0	9.0
ZrO_2@S-doped g-C_3N_4 (30%)	35.75	1.28	6.83	2.38	27.7	0.14	12.5	19.1	19.1
CuO/ZrO_2@S-doped g-C_3N_4 (5%)	27.55	1.23	13.23	1.94	28.2	0.16	0.19	15.0	21.1
CuO/ZrO_2@S-doped g-C_3N_4 (10%)	27.64	0.89	17.53	1.93	26.8	0.16	0.19	15.6	22.4
CuO/ZrO_2@S-doped g-C_3N_4 (20%)	28.00	0.85	5.80	1.90	30.2	0.17	0.25	14.9	27.6
CuO/ZrO_2@S-doped g-C_3N_4 (30%)	27.91	1.34	3.36	1.85	46.5	0.24	0.29	14.8	19.8
Pure CuO	40.98	0.29	30.09	1.76	28.2	0.04	0.06	4.1	10.0
Pure ZrO_2	46.94	0.69	13.10	3.67	56.3	0.19	0.13	10.0	7.4

D(nm)=average crystallite size

The distribution of the elements in the CuO@S-doped g-C_3N NC was further inspected using elemental mapping images of CuO@S-doped g-C_3N_4 from HR-SEM/EDS (Figure 42). The outcome confirmed a considerable amount of C, N, S, Cu and O elements homogeneously distributed in the CuO@S-doped g-C_3N_4 NC and only a very small amount of impurity on the upper surface of the CuO@S-doped g-C_3N_4 NC. In CuO@S-doped g-C_3N_4 NCs, cubic CuO NPs aggregation on the surface of S-doped g-C_3N_4 is visible. On the surface of the g-C_3N_4, on the other hand, S was sparsely scattered.

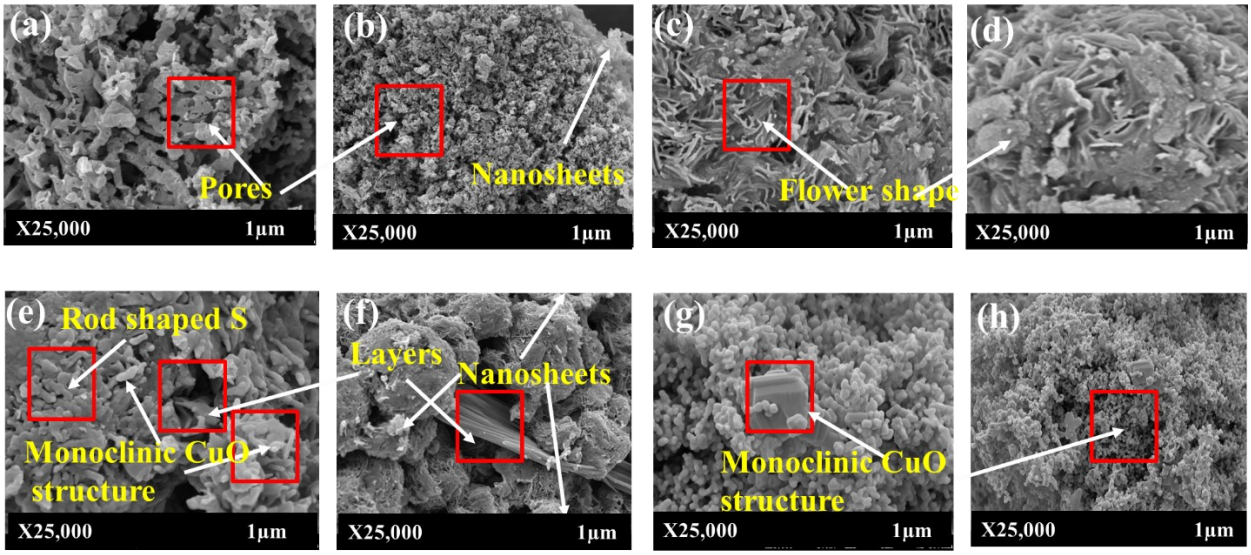

Figure 41.HR-SEM image of (a, b) pristine g-C_3N_4, (c, d), S-doped g-C_3N_4, (e, f), and (d, f) CuO@S-doped g-C_3N_4 NCs (g, h) CuO NPs with different magnifications.

From the HR-SEM/EDS analyses (Figure 42), it was observed that the C/N ratio varies from 0.75 to 0.83 in g-C_3N_4 and S-doped g-C_3N_4, giving average molecular formulas, $C_{3.5}$ N_4 and $C_{3.7}N_{3.8}$, respectively. The C/N ratio in the CuO@S-doped g-C_3N_4 NCs is 0.82, which is higher than the theoretical values of 0.75 and reported C/N = 0.67, corresponding to the composition of melon annealing at 600 ºC (Mohammad, Khan, et al., 2020). From the HR-SEM images, quantitative analysis of the CuO@S-doped g-C_3N_4 NCs (CuO = 29%) reveals the atomic weight percentages of N, C, S, Cu and O elements as 35.7, 29.3, 0.1, 17.6 and 11.4 wt.%, respectively. From the HR-SEM images, quantitative analysis of the CuO@S-doped g-C_3N_4 NCs (CuO = 29%) reveals the atomic weight percentages of N, C, S, Cu and O elements as 35.7, 29.3, 0.1, 17.6 and 11.4 wt.%, respectively. These values are close to the theoretical percentage of CuO (30%). This indicated that Cu and O elements were distributed in the entire host of the S-doped g-C_3N_4 NC. Where Cu

and O were present in the form of CuO, these analyses revealed CuO to be integrated firmly with S-doped g-C_3N_4 NCs, creating hybrid structures.

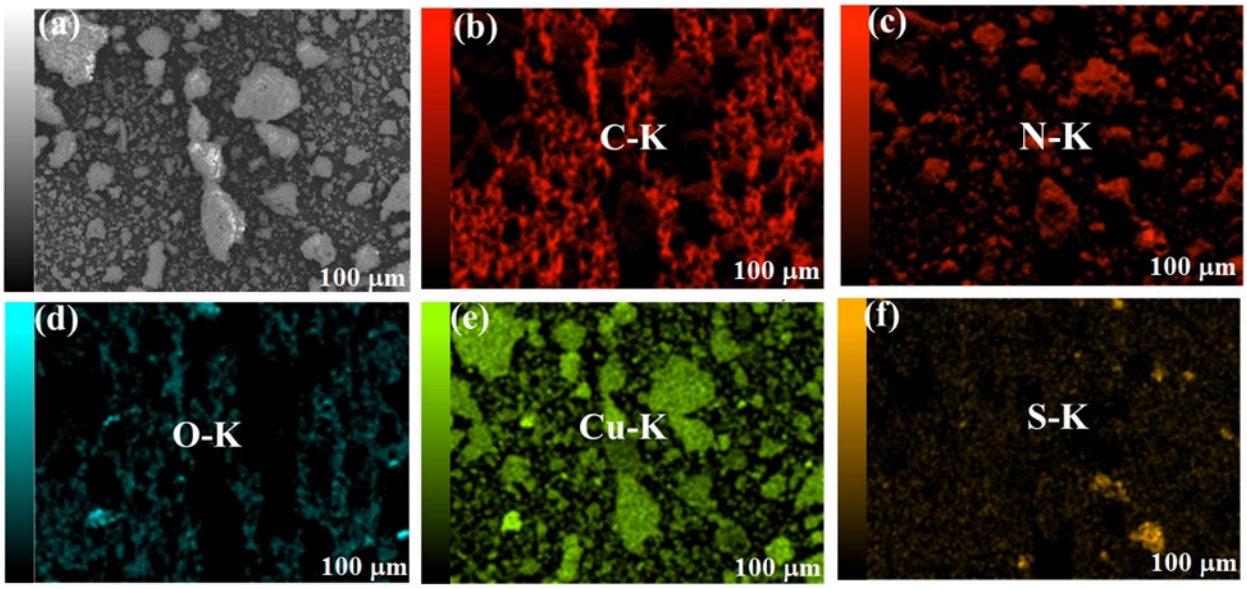

Figure 42.HRSEM/EDS mapping for different elements and in the CuO@S-doped g-C_3N_4 NCs

Similar to CuO@S-doped g-C_3N_4 NCs, the magnified images of the size, shape, elemental composition, crystallography, and other physical and chemical features of ZrO_2@S-doped g-C_3N_4 NCs were examined through HR-SEM. As shown in Figures 43 e and f, the HR-SEM studies of ZrO_2@S-doped g-C_3N_4 NCs are agglomerated with irregular shapes and varied packing densities. The surface morphology of monoclinic-shaped ZrO_2 NPs comprises numerous non-uniform NPs with many pores and voids (Figure 43 g and h). The S-doped g-C_3N_4 and ZrO_2 are very different from one another in terms of their morphology, ensuring ease of detection by scanning electron microscopy. The white irregular mass seen in Figures 43 e and f contains ZrO_2 and is coated with flaky S-doped g-C_3N_4, demonstrating a better integration.

The HR-SEM/EDS mappings (Figure 44(a-f)) revealed additional evidence for the presence of N, C, S, Zr and O elements in the ZrO_2@S-doped g-C_3N_4 NC. The composite containing ZrO_2@S-doped g-C_3N_4 displays an agglomerated structure with irregularities and small particles on the surface, which are attributed to the oxide phases generated by the calcination of $ZrOCl_2.8H_2O$. However, from the HR-SEM/SED image (Figure 44), quantitative analysis of the ZrO_2@S-doped g-C_3N_4 (ZrO_2 = 4%) reveals the atomic weight percentages of N, C, S, Zr and O elements as 59.4 36.6, 0.1 1.3 and 3.3, wt.%, respectively. These values are less than the theoretical percentage of

ZrO_2 (20%). This indicated that small amounts of Zr and O elements were distributed in the entire host of the S-doped g-C_3N_4 NC. This can be the result of some ZrO_2 NPs being lost during the synthesis process. Hence, some atoms of Zr and O were present in the form of ZrO_2, these analyses revealed ZrO_2 to be integrated firmly with S-doped g-C_3N_4 NCs, creating hybrid structures. Combined with XRD and FT-IR analysis, these findings demonstrate the successful incorporation of ZrO_2 into the S-doped g-C_3N_4 host lattice.

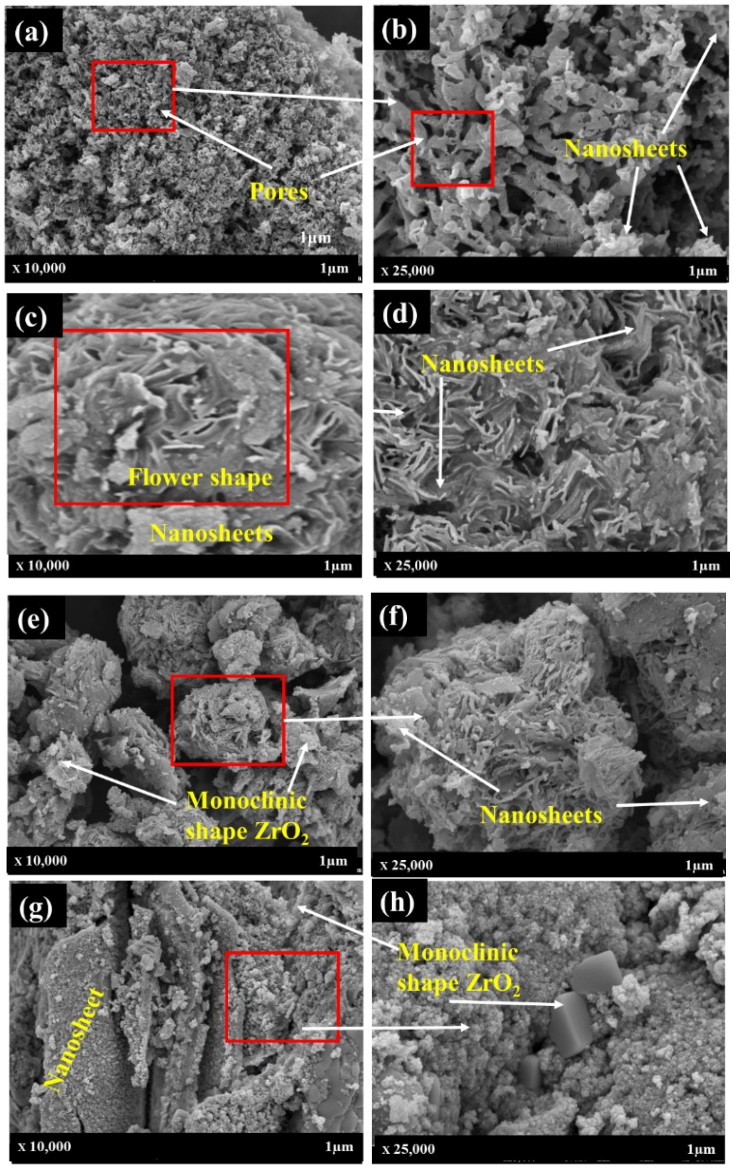

Figure 43.HR-SEM images of (a, b) pristine g-C_3N_4, (c, d) S-doped g-C_3N_4 (e, f), ZrO_2@S-doped g-C_3N_4 NCs, and (g, h) ZrO_2 NPs with different magnifications.

The surface morphology of the pristine g-C_3N_4, S-doped g-C_3N_4, CuO/ZrO_2@ S-doped g-C_3N_4 NCs, CuO and ZrO_2 NPs is depicted in Figure 45(a-e). The HR-SEM study confirms the presence of pores and nanosheets in g-C_3N_4, S-doped g-C_3N_4 and CuO/ZrO_2@ S-doped g-C_3N_4 NCs. Surprisingly, the HR-SEM/SED study (Figure 46 a-g) further confirmed the presence of N, C, S, O, Cu and Zr elements in the CuO/ZrO_2@ S-doped g-C_3N_4 NCs proving the probable existence of CuO and ZrO_2 of NPs which were difficult to discriminate in the XRD study.

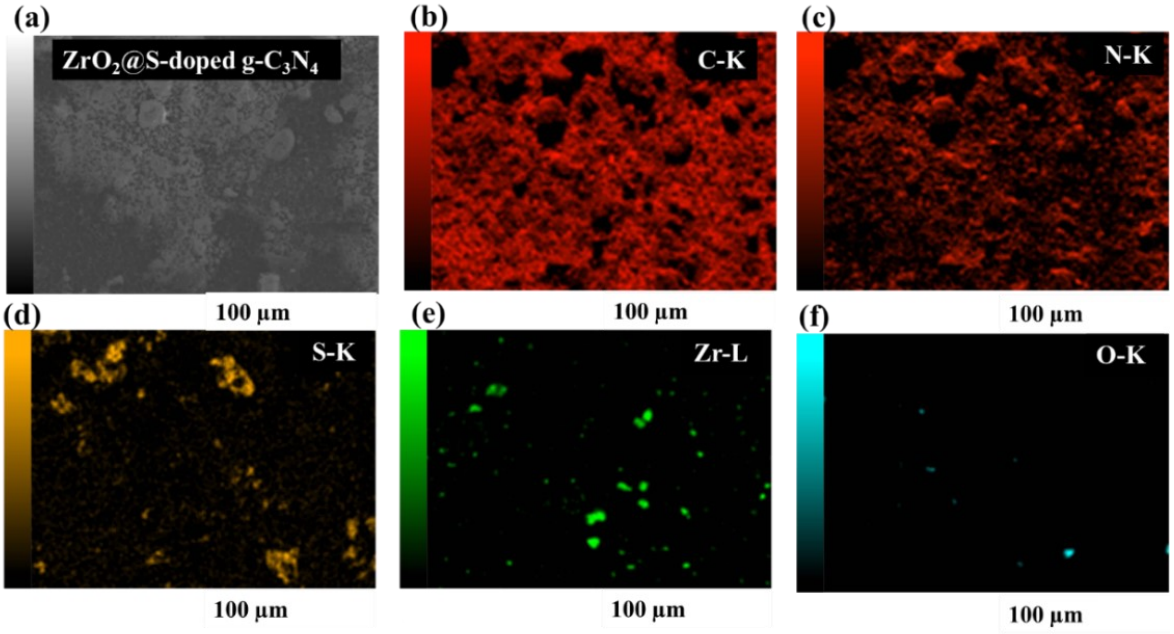

Figure 44.HR-SEM/EDS mapping (a) for ZrO_2@S-doped g-C_3N_4 NC and (b-f) the constituent elements of the NC.

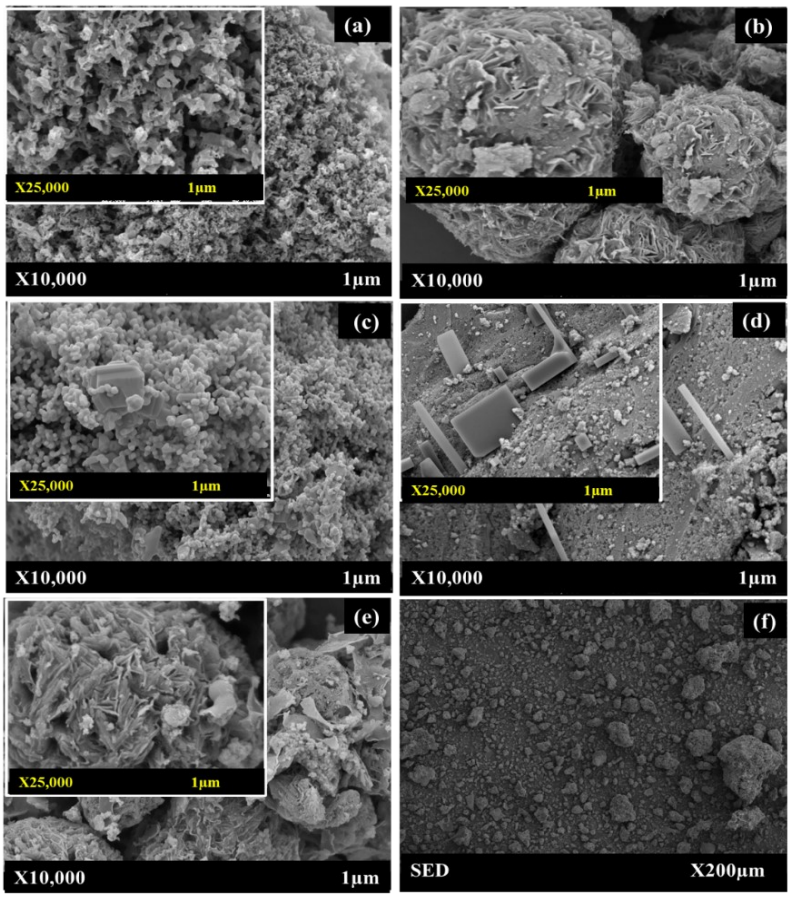

Figure 45. HRSEM images of (a) pristine g-C_3N_4; (b) S-doped g-C_3N_4;(c) Cubical shaped CuO NPs; (d) Monoclinic shaped ZrO_2 NPs; (e) and (f) SED image CuO/ZrO_2@S-doped g-C_3N_4 NCs

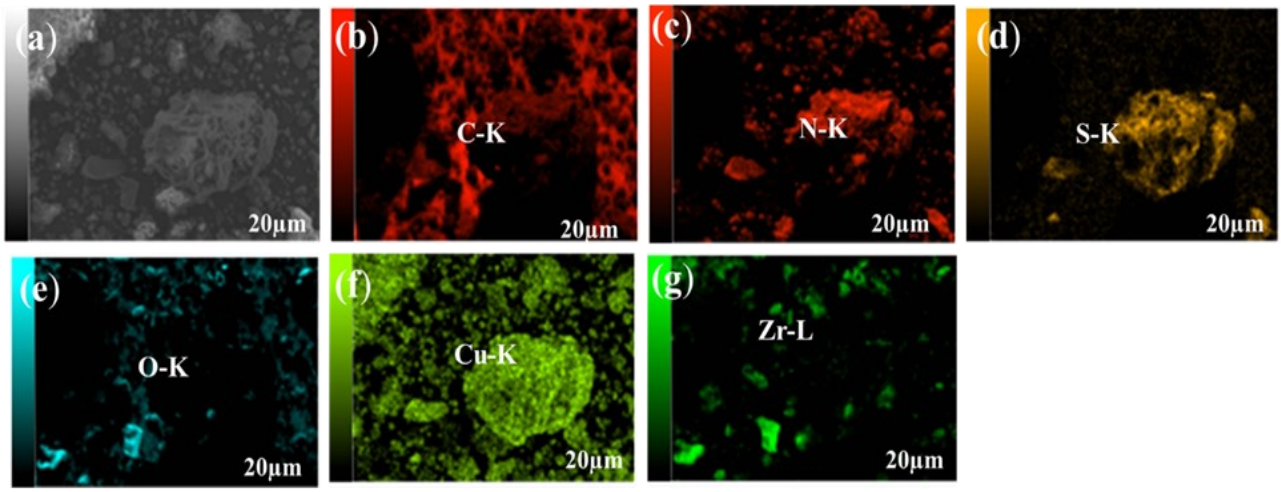

Figure 46. HR-SEM/EDS mapping for (a) CuO/ZrO_2@S-doped g-C_3N_4 and (b-g) the constituent elements.

TEM analysis

To ascertain the existence of CuO and ZrO_2 NPs in the S-doped g-C_3N_4 substrate, TEM images were provided for binary CuO@ S-doped g-C_3N_4 (30%) and ZrO_2@S-doped g-C_3N_4 (20%) NCs and ternary NCs CuO/ZrO_2@S-doped g-C_3N_4 (30%) respectively as shown in Figure 47a, b and c. The ultrathin nanosheet structure of the CuO@ S-doped g-C_3N_4 (30%) sample is demonstrated by Figure 47 a. In addition to materials that resemble nanosheets, other fragments that are thought to be small polymerized layers where the blowing gas has blocked further polymerization are also detected. It is also evident from the high-resolution TEM picture (Figure 47 d) that the copper species are evenly distributed across the -doped g-C_3N_4. Furthermore, the lattice spacing of d= 0.23 nm can be attributed to the (111) plane of monoclinic CuO, and the CuO unique lattice spacing is plainly visible (Duan, 2018). As Figure 47 b illustrates ZrO_2 NPs are spherical particles with an average lattice spacing of ZrO_2@S-doped g-C_3N_4 (20%) d= 0.33 nm (Zarei, 2020a). Furthermore, the S-doped g-C_3N_4 exhibits a planar, sheet-like structure. The morphology of ternary HRTEM images of NCs differs from that of binary NCs but, the TEM image makes it simple to distinguish between the presence of CuO and Zr NPs in CuO/ZrO_2@S-doped g-C_3N_4 (30%) sample (Figure 47 c). The ZrO_2 NPs are covered by S-doped g-C_3N_4, they can see black colour (Figure 47 b and c) and the small CuO NPs are seen as white. Even though it is difficult to determine the spotty diffraction rings of the SAED pattern for CuO and ZrO_2 NPs it is possible to differentiate the NPs constructing the composite on the TEM image (Figure 47c). With this regard, the particle size distribution analysis shows the sizes of the synthesized NCs found to be in the nanometer range (~4 – 30 nm); which complies with the XRD analysis. In conclusion, the development of ternary NCs, which was challenging to see in the XRD investigation, is visible in the TEM pictures and is consistent with the findings of HRSEM and XPS.

4.1.6 Chemical compositional analysis

XPS analysis

As shown in Figure 48a, the total XPS survey spectra of g-C_3N_4 and S-doped g-C_3N_4 NCs indicate the presence of only C and N in g-C_3N_4. The C *1s* and N *1s* peaks at 288.1 eV and 398.7 eV coincide well with the reported values indicate that the g-C_3N_4 bond is composed of only C and N (K. Li et al., 2023). The S-doped g-C_3N_4 (Figure 48b) also reveals prominent peaks for C *1s* and N *1s* at similar binding energy positions as in Figure 48a.

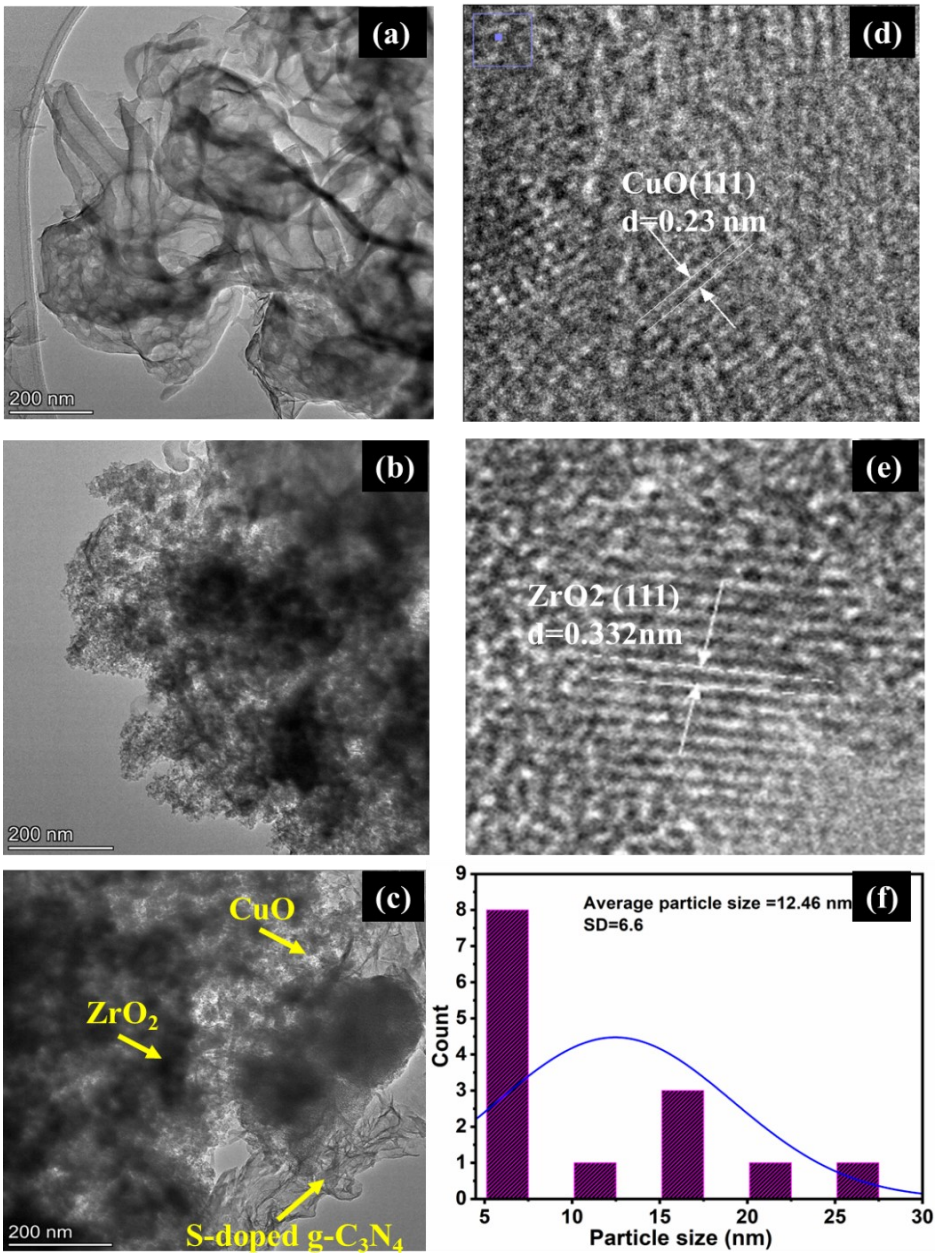

Figure 47. (a) TEM and (d)HRTEM image for CuO@ S-doped g-C_3N_4 (30%) (b) TEM and (e) HRTEM for ZrO_2@S-doped g-C_3N_4 (20%) and (c) and (f) TEM Particle size distribution of CuO/ZrO_2@ S-doped g-C_3N_4 (30%).

The N *1s* spectrum attributed to the N characteristics of C=N–C around 397.2 eV, whereas N=C-C was revealed at around 398 eV. The introduction of S as the dopant caused a marginal shift in the binding energies (Appendix 1). High-resolution XPS for C *1s*, N *1s*, and S *2p* for S-doped g-C_3N_4 are presented in Appendix 2. The N *1s* spectrum is attributed to the N characteristics of C=N–

C around 397.2 eV, whereas N=C-C was noticed around 398 eV (Mohammad, Khan, et al., 2020). In the high resolution XPS spectra of S-doped g-C_3N_4 for S *2p*, a peak located around 164.2 eV was assigned to C–S. The C *1s* spectrum shown in Appendix 1 confirms the existence of the bond between C–S–C with peaks around 285.5-287.5 eV. The peak at 284.8 eV belongs to C–C coordination, the peak centered at 288.3 eV corresponds to the C–N coordination of S-g-C_3N_4 and the C–S–C peak appears at around 284.0 eV (Huang et al., 2019). High-resolution XPS for C *1s*, N *1s*, and S *2p* for S-doped g-C_3N_4 are presented in Appendix 2. The N *1s* spectrum is attributed to the N characteristics of C=N–C around 397.2 eV, whereas N=C-C was noticed around 398 eV (J. Yuan et al., 2018).

The surface chemical compositions of the CuO@S-doped g-C_3N_4 NC were also investigated by using XPS spectroscopy (Figure 48c). The results reveal that Cu *2p*, *3p* and O *1s* peaks were detected for the presence of CuO in the CuO@S-doped g-C_3N_4 NC. Moreover, it was believed that the presence of O *1s* in the CuO sample (Figure 48d) correlated favorably with the production of pure CuO NPs. Similarly, the high-resolution peaks (Figure 49a and b) for Cu *2p* were recorded to investigate the bonding environment in the CuO@S-doped g-C_3N_4 NC and pure CuO matrix respectively. In CuO@S-g-C_3N_4 NC (Figure 49a) the two peaks at 932.7 and 952.3 eV were assigned to the Cu $2p_{3/2}$ and Cu $2p_{1/2}$ spin-orbit splitting peaks of Cu. Whereas Figure 49b shows the Cu *2p* peak for pure CuO NPs. The Cu $2p_{3/2}$ peak is seen at 933.7 eV and this together with the peak shape indicates the Cu-O bond (C. Xu et al., 2015). The binding energies of the two peaks Cu *2p* in CuO@S-doped g-C_3N_4 (Figure 49a) and in CuO (Figure 49b) are separated by 20.0 eV, revealing that Cu is in the 2^+ oxidation state which is consistent with the findings of the prior investigation concerning the CuO spectrum.. Besides this, the presence of satellite peaks on the higher binding energy around 942.5 eV confirms the existence of CuO (Lackner et al., 2019). The O *1s* peak in the CuO sample (Figure 49c) is situated at 529.6 eV, which associates well with O *1s* in CuO. Figure 49d shows the high-resolution S *2p* spectrum with two peaks at 163.8 and 165.0 eV belonging to the C–S–C structure. This analysis is in line with previous reports (Mohammad, Ehtisham, et al., 2020; P. P. Singh & Srivastava, 2022). Based on, XRD, FTIR, HRSEM, TEM and XPS results, it is concluded that the CuO @S-doped g-C_3N_4 NCs had been successfully prepared.

As shown in Figure 50, the total XPS survey spectra of pristine g-C_3N_4, S-doped g-C_3N_4 NCs, pure ZrO_2 and ZrO_2@S-doped g-C_3N_4 indicate the presence of the expected elements in each sample. The section above discusses the XPS results for g-C_3N_4 and S-doped g-C_3N_4. In this section, Figure

51a's XPS survey spectrum of ZrO_2 NPs demonstrates the presence of the bond between Zr and O elements in the ZrO_2@S-doped g-C_3N_4 NCs.

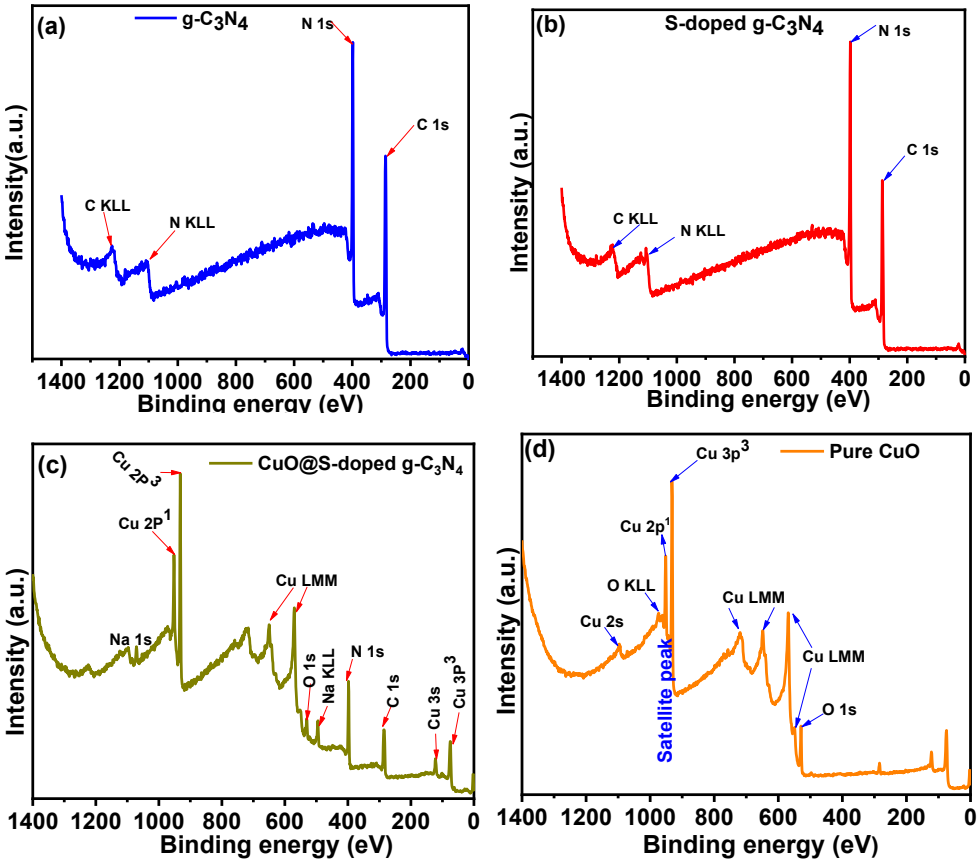

Figure 48.XPS survey spectra for (a) pristine g-C_3N_4, (b) S-doped g-C_3N_4 (c) CuO@S-doped-g-C_3N_4 NCs and (d) CuO NPs.

In the high-resolution XPS spectrum (Figure 51b), the presence of two peaks centered at 181.7 eV and 184.1 eV can be attributed to Zr *3d*$_{5/2}$ and Zr *3d*$_{3/2}$, respectively, for ZrO_2@S-doped g-C_3N_4 NCs. In addition, the Zr *3d* and O *1s* peak around 529.9 eV, as shown in Figures 51c and 52a and b, was assigned to the Zr–O bonds related to the O_2^- ions in monoclinic ZrO_2 (Alebachew et al., 2022; Ke et al., 2014; Mohammad, Khan, et al., 2020). In the XPS spectra of ZrO_2@S-doped g-C_3N_4 for S *2p*, the peak around 164.2 eV was assigned to C–S (Figure 51d). The C *1s* spectrum confirms the existence of the bond between C–S–C with peaks around 285.5 – 287.5 eV Appendix 3. This analysis is in agreement with previous reports (Ke et al., 2014; Vijayakumar et al., 2022). Based on, XRD, FTIR, HRSEM, TEM and XPS results, it is concluded that the ZrO_2@S-doped g-C_3N_4 NCs had been successfully prepared.

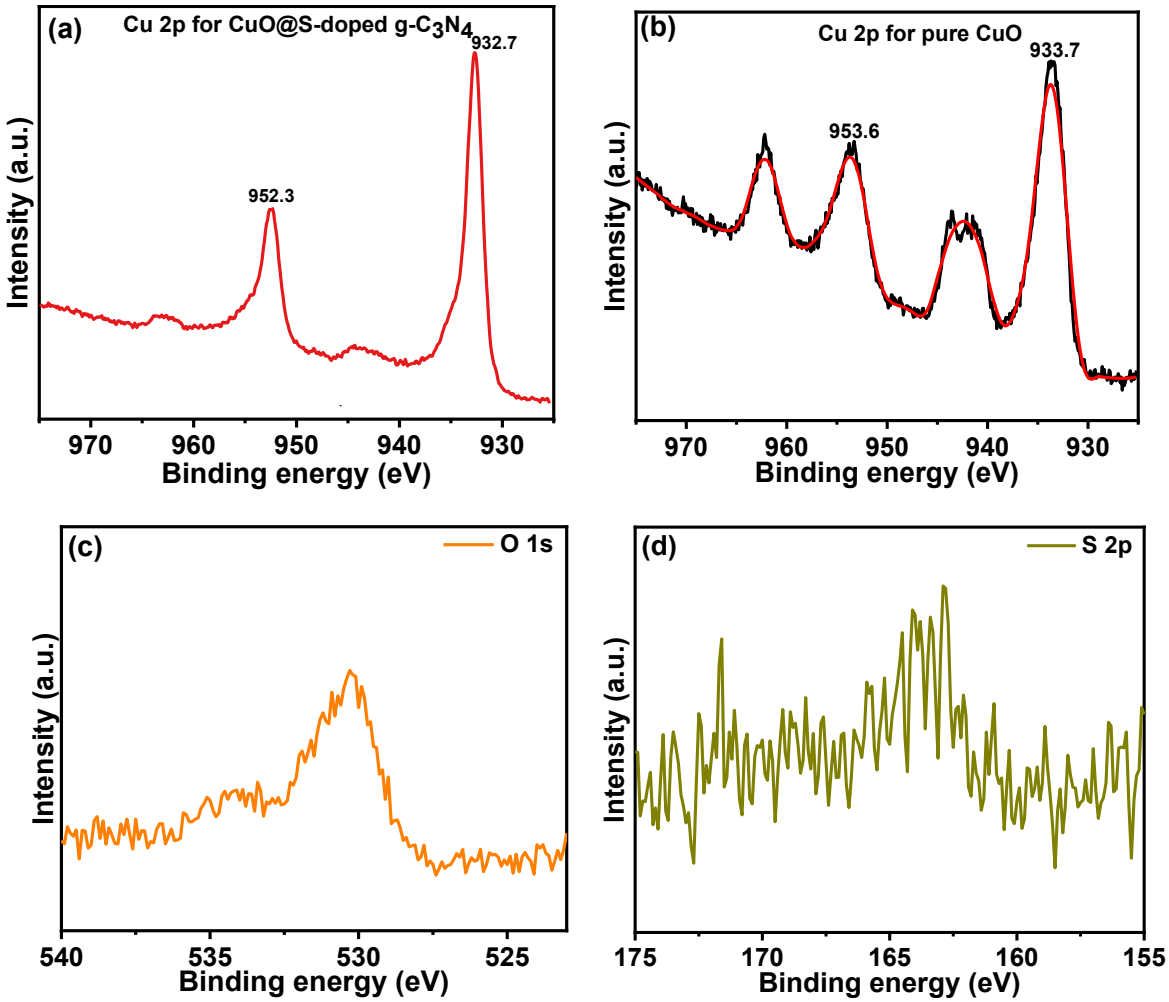

Figure 49.XPS high resolution spectra of (a) Cu *2p* peaks for CuO@S-doped g-C_3N_4, (b) Cu *2p* peaks for CuO NP(c) O *1s* (d) S *2p* for CuO@S-doped g-C_3N_4

To investigate the chemical states of CuO and ZrO_2 in the ternary NC, XPS was utilized to verify the presence of the oxidation states of Cu and Zr since we were unable to validate the XRD results. The XPS survey spectrum of pristine g-C_3N_4 (Figure 53) displayed that g-C_3N_4 is consisted of only C and N. The C *1s* and N *1s* peaks situated at 288.1 eV and 398.7 eV correlate well with reported values in the g-C_3N_4 bond. The C *1s* region of the pristine g-C_3N_4, S-doped g-C_3N_4 and CuO/ ZrO_2@S-doped g-C_3N_4 in Figure 53a showed peaks at 284.6, 287.6, and 293.3 eV, which have previously been assigned to the S-doped g-C_3N_4, sp^2 bonded carbon (N=C=N), and π-excitation, respectively. The S-doped g-C_3N_4 sample also reveals prominent peaks for C *1s* and N *1s* at similar binding energy positions as in g-C_3N_4.

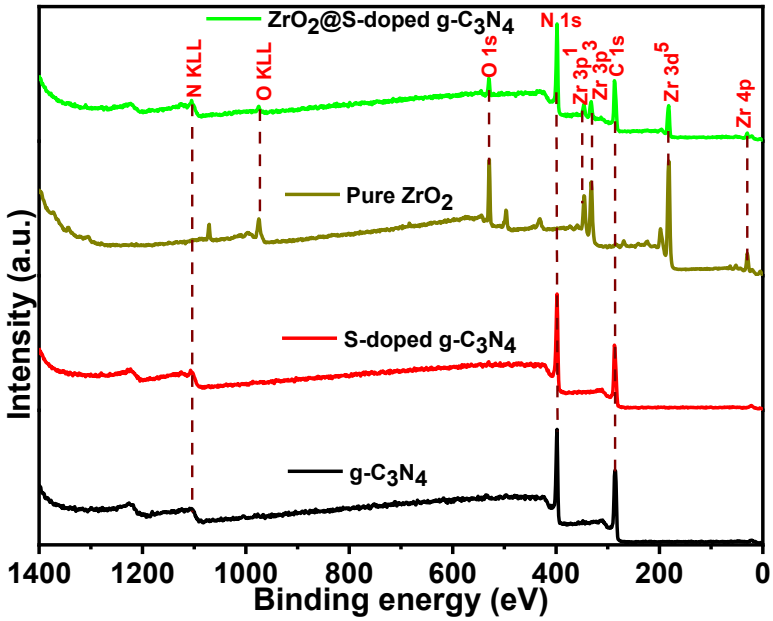

Figure 50.XPS survey spectra for pristine g-C_3N_4, S-doped g-C_3N_4, ZrO_2, and ZrO_2@ S-doped g-C_3N_4.

The survey spectra of CuO/ZrO_2@S-doped g-C_3N_4 NCs identify the presence of only core elements such as C *1s*, N *1s*, S *2p,* Cu *2p*, O *2s*, and Zr *3d*, demonstrating the substantial interaction between CuO, ZrO_2, and S-doped g-C_3N_4 (Alebachew et al., 2022; Sudrajat & Hartuti, 2018).

High-resolution XPS for O *1s*, Zr *3d,* and Cu *2p* for CuO/ZrO_2@S-g-C_3N_4 NCs, Cu *2p* for CuO and Zr *3d* for ZrO_2 are presented in the Figure 54 b-f. Similarly, the peaks at 183.2 and 181.5 eV are attributed to Zr $3d_{5/2}$ and Zr $3d_{3/2}$, respectively for pure ZrO_2 NPs. In addition, the O *1s* peak around 529.2 eV, as shown in Figure 53b, was assigned to the Zr–O bonds related to the O_2^- ions in monoclinic ZrO_2 (S. Cao et al., 2018). Similarly, in the ternary NC, the incorporation of CuO is also confirmed by the presence of a typical high intense peak at 931.6 eV and low intense peak centered at 951.6 eV for Cu $2p_{3/2}$ and Cu $2p_{1/2}$ spin-orbit splitting peaks of Cu Cu $^{2+}$ (Figure 54c). The presence of two peaks centered at 183.2 eV and 181 eV are attributed to Zr $3d_{5/2}$ and Zr $3d_{3/2}$ spin-orbit splitting peaks respectively in the CuO/ZrO_2@S-doped g-C_3N_4 NCs. Similarly, the O *1s* peak around 529.9 eV was assigned to the Zr–O bonds related to the O^{2-} ions in monoclinic ZrO_2 in CuO/ZrO_2@S-doped g-C_3N_4 NC(G et al., 2021).

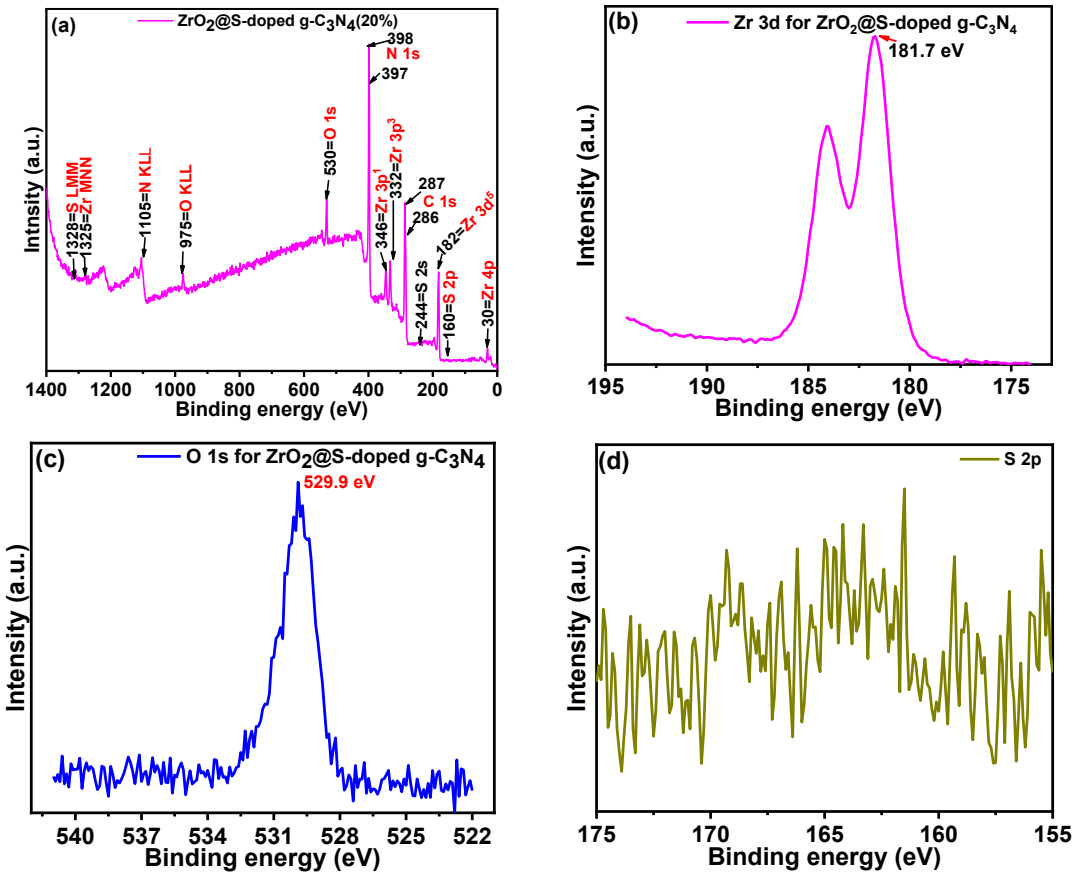

Figure 51. XPS survey(a) and high-resolution spectra of (b-f) C *1s*, N *1s*, Z *3d*, O *1s* and S *1s* ZrO_2@S-doped g-C_3N_4 NC respectively.

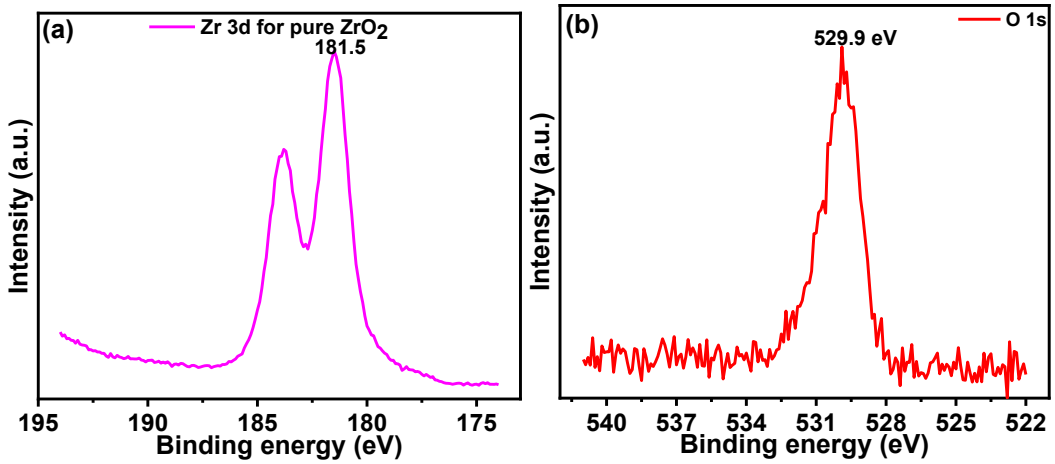

Figure 52.XPS high-resolution spectra of (a) Zr *3d* and (b) O *1s* peaks for ZrO_2 NPs.

Here in the ternary NCs, when both CuO and ZrO_2 NPs are incorporated in S-doped g-C_3N_4 NCs, we have investigated the shifting of Zr *3d* to 181 eV and 183.2 eV values (Figure 54c) and Cu *2p*

to 931.5 eV (Figure 54d). In the high-resolution XPS spectra of CuO/ZrO_2@S-doped g-C_3N_4 for S *2p*, a peak located at 164.2 eV was assigned to C–S (Verma et al., 2020).

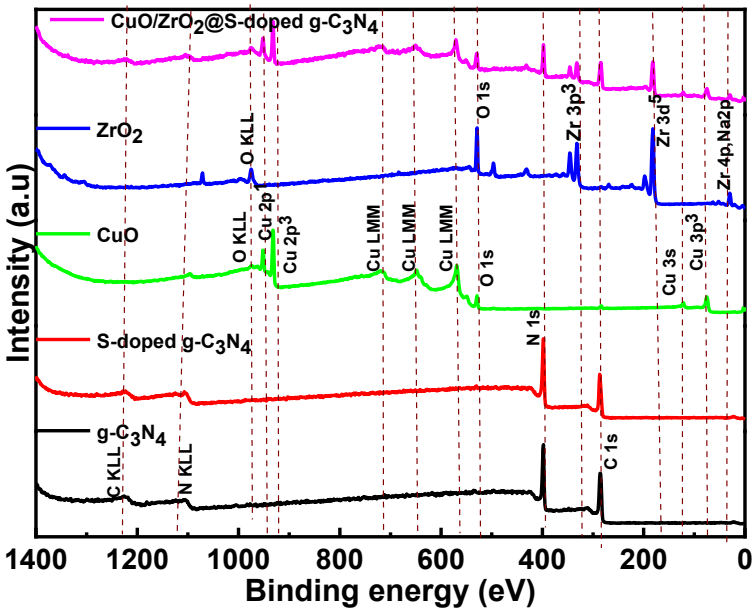

Figure 53. XPS survey spectra for g-C_3N_4, S-doped g-C_3N_4, CuO, ZrO_2 and CuO/ZrO_2@S-doped g-C_3N_4

It was observed that the peak at 167.6 eV was attributed to sulfur oxide species generated during the calcination at 550 °C. A new peak at 163.4 eV appeared in S-doped g-C_3N_4 corresponding to C-S bonds, which were formed by the substitution of sulfur with lattice nitrogen atoms (Figure 54g) (Krishna & Philip, 2022).

The high-resolution S *2p* spectrum shows the presence of S in the ternary NCs. two peaks at 163.8 and 165.0 eV belonging to the C–S–C structure. Thus, the shifting in XPS peaks revealed the presence of N, C, S, Cu, O, and Zr elements in CuO/ZrO_2@S-doped g-C_3N_4 NC (Q. Guo et al., 2016; Stolbov & Zuluaga, 2013b).

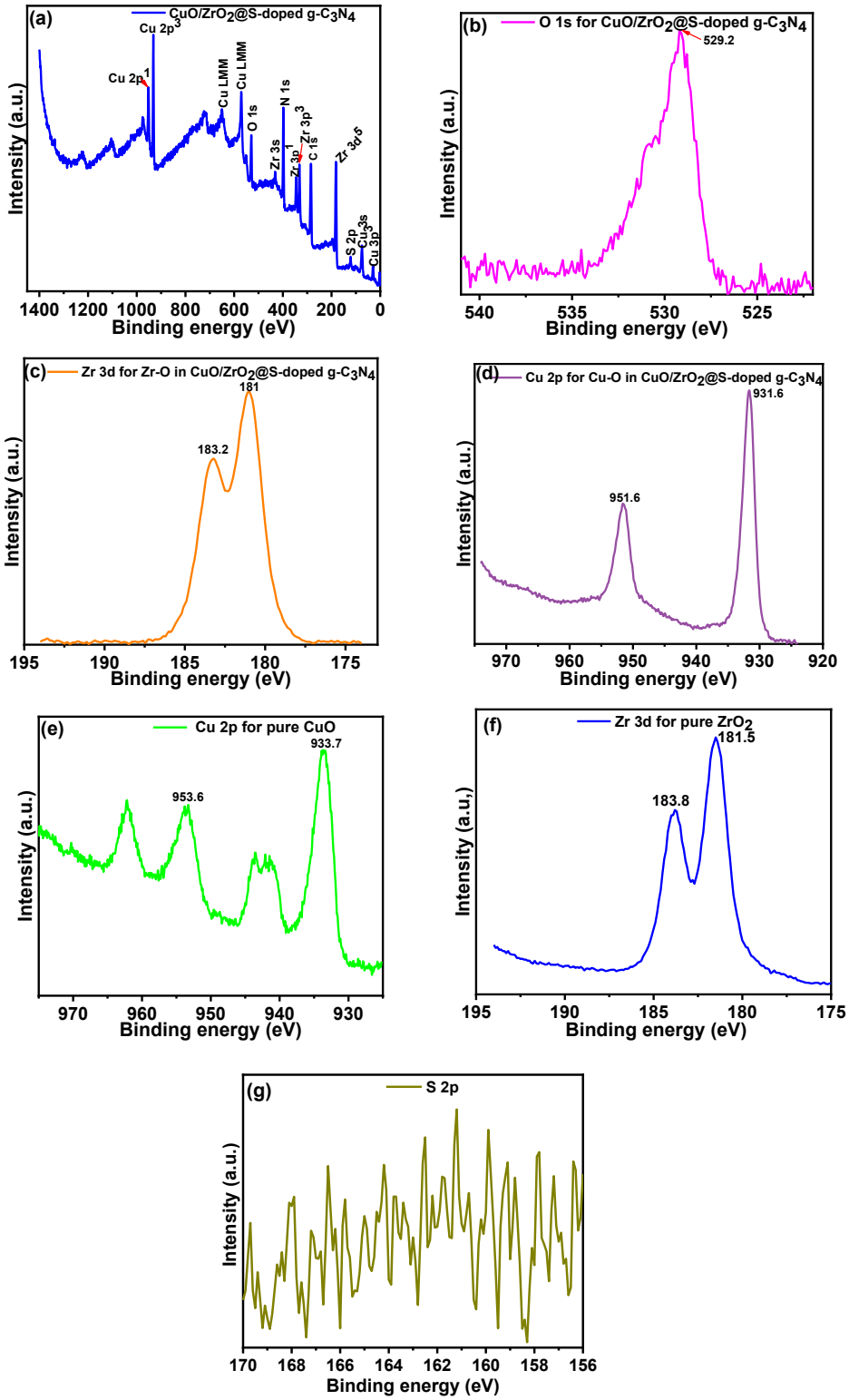

Figure 54.(a) X-ray photoelectron survey spectra of CuO/ZrO_2@S-doped g-C_3N_4 NC, high resolution spectra for (b) O *1s*,(c) Zr *3d,* (d) Cu *2p* for CuO/ZrO_2@S-doped g-C_3N_4 NC, (e) Cu *2p* for CuO, (f) Zr *3d* for ZrO_2.and (g) for S *2p*

Generally, Results from HRSEM/EDS, TEM and XPS revealed that the synthesized CuO/ZrO_2@S-doped g-C_3N_4 NC contained S-g-C_3N_4, cubical-shaped CuO and monoclinic-shaped ZrO_2. Since the sample depth for XPS is 10 nm and for XRD is in micron sizes, the CuO and ZrO_2 species may be related to the size of synthesized materials, which is the only plausible explanation for the absence of peaks for CuO and ZrO_2 in XRD investigation (Nithya & Ayyappan, 2020).

4.2 Computational studies

Since the exact position for substitution S cannot be identified experimentally, we did DFT calculations to elucidate the electronic structure of S-doped g-C_3N_4. Geometric optimizations of g-C_3N_4, S-doped g-C_3N_4, CuO and ZrO_2 models were performed with the DFT/B3LYP/6-31+G (d, p) method. An atomic structure model of g-C_3N_4 composed of melon units (S-triazine) was constructed as shown in Figure 55. In this model, three types of periodic N atoms exist in the melon system, indicated as N_1, N_2, and N_3 numbered based on their positions for S substitution. The DFT-calculated band gap of S-doped g-C_3N_4 is slightly underestimated. Among the different positions of N for the S-doped g-C_3N_4 models, the band gap for substituted melon systems was found to be 1.70 eV, 1.68 eV and 1.16 eV for N_1, N_2 and N_3 substituted melon systems, respectively. Although E_g results depend on the doping condition and type of basis set, the overall DFT result is that all considered doping scenarios are unfavorable; hence all the calculated E_g values are lower than the corresponding experimental values presented in Table 5.

It is nevertheless seen that the gap narrows down to ~1.7 eV upon doping compared to the experimental value. It is worth mentioning that the DFT calculations show a narrowing of the band gap upon doping. Since S is a much larger atom than N and C, it was found that for the optimized geometries, the substitution of N with S caused a significant lattice distortion, which in turn changed the E_g values, while in all the other cases of substitution of N with S, the structure kept a planar geometry, in agreement with previous studies (Kamal et al., 2021).

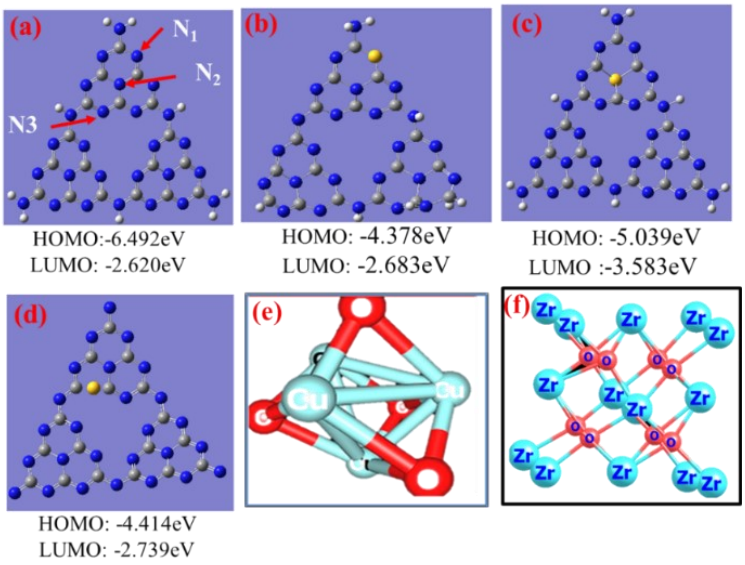

Figure 55. Molecular orbital energies (a, b, c, d) and structures of (a) g-C_3N_4, (b, c, and d) S-doped g-C_3N_4 when N substituted by S at N_1, N_2, and N_3 respectively (e) cubic CuO (f) monoclinic ZrO_2. Colour coding: grey C, blue N, yellow S, red oxygen, and white hydrogen.

Justification; after investigation of the above-discussed characterization results such as average crystal size, PL, UV-Vis/ DRS and specific surface area, electrochemical characterization (CV, M-S, and EIS), among the binary NCs; CuO@ S-doped g-C_3N_4 (30%) and ZrO_2@ S-doped g-C_3N_4 (20%), and among ternary NCs, CuO/ZrO_2@ S-doped g-C_3N_4 (30%) were selected as better materials to be used for further application tests.

4. 3 Catalytic reduction of 4-NP with synthesized catalysts

In order to evaluate the catalytic reduction efficiency of 4-NP into 4-Aminophenole (4-AP) by the synthesized samples, the results of characterization techniques were taken to select the best catalyst. With this regard, among various ratios of binary and ternary NCs, binary CuO@ S-doped g-C_3N_4 (30%), and ZrO_2@ S-doped g-C_3N_4 (20%), and CuO/ZrO_2@ S-doped g-C_3N_4 (30%) NCs were chosen for catalytic reduction studies.

As depicted in Figure 56a, before catalytic reduction studies, the UV–Visible absorbance of pure 4-NP was measured at λ_{max} =317 nm. It is obvious that aqueous solution of pure 4-NP gives a transparent yellow appearance to the naked eye and, a broad peak in a UV–Visible spectrum located at 317 nm. However, in the presence of excess $NaBH_4$, the broad peak becomes slightly narrow and shifts to a new location of 400 nm (Figure 56a). The shifting of the peak to 400 nm

indicates the formation of an intermediate 4-nitrophenolate anions in an alkaline medium caused by $NaBH_4$ (Kanti et al., 2022). In the presence of excess $NaBH_4$ and the prepared catalyst, the intensity of the 4-nitrophenolate ion absorption peak (λ_{max}= 400 nm) decreased and the simultaneous appearance of a new peak of 4-nitrirophenolate (4-AP) at λ_{max} =300 nm has occurred (Figure 56 b and c). This indicated that the reduction reaction had proceeded to be examined for the liquid phase reduction of 4- NP to 4-AP as a model reaction (Nithya & Ayyappan, 2020). To determine the best catalyst (from selected binary and ternary NCs), a similar experiment was run by mixing the 4-NP and $NaBH_4$ solution with the addition of g-C_3N_4, S-doped g-C_3N_4 and CuO@ S-doped g-C_3N_4 (30%), ZrO_2@ S-doped g-C_3N_4 (20%), and CuO/ZrO_2@ S-doped g-C_3N_4 (30%) NCs. In the reaction process, the catalytic conversion efficiency of 4-NP to 4-AP could be calculated using the equation (7).

$$Conversion\ efficiency\ \ of\ 4-NP\ (\%) = \frac{A_0 - A_t}{A_0} \times 100 \qquad (7)$$

where A_0 is the 4-nitrophenolate anions' initial absorbance at λ_{max} = 400 nm, while A_t is the absorbance at a different time (t) intervals (Alegria et al., 1959; Kamali et al., 2019).

Figures 56b and c display the UV–Vis result of mixing of the 4-NP, $NaBH_4$ and catalysts g-C_3N_4 and S-doped g-C_3N_4 merely showing a small change in the intensity at 400 nm peak without significant colour change. The percent reduction efficiency of g-C_3N_4 and S-doped g-C_3N_4 was 11.8% and 24.99% respectively. This demonstrates that even after 15 minutes, the catalytic reduction performance of both NCs (g-C_3N_4 and S-doped g-C_3N_4) was quite poor.

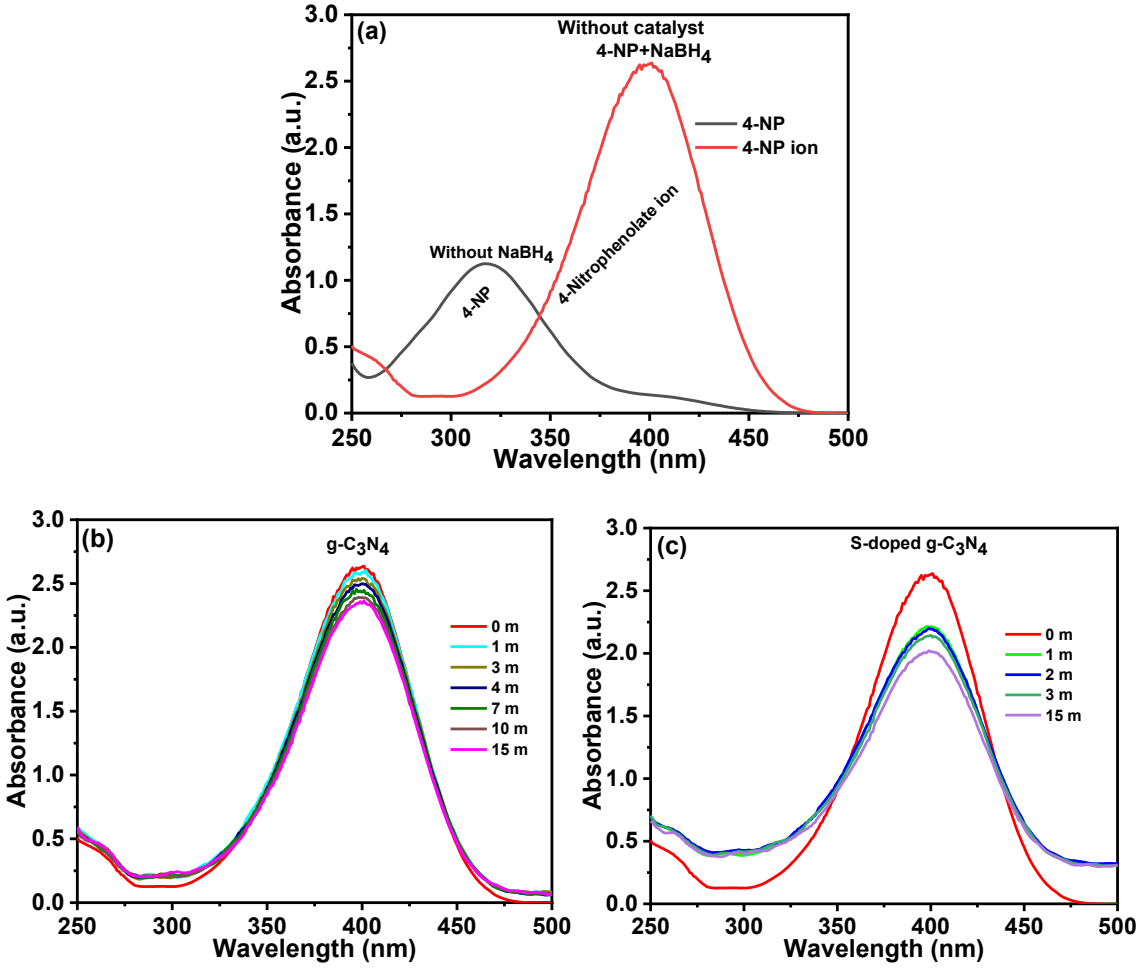

Figure 56. UV–Vis spectra of 4-NP (a) with and without $NaBH_4$ and catalyst (b) g-C_3N_4 + $NaBH_4$, (c) S-doped g-C_3N_4 + $NaBH_4$ respectively. Experimental conditions, 0.005M 4-NP solution, 0.1 M $NaBH_4$ aqueous solution and 0.01g catalyst, volume of solution 100 mL, pH=10.

4.3.1 Optimization of catalytic reduction of 4-NP

For further examination of the reduction process, the binary (CuO@ S-doped g-C_3N_4 (30%), ZrO_2@ S-doped g-C_3N_4 (20%)) and ternary CuO/ZrO_2@ S-doped g-C_3N_4 (30%) NCs were tested as a catalyst in a famous 4-NP reduction reaction. The entire conversion of the 4-NP ion to the 4-AP ion is shown by the creation of a colorless solution. To determine the best experimental conditions for the reduction process, optimization of the amount of catalyst and the effect of concentration of the analyte (4-NP) studies were conducted at the same pH and concentration of $NaBH_4$. Studies show that $NaBH_4$ aqueous solution is stable under alkaline conditions and the rate of deprotonating of (OH^-) is much reduced at higher pH conditions (Kong et al., 2017; Verma et

al., 2020).Therefore, in this study, the alkaline solution (pH=10) was chosen without further optimization. Since the concentration of $NaBH_4$ in the reaction was quite high and could be regarded as a constant throughout the reaction period, the rate constant for the reduction of 4-NP was calculated using pseudo-first-order kinetics by equation (3).

The optimization reaction was mainly carried out under the following cases

I. Constant concentration of $NaBH_4$ (0.1 M) was used for the reduction of 4-NP studies.
II. Effect of catalyst doses
III. Effect of 4-NP concentration, using the optimized catalyst doses and constant concentration of $NaBH_4$.

Effect of catalyst dose

To identify the ideal amount of CuO@S-doped g-C_3N_4 (30%), ZrO_2@S-deopd g-C_3N_4 (20%) and CuO/ZrO_2@S-deopd g-C_3N_4 (30%) NCs as a 4-NP reducing catalyst, various doses (0.01g, 0.05g, and 0.1g) of NCs were administered under identical experimental settings. Figure 57 displays the per cent reduction and the reaction rate constant of 4-NP for the 0.01g, 0.05g, and 0.1g doses of CuO@S-doped g-C_3N_4 (30%) NC reactions. From the reduction percentage analysis, the reduction of 4-NP surged well above 96.63% for 0.05g CuO@S-doped g-C_3N_4 (30%) and 95.46% for 0.1g CuO@S-doped g-C_3N_4 (30%) as a catalyst respectively. The lower (95.37%) efficiency was observed where 0.01g CuO@S-doped g-C_3N_4 (30%) was used. Moreover, as shown in Figure 57 (b, d and e,) a plot of $ln\left(A/A_0\right)$ *vs*. reduction time for the corresponding reactions experimental data were fitted to the pseudo-first-order kinetic equation as represented by a dot solid line. The rate constant values were determined from the slopes of the lines drawn over the experimental $ln\left(A/A_0\right)$ *vs.* values against time. Therefore, the highest reduction percentage observed by 0.05g of CuO@S-doped g-C_3N_4 (30%) was selected for the remaining reduction experiments.

Similarly, applying same experimental conditions for ZrO_2@S-doped g-C_3N_4 (20%) NCs, the reduction efficiency and the rate constant values of ZrO_2@S-doped g-C_3N_4 (20%) for the 0.01g, 0.05g, and 0.1g were recorded as 95.37% (k= 0.009 s^{-1}), 97.79 % (k=0.0141 s^{-1}), and 91.09 % (k= 0.009 s^{-1}) in 300 s respectively (Figure 58 a-f).

In addition, the rate constant and percentage of reduction efficiency for 0.01g, 0.05g, and 0.1g of CuO/ZrO_2@S-doped g-C_3N_4 (30%) result demonstrate that applying 0.01g of CuO/ZrO_2@S-

doped g-C_3N_4 (30%) NCs yields the highest reduction efficiency (98.19%) in contrast to 0.05g (97.22%) and 0.1g (97.17%) as indicated in Figure 59(a-f). It can be noticed that the ternary NC degrades 4-NP more efficiently than the binary NCs, CuO@S-doped g-C_3N_4 (30%), ZrO_2@S-doped g-C_3N_4 (20%). An excellent reduction efficiency for 0.01g of CuO/ZrO_2@S-doped g-C_3N_4 (30%) NC has resulted from the effective diffusion of both 4-NP and BH_4^- (an electron acceptor and donor, respectively) to the optimum active surface areas of the CuO/ZrO_2@S-doped g-C_3N_4 (30%) NCs (46.5 m^2g^{-1}) which plays the role of as electron storage during the electron transfer process. This can be attributed to the synergistic effect that exists within CuO and ZrO_2 in the S-doped g-C_3N_4. According to literature, after adding CuO/ZrO_2@S-doped g-C_3N_4 (30%) NC, the catalytic reduction is ongoing by spread of electrons from the donor BH_4^- to the acceptors 4-NP and 4-NA to the CuO/ZrO_2@S-doped g-C_3N_4 (30%) NC accept electrons from BH_4^- ions and transport them to 4-NP and 4-NA. Besides, the BH_4^- ions can hand over surface-hydrogen species to the CuO/ZrO_2@S-doped g-C_3N_4 (30%) %) NC.

On adsorption of 4-NP and 4-NA by the surface of the CuO/ZrO_2@S-doped g-C_3N_4 (30%) NC, hydrogen transfer to 4-NP and 4-NA occurs rapidly and, lastly, diffusion pointers to the separation of the product from the catalyst surface. It is important to remark that when CuO/ZrO_2@S-doped g-C_3N_4 (30%) NC catalyst and $NaBH_4$ were present, the intensity of 4-NP was lowered, and after about 300 s, the intensity of the absorption peak at 400 nm completely vanished (Figure 59a, c and e). While this was going on, a fresh absorption peak at 300 nm developed and gradually got stronger. The normal absorption of 4-AP is said to be responsible for this new peak. According to the previous studies and this finding, 4-NP was reduced catalytically to 4-AP exclusively, with no other side products being produced (Ayodhya & Veerabhadram, 2019).

Thus, the effect of the concentration of 4-NP studies was done using the optimized amount of the synthesized NCs.

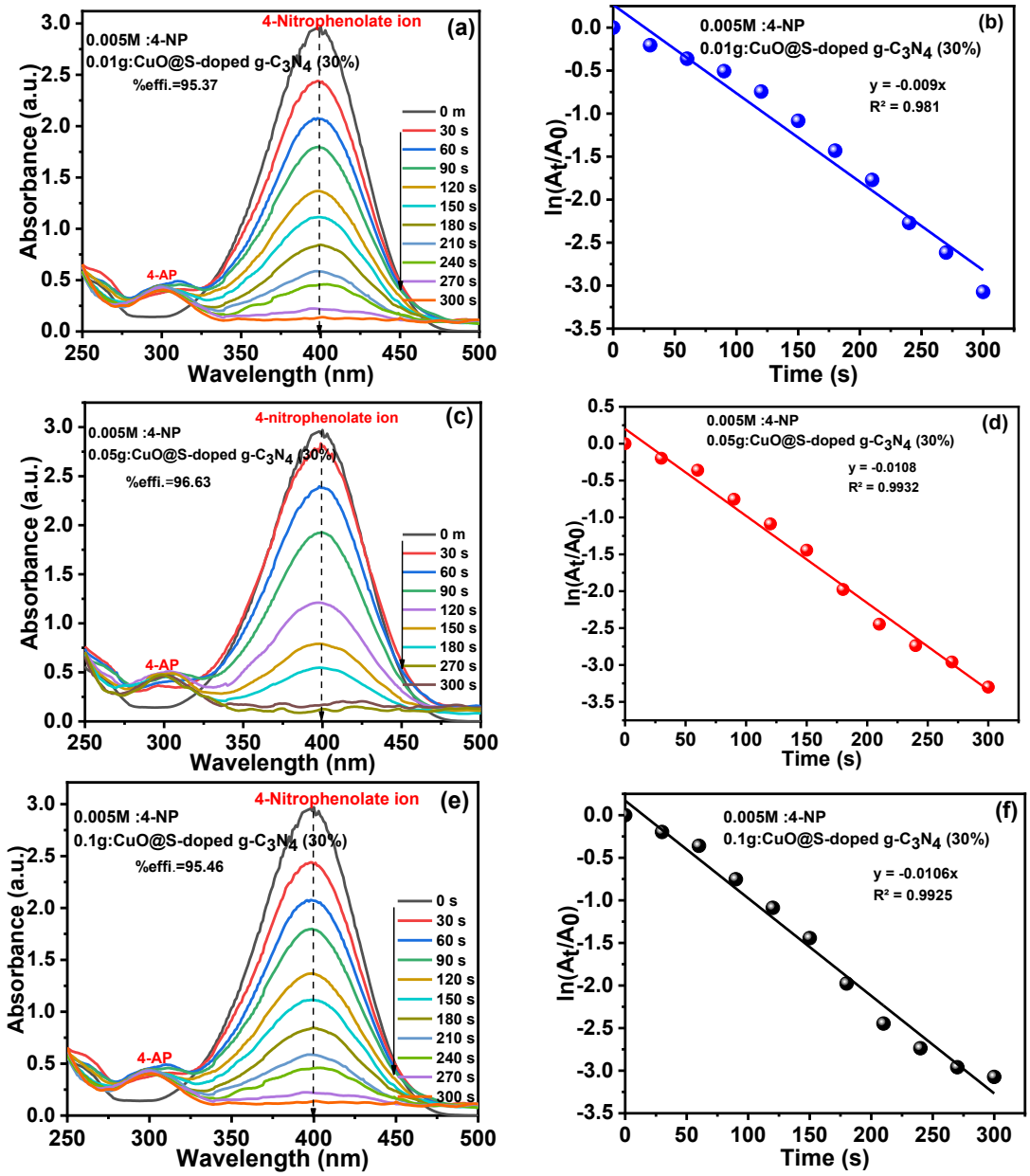

Figure 57.UV-Vis absorption spectra of the reduction of 4-NP for the effect of the amount of CuO@S-doped g-C_3N_4 (30%) NCs (a) 0.01g, (c) 0.05g and (e) 0.1g and (b, d and f) plot of $ln\left(A/A_0\right)$ at 400 nm *vs*. reduction time for the corresponding amount of catalyst respectively. Experimental conditions, 0.005M 4-NP, 0.1 M $NaBH_4$, the volume of solution 100 mL, and pH=10.

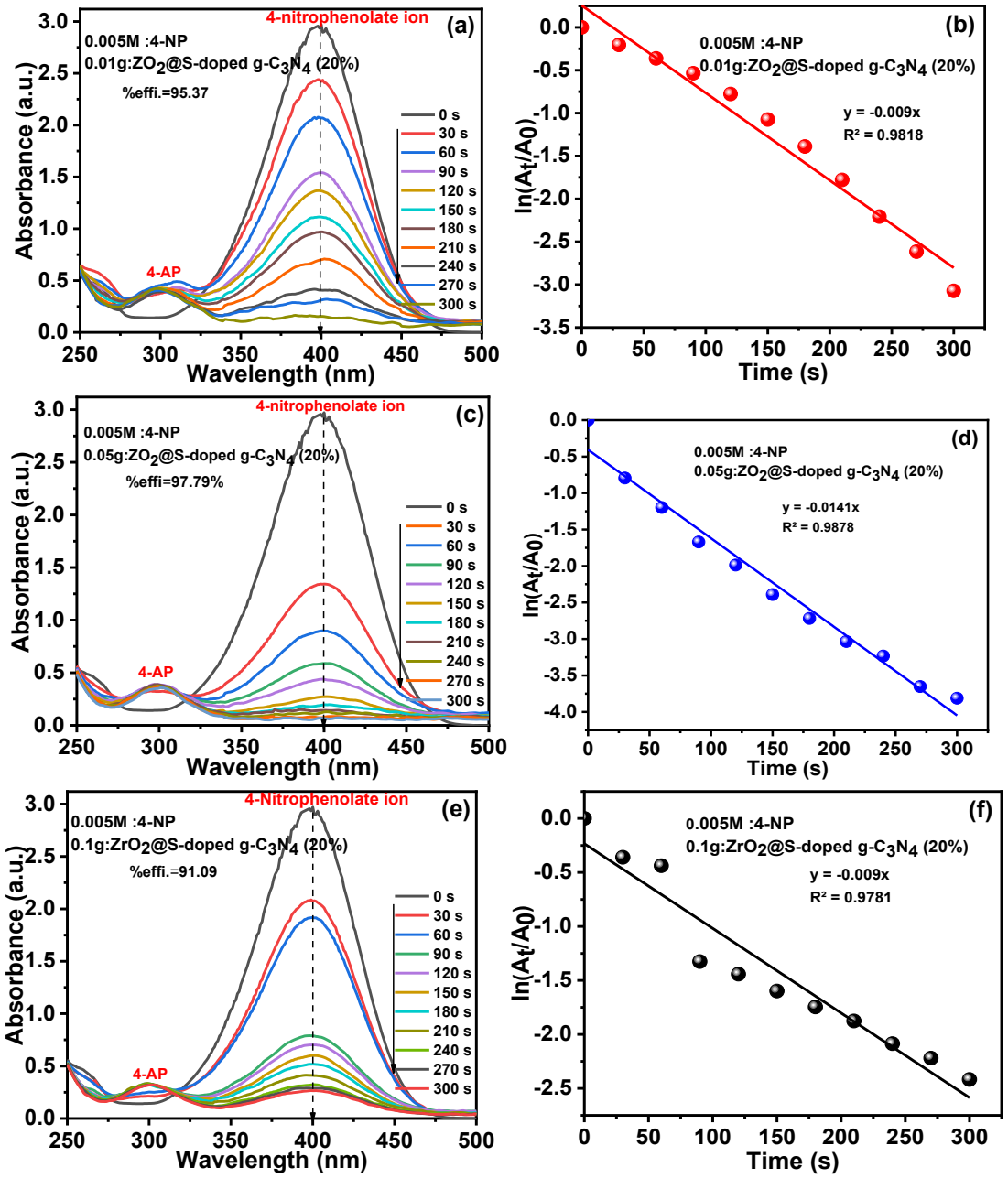

Figure 58.UV-Vis absorption spectra for the reduction of 4-NP for the effect of the amount of ZO_2@S-doped g-C_3N_4 (20%) NCs (a) 0.01g, (c) 0.05 g and (e) 0.1g and (b, d and f) plot of $ln\left(A/A_0\right)$ at 400 nm *vs.* reduction time for the corresponding amount of catalyst respectively. Experimental conditions; 0.005M 4-NP, 0.1M $NaBH_4$, volume of solution 100 mL and pH=10.

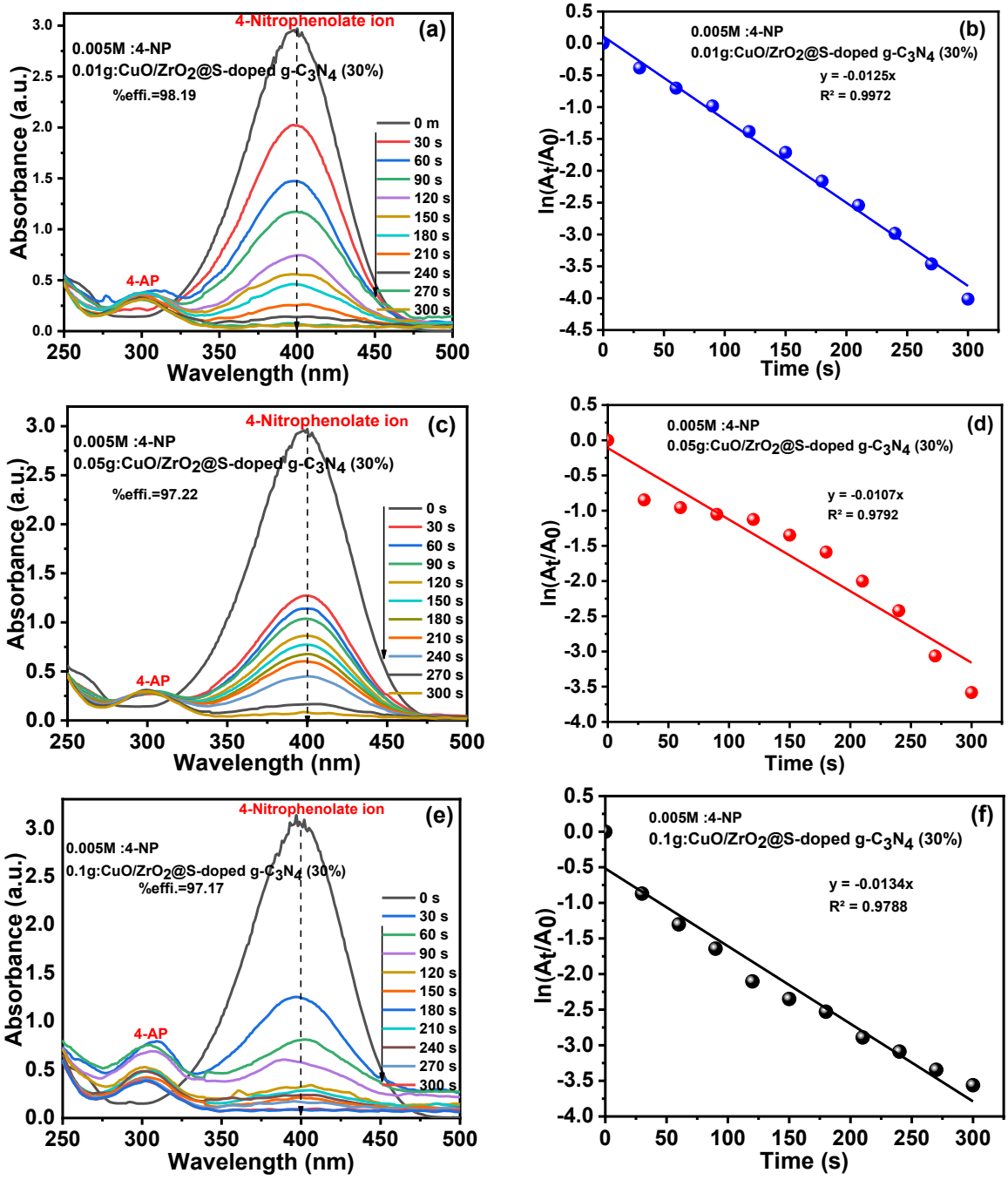

Figure 59.UV-Vis absorption spectra of the reduction of 4-NP of the effect of the amount of CuO/ZO_2@S-doped g-C_3N_4 NCs (a) 0.01g, (c) 0.05g and (e) 0.1g and (b), (d) and (f) plot of $ln\left(A/A_0\right)$ at 400 nm vs. reduction time with the corresponding catalyst respectively. Experimental conditions; 0.005 M, 4-NP 0.1M, $NaBH_4$, volume of solution 100 mL and pH=10.

Effect of concentration of 4-NP on catalytic activity

To determine the effect of 4-NP concentration, a series of kinetics experiments were conducted in a way that the amounts of BH_4 and the optimized amount of 0.05 g, CuO@S-doped g-C_3N_4 (30%) 0.05 g, ZrO_2@S-doped g-C_3N_4 (20%) and 0.01g of CuO/ZrO_2@S-doped g-C_3N_4 (30%) NCs. Whereas the 4-NP concentration was varied from 0.001M,0.005M and 0.01M following the same experimental procedure.

As can be seen in Figures 60 a, c and e, when 0.05 g of CuO@S-doped g-C_3N_4 (30%) is applied,0.005M aqueous solution of 4-NP vanished rapidly and the reaction completed within 300 s with the highest reduction efficiency of 98.15% than the 0.001M and 0.01M of 4-NP with reduction efficiency of 95.36% and 95.56% respectively. The calculated kinetic constant k was 0.013 s^{-1}, 0.0128 s^{-1} and 0.0101 s^{-1} for 0.001M, 0.005M and 0.01M concentration of 4-NP respectively. Surprisingly, the results in both the effect of dose and concentration of analyte demonstrated that the reaction was very fast with outstanding efficiency. The availability of adequate pore surface areas for the adsorption of sufficient 4-NP molecules on the surface of CuO@S-doped g-C_3N_4 (30%) NCs is responsible for the maximum efficiency for reduction of 0.005M of 4-NP.

It was observed that, the reduction rate (k) increased with an increase of 4-NP concentration to 0.01M, but further increase in 4-NP did not result in more reduction. The increase of 4-NP reduction could be due to the increased availability of 4-NP that served as a reductant upon binding to the catalyst. Above 0.005 M, it appears that the catalytic surface became fully saturated and no further enhancement of 4-NP was observed. Therefore, the 0.005 M 4-NP could be considered as an optimal concentration.

Similarly, for the binary ZrO_2@S-doped g-C_3N_4 (20%) NCs, the effect of concentration of 4-NP was conducted as shown in Figures 61(a-f). The reduction efficiency for different concentrations of 4-NP shows that, using the optimum dose (0.05g) of ZrO_2@S-doped g-C_3N_4 (20%), the highest reduction of 4-NP (98.65%) with rate constant of 0.0131 s^{-1} was recorded on using 0.005M of the 4-NP. Whereas, for the 0.001M and 0.01M 4-NP, reduction efficiency and rate constant was 97.26 %, k=0.0112 s^{-1} and 95.43 %, k=0.0112 s^{-1} respectively.

Taking the optimized amount of ternary CuO/ZrO_2@S-doped g-C_3N_4 (30%) NC, 0.01g, a similar study was conducted under similar experimental environments (Figure 62). As shown in Figure

62e the highest reduction performance was observed when 0.01M of 4-NP was used with an efficiency of 99.56% while 96.41% and 99.54% were recorded for 0.001M and 0.005M concentrations of 4-NP respectively. It is found that the required time for the reduction reaction is increased by increasing the initial concentration of 4-NP, however, in this study by recording the reduction reaction in constant time intervals (30 s) in a fixed time duration (300 s), the reduction performance of the ternary NCs shows increasing with increasing concentration of 4-NP. Hence, the optimum concentration for reduction of 4-NP is 0.01M. The rate constant for the three reactions was 0.0085 s^{-1},0.0084 $^{-1}$ and 0.0122 s^{-1} respectively. This shows that the rate of reduction is almost similar except for the performance.

When the CuO/ZrO_2@S-doped g-C_3N_4 NCs are added, it is observed that the electron donor or hydrogen supplier (BH_4^-) and electron acceptor (4-nitrophenolate) are both adsorbed on the CuO/ZrO_2@S-doped g-C_3N_4 NCs' surface and the catalytic reduction of nitrophenolate by BH_4^- begins. The catalytic parameters for the 4-NP reduction with different concentrations of 4-NP compared with CuO@S-doped g-C_3N_4 (30%) ZrO_2@S-doped g-C_3N_4 (20%) and CuO/ZrO_2@S-doped g-C_3N_4 (30%) were summarized in Table 6.

Thus, high catalytic performance for the ternary CuO/ZrO_2@ S-doped g-C_3N_4 (30%) NC is due to its high specific surface area, small particle size (3.36 nm), suitable morphology and excellent dispersion of CuO and ZrO_2 NPs on the S-doped-C_3N_4 surface, which provide more active sites for the reduction reaction process than binary NCs. In this respect, the factors indispensable for elucidating the efficiency of a catalyst are the morphology, the active surface area for NC, the and facets involved. Based on the XRD and BET analyses, it is evident that the NCs' surface areas differ from one another. This is because a particles' surface area and particles' size determine the efficiency of the prepared NCs.

With this regard, when comparing the binary NCs (CuO@S-doped g-C_3N_4 (30%) and ZrO_2@S-doped g-C_3N_4 (20%)) with the ternary NCs, CuO/ZrO_2@S-doped g-C_3N_4 (30%) have suitable specific surface area and smaller-size (CuO/ZrO_2@S-doped g-C_3N_4). These properties provide very good catalytic reaction environment. Hence, it is noteworthy that a low-cost catalyst with a highly active facet is most complimentary in bringing about the facile reduction of nitrophenol.

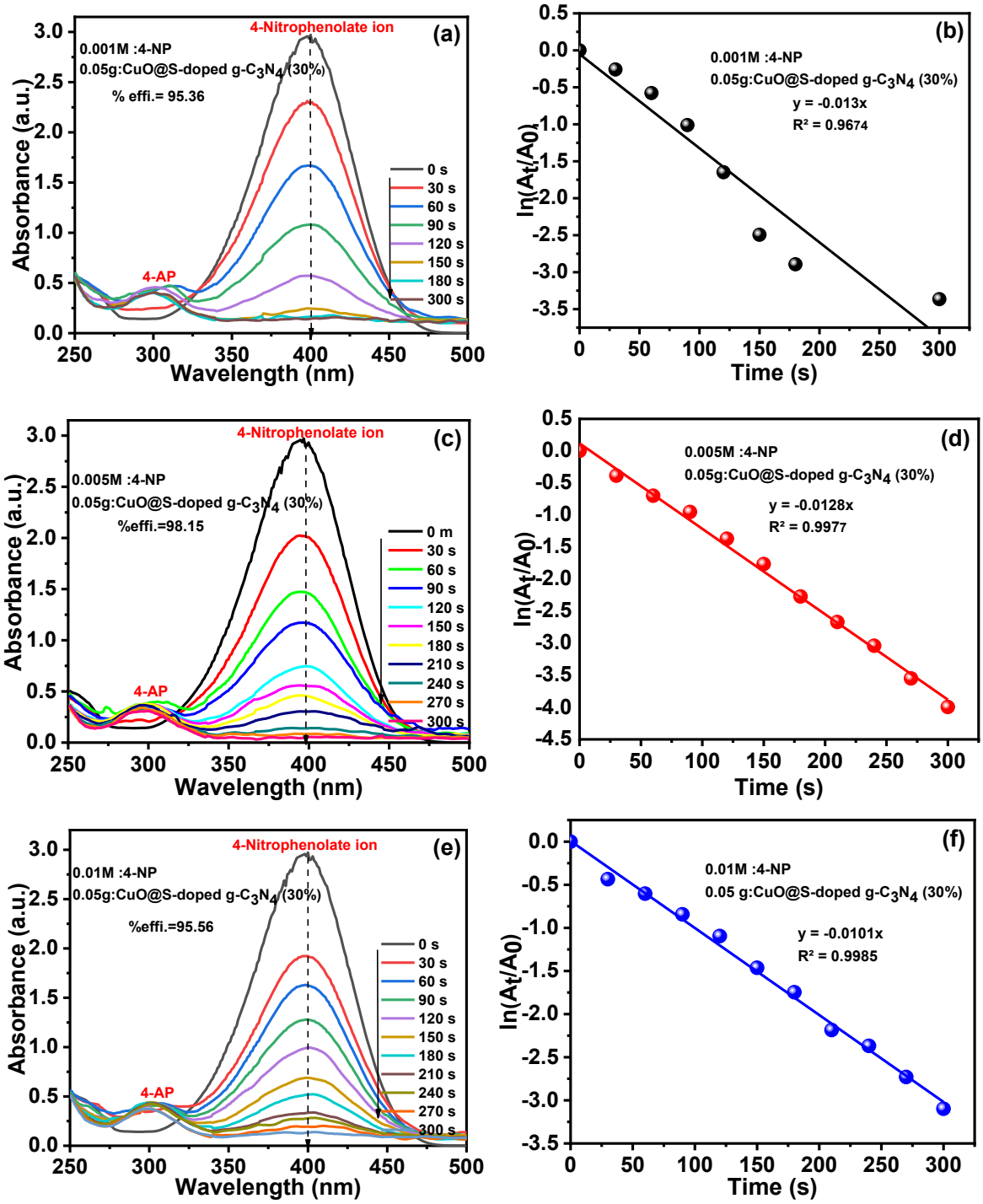

Figure 60.UV-Vis absorption reduction spectra of 4-NP and its concentrations effect 0.001 M b) 0.005M and c) 0.01 M 4-NP, and (b, c and e) Plot of $ln\left(A/A_0\right)$ at 400 nm vs reduction time with the corresponding concentrations of 4-NP. Experimental conditions; 0.05g CuO@S-doped g-C_3N_4 (30%),0.1 M $NaBH_4$, volume of solution 100 mL and pH=10.

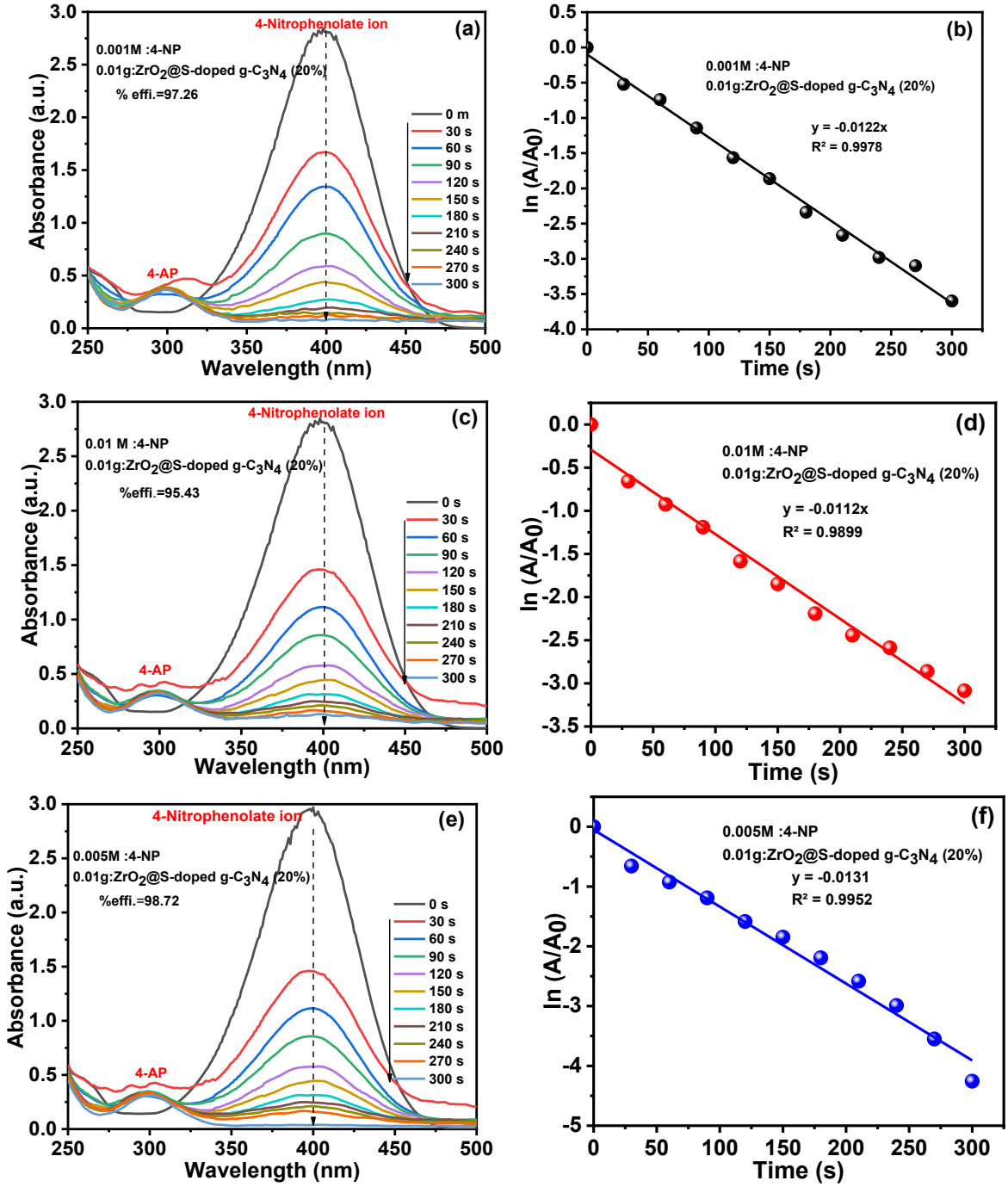

Figure 61.UV-Vis absorption spectra of the reduction of the effect of concentrations of 4-NP a) 0.001 M b) 0.005 M and c) 0.01 M 4-NP and (b, c and e) Plot of $ln\left(A/A_0\right)$ at 400 nm *vs.* reduction time with the corresponding concentrations of 4-NP. Experimental conditions; 0.05g ZrO_2@S-doped g-C_3N_4 (20%),0.1 M $NaBH_4$, volume of solution 100 mL and pH=10.

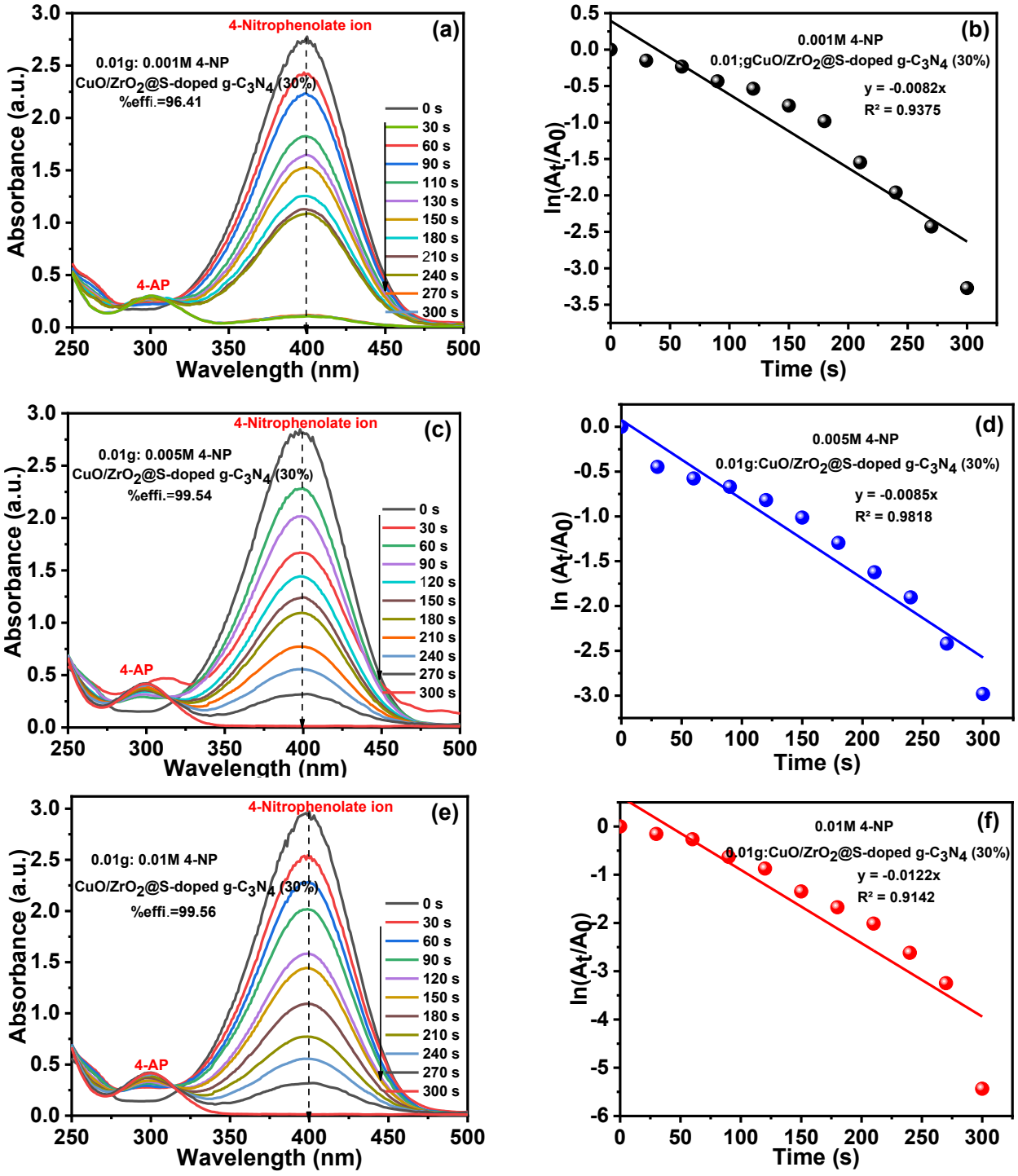

Figure 62.UV-Vis absorption spectra of the reduction of the effect of concentrations of 4-NP a) 0.01 M b) 0.005 M and c) 0.01 M 4-NP and (b, c and e) Plot of ln $\left({}^{A}/_{A_0}\right)$ at 400 nm vs. reduction time with the corresponding concentrations of 4-NP. Experimental conditions; 0.01g CuO/ZrO_2@S-doped g-C_3N_4 (30%),0.1 M $NaBH_4$, volume of solution 100 mL and pH=10.

In conclusion, from the above discussions, it was observed that all the binary and ternary NCs can catalyze and complete the reduction reaction within 300 s, and the aqueous solution of 4-NP vanished rapidly. However, for g-C_3N_4 and S-doped g-C_3N_4 samples, the time to complete the reaction was higher than the CuO@S-doped g-C_3N_4 (30%), ZrO_2@S-doped g-C_3N_4 (20%) and CuO/ZrO_2@S-doped g-C_3N_4 (30%) NCs. Even after the addition of S in the pristine g-C_3N_4, the reduction ability was not improved. Enhancement occurred when CuO and ZrO_2 NPs are incorporated only on S-doped g-C_3N_4. The synergistic effect between the monoclinic crystal of CuO, the cubic phase ZrO_2 and the flower-shaped S-doped g-C_3N_4 facilitates the adsorption of 4-NP species and also draws them towards the active sites where the CuO and ZrO_2 NPs are anchored to the S-doped g-C_3N_4 surface, providing an intimate interaction between the reactant and the catalysts. The outstanding catalytic activity of the ternary CuO/ZrO_2@S-doped g-C_3N_4 (30%) NC under the optimized parameters (0.01g and 0.01M) could be also several reasons. For one reason, this could be due to the size of the ternary (3.36 nm) CuO/ZrO_2@S-doped g-C_3N_4 NCs which influences the facility with which the substrate (4-NP) and the reducing agent (BH_4^-) are adsorbed on the NC surface. Hence, high concentrations of 4-NP (0.01M) give rise to a situation where there are high 4-NP species for a fixed amount of catalyst (0.01g), which leads to rapid and efficient electron transfer on the surface of the CuO/ZrO_2@S-doped g-C_3N_4 (30%). For the other reason, the binary NCs (CuO@S-doped g-C_3N_4 and ZrO_2@S-doped g-C_3N_4) have low specific surface area,22.9 and 35.6 m^2g^{-1} respectively which may conceal the approach and adsorption of the reactants and reduce their catalytic activity. It is important to note that, despite the fact that the bandgap of some synthesized samples is smaller than that of binary and ternary NCs, a number of parameters, including crystalline size, heterojunction formation, and charge recombination effect, can affect a catalyst's electrocatalytic performance. Thus, the binary CuO@S-doped g-C_3N_4 NC (30%) shows lower reduction activity than the ZrO_2@S-doped g-C_3N_4(20%) and CuO/ZrO_2@S-doped g-C_3N_4(30%) this could be due to the availability of a small number of active sites on the surface of the nanocomposite.

4.3.2 Mechanism of 4-NP catalytic reduction

The mechanisms proposed in previous report (Nithya & Ayyappan, 2020) clarify that the catalysis of 4-NP occurs in two or three steps, first, adsorption of the substrate and second, desorption of the product, involving the catalyst. The probable mechanism for the 4-NP catalytic reduction process to 4-aminophenol suggested that: first, a small number of bubbles appear when $NaBH_4$ is

added to water as a result of hydrogen production; this is a reduction reaction between water and $NaBH_4$. This will form an intermediate reaction on the surface of the CuO/ZO_2@S-doped g-C_3N_4 catalyst. During this catalyst addition step, more bubbles form, most likely as a result of enhanced hydrogen production. At the same time, 4-NP adsorbed on the catalyst surface, and hydrogen transferred from the catalytic hydride complex to 4-NP. The 4-nitrophenolate ion peak at 400 nm then gradually diminished, and the 4-AP peak at 300 nm progressively emerged. The 4-hydroxyl aminophenol transition state occurred during the 4-nitrophenolate ion-to-4-AP reduction process. Based on the above discussion, generally, the process of conversion of 4-NP to 4-AP takes place in 3 major steps (Figure 63): (i) adsorption of the 4-NP and BH_4^- molecules to the active site of the catalyst, (ii) transfer of electrons from BH_4^- to 4-NP and (iii) desorption of the products, namely 4-AP. Generally, in this study, the adsorption process and transfer of charged species are facilitated by the built-in electric field of the p–n heterojunction of binary and ternary NCs.

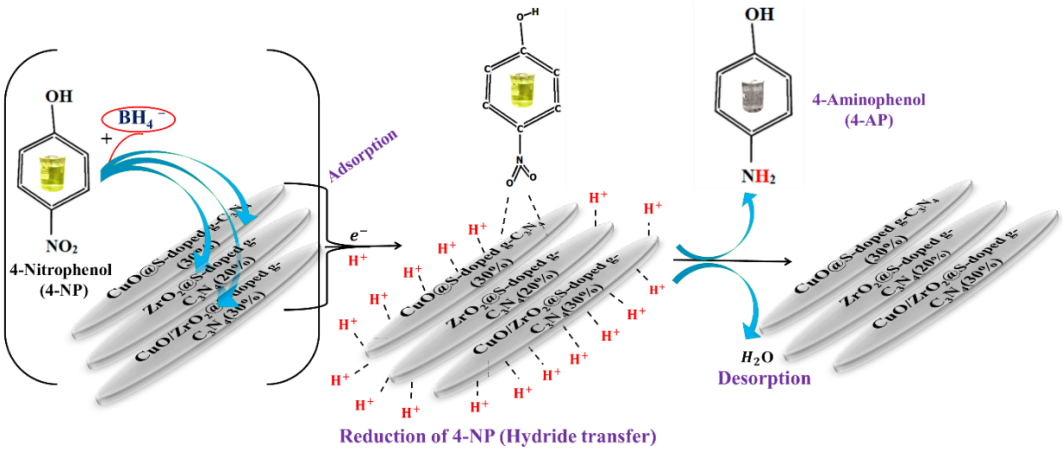

Figure 63. Proposed mechanism of 4-NP catalytic reduction by the synthesized catalysts.

Table 7 shows the comparison of the catalytic activities of the CuO@S-doped g-C_3N_4 (30%), ZrO_2@S-doped g-C_3N_4 (20%) and CuO/ZrO_2@S-doped g-C_3N_4 (30%) with the previous studies conducted in this decade. The result shows that the NCs used in this work exhibit an excellent reduction of 4-NP performance at the optimized experimental conditions.

It is critical to investigate the relationship between substrate concentration and the rate of the catalytic reduction process from a mechanistic and application perspective. Plots of characteristics of catalyst dose and pollutant concentration optimization are similar. Hence, catalyst dosage and concentration of pollutant,4-NP optimization have similar plot flow properties

Table 6. The catalytic parameters for the reduction of 4-NP using the prepared NCs (volume of solution 10 mL, 0.1 M $NaBH_4$, pH=10)

Catalyst	Effect of catalyst dose			Effect of 4-NP concentration		
	efficiency %	k, (s^{-1})	R^2	efficiency %	k, (s^{-1})	R^2
CuO@S-doped g-C_3N_4 (30%)	96.63	0.01028	0.993	98.15	0.0125	0.998
ZrO_2@S-doped g-C_3N_4(20%)	97.79	0.0141	0.987	98.65	0.0135	0.995
CuO/ZrO_2@S-doped g-C_3N_4(30%)	99.19	0.0125	0.997	99.56	0.0122	0.915

Table 7. Comparison of 4-NP reduction with g-C_3N_4-based catalysts reported in the literature with the catalyst in this work

Catalyst	Mass of Catalyst (g)	4-NP conc.(M)	Reduction time (s)	k, (s^{-1})	Conversion (%)	Ref.
g-C_3N_4/Ag_2S	0.001	0.0025	2,520	0.0239	86.54	(Verma et al., 2020)
g-C_3N_4/$ZnBi_2O_4$	N/A	N/A	3600	N/A	79	(Sadiq et al., 2018)
Ag-CuxO/g-C_3N_4	0.05	0.0072	240	0.0055	97.8	(Robati et al., 2016)
BaWO4/NRGO–g-C_3N_4	0.005	0.0001	60	0.1883	N/A	(Bian et al., 2011)
CuO@S-doped g-C_3N_4 (30%)	0.05	0.005	300	0.0125	98.15	This work
ZrO_2@S-doped g-C_3N_4 (20%)	0.05	0.005	300	0.0135	98.65	This work
CuO/ZrO_2@S-doped g-C_3N_4 (30%)	0.01	0.01	300	0.0122	99.56	This work

The effectiveness of dye adsorption declines as the initial 4-NP concentration rises following the saturation of adsorption sites on the surface of the adsorbent. When the initial 4-NP concentration of dye grows, there won't be enough sites for the dye molecules to adsorb, which lowers the removal efficiency because there won't be any unoccupied binding sites on the surface of the adsorbent (F. Chang et al., 2014). Moreover, a rise in substrate concentration may result in the production of intermediates, which may then adsorb on the catalyst's surface. The catalyst's active sites may become inactive by slow diffusion of the produced intermediates from the catalyst surface, which will slow the pace of deterioration. According to apparent first-order kinetics, the rate of degradation will be proportional to the substrate concentration at low concentrations and the number of catalytic sites won't be the limiting factor (Sadiq et al., 2018).

4.4 Photocatalytic activity of ternary nanocomposites

Based on the outstanding performance of ternary NCs in the catalytic and electrochemical sensing of 4-NP, another type of dye (MB) was chosen as the target pollutant to further evaluate the photocatalytic activity of the CuO/ZrO_2@ S-doped g-C_3N_4 NCs. For comparison, the photocatalytic activity of the prepared CuO/ZrO_2@ S-doped g-C_3N_4 (5,10, 20 and 30%) NCs was investigated by degradation of MB under visible-light irradiation as depicted in Figure 65. Figure 64 clearly shows the UV-Vis absorption spectra of MB with different concentrations (0.1, 5,10 and 20 ppm) without the addition of a catalyst. The UV-Vis absorption spectra between the concentration of MB and the absorbance reveal linearity with a linear coefficient value of R^2 =0.993.

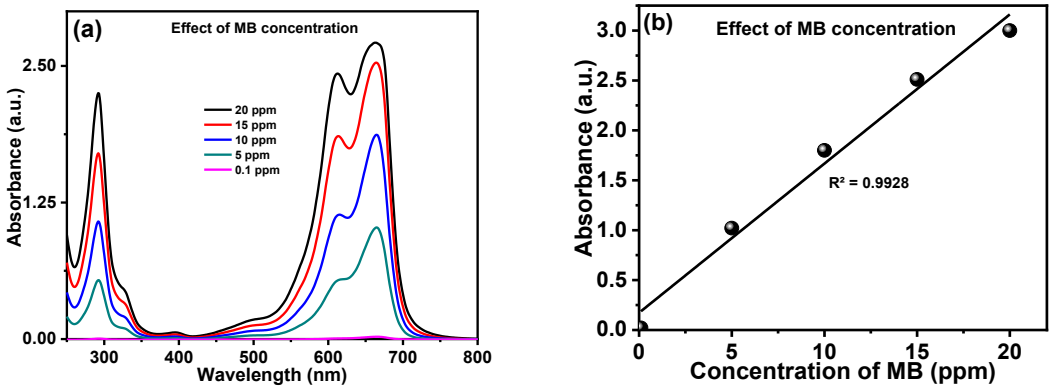

Figure 64. The UV-Vis absorbance of different concentrations of MB; volume of solution 100 mL: pH=10

As shown in Figure 65(a-g), before irradiation of UV-Vis light, by adding the fixed amount of catalyst, the reaction was exposed in the dark for 30 min to examine whether the MB was degraded or not. However, till 30 min there was no change in the colour of MB which shows the reaction couldn't be started without irradiation of light. Hence, in the absence of the light, the degradation of MB was negligible. After 30 min of dark mood environment, the irradiation of visible light was on, and within a 5 m time interval, the sample of the reaction was taken to measure the absorbance at 664 nm. After 30 min, the color of MB was degraded and as shown in Figure 65g, more than 99% of the MB is degraded in the presence of the CuO/ZrO_2@ S-doped g-C_3N_4 (30%) and UV-Visible light. The efficiency of photocatalysis degradation of the catalysis was CuO/ZrO_2@ S-doped g-C_3N_4(5%), CuO/ZrO_2@S-doped g-C_3N_4(10%), CuO/ZrO_2@S-doped g-C_3N_4(20%), and CuO/ZrO_2@ S-doped g-C_3N_4 (30%) NCs 92.30%, 93.30%,96.70% and 99.454% for 30 min visible-light irradiation respectively. The photocatalytic degradation efficiency of these samples increases in the following order CuO/ZrO_2@ S-doped g-C_3N_4(5%) < CuO/ZrO_2@ S-doped g-C_3N_4(10%)<CuO/ZrO_2@ S-doped g-C_3N_4(20%) <CuO/ZrO_2@S-doped g-C_3N_4(30). Additionally, a blue shift of the primary MB adsorption at 664 nm to around 602 nm was noticed together with the extension of the irradiation period, in comparison to the absorbance of MB. This blue shift might be attributed to a gradual demethylation of MB (Hanif et al., 2022).

A previous study shows that the bulk g-C_3N_4 degrades MB only 46.99% for 120 min under visible-light irradiation (Sadiq et al., 2018; S. Zhang et al., 2019). To explore the reaction kinetics for the MB photocatalytic degradation using the prepared photocatalyst materials, the experimental data were well fitted to first-order kinetics and second-order kinetics. The correlation coefficient (R^2) for first-order kinetics CuO/ZrO_2@ S-doped g-C_3N_4 (5,10,20 and 30%) was 0.9805,9978,9954 and 9934 whereas the correlations coefficient for second order was 0.9509, 0.958, 0.9848 and 0.9741 respectively. As a result, first-order kinetics was taken into account, and Figure 65b, d, f, and h show the corresponding diagrams.

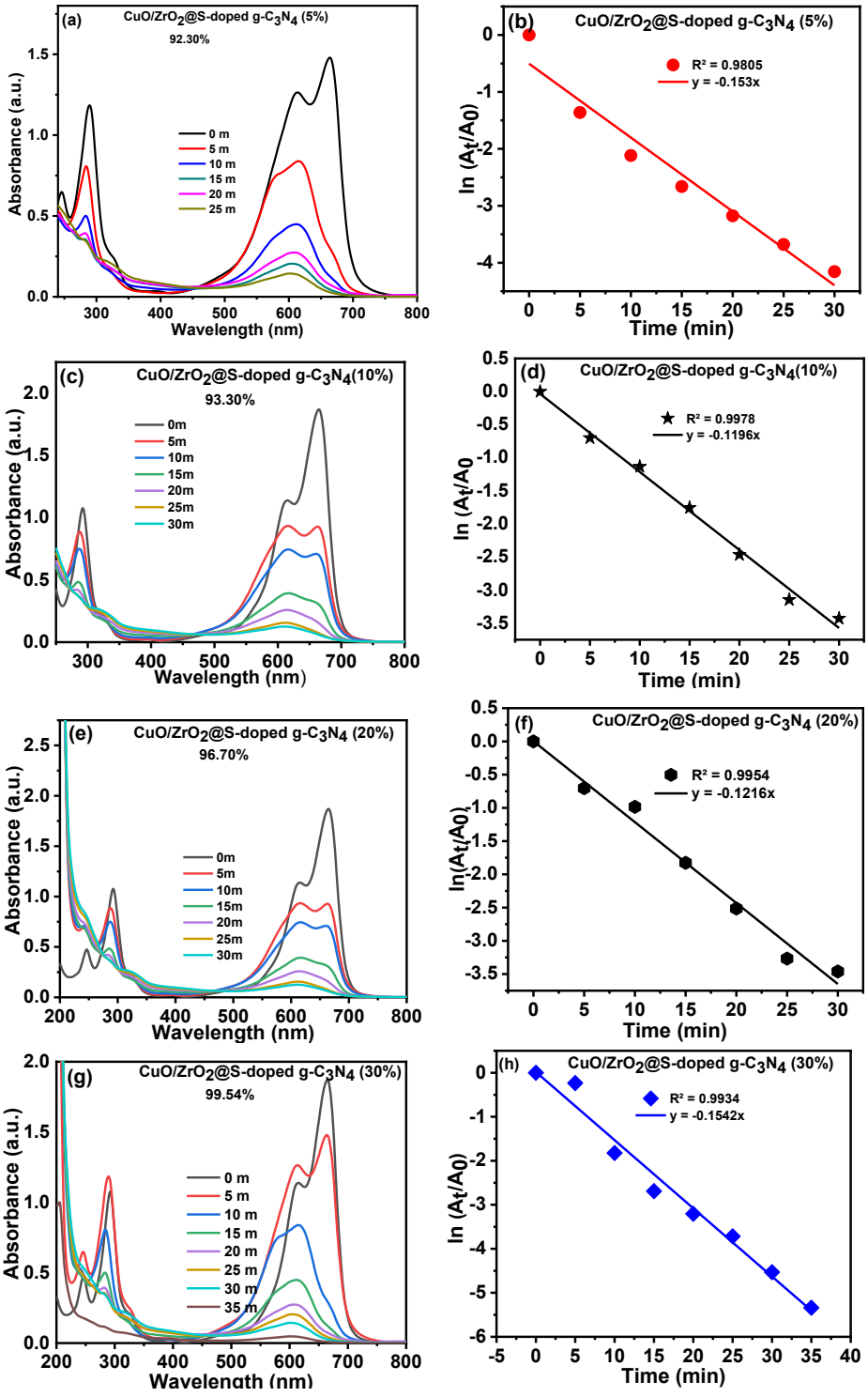

Figure 65. The photo-degradation of MB in solution for CuO/ZrO_2@ S-doped g-C_3N_4 (5,10, 20 and 30%) NCs (a, c, e g) and with the corresponding rate constant. (b, d, f, h); volume of solution 100 mL, pH=10.

The rate constant of CuO/ZrO_2@ S-doped g-C_3N_4 (30%) (0.154 min^{-1}) is about 1.02, 1.29, and 1.23 times greater than those of CuO/ZrO_2@ S-doped g-C_3N_4 (5%) (0.152 min^{-1}), CuO/ZrO_2@ S-doped g-C_3N_4 (10%) (0.119 min^{-1}), and CuO/ZrO_2@ S-doped g-C_3N_4 (20%) (0.122 min^{-1}), respectively. The enhanced performance of the CuO/ZrO_2@ S-doped g-C_3N_4 (30%) NC may be attributed to factors such as narrow band gap, modified BET surface area, the higher extent of energy absorption in the visible-light region and efficient electron-hole recombination rate, contributing significantly towards improved photodegradation of MB.

4.4.1 Photocatalytic mechanism

Based on the above results, a possible photocatalytic mechanism for the separation and migration of photogenerated carriers is proposed (Figure 66). The enhanced performance gives credit to the good light absorption by DRS testing the larger specific surface area, lower crystal size and the agglomeration of the NCs. There is an equal relationship between the Fermi level and flat band potential (V_{fb}) by the intercept on the X-axis of the M-S plot, so the varieties of the electronic states can be discussed. In addition, the flat-band potential varies from -0.42, 0.58, 1.92, -1.17 to -1.02 where shifts from g-C_3N_4 S-doped g-C_3N_4, CuO, ZrO_2 and CuO/ZrO_2@ S-doped g-C_3N_4 samples, respectively. In this case, the formation of the electric field over the heterojunctions presents in the interface between g-C_3N_4, S-doped g-C_3N_4, CuO, and ZrO_2 semiconductors due to the difference in the V_{fb} or the shift of the Fermi level. Meanwhile, the balance of the new Fermi level between g-C_3N_4, S-doped g-C_3N_4, CuO, and ZrO_2 can be formed because of the movement of electrons and holes. Accordingly, the built-in electric field of heterojunctions facilitates efficiently the separation of photogenerated electrons and holes and ultimately enhances the photocatalytic performance of CuO/ZrO_2@S-doped g-C_3N_4 heterojunctions. In addition to the lower the E_g value, the higher the photocatalytic activity of the CuO/ZrO_2@ S-doped g-C_3N_4 (30%) NC could be due to the modification of surface morphology such as heterojunction development, and the small crystallite size of the NCs (Chegeni et al., 2019). This would result in an increment of a greater number of active sites on the outer surface of CuO/ZrO_2@S-doped g-C_3N_4 NC favorable for the adsorption of reactants and diffusion of reaction products being activated by photons and catalytically active during MB photodegradation. This would have resulted from its heterojunction structure leading to low recombination of charge barriers, band gap energy and sufficient active sites (Lui et al., 2013).

Keeping in mind the aforementioned results and to comprehend the photocatalysis mechanism, three pathways for the CuO/ZrO_2@ S-doped g-C_3N_4 NCs photocatalytic reactions are proposed: (1) absorption of photons by the photocatalyst, (2) transfer the photogenerated electrons to the surface of photocatalysts, and (3) participation of the photogenerated electrons and holes in the reaction process with organic pollutant, MB (Chegeni et al., 2019b).

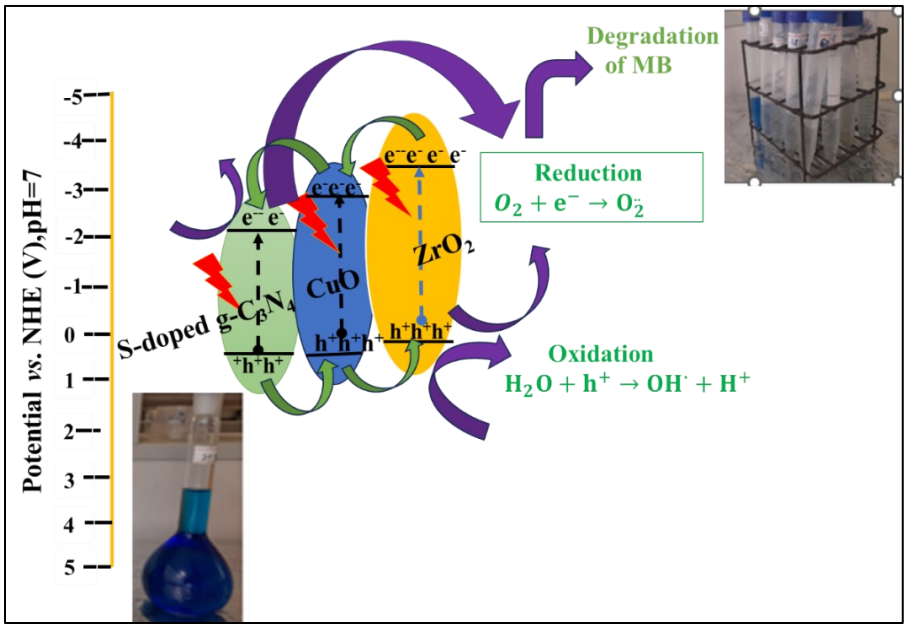

Figure 66.Mechanism for the photocatalytic degradation of MB dye under UV-Visible illumination.

4. 5 Electrochemical studies of various modified sensors

4.5.1 Electrochemical characterizations of modified electrodes

The electrochemical behavior of g-C_3N_4/FTOE, S-doped g-C_3N_4/FTOE, CuO@S-doped g-C_3N_4 /FTOE, ZrO_2@S-doped g-C_3N_4 /FTOE, ZrO_2/FTOE, CuO/FTOE and CuO/ZrO_2@S-doped g-C_3N_4 /FTOE was investigated using a 0.1 M KCl, 5 mM, $Fe(CN)_6^{3-/4-}$ redox probe electrolyte solution at a scan rate of 50 mV^{-1}. Figure 67a shows the modified CuO@S-doped g-C_3N_4(30%)/FTOE exhibiting a well-defined redox peak with a high electron transfer capability compared to g-C_3N_4, S-doped g-C_3N_4, CuO@S-doped g-C_3N_4 (5,10, and 20%) and CuO NPs. Similarly, ZrO_2@S-doped g-C_3N_4(20%)/FTOE show enhanced redox peak behavior than g-C_3N_4, S-doped g-C_3N_4, ZrO_2@S-doped g-C_3N_4 (5,10, and 30%) and ZrO_2 NPs (Figure 67b). Moreover, the CuO/ZrO_2@S-doped g-C_3N_4(30%)/FTOE (Figure 67c) exhibited a well-defined redox peak

with a high electron transfer capability compared to pristine g-C_3N_4/FTOE, S-doped g-C_3N_4 /FTOE, CuO/ZrO_2@S-doped g-C_3N_4 (5, 10, and 20%)/FTOE and bare FTOE. The low electron transfer record by g-C_3N_4/FTOE, S-doped g-C_3N_4/FTOE, CuO@S-doped g-C_3N_4 (5,10,20%)/FTOE ,ZrO_2@S-doped g-C_3N_4/FTOE(5,10,and30%),ZrO_2/FTOE, CuO/FTOE, and CuO/ZrO_2@S-doped g-C_3N_4(5,10,20%)/FTOE relative to CuO@S-doped g-C_3N_4(30%)/FTOE, ZrO_2@S-doped g-C_3N_4(20%)/FTOE and CuO/ZrO_2@S-doped g-C_3N_4(30%)/FTOE is due to the poor electrical conductivity, which limits the electron transfer probe of Fe $(CN)_6^{3-/4-}$ on the surface of the bare FTOE. Hence, the pristine g-C_3N_4 and S-doped g-C_3N_4 might have blocked diffusion of the redox probe and increased internal resistance at the electrode interfaces. Nevertheless, the CuO@S-doped g-C_3N_4(30%)/FTOE, ZrO_2@S-dopedg-C_3N_4(20%)/FTOE, and CuO.ZrO_2@S-doped g-C_3N_4(30%)/FTOE showed an efficient electron transfer capability and enhanced electrical conductivity.

Figure 68 presents the EIS plots of the pristine g-C_3N_4/FTOE, S-doped g-C_3N_4 /FTOE, CuO@S-doped g-C_3N_4/FTOE, ZrO_2@S-doped g-C_3N_4 /FTOE and CuO/ZrO_2@S-doped g-C_3N_4/FTOE, and bare (FTO) electrode, which were recorded to determine the conductivity under similar experimental condition. The complete Nyquist plot, as depicted in the Figure 68 a-c, can be split into two parts: the straight line in the low-frequency zone and a semicircular arc in the high-frequency region. The intercept of the Nyquist plot in the real part (Z') represents the internal resistance (Rs) of the material, including the ionic resistance of the electrolyte, the electronic resistance of the modified electrode, and the contact resistance at each phase interface. In the middle-frequency region, the semicircle is correlated with interfacial charge transfer resistance (R_{ct}). The smallest semicircle indicates the fastest interfacial electron transfer and efficient separation electron–hole pairs, which was often related to intraparticle and interparticle resistance (Faisal et al., 2022). The CuO@S-doped g-C_3N_4(30%), ZrO_2@S-doped g-C_3N_4 (20%) NC and CuO/ZrO_2@S-doped g-C_3N_4(30%)/FTO presented the smallest semicircle, implying faster interfacial electron transfer than that of ZrO_2, g-C_3N_4, S-doped g-C_3N_4, CuO/ZrO_2@S-doped g-C_3N_4 (5,10, and 15%)/FTO, ZrO_2@S-doped g-C_3N_4 (5, 10 and 30%), CuO/ZrO_2@S-doped g-C_3N_4 (5,10 and 20%%)/FTO and bare FTOE.

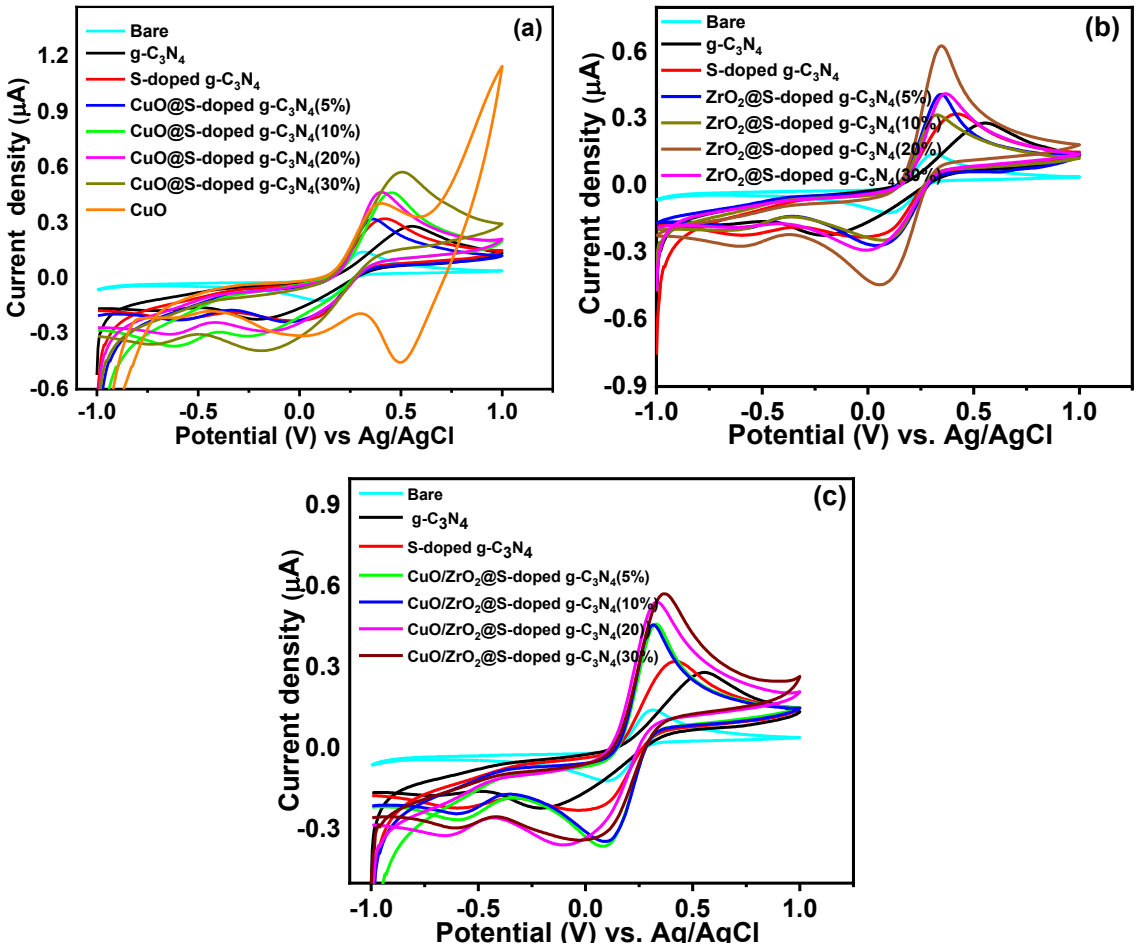

Figure 67.The electrochemical characterization for (a) g-C_3N_4, S-doped g-C_3N_4 NCs and CuO@S-doped g-C_3N_4 (5,10, 20 and 30 %), CuO, (b) ZrO_2@S-doped g-C_3N_4, (5,10, 20 and 30%), ZrO_2, and (c) CuO/ZrO_2@S-doped g-C_3N_4 (5,10,20 and 30%) and bare electrode using CV measurements, (0.1 M KCl; 5 mM Fe $(CN)_6^{3-/4-}$ scan rate = 50 mV s^{-1}).

It is important to note that the ZrO_2@S-doped g-C_3N_4 (20%)/FTOE exhibited higher redox current than the ZrO_2@S-doped g-C_3N_4 (5,10, and 30%)/FTOEs. The rationale is that by adding more ZrO_2 NPs, the heterojunction between the counterparts may be destroyed by particle aggregation, which would reduce the electrocatalytic activity.

Generally, the inset in Figure 68 is the fastest interfacial electron transfer for CuO@S-doped g-C_3N_4(30%)/FTO, ZrO_2@S-doped g-C_3N_4(20%)/FTO and CuO/ZrO_2@S-doped g-C_3N_4 (30%)/FTO modified electrodes mainly due to the optimal electron-hole recombination rate, outstanding electrical conductivity property, moderate ban gap energy, modified surface area, and average crystal size than that of the remaining modified electrodes. Overall, the results showed the

incorporation of S, CuO and ZrO_2 into the lattice of the g-C_3N_4 is believed to have played a vital role in the electrochemical applications. Thus, considering the experimental characterization and the electrochemical characterization results (CV and the EIS) as the primary selective technique for the electrochemical studies, the binary NCs CuO@S-doped g-C_3N_4/FTO (30%), ZrO_2@S-doped g-C_3N_4 (20%) NC and the ternary CuO/ZrO_2@S-doped g-C_3N_4 (30%)/FTO were selected for further electrochemical sensor studies of 4-NP and BPA.

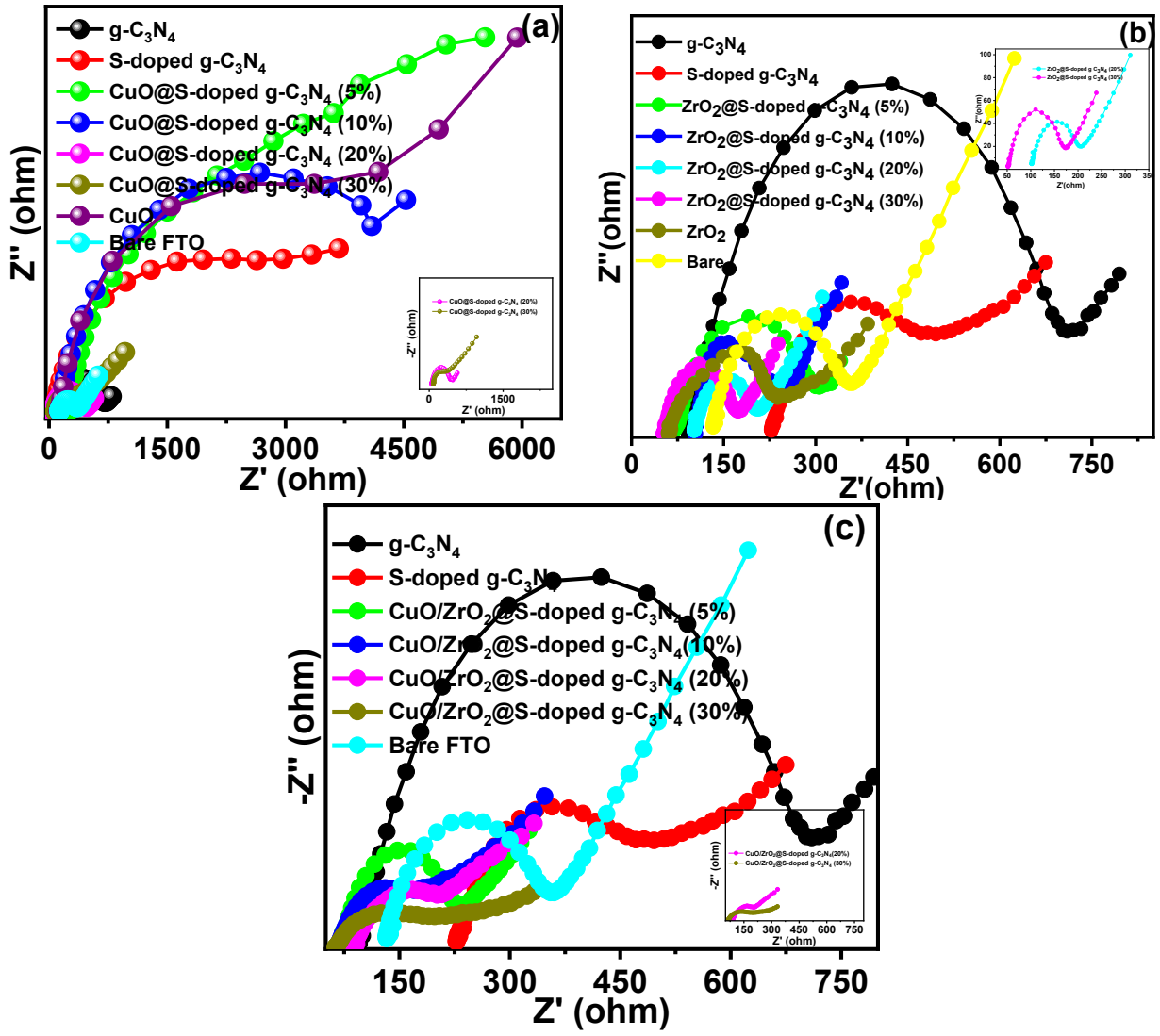

Figure 68. EIS Nyquist plots for g-C_3N_4/FTO, S-doped g-C_3N_4 /FTO, CuO@S-doped g-C_3N_4 /FTO (a), ZrO_2@S-doped g-C_3N_4 /FTO (b) and CuO/ZrO_2@S-doped g-C_3N_4 /FTO(c):0.1 M KCl, 5 mM Fe $(CN)_6^{3-/4-}$ and scan rate = 50 mV s^{-1}

The electrode active surface (EAS) of CuO@S-doped g-C_3N_4 (30%), ZrO_2@S-doped g-C_3N_4 (20%) and CuO/ZrO_2@S-doped g-C_3N_4 (30%) was determined by using the Randles-Sevcik equation (Equation 2). The cyclic voltammograms were recorded at various scan rates at all tested electrodes (Figure 69 a, c and e). The results show that the dependences of peak currents on the square root of the scan rate are linear indicating the electrochemical reaction occurring at the electrodes is a diffusion-controlled process in the scan rate from 0.1 to 200 mV s^{-1} for the anodic and cathodic peaks (Figure 70 b, d and f) (R. Wang et al., 2021). These results showed that the electrocatalytic activity was successfully improved at the surface of the modified electrode (X. Yang et al., 2016).

EAS area of the modified electrodes was calculated from the slope of the anodic peak current (I_{pa}) *vs.* the square root of the scan rate ($V^{1/2}$) plot and for comparison from the slope of cathodic peak current (I_{pc}) *vs*. $V^{1/2}$ (Table 8). The values of diffusion coefficient Dox and D_{red} were taken at $7.63 \times 10^{-6}$and 6.50×10^{-6} cm^2 s^{-1}, respectively. The result shows that the values of EAS for ternary CuO/ZrO_2@S-doped g-C_3N_4 (30%) calculated from I_{pa} and I_{pc} are slightly higher than those of the binary-modified electrodes. As presented in Table 8, incorporation of CuO and ZrO_2 in the S-doped g-C_3N_4 and introduction to the FTOE layer surface results in an increase in the electroactive surface area.

Table 8. EAS of the modified electrodes calculated from the dependence of I_{pa} and I_{pc} *vs.* $v^{1/2}$ determined in 5 mM Fe $(CN)_6^{3-/4}$ in 0.1M KCl.

Electrode	Anodic peak		Cathodic peak	
	I_{pa}*vs.*$v^{½}$slope	EAS, cm^2	I_{pc}vs.$v^{1/2}$ slope	EAS, cm^2
CuO@S-doped g-C_3N_4 (30%)	0.039	0.069	0.005	0.214
ZrO_2@S-doped g-C_3N_4 (20%)	0.017	0.234	-0.013	0.275
CuO/ZrO_2@S-doped g-C_3N_4 (30%)	0.075	1.039	-0.040	0.545

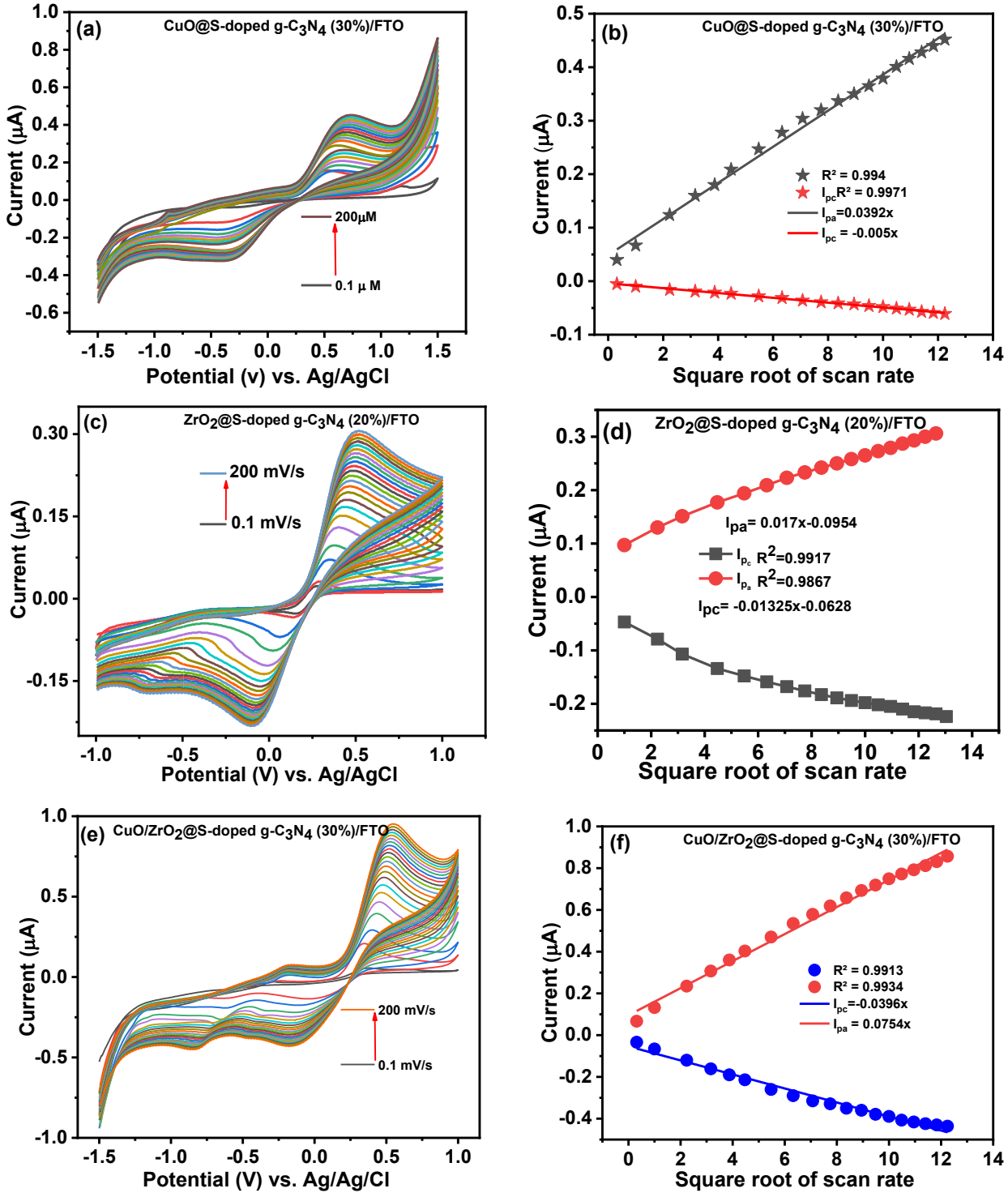

Figure 69. Effect of different scan rates (0.1 – 200 mV s^{-1}) and the corresponding plot of current *vs.* square root of scan rate for (a) CuO@S-doped g-C_3N_4 (30%)/FTOE, (c) ZrO_2@S-doped g-C_3N_4 (20%)/FTOE and (e) CuO/ZrO_2@S-doped g-C_3N_4 (30%)/FTOE (0.1 M KCl; 5 mM $Fe(CN)_6^{3-/4-}$).

Mott-Schottky (M-S) measurements were conducted to determine flat band potential values and electronic band structure shifts in 0.5 M Na_2SO_4 in the absence of light (Figure 70a–g). The positive slope of the tangent lines in Figures 70a, b, d and indicate that pristine g-C_3N_4, S-doped g-C_3N_4 and ZrO_2 NP and CuO@S-doped g-C_3N_4 (30%) NCs are n-type semiconductors for which the conduction band (CB) potential can be estimated from its flat band. For ZrO_2@S-doped g-C_3N_4 (20%) NC, CuO NPs and CuO/ZrO_2@S-doped g-C_3N_4(30%) a typical p-type semiconductor with negative slope was observed (Figure 70 c, e). Its highest valence band (VB) potential could be estimated from its flat-band potential (R. Wang et al., 2021).

To propose and compare the band structures of the binary CuO@S-doped g-C_3N_4 (30%), ZrO_2@S-doped g-C_3N_4 (30%), and ternary CuO/ZrO_2@S-doped g-C_3N_4 (30%) NCs and investigate the contribution of CuO and ZrO_2 NPs on the charge transfer the measured EIS potentials were analyzed by Nernst equation (Equation 8). By using the Nernst equation, the measured potentials can be converted to the reversible hydrogen electrode (RHE) scale.

$$E_{RHE=E_{Ag/AgCl}} +0.05916\ pH+E^{o}_{Ag/AgCl} \quad (8)$$

where $E_{RHE}$is the converted potential *vs* RHE, $E_{Ag/AgCl}$ is the experimental potential measured against the Ag/AgCl reference electrode, and $E^{o}_{Ag/AgCl}$ refers to the standard potential of Ag/AgCl at 298 K (0.1976 V). The calculated CB of g-C_3N_4, S-doped g-C_3N_4, ZrO_2, and CuO@S-doped g-C_3N_4 (30%)/FTOE were found to be 0.20. eV 0.04, -0.56, and 0.07 eV respectively, while the VB for ZrO_2@S-doped g-C_3N_4, CuO and CuO/ZrO_2@S-doped g-C_3N_4 (30%) was -0.45, 2.54 and -0.39 eV respectively. From the calculated VB and CB energies for CuO@S-doped g-C_3N_4 (30%)/FTOE, it can be concluded that the proposed n-type semiconductor exhibits optimum band gap energy. This is due to the synergistic effects among g-C_3N_4, S-doped g-C_3N_4 and CuO. Shifting of VB and CB has been observed to form CuO@S-doped g-C_3N_4 which in turn creates improved, a new electronic bad structure, and optical property.

With a similar notion, in the ZrO_2@S-doped g-C_3N_4 NC, the difference in the V_{fb} (the shift of the Fermi level) causes the electric field to form over the heterojunctions at the interface between g-C_3N_4, S-doped g-C_3N_4, and ZrO_2 semiconductors.

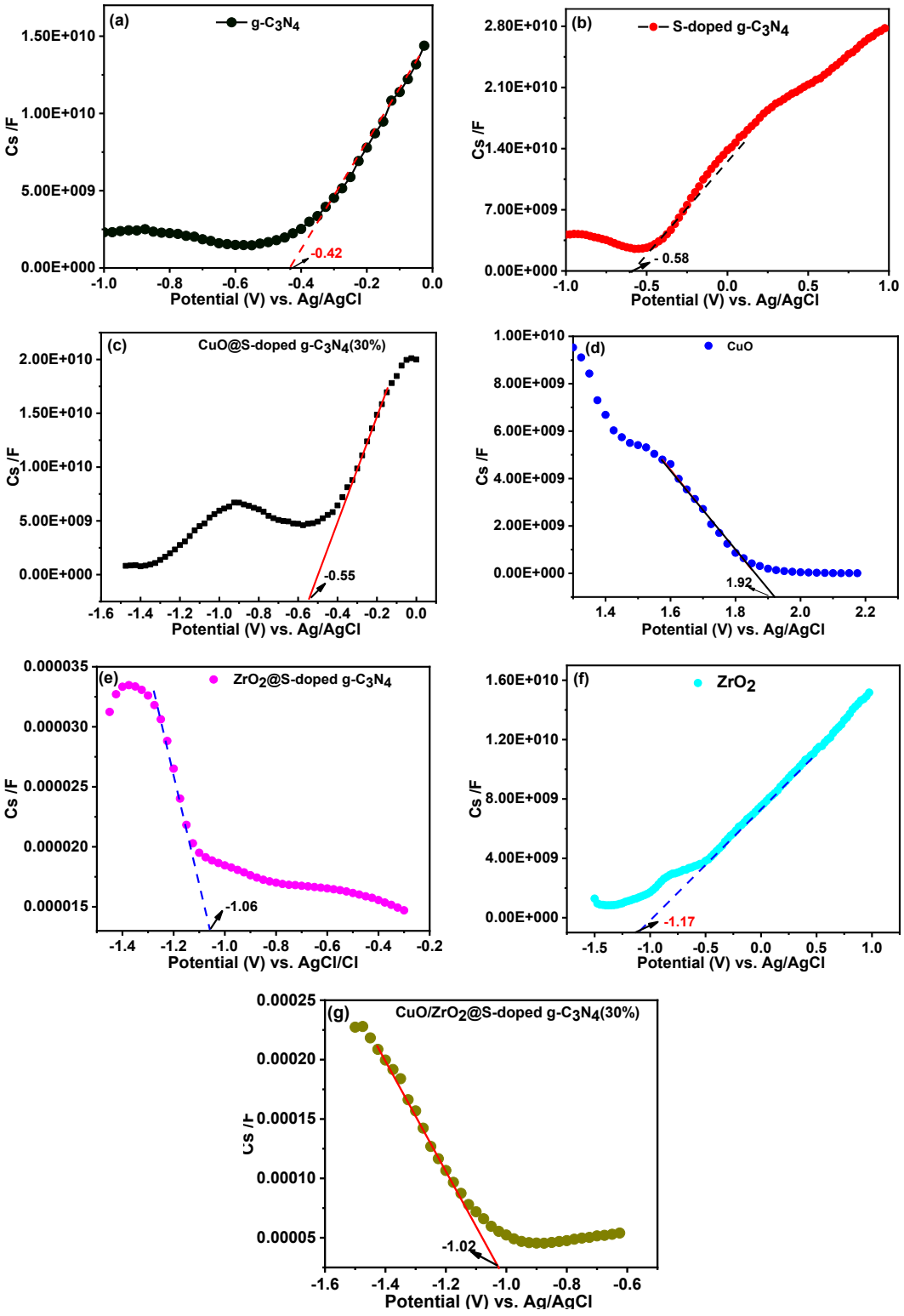

Figure 70. Mott–Schottky curve for (a) pristine g-C_3N_4, (b) S-doped g-C_3N_4, (c) CuO@S-doped g-C_3N_4(30%), (d) CuO, (e) ZrO_2@S-doped g-C_3N_4(20%). (f) ZrO_2 and (g) CuO/ZrO_2@S-doped g-C_3N_4 (30%) at a frequency of 1000 Hz in the dark.

In the meantime, the balance of the Fermi level between the pristine g-C_3N_4, S-doped g-C_3N_4 and ZrO_2 can be formed due to the movement of electrons and holes. The electron shift from V_B to C_B will modify both the energy and the momentum, which is a characteristic of an indirect band heterojunction semiconductor. This assumption was made based on Figure 71 b's explanation that S and ZrO_2 doping had a major impact on the C_B and V_B edge. A similar reason works for ternary CuO/ZrO_2@S-doped g-C_3N_4. Consequently, the built-in electric field of heterojunctions efficiently simplifies the separation of electrons and holes and ultimately enhances the electrocatalytic performance of CuO@S-doped g-C_3N_4, ZrO_2@S-doped g-C_3N_4 and CuO/ZrO_2@S-doped g-C_3N_4 NC heterojunctions. Since V_B and C_B have changed, the overall optical gap energy for CuO@S-doped g-C_3N_4(30%), ZrO_2@S-doped g-C_3N_4(20%) and CuO/ZrO_2@S-doped g- C_3N_4, (30%) have decreased as a result (Dhanasekaran et al., 2019).

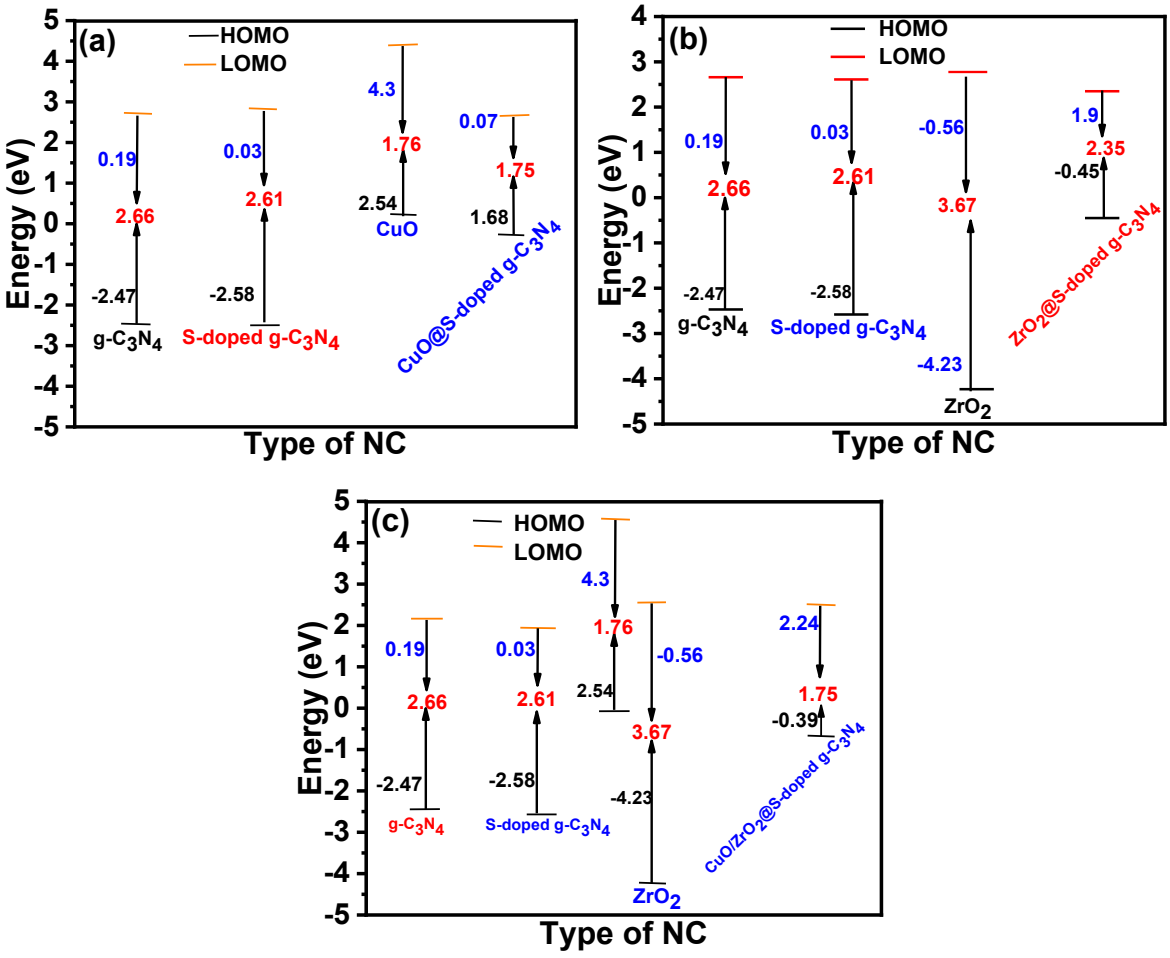

Figure 71. Comparison between proposed band structures of (a) CuO@S-doped g-C_3N_4, (b) ZrO_2@S-doped g-C_3N_4 and (c) NCs CuO/ZrO_2@S-doped g-C_3N_4 and their components.

4.5.2 Electrochemical behaviors of 4-NP at the FTO-modified electrodes

Typically, experimental parameters significantly influence electrochemical redox reactions. To increase the sensitivity of the modified electrochemical sensors, some experimental parameters such as pH and 4-NP concentration were optimized using 0.01g of CuO@S-doped g-C_3N_4 (30%)/FTOE, ZrO_2 S-doped g-C_3N_4 (20%)/FTOE and CuO/ZrO_2@ S-doped g-C_3N_4 (30%)/FTOE. For the detection of 4-NP, the fabricated electrodes were used in an aqueous media system at room temperature conditions.

Regarding the effect of pH, there are controversies among researchers concerning the effect of acidic and alkaline environments on redox processes. A few authors concluded that the acidic pH is favorable for the redox reactions of phenolic and nitro compounds, whereas some researchers reported alkaline pH is favorable for the redox reactions. Consequently, the electrochemical behavior of CuO@S-doped g-C_3N_4 (30%)/FTOE, ZrO_2@S-doped g-C_3N_4(20%)/FTOE and CuO/ZrO_2@S-doped g-C_3N_4 (30%)/FTOE was studied by using cyclic voltammetry in 0.1 M PBS, 0.5 mM 4-NP, 0.01g NCs, and various pH of 3, 5, 7, 9 and 11 (inset 9 and 11) at 50 mV s^{-1} scan rate was studied (Figure 72a-c).

The strong pH-dependent property of modified electrodes reveals the involvement of proton-accessible species. This study showed that the stability of the designed sensor was pH dependent, with the highest peak current and stability at pH = 5.0 for CuO@S-doped g-C_3N_4 (30%)/FTOE, at pH=3 for both ZrO_2@S-doped g-C_3N_4 (20%)/FTOE and CuO/ZrO_2@S-doped g-C_3N_4 (30%)/FTOE. At alkaline pH, the OH group concentration in the electrolyte solution increases. Since 4-NP also contains a hydroxyl group, intermediate polymer products may form by reaction with OH groups in the 4-NP and the surrounding environment. The formation of these polymeric intermediates will create a barrier for the flow of electrons during the electrochemical reaction of 4-NP at alkaline media. Hence, an acidic environment is more favorable for the redox reactions of 4-NP than alkaline pH, in agreement with previous reports (G et al., 2021). The higher reduction peak current may be due to the electrostatic attraction between 4-NP and the modified electrodes (CuO@S-doped g-C_3N_4 (30%)/FTOE, ZrO_2@ S-doped g-C_3N_4(20%) FTOE, and CuO/ZrO_2@S-doped g-C_3N_4 (30%)/FTOE). Thus, pH 3 was chosen for ZrO_2@S-doped g-C_3N_4 (20%)/FTOE while pH=5 for CuO@S-doped g-C_3N_4 (30%)/FTOE and CuO/ZrO_2@S-doped g-C_3N_4 (30%)/FTOE for the further 4-NP detection studies.

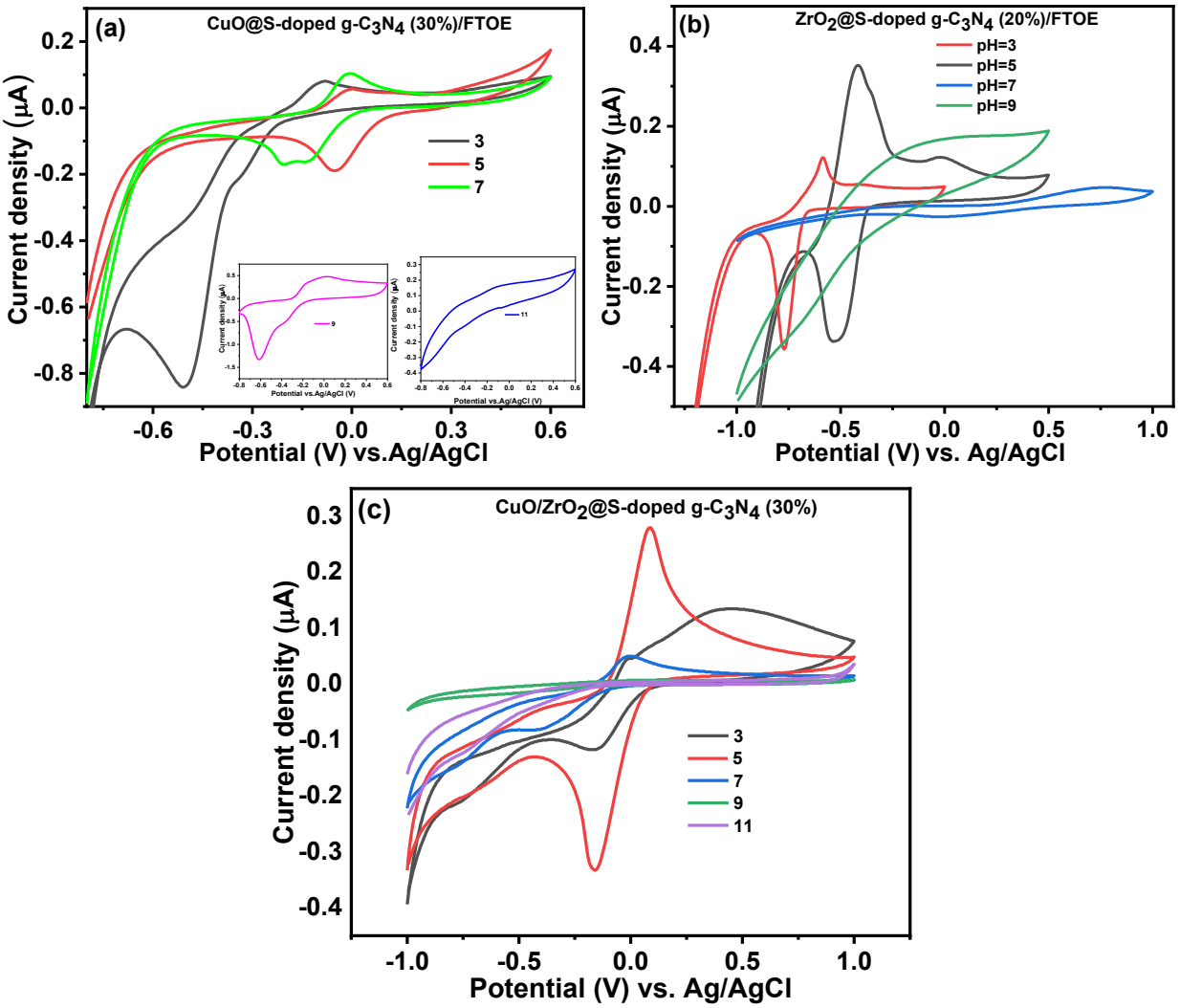

Figure 72.CV for (a) CuO@S-doped g-C_3N_4 (30%)/FTOE b) ZrO_2@ S-doped g-C_3N_4 (20%)/FTOE and (c)CuO/ZrO_2@S-doped g-C_3N_4(30%)/FTOE under different pH conditions using 0.1 M PBS, 0.5 mM 4-NP, 0.01g NCs and scan rate of 50 mV s^{-1}.

The response of CuO@S-doped g-C_3N_4 (30%)/FTOE, ZrO_2@S-doped g-C_3N_4 (20%)/FTOE and CuO/ZrO_2@S-doped g-C_3N_4 (30%)/FTOE towards detecting 4-NP at different concentrations was recorded and the results are presented in Figure 73a-c. The CVs were recorded at different concentrations (0.1 µM to 200 µM) of 4-NP in 0.1 M PBS and a scan rate of 50 mV s^{-1}. Current change was monitored as a function of 4-NP concentration using CuO@S-doped g-C_3N_4 (30%)/FTOE, ZrO_2@S-doped g-C_3N_4(20%)/FTOE and CuO/ZrO_2@S-doped g-C_3N_4 (30%)/FTOE as sensor. The results revealed that the current response increases with increasing concentration of 4-NP. By taking the current at a higher point for CuO@S-doped g-C_3N_4 (30%)/FTOE (0.65µA),

ZrO_2@S-doped g-C_3N_4 (20%)/FTOE (0.673 μA) and CuO/ZrO_2@S-doped g-C_3N_4 (30%)/FTOE (0.1115 μA), a calibration curve of the peak current against 4-NP concentration was plotted which indicates dependence of peak current on 4-NP concentration about CuO@S-doped g-C_3N_4 (30%)/FTOE, ZrO_2@S-doped g-C_3N_4(20%)/FTOE and CuO/ZrO_2@S-doped g-C_3N_4 (30%)/FTOE. The linear regression equation for CuO@S-doped g-C_3N_4 (30%)/FTOE is I_{pa} (μA)= 0.0067*C (μM), with a correlation coefficient of 0.982, for ZrO_2@S-doped g-C_3N_4 (20%)/FTOE is I_{pa} (μA) = -0.00137*C (μM), with a correlation coefficient of 0.969 and for CuO/ZrO_2@S-doped g-C_3N_4 (30%)/FTOE is I_{pa} (μA) = 0.00467*C (μM), with a correlation coefficient of 0.867, The results suggest that the fabricated sensors are very promising candidates as a sensor for detection of 4-NP under optimized experimental conditions at lower concentration of the pollutant.

The electrochemical performance of the modified CuO@S-doped g-C_3N_4 (30%)/FTOE, ZrO_2@S-doped g-C_3N_4 (20%)/FTOE and CuO/ZrO_2@S-doped g-C_3N_4 (30%)/FTOE for the estimation of 4-NP in 0.1 M of PBS was evaluated by DPV as the very sensitive and selective method. Figure 73(a, c and e) shows the representative DPV responses corresponding to the redox of various concentrations of 4-NP. The result indicates that the peak current gradually increases upon successive 4-NP additions. The linear calibration plot of the reduction peak current *vs.* concentration of 4-NP indicates the dependence of peak current on 4-NP concentration as shown in Figure 73 b, d and f. This shows the sensitivity of DPV of 4-NP with various concentrations. Towards detection of 4-NP, DPV data were further analyzed for further parameters such as LOD, sensitivity, and LOQ. The LOD of the binary and ternary modified electrodes was calculated using the equation reported elsewhere. The LOD of 4-NP was calculated from the slope of the calibration plot according to Equation 9.

$$LOD = 3.3 \times \sigma/S \quad (9)$$

where σ is the standard deviation, and S is the slope of the calibration curve.

As a result, the newly developed electrodes; CuO@S-doped g-C_3N_4 (30%)/FTOE, ZrO_2@S-doped g-C_3N_4 (20%)/FTOE and CuO/ZrO_2@S-doped g-C_3N_4 (30%)/FTOE exhibited a low detection limit and excellent sensitivity of 4-NP Table 9.

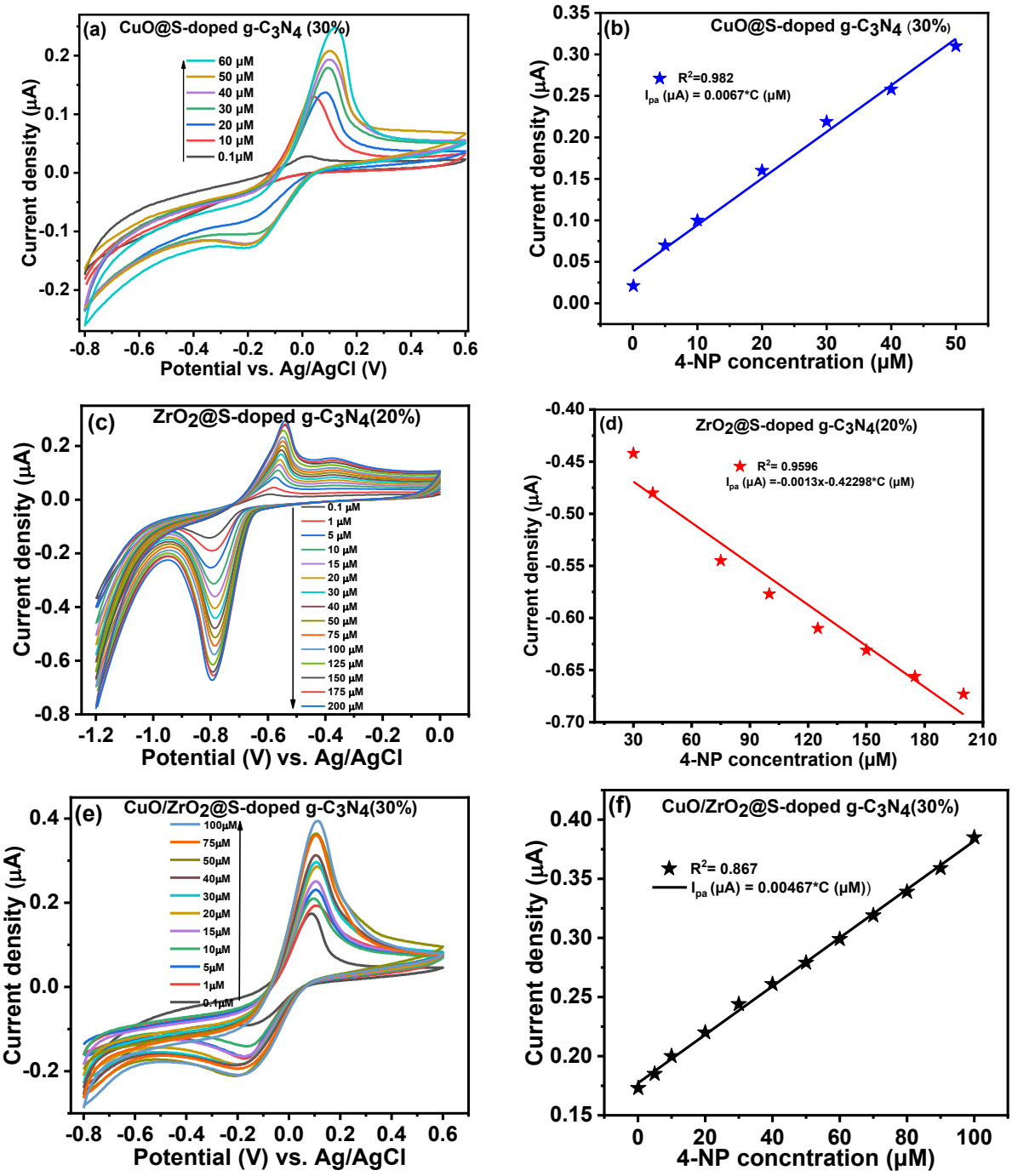

Figure 73. CV for (a) CuO@S-doped g-C_3N_4 (30%)/FTO, (b) ZrO_2@S-doped g-C_3N_4 (20%)/FTO and CuO/ZrO_2@S-doped g-C_3N_4 (30%)/FTO under different concentrations of 4-NP at a range of 0.1 µM – 200 µM. The calibration (b, d and f) plot for the corresponding (a, c and e) 4-NP concentrations against peak current (0.1 M PBS, pH 5.0 and a scan rate of 50 mV s^{-1}.

Thus, the DPV technique offered satisfactory analytical electroactive catalytic performance for detecting 4-NP. The analytical performance of the CuO@S-doped g-C_3N_4 (30%)/FTOE, ZrO_2@S-doped g-C_3N_4(20%)/FTOE and CuO/ZrO_2@S-doped g-C_3N_4(30%)/FTOE was compared with that of different modified electrodes reported in recent decades as summarized in Table 9.

On the other hand, the sensitivity of the modified electrodes was calculated from the slope of the calibration plot (Figure 74) and the EAS of the electrode. The modified electrode sensing ability was compared to the previous reports for 4-NP detection which are mentioned in Table 9. Generally, the result indicates that the modified electrodes are comparable with the previous works. Although the modified electrodes described in the table are not constructed from FTO, the manufactured sensors used in this study showed high 4-NP detection limits and good sensitivity with satisfactory linear range and high correlation coefficient. It is clearly due to CuO, ZrO_2 and S-doped g-C_3N_4 that produces a synergistic effect. The synergistic effect of cations Cu (II) and ZrO_2 +4 is contributed to in terms of better sensitivity. However, the high LOD could be due to the saturation of the kinetic behavior of the electrode processes during the reaction process. Although some other materials achieve the same or even better detection performance, these materials listed in the table require complicated synthesis processes, utilize poisonous chemicals, and demand expensive instruments, however, the S-doped g-C_3N_4 a single-step approach merged with CuO and ZrO_2 with no toxicity and simple preparation procedure and low cost. The LOQ was calculated using the Equation 10.

$$LOQ = 10\left(\sigma/S\right) \qquad (10)$$

Based on the above equation, the calculated value of LOQ was 37.9 μM,41.2 μM and 45.3 μM for CuO@S-doped g-C_3N_4(30%)/FTOE, ZrO_2@S-doped g-C_3N_4(20%)/FTOE and CuO/ZrO_2@S-doped g-C_3N_4(30%)/FTOE respectively. Even though the electrodes listed in Table 9 are chemically modified glassy carbon electrodes and have lower detection limits than what is reported here, most of them have a smaller linear range than that of the present work indicating that the fabricated sensors have a wider application range. In addition, even though Ag@Co-Al/PoPD/GCE exhibited outstanding performance with a wider linear range and lower detection limit, the hydrothermal synthesis method is more complicated with multiple and longer time steps than the simple chemical precipitation method applied in the preparation of CuO@S-doped g-C_3N_4/FTO (30%), ZrO_2@S-doped g-C_3N_4 (20%)/FTOE, and CuO/ZrO_2@S-dopedg-C_3N_4(30%)

(Rajkumar et al., 2018). In conclusion, the comparison shows the ternary NCs to provide the best platform for the 4-NP examination reported to date.

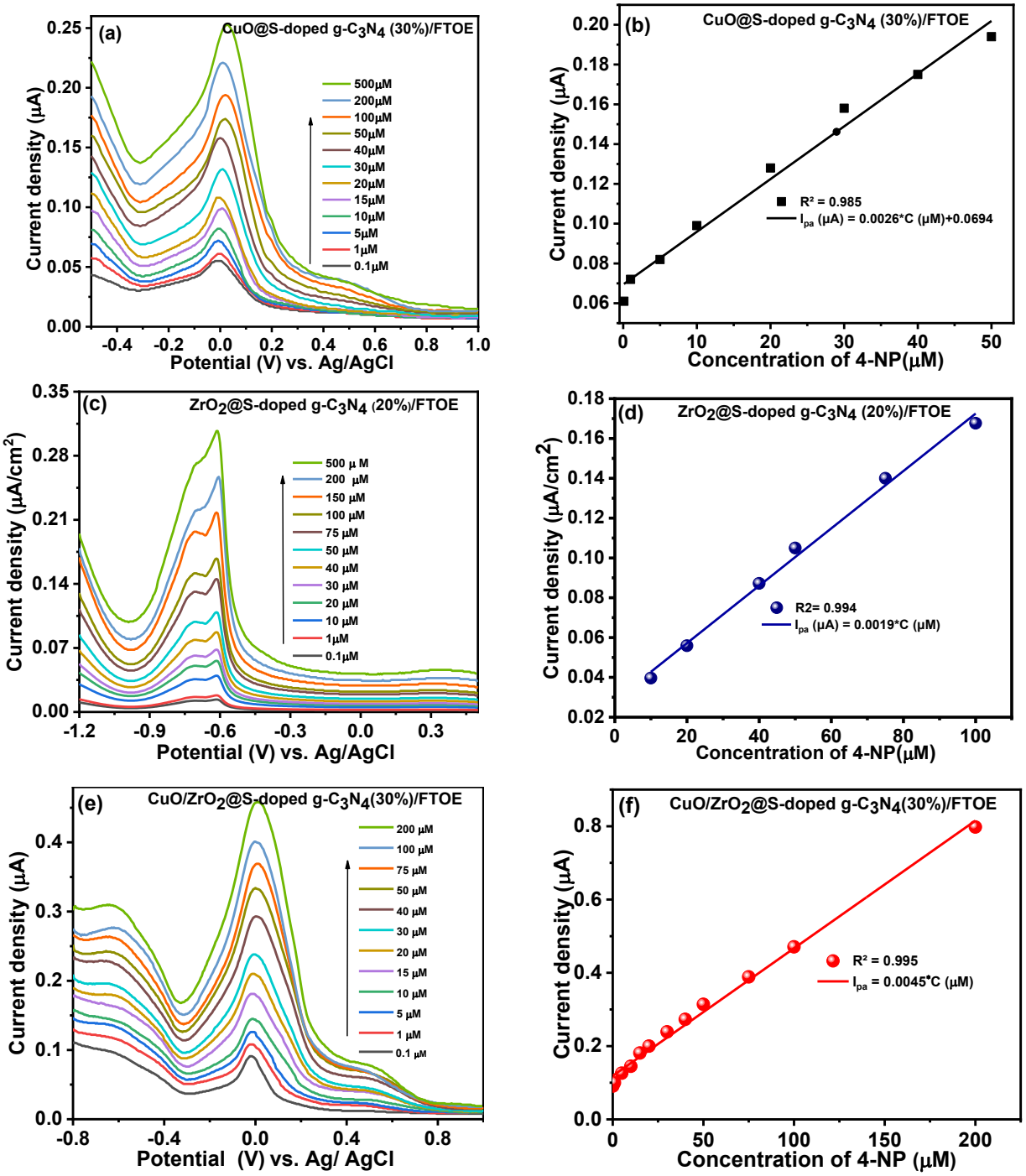

Figure 74. DPV at different concentrations of 4-NP at the (a) CuO@S-doped g-C_3N_4 (30%)/ FTOE (b) ZrO_2@S-doped g-C_3N_4 (20%)/FTOE, and (c) CuO/ZrO_2@S-doped g-C_3N_4(30%) and (b, d and f) the corresponding linear fit. Experimental conditions 0.1 M PBS, scan rate 50 mV s^{-1}.

Table 9. Comparison of previously reported results for determination of 4-NP with the current work

odified electrode	Detection method	Linear range (μM/nM)	R^2	detection limit (μM/nM)	Sensitivity ($\mu A \mu M^{-1} cm^{-2}$)	Ref.
O/ZrO_2@GCE	Amperometry	50-800 μM	0.998	14.5 μM	0.28	(Cheng, 2017)
GCN/SPCE[a]	DPV	0.05–90 μM	0.994	0.0016 μM	12.655	(S. Singh et al., 2017)
GO/Fe_3O_4NPs/GCENP[b]	DPV	0.2 – 10	0.998	0.26 μM	N/A	(P. Chen, 2018)
o-synthesized CuO NPs	SWV	10 nM – 10 mM	0.992	0.1 nM	N/A	(Dhanasekaran et a 2019)
LISS/GCE[c]	DPV	1.43 - 55.93		1.09 μM	N/A	(Bhujel et al., 2019)
g@Co-Al/PoPD/GCE[d]	DPV	0.82x10^{-9} – 1.74x 10^{-6} M	0.999	63.7 nM	N/A	(Mohammad, Khan, e al., 2020)
O@S-doped g-C_3N_4/FTO (30%)	DPV	0.1-200 μM	0.985	12.5 μM	0.017	This work
O_2@S-doped g-C_3N_4/FTO (20%)	DPV	0.1-200 μM	0.994	13.6 μM	0.007	This work
O/ZrO_2@S-dopedg-C_3N_4(30%)	DPV	0.1-200 μM	0.995	14.9 μM	0.004	This work

[a] Sulphur-doped graphitic carbon nitride/screen-printed carbon electrode
[b] Reduced graphene oxide/Fe_3O_4 nanoparticle glassy carbon electrode,
[c] Tremella-like indium silver sulfide glassy carbon electrode,
[d] Ag nanoparticles decorated Co-Al LDHs Co-Al layered double hydroxides (LDHs), Co-Al LDHs/poly(*o*-phenylenediamine) (PoPD)

4.5.3 Mechanism of 4-NP reduction at the modified FTO electrodes

The proposed detection mechanism of 4-NP as shown in Scheme 1, indicates the process that takes place on the surface of the modified electrodes. The first step (broad peak of DPV on Figure 74) is the result of a four-electron reduction of 4-NP to *p*-hydroxylaminophenol. The *p*-hydroxyl aminophenol then simply undertakes a two-electron oxidation process to give the *p*-nitrophenol. On the second narrow peak, the *p*-nitrophenol is then reduced through a reversible two-electron process back to the *p*-hydroxylaminophenol producing the redox couple. This is in line with the previously reported mechanism for the reduction of 4-NP using silver-decorated glassy carbon electrodes (Apetrei et al., 2011).

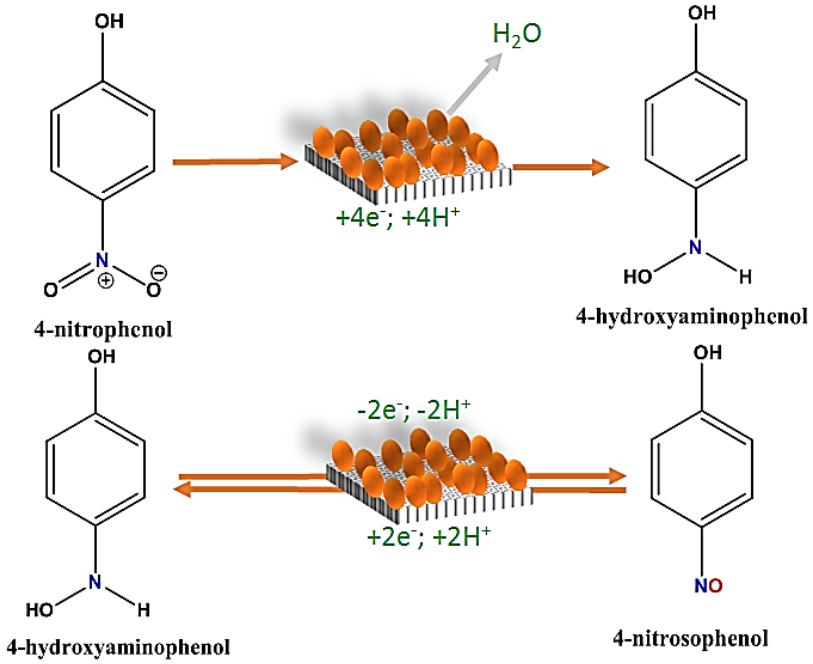

Scheme 1. Proposed mechanism for a 4-NP reduction on modified electrodes

4.6 Electrochemical behaviors of BPA at the carbon paste-modified electrodes

In this work, BPA was used as a pollutant chemical to further test the synthesized NCs' detecting capabilities. CPE was used to test the sensing performance of the binary and ternary NCs for BPA.

The electrochemical behavior of g-C_3N_4/CPE, S-doped g-C_3N_4/CPE, CuO@S-doped g-C_3N_4 (30%)/CPE, ZrO_2@S-doped g-C_3N_4 (20%)/CPE, CuO/ZrO_2@S-doped g-C_3N_4(30%)/CPE and the bare CPE was investigated using a 0.1nM BPA, scan rate 50mv/s and pH=5. The results are presented in Figure 75(a-f). It can be observed easily that except the bare CPE, the remaining

modified CPE electrodes exhibited a well-defined CV peak with various electron transfer capabilities. The bare CPE shows low electron transfer in comparison with other electrodes. This is due to its poor electrical conductivity, which limits the electron transfer probe of BPA on the surface of the CPE. The CV behavior of modified electrodes might have different shapes of redox probes at the electrode interfaces. Nevertheless, the binary CuO@S-doped g-C_3N_4(30%)/CPE, ZrO_2@S-doped g-C_3N_4(20%)/CPE and ternary CuO/ZrO_2@S-doped g-C_3N_4(30%)/CPEs showed a well-defined peak current, which gave an efficient electron transfer capability, enhanced electrical conductivity and large surface area of the NCs. Through scan rate and the impact of BPA concentration in identical experimental trends, the electrochemical responses of modified electrodes made of binary and ternary NCs/CPE materials to BPA were ascertained.

4.6.1. Effect of scan rate

To establish whether the mechanism of the electrochemical responses was diffusion-controlled or not, experiments were carried out at different scan rates. This can be understood by analyzing scan rate (ν) dependent oxidation peak currents and peak potentials for the modified pristine g-C_3N_4 /CPE, S-doped g-C_3N_4 /CPE, binary CuO@ S-doped g-C_3N_4 (30%)/CPE, ZrO_2@S-doped g-C_3N_4 (20%)/ CPE and ternary CuO/ZrO_2@ S-doped g-C_3N_4 (30%)/CPE sensors in the presence of BPA (10, 20, 30, 40, 50 mVs^{-1}). Consequently, the maximum peak current intensity of the analyte (PBA) was observed in the condition (BPA=0.1nM and pH=5). Figures 76 and 77 show the relation between peak current and scan rate for CP modified electrodes. Furthermore, to evaluate the molecular diffusion on the surface of the modified electrode, a calibration curve was plotted between peak current and square root of scan rate within a range of 10 – 50 mVs^{-1} using 0.1 nM (Figure 76 b, and d) and Figure 77 (f, h, and j). An increase in peak current with scan rate showed that the electrocatalytic activity was successfully improved at the surface of the modified electrode. With this regard, the peak current has grown linearly with the square root of the potential scan rate, therefore, the oxidation of BPA at modified electrodes CPE is the diffusion-controlled process (Kunene et al., 2020).

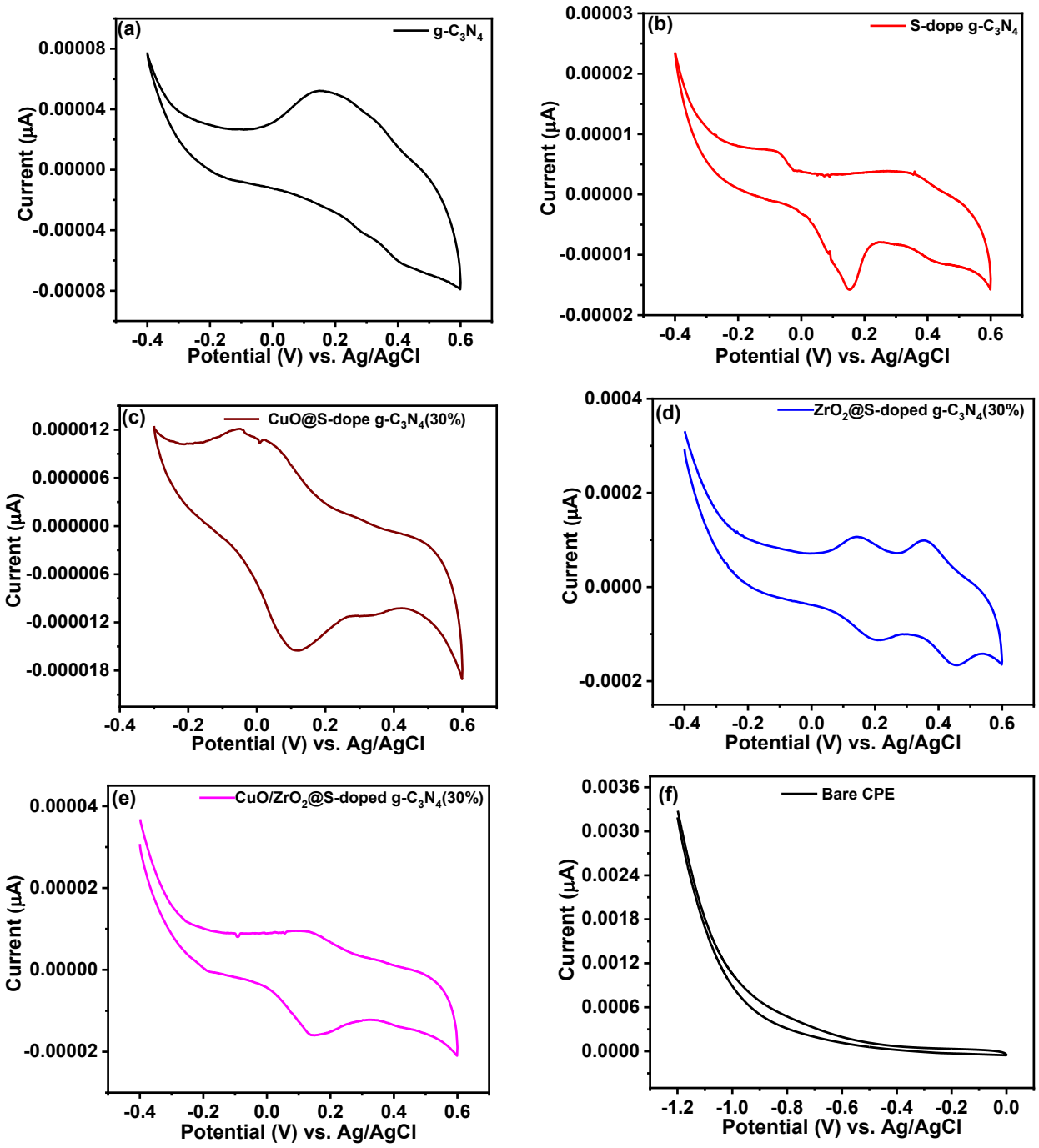

Figure 75.CV plots of (a) g-C_3N_4/CPE:(b) S-doped g-C_3N_4/CPE:(c) CuO@S-doped g-C_3N_4 (30%)/CPE: (d) ZrO_2@S-doped g-C_3N_4(20%)/CPE: (e) CuO/ZrO_2@S-doped g- C_3N_4(30%)/CPE: and (f) bare CPE. Experimental conditions: pH=5, BPA=0.1nM, and scan rate 50mv/s.

When comparing intensity of peak current among the modified electrodes, the binary CuO@S-doped g-C_3N_4 (30%)/CPE shows maximum peak current with -1.219e-5 A at potential value of

0.156V, ZrO_2@S-doped g-C_3N_4(20%)/CPE, -7.939e-5 A at potential value of 0.230 V and ternary CuO/ZrO_2@S-doped g-C_3N_4(30%)/CPE -1.152e-5 A at a potential value of 0.166 V. The slopes of the curves follow the trend ZrO_2@ S-doped g-C_3N_4 (20%)/CPE > CuO/ZrO_2@ S-doped g-C_3N_4 (30%)/CPE > CuO@S-doped g-C_3N_4 (30%)/CPE, indicating that the electron transfer is faster at the ZrO_2@ S-doped g-C_3N_4 (20%)/CPE than in CuO/ZrO_2@ S-doped g-C_3N_4 (30%)/CPE and CuO@ S-doped g-C_3N_4 (30%)/CPE (Zheng & Andou, 2022).

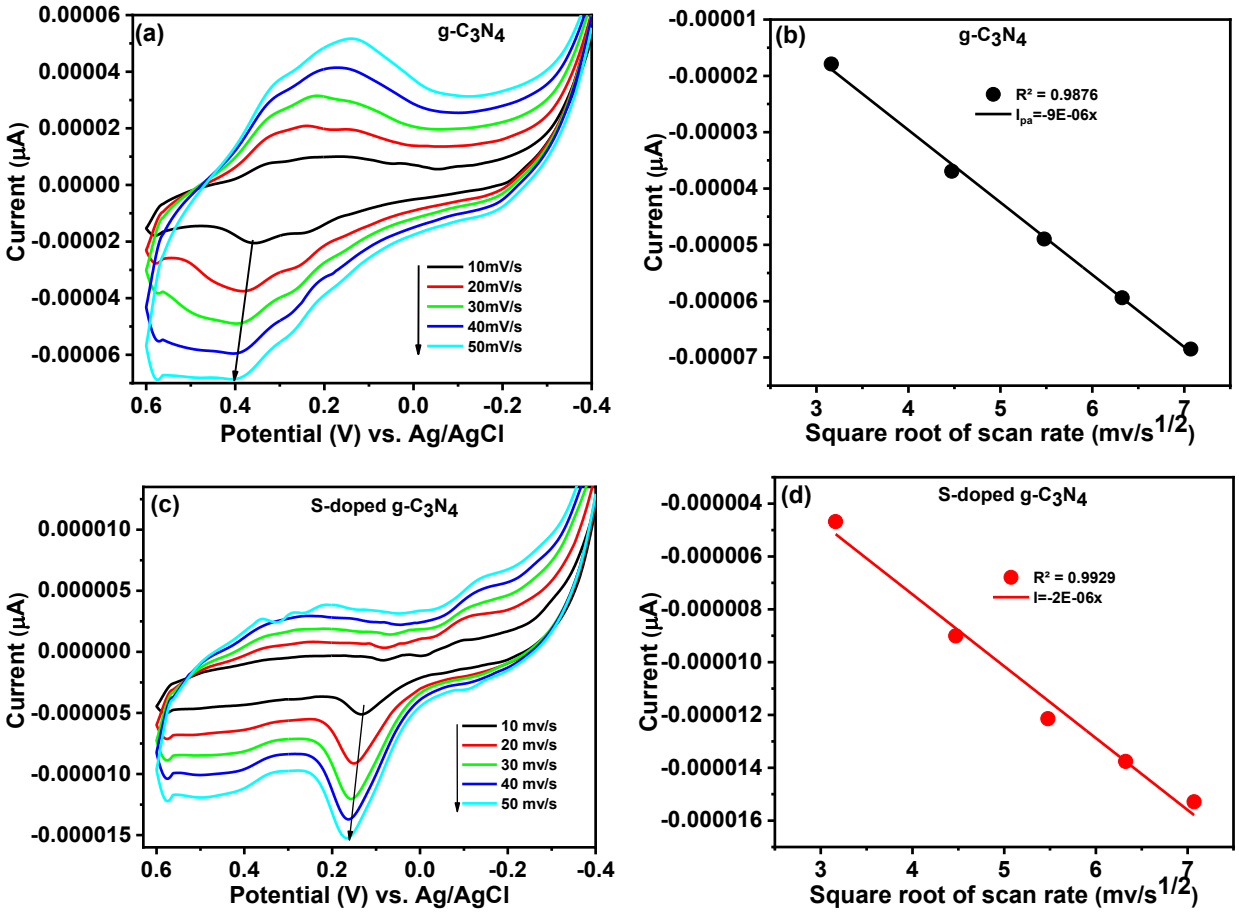

Figure 76.CV of BPA curves of (a) g-C_3N_4 (c) S-doped g-C_3N_4 at different scan rates: (b and d) relationship between peak current *vs*. square root of scan rate derived from the CV curves of Figure (a and c) respectively). BPA=0.1nM and pH=5.

4.6.2 Effect of concentration of Bisphenol A

To check the quantitative chemical analysis of the modified electrodes, the relationship between the anodic current and concentration of BPA was studied using the CV technique. The electrochemical responses obtained using the modified CPEs for different concentrations of BPA

solutions with a scan rate of 50 mv/s and the potential ranged between −0.5 V and 0.9 V are illustrated in Figure 78 (a. b and c). The three modified CPEs used in this work produced a similar response towards BPA. The CV cycles were different from the subsequent ones and consisted of one anodic broad peak at CuO@S-doped g-C_3N_4 (30%)/CPE slightly sharp anodic peak at ZrO_2@S-doped g-C_3N_4(20%)/CPE and some small anodic peaks at CuO/ZrO_2@S-doped g-C_3N_4(30%)/CPE was observed. In subsequent scans of concentrations from 1 to 6 nM BPA, two small anodic peaks were observed at ZrO_2@S-doped g-C_3N_4(20%)/CPE. This is because, in the electrooxidation of BPA, the two hydroxyl groups are converted to carbonyl groups by the loss of two electrons and protons.

According to the literature, two electrons and two protons (n) are involved in the electrooxidation of BPA (Kunene et al., 2020). Appendix 4 illustrates potential reaction pathways for BPA oxidation on the electrode surface of CuO@S-doped g-C_3N_4 (30%)/CPE, ZrO_2@S-doped g-C_3N_4(20%) and CuO/ZrO_2@S-doped g-C_3N_4(30%). The value of $\Delta E = 0.059V$ accomplished the reversibility criteria for CuO/ZrO_2@S-doped g-C_3N_4(30%)/CPE, whereas the CuO@S-doped g-C_3N_4(30%)/CPE and ZrO_2@S-doped g-C_3N_4(20%)/CPEs showed an important degree of quasi reversible indicated by the higher separation between the anodic and the cathodic wave.

The difference in intensity between the anodic and the cathodic wave is more marked in ZrO_2@S-doped g-C_3N_4(20%)/CPE, confirming the irreversibility at the surface of the modified CPE electrode. A calibration curve plotted for the peak current against BPA concentrations indicates the linearity of peak current on BPA concentration about CuO@S-doped g-C_3N_4 (30%)/ CPE, ZrO_2@S-doped g-C_3N_4(20%)/CPE and CuO/ZrO_2@S-doped g-C_3N_4 (30%)/CPE. The linear regression equations are as follows: for CuO@S-doped g-C_3N_4 (30%)/ CPE is I_{pa} (μA)= 4E-07*C (nM) - 1E-05 (R^2 =0.972) and for ZrO_2@S-doped g-C_3N_4 (20%)/CPE is I_{pa} (μA) = 0-5E-07*C (nM) - 1E-05, (R^2 = 0.964) and for CuO/ZrO_2@S-doped g-C_3N_4 (30%)/ CPE is I_{pa} (μA) = -8E-070*C (nM) - 1E-05 (R^2 = 0.9805), The results suggest that the fabricated sensors are a very promising candidates as a sensor for detection of BPA at lower concentration.

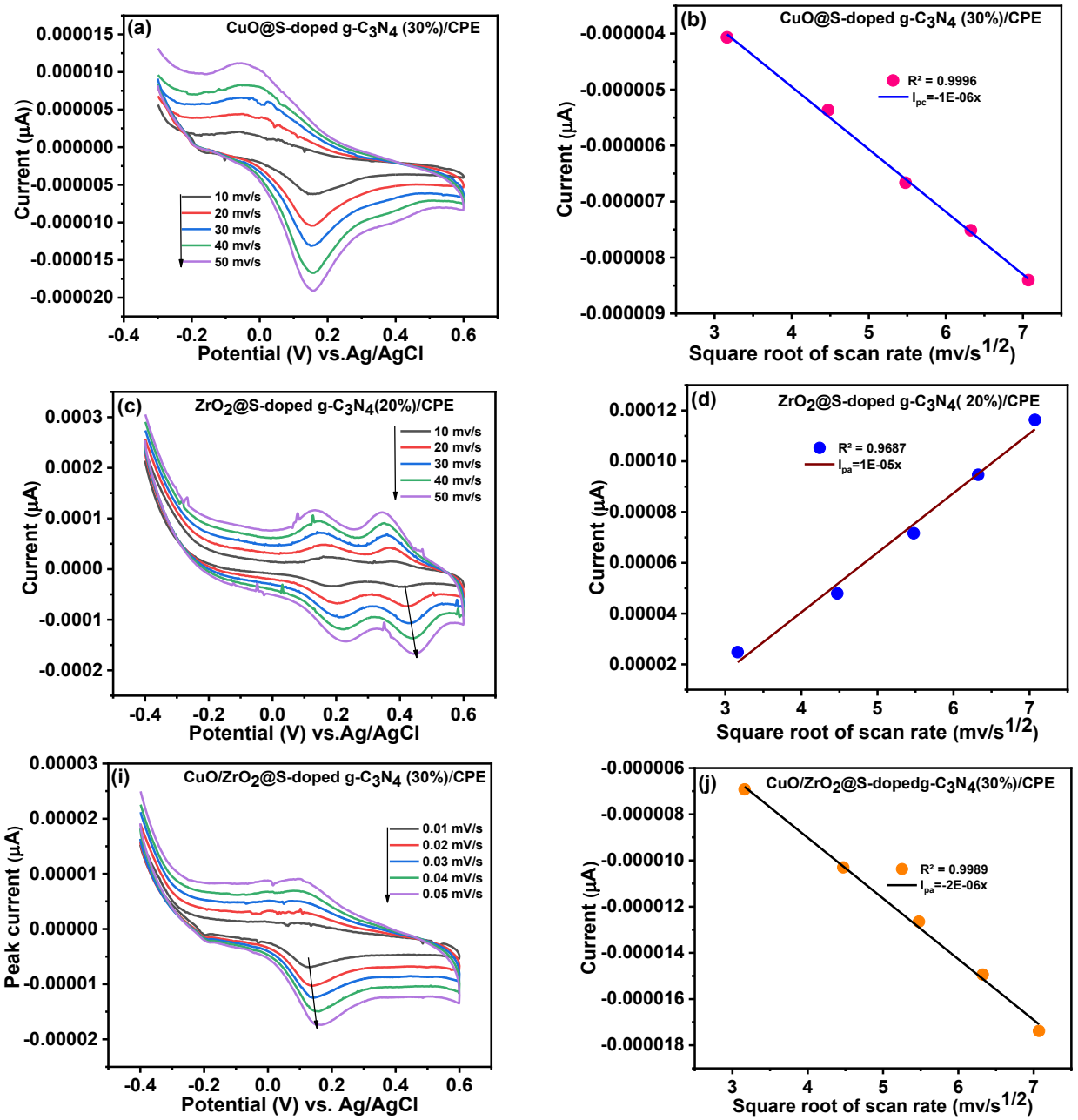

Figure 77.CV of (a) CuO@S-doped g-C_3N_4 (30%), (g) ZrO_2@S-doped g- C_3N_4(20%) and (h) CuO/ZrO_2@S-doped g-C_3N_4 (30%) at different scan rate. (f, h and j) the linear relationship between peak current *vs.* square root of scan rate derived from the CV curves of Figure (e, g and i) respectively). BPA=0.1nM and pH=5.

The CV peak current for binary CuO@S-doped g-C_3N_4 (30%)/CPE was recorded at E_p = 0.122 v with I_{pa} = -1.098e-5A, for ZrO_2@S-doped g-C_3N_4 (20%)/CPE at E_p= 0.216 v with I_{pa}= -4.436e-5A and ternary for CuO/ZrO_2@S-doped g-C_3N_4 (20%) at E_p= 0.151v with I_{pa} =-9.803e-6A

respectively, hence there is close sensitivity for BPA among the modified electrodes but the binary ZrO_2@S-doped g-C_3N_4 (20%)/CPE show maximum peak current than the rest. This is due to the synergy between the sensing activities of ZrO_2 NPs and S-doped g-C_3N_4 NC, the proposed BPA detection based on ZrO_2/g-C_3N_4 NCs can be utilized as an efficient platform for selective detection of BPA (Zheng & Andou, 2022).

The LOD of BPA was calculated from the slope value of the calibration plot according to equation (10). As a result, the newly developed binary and ternary modified CPEs exhibited a low detection limit with the values of 2.9 nM, 3.21nM and 2.03 nM for CuO@S-doped g-C_3N_4 (30%)/CPE, ZrO_2@S-doped g-C_3N_4 (20%)/CPE and CuO/ZrO_2@S-doped g-C_3N_4 (20%)/CPE respectively. The highest LOD for ZrO_2@S-doped g-C_3N_4 (20%)/CPE could be related to the interaction between the BPA and electrodes and the background current. For this reason, the conductivity of the ZrO_2@S-doped g-C_3N_4 (20%)/CPE makes difficult the detection of BPA at low concentration levels. As a result, the ternary CuO/ZrO_2@S-doped g-C_3N_4 (30%)/CPE exhibited a better detection limit. Similarly, the calculated LOQ values were 9.73, 8.79, and 6.16 nM respectively for binary CuO@S-doped g-C_3N_4(30%)/CPE, ZrO_2@S-doped g-C_3N_4(20%)/CPE and CuO/ZrO_2@S-doped g-C_3N_4 (30%)/CPE. A good LOD and LOQ value for ternary CuO/ZrO_2@S-doped g-C_3N_4 (30%)/CPE is attributed to the better synergistic effect between CuO, ZrO_2 and S-doped g-C_3N_4 and moderate specific surface area than CuO@S-doped g-C_3N_4 (30%) and ZrO_2@S-doped g-C_3N_4 (20%) NCs.

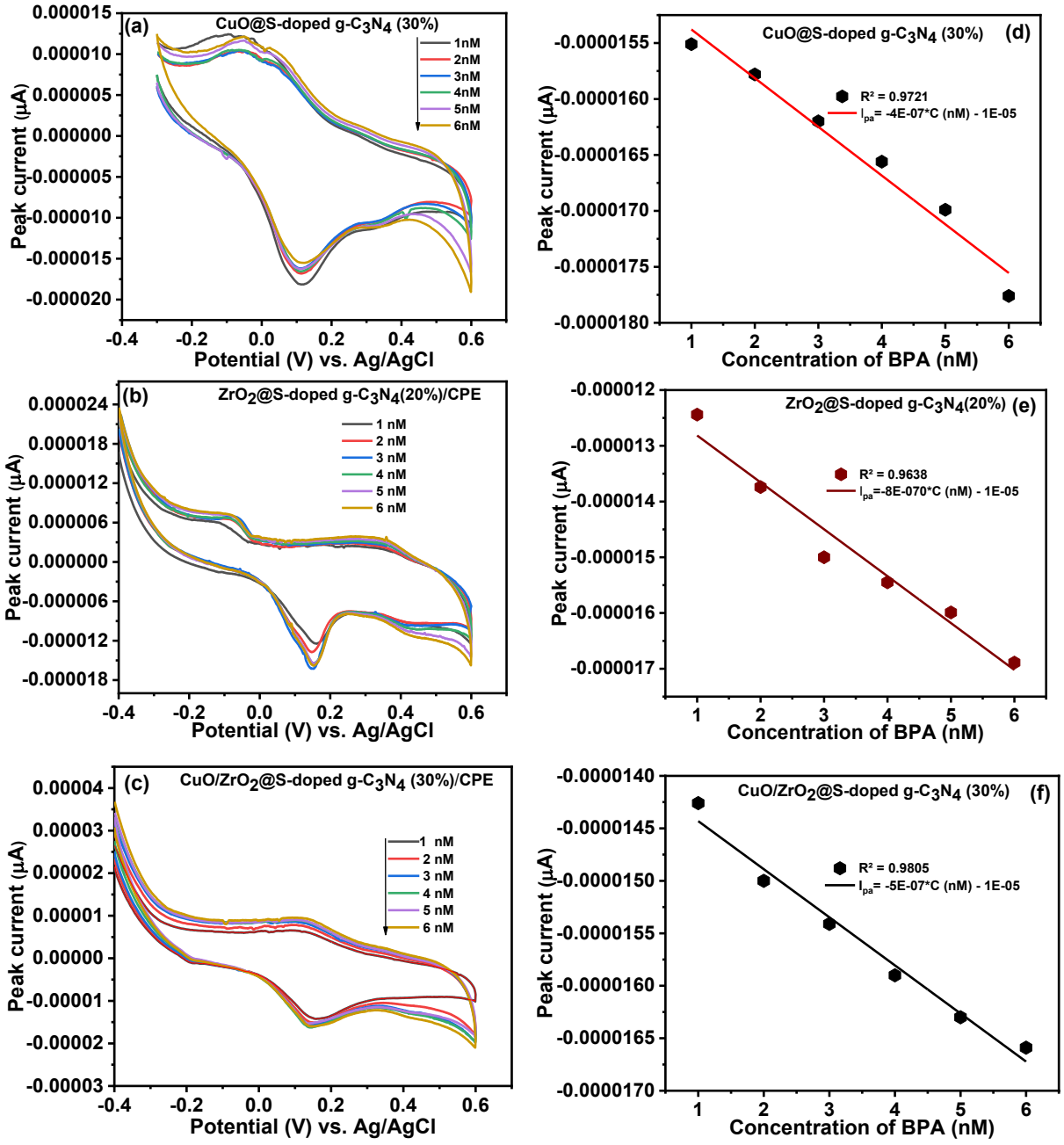

Figure 78.CV of CuO@S-doped g-C_3N_4 (30%)/CPE (b) ZrO_2@S-doped g-C_3N_4(20%) and CuO/ZrO_2@S-doped g-C_3N_4 (30%) at different concentrations of BPA (1nM-6nM), pH= 5, scan rate 30mv/s and (b, e, f) their linear curve of peak current vs. concentration of BPA.

5. CONCLUSIONS AND RECOMMENDATIONS

5.1 Conclusions

In this study, the gas-templating method was developed to realize the synchronous nano structuring S-doped g-C_3N_4 in one step. It uses the bottom-placed $(NH_4)_2SO_4$ as a bi-functional gas template source and doping agent to transform the up-placed urea into S-doped g-C_3N_4 at 550 ^oC. Due to its benefits over alternative synthetic methods, the bottom-up simple chemical precipitation procedure was chosen in this study. The crystallite size of the generated NCs was confirmed to be in the nanometer range using the XRD pattern and TEM investigations. The findings through UV-Vis/DRS and PL indicate that, compared to binary NCs, ternary NCs display the best electron–hole recombination rate and E_g. The BET analysis of the samples' pore size distribution reveals that the majority of the pores have adsorption isotherms of type IV and type H3 hysteresis loops and fall within the size range of 2 to 50 nm. The HR/SEM/EDS technique was used for a better understanding of the morphological and elemental composition in the inner and outer surface features of the prepared NCs. Thus, the formation of flower-shaped S-doped-g-C_3N_4, cubical structure of CuO and monoclinic structure of ZrO_2 NPs presence in the binary and ternary NCs was investigated by HRSEM/EDS study. Furthermore, an XPS analysis of the chemical composition of the binary and ternary NCs verified the occurrence and synthesis of N, C, S, CuO, and ZrO_2.

In the electro reduction of 4-NP, for the binary CuO@ S-doped g-C_3N_4 (30%), ZrO_2@ S-doped g-C_3N_4 (20%), and ternary CuO/ZrO_2@ S-doped g-C_3N_4 (30%) catalysts, the optimal loading amounts were found to be 0.05g, 0.05g, and 0.01g, respectively, and were fitted to the pseudo-first-order kinetics. An excellent reduction efficiency of 4-NP was achieved by the ternary CuO/ZrO_2@S-doped g-C_3N_4 (30%) (99.56%) NC within 300s.

The photocatalytic degradation efficiency of MB by ternary NCs increases in the sequence of CuO/ZrO_2@ S-doped g-C_3N_4(5%) < CuO/ZrO_2@ S-doped g-C_3N_4(10%) < CuO/ZrO_2@ S-doped g-C_3N_4(20%) < CuO/ZrO_2@ S-doped g-C_3N_4(30%). Overall, this study supports the notion that the synthesized binary and ternary NCs are good candidates for multifunctional uses as catalysts, sensors, and photocatalysts.

The electrochemical behaviour of the CuO@S-doped g-C_3N_4 (5,10,20,30%), ZrO_2@S-doped g-C_3N_4(5,10,20,30%), and CuO/ZrO_2@S-doped g-C_3N_4(5,10,20,30%), NCs was evaluated by CV, EIS and M-S techniques. The result obtained through CV and EIS methods exhibited a well-defined redox peak with a high electron transfer capability of the modified CuO@S-doped g-C_3N_4(30%), ZrO_2@S-doped g-C_3N_4(20%) and CuO/ZrO_2@S-doped g-C_3N_4(30%) electrodes compared to the pristine g-C_3N_4, S-doped g-C_3N_4 NCs, and CuO and ZrO_2 NPs. According to the M-S investigation, the binary CuO@ S-doped g-C_3N_4 (30%)/FTOE was an n-type semiconductor, while the ZrO_2@ S-doped g-C_3N_4 (20%)/FTOE and CuO/ZrO_2@ S-doped g-C_3N_4 (30%)/FTOE were p-type semiconductors.

Binder-free CuO@S-doped g-C_3N_4 (30%), ZrO_2@S-doped g-C_3N_4 (20%), and CuO/ZrO_2@S-doped g-C_3N_4 (30%) electrodes were modified using a drop-cast method. The results of 4-NP sensing indicate that binary and ternary NCs were suitable for electrochemical sensing applications. The scan rate analysis of the electrochemical behaviour studies supported the linear dependence of peak currents on the square root of the scan rate, indicating that the electrochemical reaction taking place at the electrodes was a diffusion-controlled process in the scan rate range of 0.1 to 200 mV s^{-1}. The slope of the anodic peak current (Ipa) vs. the square root of the scan rate ($V^{1/2}$) plot was used to compute the EAS area of the modified electrodes. The results demonstrate that the ternary CuO/ZrO_2@ S-doped g-C_3N_4 EAS values calculated from I_{pa} are marginally greater than those obtained from I_{pc}.

The modified electrodes' strong pH dependence suggests that the stability of the developed sensors was also pH-dependent, with pH = 3.0 having the highest peak current and stability. The sensitivity of the modified electrodes for the binary and ternary CuO@S-doped g-C_3N_4(30%)/FTOE, ZrO_2@S-doped g-C_3N_4(20%)/FTOE, and CuO/ZrO_2@S-doped g-C_3N_4(30%)/FTOE, respectively, was determined to be 0.017, 0.007 and 0.004 $\mu A \mu M^{-1} cm^{-2}$. The synergistic effect of the cations Cu (II) and ZrO_2 +4 with S-doped g-C_3N_4 was characterized as contributing to the higher sensitivity for ternary NC. In the study of BPA sensing activities of modified CPEs, surprisingly the binary ZrO_2@S-doped g-C_3N_4 (20%)/CPE presents the highest LOD (3.21nM) than the binary CuO@S-doped g-C_3N_4 (30%)/CPE and ternary CuO/ZrO_2@S-doped g-C_3N_4 (30%)/CPE. The newly created ternary CuO/ZrO_2@S-doped g-C_3N_4 (30%)/ CPE showed improved LOD, LOQ and sensitivity as a result.

5.2. Recommendations

The following future study areas are recommended based on the findings of the present study:

- Optimisation of synthesis-related parameters, including, solution pH, thermal properties at various calcination temperatures, time and amount of S.
- Comparing ternary CuO/ZrO_2@S-doped g-C_3N_4 NCs with further photocatalytic research utilizing binary CuO@S-doped g-C_3N_4 and ZrO_2@S-doped g-C_3N_4 NCs.
- Recyclability of the ternary and binary NCs prepared for tested applications.
- Catalytic sensor and photocatalysis application mechanisms identification by DFT
- Assessing the antibacterial activity of the synthesized binary and ternary NCs.
- Improving M-S conditions to allow the binary and ternary NCs to use their synergistic light response.
- Incorporating other kinds of metal oxides and creating S-doped g-C_3N_4 quaternary NCs, comparing and assessing them for multi-applications.

6. REFERENCES

A.~Y.~Liu, & M.~L.~Cohen. (1989). Prediction of New Low Compressibility Solids. *Science*, *245*(1988), 841–842. h

Abdollahi, M., & Mohammadirad, A. (2014). Nitrophenol, 4-. In *Encyclopedia of Toxicology* (Vol. 3, pp. 575–577). Elsevier.

Ahilandeswari, G. (2022). Enhanced sunlight-driven photocatalytic activity in assembled ZrO 2 / g-C 3 N 4 nanocomposite. *Journal of Materials Science: Materials in Electronics*, *33*(31), 23986–24002.

Aker, A., McConnell, R. E. R., Loch-Caruso, R., Park, S. K., Mukherjee, B., Rosario, Z. Y., Vélez-Vega, C. M., Huerta-Montanez, G., Alshawabkeh, A. N., & Cordero, J. F. (2020). Interactions between chemicals and non-chemical stressors: The modifying effect of life events on the association between triclocarban, phenols and parabens with gestational length in a Puerto Rican cohort. *Science of The Total Environment*, *708*, 134719.

Akhundi, A., & Habibi-Yangjeh, A. (2015). Ternary g-C3N4/ZnO/AgCl nanocomposites: Synergistic collaboration on visible-light-driven activity in photodegradation of an organic pollutant. *Applied Surface Science*, *358*, 261–269.

Al-saadi, T. M., & Hameed, N. A. (2015). *Synthesis and Structural Characterization of Copper Oxide Nanoparticles Preparation by Two Different Sol-Gel Methods Synthesis and Structural Characterization of Copper Oxide Nanoparticles Preparation by Two Different Sol-Gel Methods 1- Introduction Nano*. *June 2018*.

Alaghmandfard, A., & Ghandi, K. (2022). A Comprehensive Review of Graphitic Carbon Nitride (g-C3N4)–Metal Oxide-Based Nanocomposites: Potential for Photocatalysis and Sensing. *Nanomaterials*, *12*(2), 294.

Alebachew, N., Murthy, H. C. A., Abdissa, B., Demissie, T. B., von Eschwege, K. G., Langner, E. H. G., & Coetsee-Hugo, L. (2022). Synthesis and characterization of CuO@ S-doped gC 3 N 4 based nanocomposites for binder-free sensor applications. *RSC Advances*, *12*(46), 29959–29974.

Alegria, E. C. B. A., Ribeiro, A. P. C., Mendes, M., Ferraria, A. M., Botelho, A. M., & Pombeiro, A. J. L. (1959). *Effect of Phenolic Compounds on the Synthesis of Gold Nanoparticles and Its Catalytic Activity in the Reduction of Nitro Compounds*. 6–10.

An, T. D., Phuc, N. Van, Tri, N. N., Phu, H. T., Hung, N. P., & Vo, V. (2019). Sulfur-Doped g-

C_3N_4 with Enhanced Visible-Light Photocatalytic Activity. *Applied Mechanics and Materials*, *889*, 43–50.

Apetrei, C., Apetrei, I. M., Saja, J. A. De, & Rodriguez-Mendez, M. L. (2011). Carbon Paste Electrodes Made from Different Carbonaceous Materials: Application in the Study of Antioxidants. *Sensors*, *11*(2), 1328–1344.

Ayodhya, D., & Veerabhadram, G. (2019). Synthesis and characterization of g-C3N4 nanosheets decorated Ag2S composites for investigation of catalytic reduction of 4-nitrophenol, antioxidant and antimicrobial activities. *Journal of Molecular Structure*, *1186*, 423–433.

Babu, S. G., Karthik, P., John, M. C., Lakhera, S. K., Ashokkumar, M., Khim, J., & Neppolian, B. (2019). Synergistic effect of sono-photocatalytic process for the degradation of organic pollutants using CuO-TiO2/rGO. *Ultrasonics Sonochemistry*, *50*, 218–223.

Bai, L., Huang, H., Yu, S., Zhang, D., Huang, H., & Zhang, Y. (2022). Role of transition metal oxides in g-C3N4-based heterojunctions for photocatalysis and supercapacitors. *Journal of Energy Chemistry*, *64*, 214–235.

Bai, X., Yan, S., Wang, J., Wang, L., Jiang, W., Wu, S., Sun, C., & Zhu, Y. (2014). A simple and efficient strategy for the synthesis of a chemically tailored g-C3N4 material. *Journal of Materials Chemistry A*, *2*(41), 17521–17529.

Behari, J. (2010). Principles of nanoscience: An overview. *Indian Journal of Experimental Biology*, *48*(10), 1008–1019.

Berhanu, S., Gebremariam, H., & Chufamo, S. (2022). The g-C3N4@CdO/ZnO ternary composite: photocatalysis, thermodynamics and acute toxicity studies. *Heliyon*, *8*(11), e11612.

Bhujel, R., Rai, S., Baruah, K., Deka, U., Biswas, J., & Swain, B. P. (2019). Capacitive and Sensing Responses of Biomass Derived Silver Decorated Graphene. *Scientific Reports*, *9*(1), 19725.

Bi, X., Yu, S., Liu, E., Yin, X., Zhao, Y., & Xiong, W. (2020). Nano-zirconia supported by graphitic carbon nitride for enhanced visible light photocatalytic activity. *RSC Advances*, *10*(1), 524–532.

Bian, W., Song, X., Liu, D., Zhang, J., & Chen, X. (2011). The intermediate products in the degradation of 4-chlorophenol by pulsed high voltage discharge in water. *Journal of Hazardous Materials*, *192*(3), 1330–1339.

Bogireddy, N. K. R. R., Cruz Silva, R., Valenzuela, M. A., Agarwal, V., Silva, R. C., Valenzuela,

M. A., & Agarwal, V. (2020). 4-nitrophenol optical sensing with N doped oxidized carbon dots. *Journal of Hazardous Materials*, *386*, 121643.

Building, H. E. (1990). *Dtic 20tetragonal and cubic structure of Zirconia*.

Cao, J., Gong, Y., Wang, Y., Zhang, B., Zhang, H., Sun, G., Bala, H., & Zhang, Z. (2017). Cocoon-like ZnO decorated graphitic carbon nitride nanocomposite: Hydrothermal synthesis and ethanol gas sensing application. *Materials Letters*, *198*, 76–80. h

Cao, S., Fan, B., Feng, Y., Chen, H., Jiang, F., & Wang, X. (2018). Sulfur-doped g-C3N4 nanosheets with carbon vacancies: General synthesis and improved activity for simulated solar-light photocatalytic nitrogen fixation. *Chemical Engineering Journal*, *353*(May), 147–156.

Cao, S., Low, J., Yu, J., & Jaroniec, M. (2015). Polymeric Photocatalysts Based on Graphitic Carbon Nitride. *Advanced Materials*, *27*(13), 2150–2176.

Carneiro, P. A., Umbuzeiro, G. A., Oliveira, D. P., & Zanoni, M. V. B. (2010). Assessment of water contamination caused by a mutagenic textile effluent/dyehouse effluent bearing disperse dyes. *Journal of Hazardous Materials*, *174*(1–3), 694–699.

Cekic, S. D., Filik, H., & Apak, R. (2005). Simultaneous Spectrophotometric Determination of Paracetamol and p-Aminophenol in Pharmaceutical Products with Tiron Using Dissolved Oxygen as Oxidant. *Journal of Analytical Chemistry*, *60*(11), 1019–1023.

Chafi, F. Z., Salmani, E., Bahmad, L., Hassanain, N., Boubker, F., & Mzerd, A. (2018). First principle calculations with SIC correction of Fe-doped CuO compound. *Computational Condensed Matter*, *16*, e00304.

Chang, F., Zhang, J., Xie, Y., Chen, J., Li, C., Wang, J., Luo, J., Deng, B., & Hu, X. (2014). Fabrication, characterization, and photocatalytic performance of exfoliated g-C3N4–TiO2 hybrids. *Applied Surface Science*, *311*, 574–581.

Chang, G., Luo, Y., Lu, W., Qin, X., Asiri, A. M., Al-Youbi, A. O., & Sun, X. (2012). Ag nanoparticles decorated polyaniline nanofibers: synthesis, characterization, and applications toward catalytic reduction of 4-nitrophenol and electrochemical detection of H 2 O 2 and glucose. *Catalysis Science & Technology*, *2*(4), 800–806.

Chegeni, M., Goudarzi, F., & Soleymani, M. (2019). Synthesis, Characterization and Application of V2O5/S-Doped Graphitic Carbon Nitride Nanocomposite for Removing of Organic Pollutants. *ChemistrySelect*, *4*(46), 13736–13745.

Chen, G., & Gao, S.-P. (2012). Structure and electronic structure of S-doped graphitic C 3 N 4 investigated by density functional theory. *Chinese Physics B*, *21*(10), 107101.

Chen, J., Hong, Z., Chen, Y., Lin, B., & Gao, B. (2015). One-step synthesis of sulfur-doped and nitrogen-deficient g-C3N4 photocatalyst for enhanced hydrogen evolution under visible light. *Materials Letters*, *145*, 129–132.

Chen, P. (2018). Highly Effective Detection of 4-Nitrophenol by Tremella-like Indium Silver Sulfide Modified GCE. *International Journal of Electrochemical Science*, *13*(7), 6158–6168.

Cheng, Y. (2017). A Sensor for Detection of 4-nitrophenol Based on a Glassy Carbon Electrode Modified with a Reduced Graphene Oxide/Fe3O4 Nanoparticle Composite. *International Journal of Electrochemical Science*, *12*, 7754–7764.

Chu, Y.-C., Lin, T.-J., Lin, Y.-R., Chiu, W.-L., Nguyen, B.-S., & Hu, C. (2020). Influence of P,S,O-Doping on g-C3N4 for hydrogel formation and photocatalysis: An experimental and theoretical study. *Carbon*, *169*, 338–348.

Dhanasekaran, T., Manigandan, R., Padmanaban, A., Suresh, R., Giribabu, K., & Narayanan, V. (2019). Fabrication of Ag@Co-Al Layered Double Hydroxides Reinforced poly(o-phenylenediamine) Nanohybrid for Efficient Electrochemical Detection of 4-Nitrophenol, 2,4-Dinitrophenol and Uric acid at Nano Molar Level. *Scientific Reports*, *9*(1), 13250.

Dong, F., Wang, Z., Sun, Y., Ho, W., & Zhang, H. (2013). Engineering the nanoarchitecture and texture of polymeric carbon nitride semiconductor for enhanced visible light photocatalytic activity. *Journal of Colloid and Interface Science*, *401*, 70–79. h

Dong, F., Wu, L., Sun, Y., Fu, M., Wu, Z., & Lee, S. C. (2011). Efficient synthesis of polymeric g-C3N4 layered materials as novel efficient visible light driven photocatalysts. *Journal of Materials Chemistry*, *21*(39), 15171.

Dourandish, M., Simchi, A., & Hartwig, T. (2008). Sintering of zirconia/430l stainless steel bilayers for co-powder injection moulding. *Proceedings of the Euro International Powder Metallurgy Congress and Exhibition, Euro PM 2008*, *2*, 299–303.

Dourandish, M., Simchi, A., Hokamoto, K., & Tanaka, S. (2011). Phase formation during sintering of nanocrystalline zirconia/stainless steel functionally graded composite layers. *Materials Letters*, *65*(3), 523–526.

Duan, Y. (2018). Facile preparation of CuO/g-C 3 N 4 with enhanced photocatalytic degradation of salicylic acid. *Materials Research Bulletin*, *105*, 68–74. h

Esumi, K., Isono, R., & Yoshimura, T. (2004). Preparation of PAMAM- and PPI-metal (silver, platinum, and palladium) nanocomposites and their catalytic activities for reduction of 4-nitrophenol. *Langmuir : The ACS Journal of Surfaces and Colloids*, *20*(1), 237–243.

Faisal, M., Alam, M., Ahmed, J., Asiri, A. M., Jalalah, M., Alruwais, R. S., Rahman, M. M., & Harraz, F. A. (2022). *Sensitive Electrochemical Detection of 4-Nitrophenol with PEDOT : PSS Modified Pt NPs-Embedded PPy-CB @ ZnO Nanocomposites*. 1–18.

Fan, Q., Liu, J., Yu, Y., Zuo, S., & Li, B. (2016). A simple fabrication for sulfur doped graphitic carbon nitride porous rods with excellent photocatalytic activity degrading RhB dye. *Applied Surface Science*.

Fang, H. Bin, Luo, Y., Zheng, Y. Z., Ma, W., & Tao, X. (2016). Facile Large-Scale Synthesis of Urea-Derived Porous Graphitic Carbon Nitride with Extraordinary Visible-Light Spectrum Photodegradation. *Industrial and Engineering Chemistry Research*, *55*(16), 4506–4514.

Fu, J., Yu, J., Jiang, C., & Cheng, B. (2018). g-C 3 N 4 -Based Heterostructured Photocatalysts. *Advanced Energy Materials*, *8*(3), 1701503.

G, M. S., Adarakatti, P. S., & Udayakumar, V. (2021). Engineering of CuO/ZrO2 nanocomposite-based electrochemical sensor for the selective detection of hydrogen peroxide. *Ionics*, *27*(12), 5309–5322.

Ghafuri, H., Jafari, G., Goodarzi, N., & Rashidizadeh, A. (2018). ZrO2/g-C3N4 Hybrid Nanocomposite: An Efficient and Eco-Friendly Recyclable Catalyst for the Trimethylsilyl Protection of Hydroxyl Groups and Synthesis of α-Aminophosphonates. *Proceedings*, *9*(1), 51.

Guan, K., Li, J., Lei, W., Wang, H., Tong, Z., Jia, Q., Zhang, H., & Zhang, S. (2021). Synthesis of sulfur doped g-C 3 N 4 with enhanced photocatalytic activity in molten salt. *Journal of Materiomics*, *xxxx*.

Guo, H., Shu, Z., Chen, D., Tan, Y., Zhou, J., Meng, F., & Li, T. (2020). One-step synthesis of S-doped g-C3N4 nanosheets for improved visible-light photocatalytic hydrogen evolution. *Chemical Physics*, *533*(February), 110714.

Guo, Q., Zhang, Y., Qiu, J., & Dong, G. (2016). Engineering the electronic structure and optical properties of g-C 3 N 4 by non-metal ion doping. *Journal of Materials Chemistry C*, *4*(28), 6839–6847.

HAMEED, B., DIN, A., & AHMAD, A. (2007). Adsorption of methylene blue onto bamboo-based

activated carbon: Kinetics and equilibrium studies. *Journal of Hazardous Materials*, *141*(3), 819–825. h

Hanafi, M. F., & Sapawe, N. (2020). Effect of initial concentration on the photocatalytic degradation of remazol brilliant blue dye using nickel catalyst. *Materials Today: Proceedings*, *31*, 318–320.

Hanif, M. A., Akter, J., Kim, Y. S., Kim, H. G., Hahn, J. R., & Kwac, L. K. (2022). Highly Efficient and Sustainable ZnO/CuO/g-C3N4 Photocatalyst for Wastewater Treatment under Visible Light through Heterojunction Development. *Catalysts*, *12*(2), 151.

Harish, S., Archana, J., Sabarinathan, M., Navaneethan, M., Nisha, K. D., Ponnusamy, S., Muthamizhchelvan, C., Ikeda, H., Aswal, D. K., & Hayakawa, Y. (2017). Controlled structural and compositional characteristic of visible light active ZnO/CuO photocatalyst for the degradation of organic pollutant. *Applied Surface Science*, *418*, 103–112.

He, T., Wu, Y., Jiang, C., Chen, Z., Wang, Y., Liu, G., Xu, Z., Ning, G., Chen, X., & Zhao, Y. (2020). Novel magnetic Fe3O4/g-C3N4/MoO3 nanocomposites with highly enhanced photocatalytic activities: Visible-light-driven degradation of tetracycline from aqueous environment. *PLOS ONE*, *15*(8), e0237389.

Henderson, M. A. (2011). A surface science perspective on TiO2 photocatalysis. *Surface Science Reports*, *66*(6–7), 185–297.

Hosseini, H. S. M., Moakhar, R. S., Soleimani, F., Sadrnezhaad, S. K., Masudy-panah, S., Katal, R., Seza, A., Ghane, N., & Ramakrishna, S. (2020). One-Pot Microwave Synthesis of Hierarchical C-doped CuO Dandelions / g-C 3 N 4 Nanocomposite with Enhanced Photostability for Photoelectrochemical Water Splitting. *Applied Surface Science*, 147271.

Huang, Y., Tan, Y., Feng, C., Wang, S., Wu, H., & Zhang, G. (2019). Synthesis of CuO/g-C3N4 composites, and their application to voltammetric sensing of glucose and dopamine. *Microchimica Acta*, *186*(1), 10.

Idris, A. O., Oseghe, E. O., Msagati, T. A. M., Kuvarega, A. T., Feleni, U., & Mamba, B. (2020). Graphitic Carbon Nitride: A Highly Electroactive Nanomaterial for Environmental and Clinical Sensing. *Sensors*, *20*(20), 5743.

Imran Din, M., Ahmed, M., Ahmad, M., Saqib, S., Mubarak, W., Hussain, Z., Khalid, R., Raza, H., & Hussain, T. (2023). Novel and Facile Synthesis of Carbon Quantum Dots from Chicken Feathers and Their Application as a Photocatalyst to Degrade Methylene Blue Dye. *Journal*

of Chemistry, *2023*, 1–11.

Jia, X., Dai, R., Sun, Y., Song, H., & Wu, X. (2016). One-step hydrothermal synthesis of Fe3O4/g-C3N4 nanocomposites with improved photocatalytic activities. *Journal of Materials Science: Materials in Electronics*, *27*(4), 3791–3798.

Jiang, L., Yuan, X., Pan, Y., Liang, J., Zeng, G., Wu, Z., & Wang, H. (2017). Doping of graphitic carbon nitride for photocatalysis: A review. *Applied Catalysis B: Environmental*, *217*(November), 388–406.

Jo, W., & Selvam, N. C. S. (2017). Z-scheme CdS/C3N4 composites with RGO as an electron mediator for efficient photocatalytic H2 production and pollutant degradation. *Chemical Engineering Journal*.

Jones, J. M., & Rollinson, A. N. (2013). Thermochimica Acta Thermogravimetric evolved gas analysis of urea and urea solutions with nickel alumina catalyst. *Thermochimica Acta*, *565*, 39–45.

Kamal, T., Asiri, A. M., & Ali, N. (2021). Catalytic reduction of 4-nitrophenol and methylene blue pollutants in water by copper and nickel nanoparticles decorated polymer sponges. *Spectrochimica Acta Part A: Molecular and Biomolecular Spectroscopy*, *261*, 120019.

Kamali, M., Samari, F., & Sedaghati, F. (2019). Low-temperature phyto-synthesis of copper oxide nanosheets: Its catalytic effect and application for colorimetric sensing. *Materials Science and Engineering C*, *103*(May), 109744.

Kamat, P. V. (2012). Manipulation of Charge Transfer Across Semiconductor Interface . *The Journal of Physical Chemistry Letters*, *3*(5), 663–672.

Kanti, T., Narayan, D., & Das, C. (2022). Advances on catalytic reduction of 4 - nitrophenol by nanostructured materials as benchmark reaction. *International Nano Letters*, *12*(3), 223–242.

Karthik, P., Naveen Kumar, T. R., & Neppolian, B. (2020). Redox couple mediated charge carrier separation in g-C3N4/CuO photocatalyst for enhanced photocatalytic H2 production. *International Journal of Hydrogen Energy*, *45*(13), 7541–7551.

Kavil, J., Anjana, P. M., Joshy, D., Babu, A., Raj, G., Periyat, P., & Rakhi, R. B. (2019). g-C 3 N 4 /CuO and g-C 3 N 4 /Co 3 O 4 nanohybrid structures as efficient electrode materials in symmetric supercapacitors. *RSC Advances*, *9*(66), 38430–38437.

Ke, Y., Guo, H., Wang, D., Chen, J., & Weng, W. (2014). ZrO2/g-C3N4 with enhanced photocatalytic degradation of methylene blue under visible light irradiation. *Journal of*

Materials Research, *29*(20), 2473–2482.

Kessler, F. K., Zheng, Y., Schwarz, D., Merschjann, C., Schnick, W., Wang, X., & Bojdys, M. J. (2017). Functional carbon nitride materials — design strategies for electrochemical devices. *Nature Reviews Materials*, *2*(6), 17030.

Khan, S. B., Rahman, M. M., Akhtar, K., Asiri, A. M., & Rub, M. A. (2014). *Nitrophenol Chemi-Sensor and Active Solar Photocatalyst Based on Spinel Hetaerolite Nanoparticles*. *9*(1).

Kimmel, D. W., LeBlanc, G., Meschievitz, M. E., & Cliffel, D. E. (2012). Electrochemical Sensors and Biosensors. *Analytical Chemistry*, *84*(2), 685–707.

Kong, X., Zhu, H., Chen, C., & Huang, G. (2017). Insights into the Reduction of 4-Nitrophenol to 4-Aminophenol on Catalysts. *Chemical Physics Letters*.

Krishna, D. N. G., & Philip, J. (2022). Review on surface-characterization applications of X-ray photoelectron spectroscopy (XPS): Recent developments and challenges. *Applied Surface Science Advances*, *12*(November), 100332.

Kroke, E., Schwarz, M., Horath-Bordon, E., Kroll, P., Noll, B., & Norman, A. D. (2002). Tri-s-triazine derivatives. Part I. From trichloro-tri-s-triazine to graphitic C3N4 structuresPart II: Alkalicyamelurates M3[C6N7O3], M = Li, Na, K, Rb, Cs, manuscript in preparation. *New Journal of Chemistry*, *26*(5), 508–512.

Kumari, L., Li, W., & Wang, D. (2008). Monoclinic zirconium oxide nanostructures synthesized by a hydrothermal route. *Nanotechnology*, *19*(19), 195602.

Kumunda, C., Adekunle, A. S., Mamba, B. B., Hlongwa, N. W., & Nkambule, T. T. I. (2021). Electrochemical Detection of Environmental Pollutants Based on Graphene Derivatives: A Review. *Frontiers in Materials*, *7*(February).

Kunene, K., Sabela, M., Kanchi, S., & Bisetty, K. (2020). High Performance Electrochemical Biosensor for Bisphenol A Using Screen Printed Electrodes Modified with Multiwalled Carbon Nanotubes Functionalized with Silver-Doped Zinc Oxide. *Waste and Biomass Valorization*, *11*(3), 1085–1096.

Lachheb, H., Puzenat, E., Houas, A., Ksibi, M., Elaloui, E., Guillard, C., & Herrmann, J.-M. (2002). Photocatalytic degradation of various types of dyes (Alizarin S, Crocein Orange G, Methyl Red, Congo Red, Methylene Blue) in water by UV-irradiated titania. *Applied Catalysis B: Environmental*, *39*(1), 75–90.

Lackner, P., Zou, Z., Mayr, S., Diebold, U., & Schmid, M. (2019). Using photoelectron

spectroscopy to observe oxygen spillover to zirconia. *Physical Chemistry Chemical Physics*, *21*(32), 17613–17620.

Li, J., Liu, C. Y., & Liu, Y. (2012). Au/graphene hydrogel: Synthesis, characterization and its use for catalytic reduction of 4-nitrophenol. *Journal of Materials Chemistry*, *22*(17), 8426–8430.

Li, J., Sun, F., Gu, K., Wu, T., Zhai, W., Li, W., & Huang, S. (2011). Preparation of spindly CuO micro-particles for photodegradation of dye pollutants under a halogen tungsten lamp. *Applied Catalysis A: General*, *406*(1–2), 51–58.

Li, K., Chen, M., Chen, L., Zhao, S., Xue, W., Han, Z., & Han, Y. (2023). Synthesis of g-C3N4 Derived from Different Precursors for Photodegradation of Sulfamethazine under Visible Light. *Processes*, *11*(2), 528.

Li, L., Hu, Y., Deng, D., Song, H., & Lv, Y. (2016). Highly sensitive cataluminescence gas sensors for 2-butanone based on g-C3N4 sheets decorated with CuO nanoparticles. *Analytical and Bioanalytical Chemistry*, *408*(30), 8831–8841.

Li, M., Zhang, L., Wu, M., Du, Y., Fan, X., Wang, M., Zhang, L., Kong, Q., & Shi, J. (2016). Mesostructured CeO2/g-C3N4 nanocomposites: Remarkably enhanced photocatalytic activity for CO2 reduction by mutual component activations. *Nano Energy*, *19*, 145–155.

Li, Y., He, D., Cheng, Z., Su, C., Li, J., & Zhu, Q. (2001). Effect of calcium salts on isosynthesis over ZrO2 catalysts. *Journal of Molecular Catalysis A: Chemical*, *175*(1–2), 267–275.

Li, Y., Ho, W., Lv, K., Zhu, B., & Lee, S. C. (2018). Carbon vacancy-induced enhancement of the visible light-driven photocatalytic oxidation of NO over g-C 3 N 4 nanosheets. *Applied Surface Science*, *430*(8), 380–389.

Liu, D., Lu, C., & Wu, J. (2018). CuO/g-C3N4 nanocomposite for elemental mercury capture at low temperature. *Journal of Nanoparticle Research*, *20*(10), 277.

Liu, G., Niu, P., Sun, C., Smith, S. C., Chen, Z., Qing, G., Lu, M., Cheng, H.-M., Lu, G. Q., & Cheng, H.-M. (2010). Unique electronic structure induced high photoreactivity of sulfur-doped graphitic C3N4. *Journal of the American Chemical Society*, *132*(33), 11642–11648.

Liu, G., Qiao, X., Gondal, M. A., Liu, Y., Shen, K., & Xu, Q. (2017). Comparative Study of Pure g-C 3 N 4 and Sulfur-Doped g-C 3 N 4 Catalyst Performance in Photo-Degradation of Persistent Pollutant Under Visible Light . *Journal of Nanoscience and Nanotechnology*, *18*(6), 4142–4154.

Liu, J., Zhang, T., Wang, Z., Dawson, G., & Chen, W. (2011). Simple pyrolysis of urea into

graphitic carbon nitride with recyclable adsorption and photocatalytic activity. *Journal of Materials Chemistry*, *21*(38), 14398.

Liu, S., Zhu, H., Yao, W., Chen, K., & Chen, D. (2018). One step synthesis of P-doped g-C3N4 with the enhanced visible light photocatalytic activity. *Applied Surface Science*, *430*, 309–315.

López, R., & Gómez, R. (2012). Band-gap energy estimation from diffuse reflectance measurements on sol–gel and commercial TiO2: a comparative study. *Journal of Sol-Gel Science and Technology*, *61*(1), 1–7.

Lu, C., Zhang, P., Jiang, S., Wu, X., Song, S., Zhu, M., Lou, Z., Li, Z., Liu, F., Liu, Y., Wang, Y., & Le, Z. (2017). Photocatalytic reduction elimination of UO22+ pollutant under visible light with metal-free sulfur doped g-C3N4 photocatalyst. *Applied Catalysis B: Environmental*, *200*, 378–385.

Lui, G., Liao, J., Duan, A., Zhang, Z., Fowler, M., & Yu, A. (2013). Graphene-wrapped hierarchical TiO2 nanoflower composites with enhanced photocatalytic performance. *Journal of Materials Chemistry A*, *1*(39), 12255.

Luo, Y., Zhu, Y., Han, Y., Ye, H., Liu, R., Lan, Y., Xue, M., Xie, X., Yu, S., Zhang, L., Yin, Z., & Gao, B. (2023). g-C3N4-based photocatalysts for organic pollutant removal: a critical review. *Carbon Research*, *2*(1), 14.

Ma, X., Lv, Y., Xu, J., Liu, Y., Zhang, R., & Zhu, Y. (2012). A strategy of enhancing the photoactivity of g-C 3N 4 via doping of nonmetal elements: A first-principles study. *Journal of Physical Chemistry C*, *116*(44), 23485–23493.

Mammadova, S., Nasibova, A., Khalilov, R., Mehralıyeva, S., Valiyeva, M., Gojayev, A. S., Zhdanov, R. I., & Eftekhari, A. (2022). Nanomaterials application in air pollution remediation. *Eurasian Chemical Communications*, *4*(2), 160–166.

Mao, N. (2019). Investigating the Heteronjunction between ZnO/Fe2O3 and g-C3N4 for an Enhanced Photocatalytic H2 production under visible-light irradiation. *Scientific Reports*, *9*(1), 12383.

Maragou, N. C., Makri, A., Lampi, E. N., Thomaidis, N. S., & Koupparis, M. A. (2008). Migration of bisphenol A from polycarbonate baby bottles under real use conditions. *Food Additives & Contaminants: Part A*, *25*(3), 373–383.

Matějka, V., Škuta, R., Foniok, K., Novák, V., Cvejn, D., Martaus, A., Michalska, M., Pavlovský,

J., & Praus, P. (2022). The role of the g-C3N4 precursor on the P doping using HCCP as a source of phosphorus. *Journal of Materials Research and Technology*, *18*, 3319–3335.

Miller, T. S., Jorge, A. B., Suter, T. M., Sella, A., Corà, F., & McMillan, P. F. (2017). Carbon nitrides: synthesis and characterization of a new class of functional materials. *Physical Chemistry Chemical Physics*, *19*(24), 15613–15638.

Mishra, A. K., Roldan, A., & de Leeuw, N. H. (2016). CuO Surfaces and CO 2 Activation: A Dispersion-Corrected DFT+ U Study. *The Journal of Physical Chemistry C*, *120*(4), 2198–2214.

Mitra, A., Howli, P., Sen, D., Das, B., & Chattopadhyay, K. K. (2016). Cu 2 O/g-C 3 N 4 nanocomposites: an insight into the band structure tuning and catalytic efficiencies. *Nanoscale*, *8*(45), 19099–19109.

Mo, Z., She, X., Li, Y., Liu, L., Huang, L., Chen, Z., Zhang, Q., Xu, H., & Li, H. (2015). Synthesis of gC 3 N 4 at different temperatures for superior visible/UV photocatalytic performance and photoelectrochemical sensing of MB solution. *RSC Advances*, *5*(123), 101552–101562.

Moeinian, M., & Akhbari, K. (2015). How the guest molecules in nanoporous Zn(II) metal-organic framework can prevent agglomeration of ZnO nanoparticles. *Journal of Solid State Chemistry*, *225*(Ii), 459–463.

Mohammad, A., Ehtisham, M., & Hwan, M. (2020). Sulfur-doped- graphitic -carbon nitride (S- g -C 3 N 4) for low cost electrochemical sensing of hydrazine. *Journal of Alloys and Compounds*, *816*, 152522.

Mohammad, A., Khan, M. E., & Cho, M. H. (2020). Sulfur-doped-graphitic-carbon nitride (S-g-C3N4) for low cost electrochemical sensing of hydrazine. *Journal of Alloys and Compounds*, *816*, 152522.

Monsef, R., Ghiyasiyan-Arani, M., & Salavati-Niasari, M. (2021). Design of Magnetically Recyclable Ternary Fe 2 O 3 /EuVO 4 /g-C 3 N 4 Nanocomposites for Photocatalytic and Electrochemical Hydrogen Storage. *ACS Applied Energy Materials*, *4*(1), 680–695.

Mousavi, M., & Habibi-Yangjeh, A. (2016). Magnetically separable ternary g-C3N4/Fe3O4/BiOI nanocomposites: Novel visible-light-driven photocatalysts based on graphitic carbon nitride. *Journal of Colloid and Interface Science*, *465*, 83–92.

Najibi-Ilkhechi, N., Koozegar-Kaleji, B., & Salahi, E. (2015). Effect of heating rate on structural and optical properties of Si and Mg co-doped $$\hbox {ZrO} _ {2} $$ ZrO 2 nanopowders.

Optical and Quantum Electronics, *47*(5), 1187–1195.

Name, C., Lists, A., & Category, P. (2013). The Hazardous 100 + List of Chemicals of High Concern The Hazardous 100 + List of Chemicals of High Concern. *Safer Chemicals*, 3–6.

Nehru, R., Gopi, P. K., & Chen, S. (2020). Enhanced sensing of hazardous 4-nitrophenol by pollutant monitoring applications †. *New Journal of Chemistry*, 16–26.

Nishimura, C. (1992). Technological approach to biofeedback : Instrumentaion and modelling. In *Japanese journal of biofeedback research* (Vol. 19, Issue September).

Nithya, R., & Ayyappan, S. (2020). Novel exfoliated graphitic-C3N4 hybridised ZnBi2O4 (g-C3N4/ZnBi2O4) nanorods for catalytic reduction of 4-Nitrophenol and its antibacterial activity. *Journal of Photochemistry and Photobiology A: Chemistry*, *398*(May), 112591.

Ong, W.-J., Tan, L.-L., Chai, S.-P., & Yong, S.-T. (2015). Graphene oxide as a structure-directing agent for the two-dimensional interface engineering of sandwich-like graphene–g-C 3 N 4 hybrid nanostructures with enhanced visible-light photoreduction of CO 2 to methane. *Chemical Communications*, *51*(5), 858–861.

Ong, W.-J., Tan, L.-L., Ng, Y. H., Yong, S.-T., & Chai, S.-P. (2016). Graphitic Carbon Nitride (g-C 3 N 4)-Based Photocatalysts for Artificial Photosynthesis and Environmental Remediation: Are We a Step Closer To Achieving Sustainability? *Chemical Reviews*, *116*(12), 7159–7329.

Paixão, T. R. L. C. (2020). Measuring Electrochemical Surface Area of Nanomaterials versus the Randles−Ševčík Equation. *ChemElectroChem*, *7*(16), 3414–3415.

Paquin, F., Rivnay, J., Salleo, A., & Silva-acun, C. (2015). *dissociation in neat semicrystalline polymeric semiconductors*.

Paquin, F., Rivnay, J., Salleo, A., Stingelin, N., & Silva, C. (2013). Multi-phase semicrystalline microstructures drive exciton dissociation in neat plastic semiconductors. *Journal of Materials Chemistry C*, *3*(41), 10715–10722.

Pei, D.-N. N., Zhang, A.-Y. Y., Pan, X.-Q. Q., Si, Y., & Yu, H.-Q. Q. (2018). Electrochemical Sensing of Bisphenol A on Facet-Tailored TiO2 Single Crystals Engineered by Inorganic-Framework Molecular Imprinting Sites. *Analytical Chemistry*, *90*(5), 3165–3173.

Peng, B., Zhang, S., Yang, S., Wang, H., Yu, H., Zhang, S., & Peng, F. (2014). Synthesis and characterization of g-C3N4/Cu2O composite catalyst with enhanced photocatalytic activity under visible light irradiation. *Materials Research Bulletin*, *56*, 19–24.

Pollutant, P., & Visible, U. (2017). *Persistent Pollutant Under Visible Light*. *17*(xx), 1–13.

Pradhan, N., Pal, A., & Pal, T. (2002). *Silver nanoparticle catalyzed reduction of aromatic nitro compounds*. *196*, 247–257.

Rajkumar, C., Veerakumar, P., Chen, S. M., Thirumalraj, B., & Lin, K. C. (2018). Ultrathin Sulfur-Doped Graphitic Carbon Nitride Nanosheets As Metal-Free Catalyst for Electrochemical Sensing and Catalytic Removal of 4-Nitrophenol. *ACS Sustainable Chemistry and Engineering*, *6*(12), 16021–16031.

Ran, J., Ma, T. Y., Gao, G., Du, X. W., & Qiao, S. Z. (2015). Porous P-doped graphitic carbon nitride nanosheets for synergistically enhanced visible-light photocatalytic H2 production. *Energy and Environmental Science*, *8*(12), 3708–3717.

Rashid, J., Parveen, N., Iqbal, A., Awan, S. U., Iqbal, N., Talib, S. H., Hussain, N., Akram, B., Ulhaq, A., Ahmed, B., & Xu, M. (2019). Facile synthesis of g-C3N4(0.94)/CeO2(0.05)/Fe3O4(0.01) nanosheets for DFT supported visible photocatalysis of 2-Chlorophenol. *Scientific Reports*, *9*(1), 10202.

Robati, D., Mirza, B., Ghazisaeidi, R., Rajabi, M., Moradi, O., Tyagi, I., Agarwal, S., & Gupta, V. K. (2016). Adsorption behavior of methylene blue dye on nanocomposite multi-walled carbon nanotube functionalized thiol (MWCNT-SH) as new adsorbent. *Journal of Molecular Liquids*, *216*, 830–835.

Sadiq, M. M. J., Shenoy, U. S., & Bhat, D. K. (2018). Synthesis of BaWO4/NRGO–g-C3N4 nanocomposites with excellent multifunctional catalytic performance via microwave approach. *Frontiers of Materials Science*, *12*(3), 247–263.

Sahiner, N., Ozay, H., Ozay, O., & Aktas, N. (2010). A soft hydrogel reactor for cobalt nanoparticle preparation and use in the reduction of nitrophenols. *Applied Catalysis B: Environmental*, *101*(1–2), 137–143.

Sahoo, S. K., Padhiari, S., Biswal, S. K., Panda, B. B., & Hota, G. (2020). Fe3O4 nanoparticles functionalized GO/g-C3N4 nanocomposite: An efficient magnetic nanoadsorbent for adsorptive removal of organic pollutants. *Materials Chemistry and Physics*, *244*, 122710.

Sathyaseelan, B., Manikandan, E., Baskaran, I., Senthilnathan, K., Sivakumar, K., Moodley, M. K., Ladchumananandasivam, R., & Maaza, M. (2017a). Studies on structural and optical properties of ZrO2nanopowder for opto-electronic applications. *Journal of Alloys and Compounds*, *694*, 556–559.

Sathyaseelan, B., Manikandan, E., Baskaran, I., Senthilnathan, K., Sivakumar, K., Moodley, M.

K., Ladchumananandasivam, R., & Maaza, M. (2017b). Studies on structural and optical properties of ZrO2 nanopowder for opto-electronic applications. *Journal of Alloys and Compounds*, *694*(October), 556–559.

Sharma, K., Raizada, P., Hosseini-bandegharaei, A., & Thakur, P. (2020). Fabrication of efficient CuO / graphitic carbon nitride based heterogeneous photo-Fenton like catalyst for degradation of 2 , 4 dimethyl phenol. *Process Safety and Environmental Protection*, *142*, 63–75.

Shi, R., Liang, J., Zhao, Z., Liu, A., & Tian, Y. (2017). Talanta An electrochemical bisphenol A sensor based on one step electrochemical reduction of cuprous oxide wrapped graphene oxide nanoparticles modi fi ed electrode. *Talanta*, *169*(December 2016), 37–43.

Shylo, A., Gorban, O., Danilenko, I., Doroshkevich, A., Lyubchyk, A., Gorban, A., & Konstantinova, T. (2019). *Oct 16*. 555–560.

Siddiquee, S., Hong, M. G. J., & Rahman, M. M. (2020). Composite Materials: Applications in Engineering, Biomedicine and Food Science. In S. Siddiquee, M. Gan Jet Hong, & M. Mizanur Rahman (Eds.), *Composite Materials: Applications in Engineering, Biomedicine and Food Science*. Springer International Publishing. https://doi.org/10.1007/978-3-030-45489-0

Singh, P. P., & Srivastava, V. (2022). Recent advances in visible-light graphitic carbon nitride (g-C 3 N 4) photocatalysts for chemical transformations. *RSC Advances*, *12*(28), 18245–18265.

Singh, S., Kumar, N., Kumar, M., Jyoti, Agarwal, A., & Mizaikoff, B. (2017). Electrochemical sensing and remediation of 4-nitrophenol using bio-synthesized copper oxide nanoparticles. *Chemical Engineering Journal*, *313*, 283–292.

Sonavane, S. U., Gawande, M. B., Deshpande, S. S., Venkataraman, A., & Jayaram, R. V. (2007). Chemoselective transfer hydrogenation reactions over nanosized γ-Fe2O3 catalyst prepared by novel combustion route. *Catalysis Communications*, *8*(11), 1803–1806.

Srinivasan, R., Davis, B. H., Cavin, O. B., & Hubbard, C. R. (1992). Crystallization and Phase Transformation Process in Zirconia: An in situ High-Temperature X-ray Diffraction Study. *Journal of the American Ceramic Society*, *75*(5), 1217–1222.

Srinivasan, R., De Angelis, R. J., Ice, G., & Davis, B. H. (1991). Identification of tetragonal and cubic structures of zirconia using synchrotron x-radiation source. *Journal of Materials Research*, *6*(6), 1287–1292.

Srinivasan, R., Harris, M. B., Simpson, S. F., De Angelis, R. J., & Davis, B. H. (1988). Zirconium

oxide crystal phase: The role of the p H and time to attain the final p H for precipitation of the hydrous oxide. *Journal of Materials Research*, *3*(4), 787–797.

Stephens, P. J., & Devlin, F. J. (1995). Ab Initio Calculation of Vibrational Absorption and. *J. Phys. Chem*, *98(45)*, 11623–11627.

Stolbov, S., & Zuluaga, S. (2013a). Sulfur doping effects on the electronic and geometric structures of graphitic carbon nitride photocatalyst: insights from first principles. *Journal of Physics: Condensed Matter*, *25*(8), 085507.

Stolbov, S., & Zuluaga, S. (2013b). Sulfur doping effects on the electronic and geometric structures of graphitic carbon nitride photocatalyst: insights from first principles. *Journal of Physics: Condensed Matter*, *25*(8), 085507.

Sudhaik, A., Raizada, P., Shandilya, P., Jeong, D.-Y. Y., Lim, J.-H. H., & Singh, P. (2018). Review on fabrication of graphitic carbon nitride based efficient nanocomposites for photodegradation of aqueous phase organic pollutants. *Journal of Industrial and Engineering Chemistry*, *67*, 28–51.

Sudrajat, H., & Hartuti, S. (2018). Structural properties and catalytic activity of a novel ternary CuO/gC3N4/Bi2O3 photocatalyst. *Journal of Colloid and Interface Science*, *524*, 227–235.

Szczepankiewicz, S. H., Colussi, A. J., & Hoffmann, M. R. (2000). Infrared spectra of photoinduced species on hydroxylated titania surfaces. *Journal of Physical Chemistry B*, *104*(42), 9842–9850.

Tahir, M. N., Gorgishvili, L., Li, J., Gorelik, T., Kolb, U., Nasdala, L., & Tremel, W. (2007). Facile synthesis and characterization of monocrystalline cubic ZrO2 nanoparticles. *Solid State Sciences*, *9*(12), 1105–1109.

Tan, L., Xu, J., Zhang, X., Hang, Z., Jia, Y., & Wang, S. (2015). Synthesis of g-C 3 N 4 /CeO 2 nanocomposites with improved catalytic activity on the thermal decomposition of ammonium perchlorate. *Applied Surface Science*, *356*, 447–453.

Teter, D. M., & Hemley, R. J. (1996). Low-Compressibility Carbon Nitrides. *Science*, *271*(5245), 53–55.

Thomas, A., Fischer, A., Goettmann, F., Antonietti, M., Müller, J.-O., Schlögl, R., & Carlsson, J. M. (2008). Graphitic carbon nitride materials: variation of structure and morphology and their use as metal-free catalysts. *Journal of Materials Chemistry*, *18*(41), 4893–4908.

Tian, C., Zhao, H., Mei, J., & Yang, S. (2019). Cost-Efficient Graphitic Carbon Nitride as an

Effective Photocatalyst for Antibiotic Degradation: An Insight into the Effects of Different Precursors and Coexisting Ions, and Photocatalytic Mechanism. *Chemistry - An Asian Journal*, *14*(1), 162–169.

Vasiljevic, Z. Z., Dojcinovic, M. P., Vujancevic, J. D., Jankovic-Castvan, I., Ognjanovic, M., Tadic, N. B., Stojadinovic, S., Brankovic, G. O., & Nikolic, M. V. (2020). Photocatalytic degradation of methylene blue under natural sunlight using iron titanate nanoparticles prepared by a modified sol–gel method. *Royal Society Open Science*, *7*(9), 200708.

Verma, A., Kumar, S., Chang, W.-K., & Fu, Y.-P. (2020). Bi-functional Ag-Cu x O/gC 3 N 4 hybrid catalysts for the reduction of 4-nitrophenol and the electrochemical detection of dopamine. *Dalton Transactions*, *49*(3), 625–637.

Vijayakumar, E., Raj, M. G., Narendran, M. G., Preetha, R., Mohankumar, R., Neppolian, B., & Bosco, A. J. (2022). *Promoting Spatial Charge Transfer of ZrO 2 Nanoparticles : Embedded on Layered MoS 2 / g - C 3 N 4 Nanocomposites for Visible- Light-Induced Photocatalytic Removal of Tetracycline*.

Vu, M.-H. H., Sakar, M., Nguyen, C.-C. C., & Do, T.-O. O. (2018). Chemically bonded Ni cocatalyst onto the S doped g-C3N4 nanosheets and their synergistic enhancement in H2 production under sunlight irradiation. *ACS Sustainable Chemistry & Engineering*, *6*(3), 4194–4203.

Wang, C.-C., Yi, X.-H., & Wang, P. (2019). Powerful combination of MOFs and C3N4 for enhanced photocatalytic performance. *Applied Catalysis B: Environmental*, *247*, 24–48.

Wang, C., Salmon, L., Ciganda, R., Yate, L., Moya, S., Ruiz, J., & Astruc, D. (2017). An efficient parts-per-million α-Fe 2 O 3 nanocluster/graphene oxide catalyst for Suzuki–Miyaura coupling reactions and 4-nitrophenol reduction in aqueous solution. *Chemical Communications*, *53*(3), 644–646.

Wang, K., Li, Q., Liu, B., Cheng, B., Ho, W., & Yu, J. (2015). Sulfur-doped g-C3N4 with enhanced photocatalytic CO2-reduction performance. *Applied Catalysis B: Environmental*, *176*, 44–52.

Wang, R., Wang, Y., Mao, S., Hao, X., Duan, X., & Wen, Y. (2021). Different Morphology MoS2 Over the g-C3N4 as a Boosted Photo-Catalyst for Pollutant Removal Under Visible-Light. *Journal of Inorganic and Organometallic Polymers and Materials*, *31*(1), 32–42.

Wang, T., Song, B., & Wang, L. (2020). A New Filler for Epoxy Resin: Study on the Properties

of Graphite Carbon Nitride (g-C3N4) Reinforced Epoxy Resin Composites. *Polymers*, *12*(1), 76.

Wang, X., Blechert, S., & Antonietti, M. (2012). Polymeric Graphitic Carbon Nitride for Heterogeneous Photocatalysis. *ACS Catalysis*, *2*(8), 1596–1606.

Wang, X., Maeda, K., Chen, X., Takanabe, K., Domen, K., Hou, Y., Fu, X., & Antonietti, M. (2009). Polymer semiconductors for artificial photosynthesis: Hydrogen evolution by mesoporous graphitic carbon nitride with visible light. *Journal of the American Chemical Society*, *131*(5), 1680–1681.

Wang, Y., Liu, L., Ma, T., Zhang, Y., & Huang, H. (2021). 2D Graphitic Carbon Nitride for Energy Conversion and Storage. *Advanced Functional Materials*, *31*(34), 2102540.

Wang, Y., Tian, Y., Yan, L., & Su, Z. (2018). DFT Study on Sulfur-Doped g-C 3 N 4 Nanosheets as a Photocatalyst for CO 2 Reduction Reaction. *The Journal of Physical Chemistry C*, *122*(14), 7712–7719.

Wang, Y., Zhang, Y., Lu, H., Chen, Y., Liu, Z., Su, S., Xue, Y., Yao, J., & Zeng, H. (2018). Novel N-doped ZrO 2 with enhanced visible-light photocatalytic activity for hydrogen production and degradation of organic dyes. *RSC Advances*, *8*(13), 6752–6758.

Wang, Z., Xu, C., Gao, G., & Li, X. (2014). Facile synthesis of well-dispersed Pd-graphene nanohybrids and their catalytic properties in 4-nitrophenol reduction. *RSC Advances*, *4*(26), 13644–13651.

Wiench, P., Grzyb, B., González, Z., Menéndez, R., Handke, B., & Gryglewicz, G. (2017). pH robust electrochemical detection of 4-nitrophenol on a reduced graphene oxide modified glassy carbon electrode. *Journal of Electroanalytical Chemistry*, *787*, 80–87.

Xing, J., Zhang, S., Zhang, M., & Hou, J. (2022). A critical review of presence, removal and potential impacts of endocrine disruptors bisphenol A. *Comparative Biochemistry and Physiology Part C: Toxicology & Pharmacology*, 109275.

Xu, B.-Q., Wei, J.-M., Yu, Y.-T., Li, Y., Li, J.-L., & Zhu, Q.-M. (2003). Size Limit of Support Particles in an Oxide-Supported Metal Catalyst: Nanocomposite Ni/ZrO 2 for Utilization of Natural Gas. *The Journal of Physical Chemistry B*, *107*(22), 5203–5207.

Xu, C., Han, Q., Zhao, Y., Wang, L., Li, Y., & Qu, L. (2015). Sulfur-doped graphitic carbon nitride decorated with graphene quantum dots for an efficient metal-free electrocatalyst. *Journal of Materials Chemistry A*, *3*(5), 1841–1846. https://doi.org/10.1039/C4TA06149G

Xu, H.-Y. Y., Wu, L.-C. C., Zhao, H., Jin, L.-G. G., & Qi, S.-Y. Y. (2015). Synergic Effect between Adsorption and Photocatalysis of Metal-Free g-C3N4 Derived from Different Precursors. *PLoS ONE*, *10*(11), e0142616.

Xu, H., She, X., Fei, T., Song, Y., Liu, D., Li, H. H., Yang, X., Yang, J., Li, H. H., Song, L., Ajayan, P. M., & Wu, J. (2019). Metal-Oxide-Mediated Subtractive Manufacturing of Two-Dimensional Carbon Nitride for High-Efficiency and High-Yield Photocatalytic H2 Evolution. *ACS Nano*, *13*(10), 11294–11302.

Yan, X., Zhou, C., Yan, Y., & Zhu, Y. (2015). A Simple and Renewable Nanoporous Gold-based Electrochemical Sensor for Bisphenol A Detection. *Electroanalysis*, *27*(12), 2718–2724.

Yang, P., Zhuzhang, H., Wang, R., Lin, W., & Wang, X. (2019). Carbon Vacancies in a Melon Polymeric Matrix Promote Photocatalytic Carbon Dioxide Conversion. *Angewandte Chemie International Edition*, *58*(4), 1134–1137.

Yang, T., Chen, H., Yang, R., Jiang, Y., Li, W., & Jiao, K. (2015). A glassy carbon electrode modified with a nanocomposite consisting of molybdenum disulfide intercalated into self-doped polyaniline for the detection of bisphenol A. *Microchimica Acta*, *182*(15–16), 2623–2628.

Yang, X., Qian, F., Zou, G., Li, M., Lu, J., Li, Y., & Bao, M. (2016). Facile fabrication of acidified g-C3N4/g-C3N4 hybrids with enhanced photocatalysis performance under visible light irradiation. *Applied Catalysis B: Environmental*, *193*, 22–35.

Yang, X., Zhao, L., Wang, S., Li, J., & Chi, B. (2021). Recent progress of g-C3N4 applied in solar cells. *Journal of Materiomics*, *7*(4), 728–741.

Yin, H., Zhou, Y., Ai, S., Liu, X., Zhu, L., & Lu, L. (2010). Electrochemical oxidative determination of 4-nitrophenol based on a glassy carbon electrode modified with a hydroxyapatite nanopowder. *Microchimica Acta*, *169*(1), 87–92.

You, R., Dou, H., Chen, L., Zheng, S., & Zhang, Y. (2017). Graphitic carbon nitride with S and O codoping for enhanced visible light photocatalytic performance. *RSC Advances*, *7*(26), 15842–15850.

Yu, H., Shi, R., Zhao, Y., Bian, T., Zhao, Y., Zhou, C., Waterhouse, G. I. N., Wu, L.-Z., Tung, C.-H., & Zhang, T. (2017). Alkali-Assisted Synthesis of Nitrogen Deficient Graphitic Carbon Nitride with Tunable Band Structures for Efficient Visible-Light-Driven Hydrogen Evolution. *Advanced Materials*, *29*(16), 1605148.

Yuan, H., Yu, J., Feng, S., & Gong, Y. (2016). Highly photoluminescent pH-independent nitrogen-doped carbon dots for sensitive and selective sensing of p-nitrophenol. *RSC Advances*, *6*(18), 15192–15200.

Yuan, J., Zhang, J. J., Yang, M. P., Meng, W. J., Wang, H., & Lu, J. X. (2018). Cuo nanoparticles supported on Tio2 with high efficiency for CO2 electrochemical reduction to ethanol. *Catalysts*, *8*(4).

Yuan, Y.-P., Xu, W.-T., Yin, L.-S., Cao, S.-W., Liao, Y.-S., Tng, Y.-Q., & Xue, C. (2013). Large impact of heating time on physical properties and photocatalytic H2 production of g-C3N4 nanosheets synthesized through urea polymerization in Ar atmosphere. *International Journal of Hydrogen Energy*, *38*(30), 13159–13163.

Zarei, M. (2020a). Sensitive visible light-driven photoelectrochemical aptasensor for detection of tetracycline using ZrO2/g-C3N4 nanocomposite. *Sensors International*, *1*(July), 100029.

Zarei, M. (2020b). Ultrasonic-assisted preparation of ZrO2/g-C3N4 nanocomposites with high visible-light photocatalytic activity for degradation of 4-chlorophenol in water. *Water-Energy Nexus*, *3*, 135–142.

Zhang, G., Zhang, J., Zhang, M., & Wang, X. (2012). Polycondensation of thiourea into carbon nitride semiconductors as visible light photocatalysts. *Journal of Materials Chemistry*, *22*(16), 8083–8091.

Zhang, J., Zhang, M., Zhang, G., & Wang, X. (2012). Synthesis of carbon nitride semiconductors in sulfur flux for water photoredox catalysis. *ACS Catalysis*, *2*(6), 940–948.

Zhang, J., Zheng, Y., Zheng, H., Jing, T., Zhao, Y., & Tian, J. (2022). Porous Oxygen-Doped g-C3N4 with the Different Precursors for Excellent Photocatalytic Activities under Visible Light. *Materials*, *15*(4), 1391.

Zhang, K., Zhou, M., Yu, C., Yang, K., Li, X., Dai, W., Guan, J., Shu, Q., & Huang, W. (2020). Construction of S-scheme g-C3N4/ZrO2 heterostructures for enhancing photocatalytic disposals of pollutants and electrocatalytic hydrogen evolution. *Dyes and Pigments*, *180*(May), 108525.

Zhang, R., Zhang, X., & Hu, S. (2010). High temperature and pressure chemical sensors based on Zr/ZrO2 electrode prepared by nanostructured ZrO2 film at Zr wire. *Sensors and Actuators B: Chemical*, *149*(1), 143–154.

Zhang, S., Gao, L., Fan, D., Lv, X., Li, Y., & Yan, Z. (2017). Synthesis of boron-doped g-C3N4

with enhanced electro-catalytic activity and stability. *Chemical Physics Letters*, *672*, 26–30.

Zhang, S., Su, C., Ren, H., Li, M., Zhu, L., Ge, S., Wang, M., Zhang, Z., Li, L., & Cao, X. (2019). In-Situ Fabrication of g-C3N4/ZnO Nanocomposites for Photocatalytic Degradation of Methylene Blue: Synthesis Procedure Does Matter. *Nanomaterials*, *9*(2), 215.

Zhang, Y., Liu, J., Chu, X., Liang, S., & Kong, L. (2020). Preparation of g–C3N4–SnO2 composites for application as acetic acid sensor. *Journal of Alloys and Compounds*, *832*, 153355.

Zhao, W., Feng, Y., Huang, H., Zhou, P., Li, J., Zhang, L., Dai, B., Xu, J., Zhu, F., & Sheng, N. (2019). A novel Z-scheme Ag3VO4/BiVO4 heterojunction photocatalyst: study on the excellent photocatalytic performance and photocatalytic mechanism. *Applied Catalysis B: Environmental*, *245*, 448–458.

Zheng, A. L. T., & Andou, Y. (2022). Detection and remediation of bisphenol A (BPA) using graphene-based materials: mini-review. *International Journal of Environmental Science and Technology*, *19*(7), 6869–6888.

Zhou, C., Wu, Y., Yan, X., Wang, J.-J., Wang, Q., Wang, D., Yuan, X., Pan, J., & Cheng, X. (2020). Is CuO Suitable for Improving the Electrochemical Properties of g-C 3 N 4 ? *Journal of Nanoscience and Nanotechnology*, *20*(6), 3415–3423.

Zhou, Y., Zhang, L., Liu, J., Fan, X., Wang, B., Wang, M., Ren, W., Wang, J., Li, M., & Shi, J. (2015). Brand new P-doped g-C 3 N 4 : enhanced photocatalytic activity for H 2 evolution and Rhodamine B degradation under visible light. *Journal of Materials Chemistry A*, *3*(7), 3862–3867.

Zhu, D., & Zhou, Q. (2021). Nitrogen doped g-C3N4 with the extremely narrow band gap for excellent photocatalytic activities under visible light. *Applied Catalysis B: Environmental*, *281*(September 2020), 119474.

Zhu, J., Wei, Y., Chen, W., Zhao, Z., & Thomas, A. (2010). Graphitic carbon nitride as a metal-free catalyst for NO decomposition. *Chemical Communications*, *46*(37), 6965–6967.

Zhu, J., Xiao, P., Li, H., & Carabineiro, S. A. C. S. A. C. (2014). Graphitic Carbon Nitride: Synthesis, Properties, and Applications in Catalysis. *ACS Applied Materials & Interfaces*, *6*(19), 16449–16465.

Zou, J., Wu, S., Liu, Y., Sun, Y., Cao, Y., Hsu, J. P., Shen Wee, A. T., & Jiang, J. (2018). An ultra-sensitive electrochemical sensor based on 2D g-C3N4/CuO nanocomposites for dopamine

detection. *Carbon*, *130*, 652–663.

Zou, J., Yu, Y., Yan, W., Meng, J., Zhang, S., & Wang, J. (2019). A facile route to synthesize boron-doped g-C3N4 nanosheets with enhanced visible-light photocatalytic activity. *Journal of Materials Science*, *54*(9), 6867–6881.

Zou, X.-X., Li, G.-D., Wang, Y.-N., Zhao, J., Yan, C., Guo, M.-Y., Li, L., & Chen, J.-S. (2011). Direct conversion of urea into graphitic carbon nitride over mesoporous TiO 2 spheres under mild condition. *Chemical Communications*, *47*(3), 1066–1068.

7. APPENDICES

Appendix 1. High-resolution spectra of the constituent elements S *2p*, C *1s*, N *1s*, O *1s*, and Cu *2p* of CuO@S-doped g-C_3N_4 nanocomposites

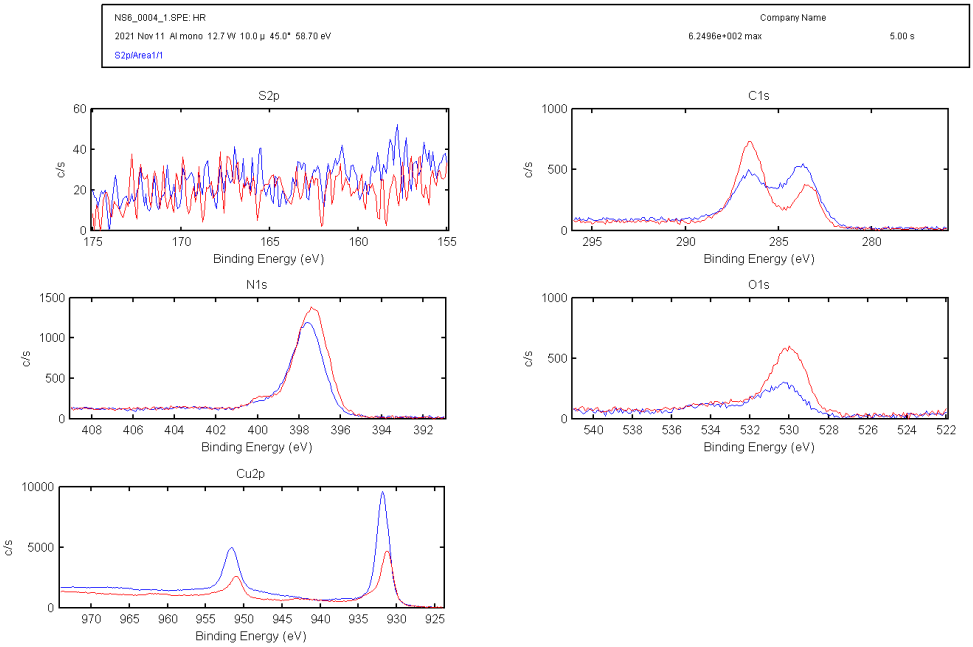

Appendix 2. High-resolution XPS for C *1s*, N *1s*, and S *2p*

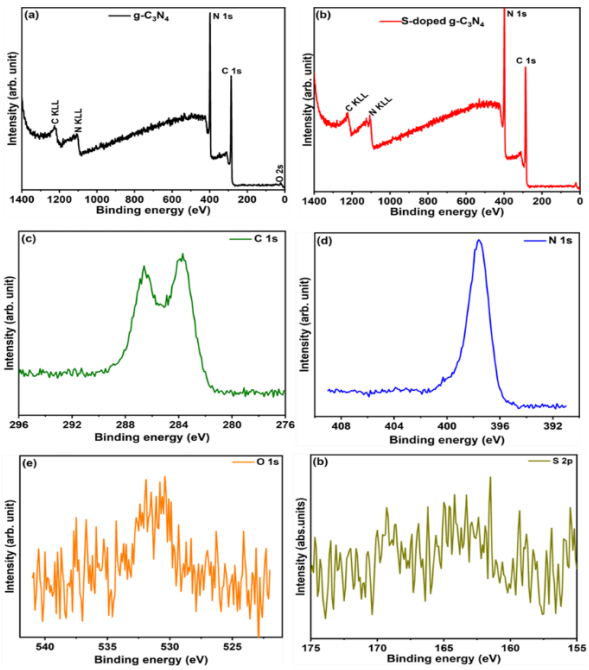

Appendix 3. High-resolution spectra of the constituent elements C *1s*, and N *1s*, of ZrO_2@S-doped g-C_3N_4 nanocomposites

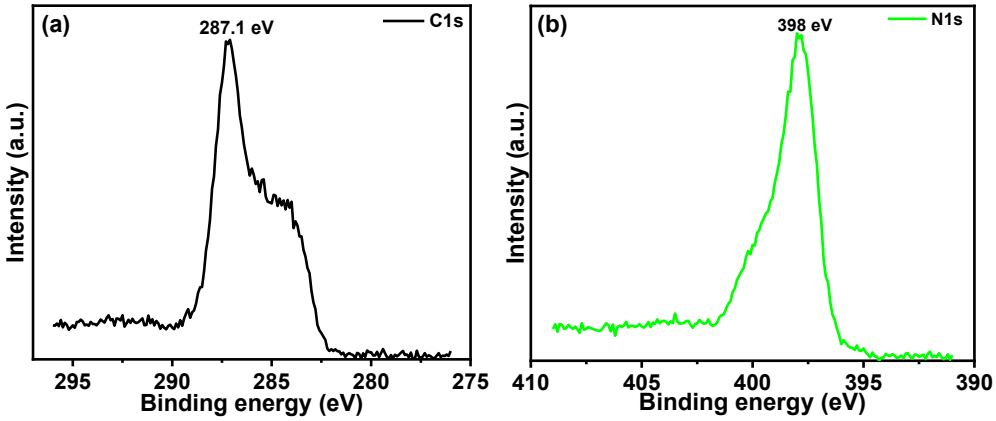

Appendix 4. M-S curves for CuO@S-doped g-C_3N_4, CuO/ZrO_2@S-doped g-C_3N_4 and CuO@S-doped g-C_3N_4 NCs.

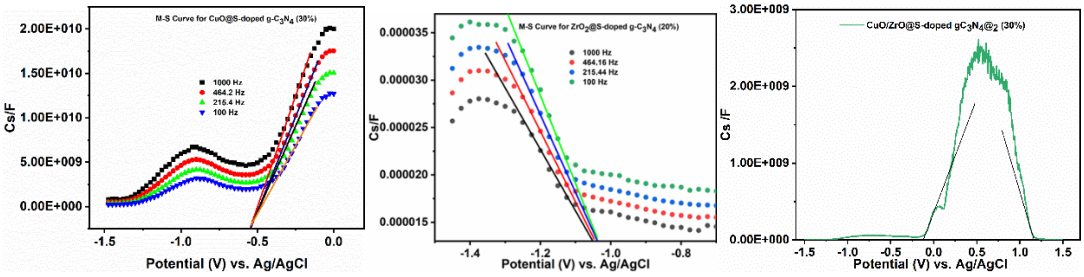

Appendix 5. Electrochemical oxidation reaction mechanism of BPA at CuO@S-doped g-C3N4 (30%)/CPE, ZrO2@S-doped g-C3N4(20%)/CPE and CuO/ZrO2@S-doped g-C3N4(30%/CPE

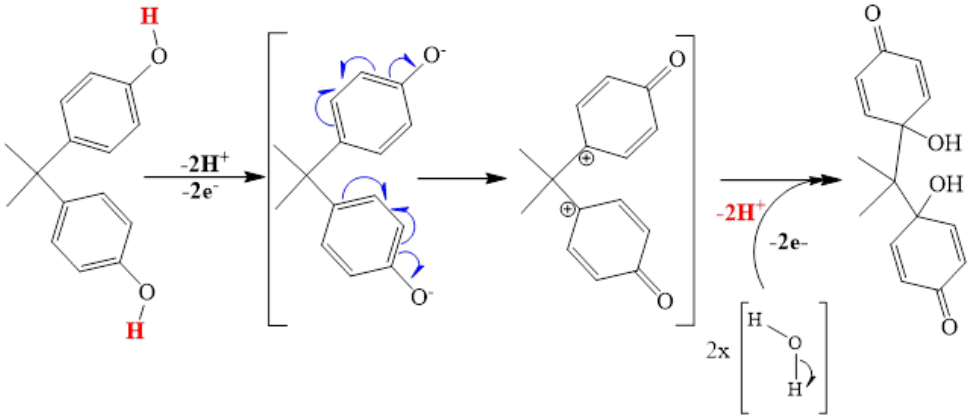

Appendix 6.Publications from this work

1. Nigussie Alebachew, H. C. Ananda Murthy, Bedassa Abdissa, Taye B. Demissie, Karel G. von Eschwege, Ernst H. G. Langner and Liza Coetsee-Hugo· Synthesis and characterization of CuO@S-doped g-C_3N_4 based nanocomposites for binder-free sensor applications. The Royal Society of Chemistry. (Impact factor = 4.036) DOI: 10.1039/d2ra04752g RSC Adv., 2022, 12, 29959.

2. Nigussie Alebachew, H. C. Ananda Murthy, Bedasa Abdisa, Karel G. von Eschweg, Ernst H. G. Langner, and E. Coetsee, Taye B. Demissie. Nanocomposites with ZrO_2@S-Doped g-C_3N_4 as an Enhanced Binder-Free Sensor: Synthesis and Characterization. ACS Publications. (Impact factor = 4.132) https://doi.org/10.1021/acsomega.2c08174 ACS Omega 2023, 8, 15, 13775–13790

3. A Nigussie, AM HC, A Bedassa - A Review on Synthesis, Characterization and Photocatalytic Applications of Copper Oxide Nanostructures Research Journal of Chemistry and Environment. Vol. 25 (6) June (2021) Res. J. Chem. Environ.

4. H. C. Ananda Murthy, Nigussie Alebachew, K B Tan, R Balachandran, Kah-Yoong Chan, C R Ravikumar. Metal-Doped Graphene Materials as Electrocatalysts in Sensors, Graphene-Based Nanomaterial Catalysis (2022). https://doi.org/10.2174/9789815040494122010009 Pp: 114-129 (16)

5. Nigussie Alebachew, H. C. Ananda Murthy, Bedasa Abdisa, Taye B. Demissie
   Important Features of Nanomaterials for Environmental Remediation. Green nano remediation pp 1-23 Springer Nature
   https://doi.org/10.1007/978-3-031-30558-